# Spin transfer torque driven magnetization switching in magnetic tunnel junction

Marion Lavanant

THÈSE

Pour l'obtention du titre de :

DOCTEUR DE L'UNIVERSITÉ DE LORRAINE

Spécialité : Physique

Présentée par :

MARION LAVANANT

# Retournement de l'aimantation dans des jonctions tunnels magnétiques par effet de transfert de spin

–

# Spin transfer torque driven magnetization switching in magnetic tunnel junctions

Thèse soutenue publiquement le 8 septembre 2017 à Nancy devant le jury composé de :

| | | | |
|---|---|---|---|
| Président du jury | Andrew D. Kent | Professeur | New York University |
| Rapporteurs | Claire Baraduc | Chercheur CNRS | SPINTEC - CEA Grenoble |
| | Dafiné Ravelosona | Directeur de recherche CNRS | IEF - Paris |
| Examinateurs | Grégoire de Loubens | Chercheur CNRS | SPEC - CEA Saclay |
| | Anne Bernand-Mantel (absente) | Chercheur CNRS | Institut Néel - Grenoble |
| | Vitaliy Lomakin | Professeur | CMRR - UC San Diego |
| Directeurs de thèse | Renaud Presberg (absent) | PDG | Vinci - Technologies |
| | Stéphane Mangin | Professeur | IJL – Nancy |
| | Sébastien Petit-Watelot | Maitre de conférences | IJL – Nancy |

Institut Jean Lamour, UMRS CNRS 7168
Université de Lorraine – Pôle M4 : matière, matériaux, métallurgie, mécanique

# Contents

# Remerciements

Ce manuscrit a pu voir le jour grâce au soutien d'un certain nombre de personnes que je tiens à remercier. Tout d'abord, mon directeur de thèse, Stéphane Mangin, pour m'avoir donné l'opportunité de réaliser cette thèse CIFRE au sortir de mon école d'ingénieurs, puis pour m'avoir soutenue au cours de ces trois années et demi de travail, tant au niveau scientifique qu'humain. Et un grand merci pour ses judicieux conseils lors de la préparation de la soutenance.

Comment ne pas mentionner Sébastien Petit-Watelot, mon co-directeur et mentor ? Sans ton suivi attentif de mon travail, nos nombreuses discussions scientifiques, cette thèse n'aurait pas eu la même teneur. Par ailleurs, je te sais gré de m'avoir formée aux mesures haute fréquence, à l'instrumentation des appareils de mesures et de m'avoir incluse dans l'élaboration du dispositif de mesures dynamiques.

Pour cette aventure qui n'était autre qu'un contrat CIFRE financé par Vinci Technologies, je tiens à remercier tout particulièrement M. Renaud Presberg, directeur industriel de ma thèse, pour m'avoir offert la chance de participer à ce sujet de recherche.

Cette thèse s'est faite en collaboration avec NYU et j'aimerais signifier l'allégresse que m'a procuré l'accueil du Pr. Andrew Kent pendant plus d'un an au sein de son équipe, les discussions scientifiques et la collaboration fructueuse que nous avons entretenues, ainsi que pour avoir fait le déplacement jusqu'à Nancy pour présider le jury de ma soutenance de thèse. Thank you Andy for your welcome in the group, our scientific discussions and for chairing my PhD defence.

Un autre partenariat est à mettre en exergue. De Pr. Vitaliy Lomakin de UCSD, a dépendu le succès de mes modélisations micromagétiques, notamment grâce à son aide avec l'implémentation

et la prise en main du logiciel FASTMAG (logiciel développé par son équipe). En outre, je le remercie de sa présence durant ma soutenance. Thank you Vitaliy for your help with FASTMAG and for coming to my defence.

Je voudrais exprimer ma gratitude aux rapporteurs de mon manuscrit, Claire Baraduc et Dafiné Ravélosona, ainsi qu'à l'examinateur de ma soutenance, Grégoire de Loubens, pour leurs lectures attentives et leurs commentaires sur ce manuscrit, ainsi que leurs questions avisées durant la soutenance.

Bien entendu, une thèse ne s'effectue pas dans la solitude, et j'ai eu le privilège de partager mon temps entre l'équipe «Nanomagnétisme et électronique de spin» de l'I.J.L., ainsi que le groupe du Pr. Andrew Kent a New York. Un grand merci à tous ceux qui m'ont accueillie dans ces groupes et m'ont permis de développer mon esprit scientifique et d'expérimentatrice.

Ces trois dernières années n'auraient pas été les mêmes sans le groupe de doctorants et post-doctorants que j'ai eu la bonne fortune de rencontrer. L'esprit de camaraderie de cette joyeuse confrérie, nos sorties, nos repas de midi et jeux de cartes, sans oublier des soirées jeux des plus conviviales qu'il soit, m'ont permis de faire face et surmonter les embûches de la vie de doctorant. Donc merci Damien, Sarah, Chris, Pierre, Seb, Kathleen, Julien, Thai Ha, Vincent, Charles, Elmer, Philippe ! Et plus spécifiquement, de très grands remerciements à mes colocataires et éditeurs, Alexandre et Thibaud (qui en ce moment même de sérénité nouvelle, s'amusent à retoucher ce recueil de remerciements), pour leur fort soutien moral dans les moments difficiles de la rédaction et la traque aux fautes d'orthographe dans mon manuscrit.

Pour terminer, je tiens à remercier fortement ma famille, pour leur soutien et leur aide continus : mes parents, Hélène et Vincent, pour avoir fait les déplacements depuis le sud pour venir me voir, que ce soit à New York ou à Nancy, et Aurélie, Florent et Martin pour m'avoir accueillie chez eux de nombreux weekends.

# Introduction – Français

Au cours des cinquante dernières années, les techniques de dépôts de couches minces, telles que la pulvérisation cathodique (P.V.D.) ou l'épitaxie par jet moléculaire (M.B.E.), ont connu un fort développement, permettant un contrôle précis de l'épaisseur, de la structure cristallographique et de la composition chimique des couches élaborées. Pour réaliser ces dernières et s'assurer de leur qualité, il est nécessaire de déposer les matériaux dans une enceinte sous ultravide, c'est-à-dire $10^{-7}$ – $10^{-10}$ mbar. Chacune de ces techniques de dépôt est utilisée spécifiquement pour obtenir un certain type de structure. Ainsi, par P.V.D., le dépôt est amorphe, tandis qu'en M.B.E., sa structure est contrôlée par le choix du substrat. Pouvoir analyser efficacement la structure cristallographique est nécessaire pour obtenir des films répondant aux attentes. Dans cette optique, dans divers laboratoires internationaux, des instruments pour permettre de relier les systèmes de dépôt et de caractérisation se développent : à Nancy par exemple, le Tube Davm, développé par l'institut Jean Lamour et Vinci Technologies, connecte près de trente systèmes de dépôt et chambres de caractérisation sous ultravide dans un tube de soixante-dix mètres de long. Ce doctorat a été financé par Vinci Technologies, entreprise spécialisée dans le développement d'enceintes sous ultravide, plus particulièrement de P.V.D. et M.B.E..

Grâce à l'avancée de ces techniques, Jullière en 1975 [1] a découvert la magnétorésistance tunnel (T.M.R.) : dans des structures magnétiques/non-magnétiques/ magnétiques, la résistance dépend de l'orientation relative des deux directions d'aimantation des couches magnétiques. Cet effet ne peut être observé que si la couche non magnétique est un isolant et qu'elle est suffisamment fine pour agir comme une barrière de potentiel, forçant les électrons à se déplacer par effet tunnel et si une seule des deux couches magnétiques, appelée couche libre, peut être manipulée par le champ magnétique appliqué au pilier, tandis que l'aimantation de l'autre couche, appelée

couche référence, être fixée.

Jullière utilisait un semiconducteur pour sa couche non-magnétique (Fe/Ge/Pd et Fe/Ge/Co) et a montré qu'à une température de 4 K, la résistance de l'échantillon dépend de la polarisation des électrons qui traversent la barrière de potentiel (couche de germanium) par effet tunnel. Ces électrons forment un courant polarisé en spin. Les aimantations dans les couches magnétiques peuvent être alignées parallèlement ou antiparallèlement entre elles, ce qui crée une résistance respectivement faible ou forte. Dans les années suivantes, un effet similaire, appelé magnétorésistance géante, a été étudié de manière extensive dans un autre type de tri-couches magnétique/non magnétique/magnétique appelé "vannes de spin", où l'effet de magnétorésistance géante existe à température ambiante. Ces découvertes ont ouvert un nouveau champ d'application, l'électronique de spin ou spintronique, qui a conduit au prix Nobel de Albert Fert et Peter Grünberg en 2007. Depuis 1995, des jonctions tunnel magnétiques avec une structure magnétique/isolant/magnétique sont étudiées à température ambiante. A la difference des vannes de spin, elles présentent de larges magnétorésistances dues à l'effet tunnel [2, 3].

La spintronique est un pan de l'electronique qui s'interesse aux interactions entre le moment angulaire intrinsèque des electrons, leur spin, et l'aimantation de couches minces ferromagnétiques. Dans un premier temps, il a été démontré que le courant polarisé en spin était modifié par la direction de l'aimantation dans la couche mince, ce qui a conduit aux travaux sur la magnétorésistance géante et la magnétorésistance tunnel. La possibilité d'obtenir de larges rapports de magnétorésistance en fait des dispositifs intéressants pour la conservation des données numériques. En effet, les jonctions tunnel magnétiques peuvent être considérées comme des systèmes binaires où la configuration est discernable grâce à la lecture de la résistance par un courant [4]. Le développement des dispositifs de la spintronique a pu se faire grâce aux améliorations des systèmes de dépôt.

Les mémoires non volatiles magnétiques (MRAM) et les disques durs sont basés sur l'effet de magnétorésistance. Une façon de manipuler l'information, c'est-à-dire retourner la direction de l'aimantation de l'une des deux couches magnétiques, est d'appliquer un champ magnétique externe additionel. Une autre façon d'écrire l'information à été introduite en 1996 par Slonczewski [5] et Berger [6]. De manière indépendante, ils ont prédit qu'un courant polarisé en spin peut

manipuler la direction de l'aimantation en fonction du signe du courant appliqué. Cet effet, appelé couple de transfert de spin, devient intéressant pour des applications industrielles quand il est associé à la réduction de la taille des dispositifs jusqu'à des grandeurs compatibles avec les technologies des transistors [7]. La technologie associée s'appelle STT-MRAM. Afin qu'elle soit compétitive avec les autres types de mémoires, l'évolution de cette technologie s'est concentrée dans un premier temps sur l'amélioration du rapport de magnétorésistance tunnel, puis s'est intéressée aux solutions de réduction de la puissance nécessaire pour écrire l'information tout en conservant une stabilité thermique suffisante en vue d'assurer la conservation de l'information. Les matériaux utilisés en particulier pour obtenir une magnétorésistance tunnel adéquate ont la structure suivante : Ta/CoFeB/MgO /CoFeB/Ta et les rapports de magnétorésistance tunnel obtenus peuvent atteindre 600% [8].

Depuis 2010, les jonctions tunnel magnétiques avec une direction de l'aimantation hors du plan de la couche mince sont au centre de l'attention. Grâce à un procédé spécifique demandant la maîtrise de l'épaisseur et de la composition chimique des couches magnétiques, il est possible d'obtenir une aimantation hors du plan tout en conservant le rapport de T.M.R.. Dans cette configuration la puissance nécessaire à l'écriture est réduite du fait de la compétition du champ démagnétisant, tendant à aligner l'aimantation dans le plan, et l'anisotropie de surface, qui lui donne son orientation hors du plan. Les jonctions tunnel magnétiques sont composées d'une couche libre et d'une couche de référence. La couche de référence est maintenue dans une direction fixée grâce à un empilement de couches magnétiques formant une structure antiferromagnétique artificielle (SAF). Celle-ci a pour double objectif de fixer la direction de l'aimantation de la couche de référence et de réduire les effets de décalage en champ dus à la structure magnétique complexe de la jonction elle-même [9].

Le sujet de ce manuscrit est de comprendre les effets de cette structure sur le retournement de l'aimantation de la couche libre par effet de couple de transfert de spin dans des jonctions tunnel magnétiques à aimantation perpendiculaire. Plus précisément, il cherche à répondre aux questions suivantes : Est-il possible de décrire les conditions du retournement de l'aimantation de la couche libre à l'aide d'un modèle macrospin simple? Quelle serait l'influence de la direction de l'anisotropie? Sous quelles conditions des oscillateurs magnétiques peuvent-ils être obtenus dans des jonctions tunnel magnétiques à aimantation perpendiculaire ? Ce manuscrit, le retournement

de la couche libre d'un dispositif suite à l'effet du couple de transfert de spin sera décrit. Quelle est l'influence de la structure et de la dimension de la jonction sur le processus de retournement? Enfin, ce type de comportement peut-il être représenté à l'aide de simulations micromagnétiques ?

Tout d'abord, nous traiterons de l'élaboration des jonctions tunnel magnétiques à aimantation perpendiculaire tout en introduisant le couple de transfert de spin, puis nous étudierons un modèle macrospin basé sur la puissance dissipée et les effets de différentes géométries sur les états stables de l'aimantation dans la jonction. La troisième partie présentera une description probabiliste du retournement de l'aimantation par activation thermique puis par effet du couple de transfert de spin en fonction du champ magnétique appliqué. Nous y discuterons notamment de la différence de stabilité des deux configurations magnétiques de la jonction tunnel, en fonction de sa structure et de sa taille. Enfin, nous présenterons une modélisation micromagnétique du système afin d'affiner notre compréhension du processus de retournement de l'aimantation. Nous conclurons sur des stratégies pour réduire la puissance d'écriture.

# Introduction – English

In the last fifty years, thin film deposition systems, such as Physical Vapor Deposition (PVD) and Molecular Beam Epitaxy (MBE), improved vastly, allowing a precise control of the deposited film thicknesses, structures and compositions. Ultra-high vacuum growth chambers, down to $10^{-7}$ – $10^{-10}$ mbar, allow the control of the quality and the composition of the deposited layers. The elaboration of thin films for specific applications needs a comprehensive choice of substrate and analysis of the system crystallography. Each deposition system is dedicated to a certain type of materials. In a PVD, the thin-film deposited is amorphous, whereas in an MBE its structure is determined by the substrate choice. Analysis of the thin film structure is necessary to control the quality of the deposited material to be of use in the corresponding applications. For this purpose, in several international laboratories, solutions to link deposition systems and characterization tools are developed. In Nancy, a tool called Tube Davm was developed by the Institut Jean Lamour and Vinci-Technologies, to connect under ultra-high vacuum about thirty deposition systems and characterization chambers on a distance over seventy meter long. My PhD was sponsored by Vinci Technologies, which is a medium sized company specialized in the development of ultra-high vacuum deposition chambers, especially PVD and MBE systems.

The refinement of these deposition techniques led to the discovery of the tunnel magnetoresistance (TMR) by Jullière in 1975 [1]. In ferromagnetic/non-ferromagnetic/ferromagnetic structure, the resistance depends on the relative orientation of the two ferromagnets thin film magnetization directions. This effect can only be observed if the non-magnetic layer is an insulator and is thin enough to act as a tunnel barrier and that only one of the ferromagnetic layers, the free layer, is sensitive to an external applied magnetic field while the magnetization of the other layer, the reference layer, is pinned.

Using trilayers with a semiconducting non-magnetic layer (Fe/Ge/Pd and Fe/Ge/Co) at low temperature (4K), Jullière showed that the resistance of the device depends on the polarization of the electrons tunneling through the germanium layer, forming a spin-polarized current. The magnetization in the ferromagnetic layers can align parallel or antiparallel to each other, leading respectively to a small or large resistance. In the following years, another effect present similar resistance variations behaviors, the giant magnetoresistance (GMR), was extensively studied in another type of ferromagnetic/non-magnetic/ferromagnetic trilayer structures, called spin valves, where the non-magnetic layer is conducting. These discoveries opened a new field of applications called spin electronics or spintronics and led to the Nobel prize given to Albert Fert and Peter Grünberg in 2007. Since 1995, room temperature magnetic tunnel junctions (MTJ) with a ferromagnet/insulator/ferromagnet structures have been studied and very large tunnel magnetoresistances have been measured [2, 3].

Spintronics is the study of the interaction between a spin-polarized current and ferromagnetic thin films. First, it has been demonstrated that the spin-polarized current is affected by the magnetization orientation, seen in the giant magnetoresistance and tunnel magnetoresistance studies. The large magnetoresistance ratio made the magnetic tunnel junctions interesting for information storage. It can be considered as a binary system where the state can be determined by resistance measurements [4]. The development of spintronics devices was made possible thanks to the improvement of deposition systems.

Magnetic random access memories (MRAM) and hard drives, are based on this principle where each memory point is a magnetic tunnel junction. Information is written by switching the magnetization direction in one of the two magnetic layers using a magnetic field. Another way to write the information has been predicted in 1996 by Slonczewski [5] and Berger [6]. They independently showed that depending on the applied current sign, the polarized current can modify the direction of the magnetization. This effect, called spin transfer torque, associated with the scalability of magnetic tunnel junctions [7], makes this type of memory highly compatible with CMOS technologies. The technology based on this effect is called “STT-MRAM”. In order to be competitive with other types of computer memories, the devices need a consequential TMR ratio as well as solutions to reduce the writing power and the writing time, while keeping the thermal stability large enough to be compatible with information storage. The most proficient structure

used nowadays is a Ta/CoFeB/MgO/CoFeB/Ta multilayer structure that offers an easy free layer manipulation and a large TMR ratio (up to 600%) [8].

Since 2010, magnetic tunnel junctions with an out-of-plane direction of the magnetization are investigated. By using specific thicknesses and elaboration process for the CoFeB layer, it is possible to obtain perpendicular magnetic layers while keeping a good TMR ratio. In that configuration, the writing power is reduced due to the competition between the in-plane and out-of-plane magnetic contributions of the structure. The magnetic tunnel junctions are composed of one free layer and one reference layer; the reference layer is pinned in a certain direction using a complex structure of magnetic layers forming a synthetic antiferromagnetic structure (SAF) that has the double aim to pin the reference layer magnetization direction and to remove offsets in magnetic field switching due to stray fields from the internal tunnel junction structure [9].

The subject of this manuscript is to investigate the effects of this complex structure in a perpendicularly polarized tunnel junction during a spin transfer driven magnetization switching. Especially, it aims to answer the following questions: Is it possible to describe the switching condition in a magnetic tunnel junction using a simple macrospin model? What are the condition to obtain steady state oscillators in fully perpendicular magnetic tunnel junction? In regard to the switching, spin transfer torque driven switching is often treated as an effective temperature to express the corresponding switching probability. Can thermally activated switching and spin transfer driven switching be compared? What are the influences of the structure and of the junction size on the switching process? Can this type of behavior be modeled using micromagnetic simulations?

First, this manuscript will discuss the elaboration of a perpendicularly magnetized magnetic tunnel junction while introducing the different theories on spin-polarized torque. Then it will discuss a macrospin model based on power dissipation and the effects of different geometries on the magnetization stable states in a tunnel junction. The next part introduces a probabilistic description of thermally activated and spin transfer torque driven switching. It will discuss the difference in stability of the two magnetic configurations in the tunnel junction, depending on its structure and size. Finally, a micromagnetic representation of the tunnel junctions from the third part using the software FASTMAG will be presented, in order to verify our interpretation of the

asymmetry of the energy barrier in the tunnel junction found in the third part. The conclusion will focus on strategies to reduce the writing power in the tunnel junction.

# Chapter I

# State of the art and characteristic parameters

## Résumé en français

Cette partie introduit succintement les principes du magnétisme et de l'électronique de spin nécessaires à la description de la dynamique de l'aimantation sous l'effet d'un courant polarisé en spin. Un état de l'art de l'élaboration des jonctions tunnel magnétiques est aussi présenté.

Le développement et l'amélioration des techniques de dépôt de couches minces sous ultra-vide a permi l'évolution des dispositifs magnétiques se basant sur le principe de l'électronique de spin. Le contrôle des couches à l'échelle atomique est nécessaire pour réaliser de tels dispositifs, en particulier les jonctions tunnels magnétiques (MTJ). Cette maîtrise accrue de l'épaisseur, de la structure et des propriétés électroniques des matériaux déposés apporte en conséquence une meilleure compréhension des phénomènes fondamentaux régissant les propriétés des effets de transfert de spin dans les MTJ.

Les jonctions tunnels magnétiques sont composées de deux couches minces magnétiques séparées par une couche isolante formant une barrière tunnel. Elles sont élaborées de manière à présenter deux configurations stables : l'alignement parallèle des aimantations dans les deux couches magnétiques, correspondant en général à une basse résistance et celui antiparallèle, correspondant à une haute résistance. L'équation décrivant la dynamique de l'aimantation dans les couches magnétiques est appelée équation de Landau-Lifshitz-Gilbert. Elle permet d'exprimer la trajectoire d'un moment magnétique quelconque soumis à un champ magnétique, prenant

en compte les interactions magnétiques propres aux matériaux et un effet observé phénoménologiquement de la dissipation d'énergie (amortissement). Afin de représenter complètement les interactions dans notre système, d'autres paramétres doivent être integrés. En effet, la jonction tunnel étant constituée d'une couche libre et d'une couche de référence (fixe), il faut tenir compte de l'influence d'une couche sur l'autre par l'intermédiaire des champs dipolaires ou champs rayonnés. Ces champs dépendent de la géometrie considérée et leur intensité peut varier avec la position. Pour introduire l'évolution spatiale de l'aimantation d'une jonction tunnel, une description micromagnétique est utilisée.

La dépendance de la résistance d'une jonction tunnel magnétique en fonction de sa configuration magnétique s'appelle la magnétorésistance tunnel (TMR) : pour un alignement parallèle des aimantations, la résistance de la jonction tunnel est basse, comparée à la résistance pour la configuration où les aimanations des électrodes sont antiparallèles. Ce phénomène est expliqué par la polarisation en spin des électrons: lors du déplacement d'électrons dans une couche magnétique, leurs spins s'alignent dans la direction de l'aimantation de la couche. De plus, les électrons pouvant traverser la barrière tunnel (couche isolante) par effet tunnel sont sélectionnés en fonction de la direction de leur spin, en suivant la régle d'or de Fermi. Ceux dont le spin est aligné avec la direction de l'aimantation de la couche magnétique de l'autre côté de la barrière tunnel sont majoritaires à traverser la barrière. La capacité des électrons à se propager dans le dispositif dépend donc de la configuration relative des aimantations des deux électrodes et la quantité d'électrons pouvant être polarisés par la couche magnétique dépend de la qualité de son interface avec la couche isolante.

L'effet réciproque de la sélection des électrons pouvant traverser les interfaces implique, par conservation du moment angulaire, que le courant de spin peut modifier la direction de l'aimantation dans une couche magnétique : ce phénoméne est appelé couple de transfert de spin (STT). Cet effet a été prédit par Slonczewski et Berger en 1996[5, 6] et son action permet de manipuler la direction de l'aimantation de la couche libre dans une jonction tunnel ou une vanne de spin. L'équation L.L.G.S. (Landau-Lifshitz-Gilbert-Slonczewski) permet de décrire l'évolution de l'aimantation quand elle est soumise à trois couples : le couple dû au champ appliqué qui provoque la précession de l'aimantation, le couple qui permet de décrire l'amortissement du système (dissipation d'énergie) et le couple de transfert de spin. Ce dernier a la même direction que le

couple d'amortissement pour des nanopiliers où les aimantations des deux couches magnétiques sont orientées dans la même direction à l'équilibre. Suivant la direction de la tension appliquée, l'amortissement de la trajectoire de l'aimantation est soit favorisée par le couple de transfert de spin, soit ralentie.

La figure I.1 ci-dessous schématise la direction des différents couples. La valeur du couple de transfert de spin est fonction de l'angle entre les deux aimantions et dépend de la structure de l'électrode. Suivant le raisonnement précédent, la tension nécessaire au retournement de l'aimantation d'une des couches dépend de la compétition entre le couple de transfert de spin (STT) et celui d'amortissement, ainsi que d'un paramètre qui permet de caractériser la stabilité du dispositif face à l'excitation thermique : la hauteur de barrière d'énergie entre les deux configurations stables.

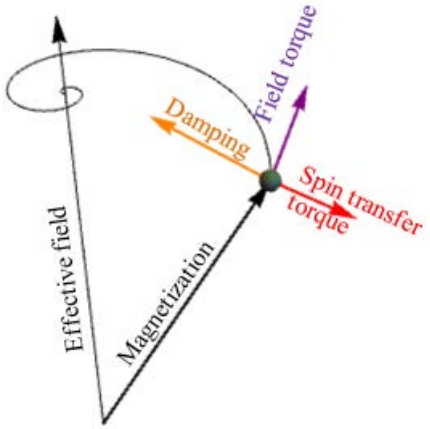


*Figure I.1: Effets des différents couples (amortissement en orange, field-like torque en violet et couple de transfert de spin en rouge) sur l'aimantation*

Les mémoires magnétiques nommées STT-MRAM sont basées sur la manipulation de la direction de l'aimantation des points mémoires grâce au couple de transfert de spin pour écrire l'information. Les dispositifs sont optimisés dans le but d'obtenir une bonne efficacité énergétique (soit une tension faible appliquée nécessaire pour retourner l'aimantation) tout en maintenant une bonne stabilité thermique (soit la barrière de potentiel entre les deux états d'équilibre suffisament grande). Une manière d'obtenir un bon compromis entre tension de retournement faible et stabilité thermique est d'utiliser des matériaux où l'aimantation est perpendiculaire au plan des électrodes. Les structures de type Ta/CoFeB/MgO/CoFeB/Ta permettent d'obtenir des

jonctions tunnels magnétiques présentant à la fois une anisotropie magnétique perpendiculaire et un grand pourcentage de TMR. [4, 10]

Dans une jonction tunnel, il est important qu'une seule des deux électrodes puisse voir la direction de son aimantation modifiée, on appelle cette couche la couche libre, à la différence de la couche de référence dont la direction d'aimantation est piégée, généralement en la couplant à une couche antiferromagnétique. Par ailleurs, afin de minimiser l'influence d'une couche sur l'autre au travers du rayonnement de son champ dipolaire une multicouche appelée SAF (synthetic antiferromagnet) est utilisée. L'aimantation moyenne de la structure SAF et son champ dipolaire rayonné sont nuls.

Pour que la technologie STT-MRAM soit viable, les jonctions tunnels magnétiques doivent présenter un faible taux d'erreur à l'écriture [11], un processus de retournement de l'aimantation rapide [4] et un couple de transfert de spin efficace [12] ; la taille des dispositifs doit également pouvoir être réduite [7].

# Introduction

Spintronics is a global term for the applications of the interactions between a spin-polarized current and a magnetic material. The development of this research field has been concomitant with the improvement of thin films deposition techniques. This part aims to introduce the basic concepts of magnetism needed to understand the evolution of a ferromagnetic thin film magnetization under an applied magnetic field and an applied bias voltage while in presence of other magnetic layers.

The magnetization behavior in a ferromagnetic material in a uniform applied field is governed by a conservative torque due to the effective magnetic field (applied magnetic field and internal contribution of the material) and by a non-conservative torque, named damping torque due to a dissipation of energy. The equation describing the magnetization dynamic is the Landau-Lifshitz-Gilbert (LLG) equation.

Spin torque effects were predicted in 1996 by MM. Slonczewski and Berger.[5, 6, 13] The most studied effect, already in use for industrial applications, is the spin transfer torque. It is mainly used for data recording [4], memories and logic application [4, 7, 14, 15]. Other applications of the spin transfer torque are oscillators [16–18], and the propagation of domain walls in nanowires [19–25]. Another phenomenon, called spin-orbit torque, is gathering a lot of interest as it is also able to manipulate the magnetization direction using either the spin-Hall effect or the Rashba effect [26–31]. This manuscript will focus on the spin transfer torque effect for memory applications and especially magnetic random access memories (MRAM).

MRAM memory bits are magnetic tunnel junctions (MTJ). A magnetic tunnel junction is shaped as a nanopillar, where two ferromagnetic layers are separated by an oxide layer, forming a tunnel barrier. When a current flows through the device, it is first polarized by the first ferromagnetic layer, then its ability to tunnel through the barrier is controlled by the direction of the second layer according to Fermi golden rules. The device resistance depends on the relative alignment of the magnetization in the two magnetic layers and can take two stable states: a parallel alignment, generally corresponding to a low resistance and an antiparallel alignment generally corresponding to a high resistance. This effect is named the tunnel magnetoresistance

(TMR) and it can be used to store the binary information.

In this manuscript, we are interested in a new type of magnetic memories using the reciprocal effect of polarization of the electrons, the spin transfer torque (STT). In these memories, called STT-MRAM, both the writing and the reading of the information are performed using current. The spin transfer torque can be understood as the conservation of momentum of the electron during the crossing of the tunnel barrier. It acts as a torque collinear to the damping torque, but its sign depends on the applied current sign, thus it can impede or accelerate the damping effect or even switch the magnetization direction.

The switching voltage value to change the configuration of the tunnel junction is determined by the relative efficiency of the spin transfer torque compared to the damping torque, but also by the energy barrier between the two configurations. This energy barrier denotes the thermal stability of the device. The benefit of using this technique to write the information lays in the speed of the writing process, the compatibility of the technology with CMOS applications, the possibility to embed the memory point close to the transistor and the low power consumption of such devices[3].

In this part, we first introduce briefly the origin of ferromagnetism in materials and the different magnetic interactions in a ferromagnetic material, before discussing the elaboration of magnetic tunnel junction and the tunnel magnetoresistance. This part then focuses on the spin transfer torque, and concludes on the equation of the magnetization dynamics that will be used in the following of the manuscript.

## I.1 Ferromagnetic materials

This part aims to introduce the basic definition of magnetism in materials. It focuses first on the definition of magnetism in matter and the physical origin of ferromagnetism, before describing the structure of magnetic tunnel junctions and the materials requirements.

### I.1.1 Magnetism in materials

For any material a magnetization $M$ can be defined, and if a magnetic field $H$ is applied on this material, in first order $M$ is given by:

$$M = \chi H \tag{I.1}$$

where $\chi$ is called the magnetic susceptibility. The different magnetic responses to a magnetic field define the main types of magnetism in materials:

- Diamagnetism: It is present in all materials and is easily evidenced when the material is non-magnetic. The magnetic response comes from the deformation of electronic orbitals by an applied field (Lenz law). In this case the susceptibility is negative, temperature independent and usually weak ($10^{-6}$ units) except for superconducting materials where $\chi = -1$.

- Paramagnetism: It is observed if the material can be described as made of atoms carrying a magnetic moment, but thermal activation and the lack of interaction between them lead to fluctuation and random orientation, thus a null magnetization when no magnetic field is applied. The susceptibility is positive and given by the Curie law:

$$\chi = \frac{C}{T} \tag{I.2}$$

- Ferromagnetism: in the same way to paramagnetism the material can be described as an assembly of magnetic atoms. Interactions between the moments lead to a parallel alignment; this is due to the exchange interaction between spins described below. For two spins $S_1$ and $S_2$, it is given by:

$$E_{exch} = -J\boldsymbol{S}_1 \cdot \boldsymbol{S}_2 \tag{I.3}$$

  with $J$ a positive coefficient

- Anti-ferromagnetism is observed when the exchange constant J is negative and ferrimagnetism is observed when two sublattices are present in the material. The total magnetization is obtained by defining sublattices of parallel moment and summing their contributions.

In this manuscript, we are interested in the ferromagnetic material constituting the magnetic tunnel junction. The next part is dedicated to describe succinctly the origin of the magnetic moment carried by an atom and itinerant magnetism, the two approaches to study electron motion between two transition metal electrodes in a magnetic tunnel junction.

## I.1.2 Origin of ferromagnetism in material

### *Magnetism in isolated atoms*

The magnetic moment $\boldsymbol{m}$ created by a moving charge is given by:

$$\boldsymbol{m} = \frac{1}{2}\int_{\mathcal{V}} \boldsymbol{r} \times \mathbf{j}(r) d\mathcal{V} \tag{I.4}$$

where **j** is the current density, **r** the radius and $\mathcal{V}$ the volume. In the classical approach, an approximation is to consider the electron rotating in a circular orbit around a nucleus, such as represented in figure I.2.

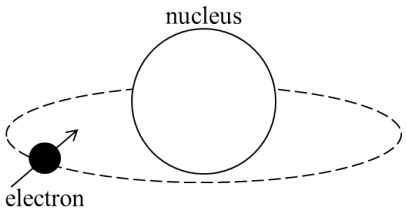


*Figure I.2: schematic of an electron orbiting around a nucleus in a circular orbit.*

The electron presents in that case a total magnetic moment $\boldsymbol{m}_t$ composed of the orbital magnetic moment $\boldsymbol{m}_o$ due to its rotation around the nucleus and an additional magnetic moment $\boldsymbol{m}_s$ due to the intrinsic movement of the electron, called spin.

$$\boldsymbol{m}_t = \boldsymbol{m}_o + \boldsymbol{m}_s \tag{I.5}$$

Using a quantum representation, we define the angular moments $\boldsymbol{\mathcal{L}}_o$ and $\boldsymbol{\mathcal{L}}_s$ corresponding respectively to the orbital and spin magnetic moments of the electron:

$$\begin{cases} \boldsymbol{\mathcal{L}}_o &= \hbar\boldsymbol{\ell} \\ \boldsymbol{\mathcal{L}}_s &= \hbar\boldsymbol{s} \end{cases} \tag{I.6}$$

with $\hbar$ the Planck constant divided by $2\pi$, and $\boldsymbol{\ell}$ and $\boldsymbol{s}$ unitless vector operators characterized by their eigenvalues:

$$\begin{cases} \langle \ell^2 \rangle &= \ell(\ell+1) \quad \& \quad \langle \ell_z \rangle &= m \\ \langle s^2 \rangle &= s(s+1) \quad \& \quad \langle s_z \rangle &= \sigma \end{cases} \tag{I.7}$$

with $\ell$ and $m$ integer value depending on the energy level of the electron, $s = \frac{1}{2}$ and $\sigma = \pm\frac{1}{2}$. The sign of $\sigma$ gives the electron spin value. It can take two configurations; electrons are said to

have a "spin-up" or "spin-down", noted respectively $\uparrow$ and $\downarrow$ in the following of the manuscript. In that notation, the magnetic moments of the electron have the following expression:

$$\begin{cases} \boldsymbol{m}_o &= -\mu_B \boldsymbol{\ell} \\ \boldsymbol{m}_s &= -2\mu_B \boldsymbol{s} \end{cases} \tag{I.8}$$

with $\mu_B = \frac{\hbar e}{2m_e}$, where $e$ is the charge of an electron, $m_e$ the electron mass and $\mu_B$ is called the Bohr magneton. This Bohr magneton is the smallest magnetic quantity and is used as a reference quantity. The previous computation is realized for an atom with one electron. In order to obtain the magnetic moment of the atom, considering all of its electrons, one have to take into account the repartitions of the electron on the electron shells, or electron orbitals, each corresponding to a different energy level. The electrons fill the lower energy level first before changing orbitals and the number of electrons able to stay on one orbital is given by $2(2\ell+1)$. The orbital and spin angular moments of the electronic structure is given by:

$$\begin{cases} \boldsymbol{L} &= \sum \boldsymbol{\ell}_i \\ \boldsymbol{S} &= \sum \boldsymbol{s}_i \end{cases} \tag{I.9}$$

Note that for a full electronic shell, the magnetic moments are zero, thus $\boldsymbol{L}$ and $\boldsymbol{S}$ of the non-full shell will give the orbital and spin moments of the isolated atom. The interaction between the orbital and spin moments of each electron can be decribed in one global interaction $\mathcal{H}_{so}$ named the spin-orbit coupling.

$$\mathcal{H}_{so} = \lambda \boldsymbol{L} \cdot \boldsymbol{S} \tag{I.10}$$

The sign of the parameter $\lambda$ is shown to depend on the filling of the electron shell, as it is negative for a less than half-full shell and positive for a more than half full shell.

Finally the total angular momentum of an atom $\hbar\boldsymbol{J}$ is given by the contribution of the sum of orbital and spin angular moments in the atom $\boldsymbol{J} = \boldsymbol{L} + \boldsymbol{S}$ and the corresponding magnetic moment is given by:

$$\boldsymbol{m} = -g_L \mu_B \boldsymbol{J} \tag{I.11}$$

where $g_L$ is the Landé factor. The value of this factor depends on the quantic number of the electron shell carrying the non-zero moments. In the extreme cases where only the orbital moment or the spin moment is present, $g_L$ is respectively equal to $1$ or $2$, but in general it can take values outside of these bonds.

This description applies to isolated atoms, and thus is used to explain magnetism from localized electrons around a nucleus when the non-full electronic shells are not pertubated by the interaction with the other atoms. However for any substance with a magnetic moment $\boldsymbol{m}$ and an angular momentum $\boldsymbol{\mathcal{L}}$ it is possible to write:

$$\boldsymbol{m} = -g_L \frac{e}{2m_e} \boldsymbol{\mathcal{L}} = \gamma \boldsymbol{\mathcal{L}} \tag{I.12}$$

with $\gamma$ the gyromagnetic ratio, whose value depends on the spin and the orbital contributions.

### *Itinerant magnetism*

Another representation of magnetism consists in considering that all the valence electrons are delocalized in the material: this approach is called itinerant magnetism and it is based on the consideration of the energy band structures as a function of the spin density of states in magnetic and non-magnetic metals [32, 33]. In a simple description, if a metal is non-magnetic there is an equipartition of the spin directions as a function of the state density (figure I.3 a) and the energy band is filled up to the Fermi energy ($E_F$).

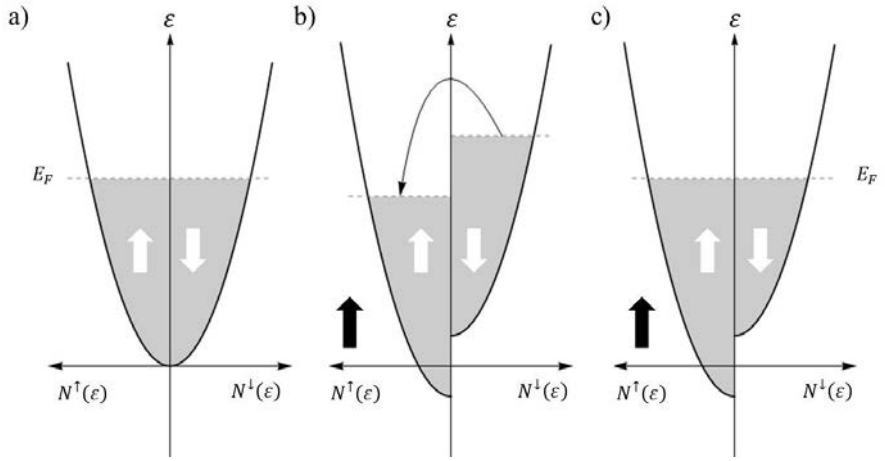


*Figure I.3: Band structure of a 3d metal as a function of the density of states for spin-up and spin-down. a) for no external applied field, b) the response for an extenal applied field (vertical black arrow), c) final distribution of states.*

Under an applied field, electrons whose spin aligned with the field will lose energy and those with a spin in the opposite direction will gain energy (figure I.3 b). Consequently, the energy in the metal is minimized when electrons with higher energy will flip their spins (figure I.3 c) and

as the magnetization is then given by the number of spin-up (spin-down) electrons, respectively $N^{\uparrow}$ ($N^{\downarrow}$), the total moment in $\mu_B$ is then given by:

$$\frac{m}{\mu_B} = (N^{\uparrow} - N^{\downarrow}) = \frac{1}{N}\sum_k [f(E_{k^{\uparrow}}) - f(E_{k^{\downarrow}}) \tag{I.13}$$

where $E_{k^{\uparrow}}$ ($E_{k^{\downarrow}}$) is the energy of the $k$ states for spin-up (spin-down), $N$ is the density of state of one spin direction at the Fermi energy level by units of volume and energy, and $f(E)$ the Fermi-Dirac distribution:

$$f(E) = \left[1 + \exp\left(\frac{E-\mu}{k_B T}\right)\right]^{-1} \tag{I.14}$$

with $\mu$ the chemical potential. This equation determines the repartition of the electrons on the different energy levels. This difference between spin-up and spin-down can be due to an external applied field for paramagnetic materials but can also owe to the exchange interaction in the case of ferromagnetic materials.

Both models are partial representations of the magnetism in a metal; in the localized model, the electrons still interact with the other electrons of the material and in the itinerant description, the electrons will be affected by the ionic potential of the atoms. However, materials like rare earths are better described with a localized description whereas itinerant magnetism is more suitable to represent the behavior in transition metals. In the following, we will use the latter approach to represent the ferromagnetism of the electrodes of the magnetic tunnel junctions.

## I.2 Magnetic tunnel junctions

A magnetic tunnel junction is composed of two ferromagnetic electrodes separated by an insulating layer thin enough to let the electrons in the device tunnel from one electrode to the other, forming a tunnel barrier (figure I.4). The magnetization of one of the layer is pinned in a given direction, that layer is called “reference layer”, whereas in the second layer, the magnetization is able to reverse, thus this layer is called “free layer” .

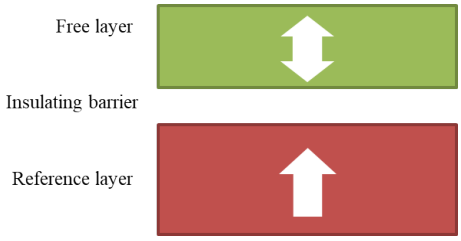


*Figure I.4: Schematic of a perpendicularly magnetized tunnel junction with the free layer in green and the reference layer in red.*

When considering a voltage applied through a magnetic tunnel junction MTJ, the electrons have to tunnel through the insulating layer, and depending on the relative orientation of the magnetization in the electrodes the resistance of the device varies. This effect is called the tunnel magneto resistance (TMR) and has been first demonstrated by Jullière in 1975 [1] in semiconductors at low temperature (4 K) with a TMR of about $15\%$. Nowadays, thanks to the improvement of the deposition systems, this effect is detectable at room temperature and the ratio between the maximum and minimum resistance can be up to several hundreds of percent [8] and give rise to many applications in the field of data storage [34], memories [14] and logic [15].

In this part, we first introduce the TMR effect and the theories of Jullière and Slonczewski describing it, before discussing the deposition system used to elaborate MTJs and finally commenting on the industrial improvements realized on MTJs.

### I.2.1 Tunnel magnetoresistance

Magnetic tunnel junctions are designed to present two stable magnetic configurations: a parallel and an antiparallel alignment of the magnetizations of the electrodes, to which correspond respectively two values of resistance: $R_P$ and $R_{AP}$, and the ratio between both gives the magnetoresistance (MR) efficiency of the system:

$$TMR = \frac{R_{AP} - R_P}{R_P} \tag{I.15}$$

In these devices, the free layer has a low coercivity (small switching field) whereas the reference layer has a large coercivity in order to be insensitive to low values of applied fields. This large coercivity can be induced by using either a hard magnetic material with a large anisotropy or the exchange bias effect, where an anti-ferromagnetic layer is exchange-coupled to the ferromagnetic layer to pin it along one direction.

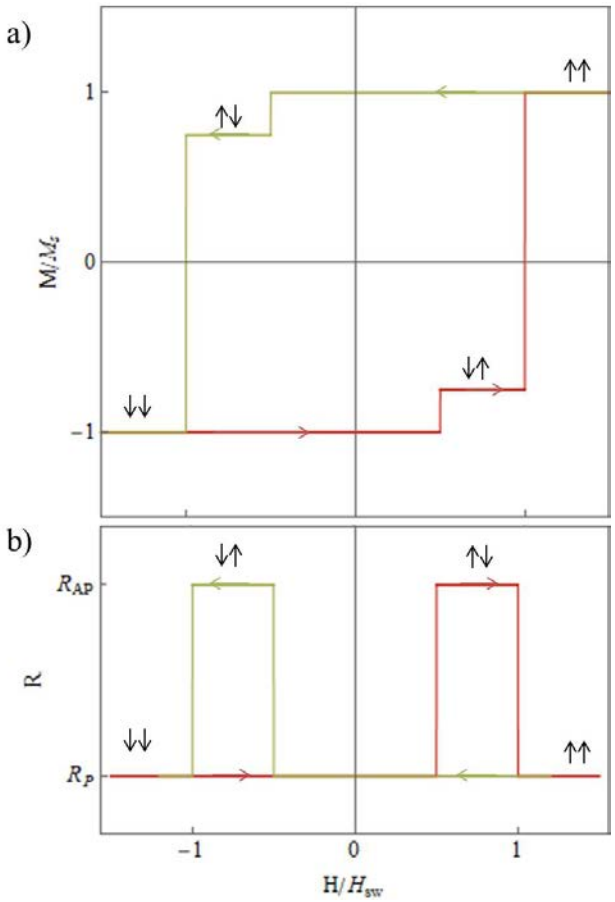


*Figure I.5: a) Magnetization and b) Resistance as a function of the applied magnetic field for a magnetic tunnel junction made of two magnetic layers seperated by an oxide layer. In red increasing field, in green decreasing field. The black arrows indicate the direction of the magnetization in the two layers.*

A typical behavior for magnetic tunnel junctions as a function of a field sweep is described in figure I.5, both in magnetization (fig I.5. a) and in resistance (fig I.5. b). From the right-hand side of the figure, the field is large enough to align both the magnetization of the reference and of the free layer (black arrows) in the same direction; the resistance is low since the magnetizations are parallel. When the field decreases (green curve) the magnetization of the free layer switches first and consequently the magnetizations are antiparallel. It corresponds to an increase of resistance and a decrease in the total magnetization of the system. At larger negative fields, the magnetization of the reference layer switches again, the magnetizations are parallel, which leads to a sign inversion of the magnetization and the resistance becomes low again. When the field value increases (red curve), the same behavior is observed, where the free layer magnetization flips first, leading to the corresponding increase in resistance, before the two magnetizations are

parallel and the resistance becomes low again.

The TMR effect is based on the spin dependent tunneling [35, 36]: in a tunnel junction, the tunneling probability of an electron depends on the density of states at the Fermi level in each magnetic layer and for both spin orientations, which results in the two-currents model with a majority spin electron current and a minority spin electron current. It follows that depending on the magnetic configuration at the second interface, one current is larger than the other, which will determine the conductance of the device.

### *Jullière's model for TMR*

In his article of 1975, Jullière proposed a simple model to describe the TMR effect [1], linking its magnitude to the spin polarization of the ferromagnetic electrode. He considered that the total electronic density of state at the Fermi level is the only quantity responsible for the spin polarization. His first assumption was the spin conservation of the electrons during tunneling, and the second was that for an electron with a given energy and a given spin leaving one electrode, it was transmitted to a free state with the same energy and spin (Fermi golden rule) on the other electrode. In this model, the TMR ratio is expressed as:

$$TMR = \frac{2P_1P_2}{1 - P_1P_2} \tag{I.16}$$

where $P_1$ and $P_2$ are the conduction electrons spin polarizations of the ferromagnetic electrodes. The total conductance of the tunnel junction is the sum of the conductance for up-spin-polarized current and down-spin-polarized current. By considering that the conductance of the device is due to the tunneling electrons and by neglecting spin-flips effet, the polarization P of the electrode at the ferromagnet-barrier interface is:

$$P = \frac{\rho^{\uparrow} - \rho^{\downarrow}}{\rho^{\uparrow} + \rho^{\downarrow}} \tag{I.17}$$

with $\rho^{\sigma}$ the density of states at Fermi level ($\sigma = \pm \uparrow, \downarrow$). Figure I.6 represents the conduction of the electron of the parallel and antiparallel configurations of the electrodes. When the layers magnetizations are parallel (figure I.6 a), the majority electrons tunnel from the reference layer to the free layer, inducing a high conductance in the tunnel barrier whereas the tunneling of the minority electrons can be neglected. On the contrary, when the magnetizations of the electrodes are aligned antiparallel (figure I.6 b), the conductance is the result of the tunneling of both spins

populations as neither is consequently larger than the other. The tunneling of minority electrons is less favored than the tunneling of the majority ones and the conductance of the device is small.

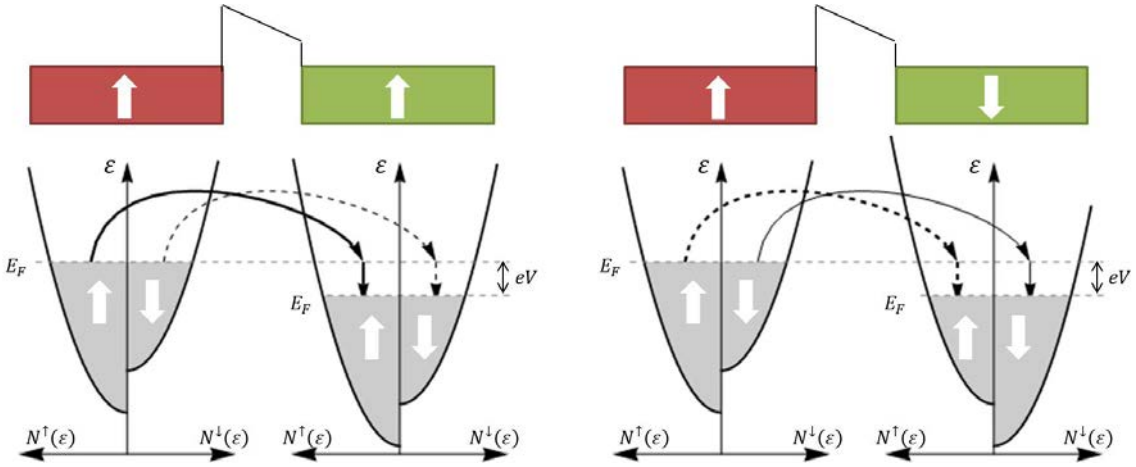


*Figure I.6: Energy as function of the density of state of the electrons tunneling for two magnetic configurations (large vertical white arrows), a) parallel, the majority electrons tunnel in priority (full black arrow) in comparison with the minority (dashed black arrow), b) antiparallel, the minority electrons tunnel in priority (full black arrow) in comparison with the majority (dashed black arrow).*

This simple model was the first model used to describe TMR, but it was proved not to be sufficient to match experimental results, even in Julliere's paper as the measured TMR was of $15\%$ and the expected one of $25\%$ [35]. The theory was further developed, notably by Stearns who showed that the polarization electrons comes from an s-d hybridization [37]. This latter description served as a basis for Slonczewski's work on the tunnel magnetoresistance [38].

### *Angular dependence of the TMR effect*

Slonczewski described the spin current density and the areal charge current as a function of the relative orientation of the magnetic layers on each side of the barrier. In order to do this, he considered two ferromagnetic electrodes with the same material properties separated by a non-magnetic barrier. The calculation is detailed in Annex 1. From his equation of conductance, he distinguished two cases depending on the number of band taken into account. In the one-band case, he found that the conductance $G$ goes to $G = 0$ when $\theta = \pi$ and $G$ was independent of the effective field value of the ferromagnets; whereas when two bands were taken into account in the computations, the junction is not "perfect" and the approximation holds the following expression

of the conductance:

$$G = G_0 \left(1 + P^2 \cos\theta\right), |P| \leq 1 \tag{I.18}$$

with $G_0$ the mean surface conductance, and $P$ the effective spin polarization of the interface:

$$P = \frac{k^{\uparrow} - k^{\downarrow}}{k^{\uparrow} + k^{\downarrow}} \frac{\kappa - k^{\uparrow}k^{\downarrow}}{\kappa + k^{\uparrow}k^{\downarrow}} \tag{I.19}$$

where

$$k_{\sigma}^2 = \frac{2m}{\hbar^2} E_{\sigma} \text{ and } \kappa^2 = \frac{2m}{\hbar^2} B \tag{I.20}$$

where $E_{\sigma}$ is the kinetic energy of the electron $\sigma$ at the Fermi level and $B$ the potential barrier of the MTJ measured at the Fermi level. For ferromagnets with different magnetic properties on each electrode, the conductance expression becomes:

$$G = G_0 \left(1 + P_{rl} P_{fl} \cos\theta\right), |P| \leq 1 \tag{I.21}$$

where $P_{rl}$ is the spin polarization of the reference layer and $P_{fl}$ the one of the free layer. This expression shows the angular dependence of the magnetic tunnel junction resistance. In this article, Slonczewski introduced the concept of "spin transfer torque", which can be considered as the inverse effect of the magnetoresistance. Indeed for TMR the polarization of the current is affected by the orientation of the magnetizations whereas in the case of spin transfer torque the transmitted spin-polarized current affects the orientation of the free layer magnetization. The spin transfer torque will be described in more detail in the following.

### I.2.2 Elaboration and optimization of MTJs

Magnetic tunnel junctions are made from the thin film stacks of different materials, each usually in the nanometer thickness and shaped as pillars a few nanometers wide (nanopillars). In order to optimize the TMR ratio and obtain MTJs compatible with MRAM technologies, the thin film stacks have to be carefully designed and the properties of each layer have to be optimized. For instance, the TMR ratio has to be large enough so as to be able to detect the resistance change with a low bias, as larger applied voltages may damage the oxide layer. Another industrial challenge is to create devices with a large enough thermal stability ensuring the retention of information, or magnetic configuration, in time. The usual time scale for industrial devices is a stability of the information over $10$ years.

### *Sputtering deposition devices*

The development and the improvement of sputtering deposition systems or epitaxial growing systems made possible the developement of spintronics. The deposition chambers must enable the control of deposited layers to the nanoscale and even lower, while monitoring the crystallography of said layers.

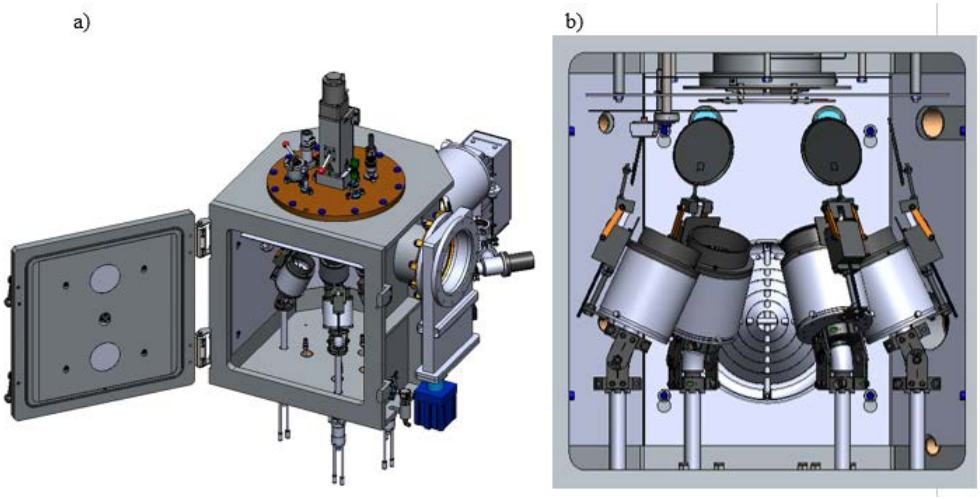


*Figure I.7: Sputtering depostion system from Vinci – Technologies 87006 PVD20 a) outside of the deposition chamber and b) inside*

One of the most used thin film deposition systems to elaborate spintronic devices is the physical vapor deposition (PVD) that deposits selected materials on top of a chosen substrate. The ultra-high vacuum chamber ($< 10^{-7}$ mbar) is equipped with cathodes where the material to be deposited are located, and an anode where the substrate is located. There are usually from 4 to 8 targets (corresponding to the cathodes) isolated by a shutter when not in use. An argon gas is introduced in the chamber and is ionized. The argon ions are attracted to the cathode and the collisions with the target eject material toward the substrate. To reinforce the accuracy of the collision range, the cathode is usually assorted with a magnetron that concentrates a magnetic field around the target, guiding the argon ions so as to improve the efficiency of the deposition. Several parameters are responsible for the quality of the deposition: the yield of the pulverization, the speed of deposition, the power controlling the potential difference between the anode and the cathode, the argon pressure and the initial vacuum.

We focused our study on magnetic tunnel junctions elaborated by sputtering stacks of amorphous CoFeB deposited below and above an MgO layer with a [001] structure. In that case, after annealing at 300°C and higher [39, 40], the ferromagnetic metal regains a body-centered cubic (bcc) crystalline structure over a few monolayers. Due to the strain at the interface CoFeB / MgO, this structure can give rise to an out-of-plane magnetized electrode, while the TMR of the junction depends on the CoFeB composition and thickness [41].

### *TMR improvement*

The first TMR results were obtained by Jullière [1] on semiconducting devices, at 4K. Tunnel magnetoresistance at room temperature were obtained in 2005 with a $Al_2O_3$ interface [42, 43] with low TMR ratios (5-15%), opening the field to industrial applications. CoFeB electrodes have been used for their low moment and dual spin filter structure [44]. The use of MgO barrier was predicted [45, 46] to improve the TMR ratio due to the Fe-O bonding at the interface [47–52] and it was shown experimentally in 2004, with TMR ratios up to 70%. The addition of a Mg layer at the interface of the CoFeB/MgO is also reported to improve the TMR from 10% in regular structures (not annealed) to 30% [53, 54].

The maximum TMR ratio demonstrated was 600% [8] in 2008 by Ikeda. He showed that the factors affecting the TMR ratio were the strain at the interface between the ferromagnet and the insulator and the tantalum diffusion through the CoFeB to the MgO during annealing. By increasing the thickness of the electrode and keeping a large annealing temperature, he obtains this large TMR ratio. In 2010, by keeping the same elaboration process, Ideka proposed the first perpendicularly magnetized magnetic tunnel junction (pMTJ) based on MgO/CoFeB[10], using the interfacial perpendicular magnetic anisotropy between the MgO and the CoFeB and showing a TMR ratio of 120%.

### *Scaling down*

Finally, the last step in the process is the patterning of the magnetic tunnel junctions into nanopillars. The patterning techniques are usually electron beam lithography [55], and ion beam etching and milling. Due to strain constraints relaxed during patterning, defects can appear and

deform the shape and crystalline structure of the tunnel junction [56].

The size effect on thermal stability and on the spin transfer torque efficiency has been investigated; the threshold current has been shown to scale with the junction area as the spin waves are sensitive to both the surface out-of-plane anisotropy and the bulk in-plane anisotropy of the free layer. In contrast, the thermal stability scales linearly with the magnetic volume of the free layer [12].

### *Data recording*

The magnetic tunnel junctions are a two-state system used in industry as magnetic memories (M-RAM) to store binary information. The reading of the information is carried out through resistance measurements, whereas the writing process is achieved by manipulating the magnetization of the free layer. This can be done by applying an external field or by using the spin transfer torque. In order to make this application fast and energy efficient, it is of interest to reduce the power needed to write the information and the duration of the writing. In the next section, we will discuss how the magnetic orientation of the free layer can be manipulated by an applied external field or a polarized spin current.

## I.3 Magnetization manipulation

Writing the information in MRAM consists in changing the direction of the magnetization of MTJs free layer. This can be achieved by two effects, either the magnetization property to be affected by a magnetic field, or the spin transfer torque, which can be considered to be the inverse of the TMR effect, where a spin-polarized current influences the magnetization direction.

The magnetic field manipulation of magnetization is a well-known effect, used since several centuries (compass) and described in the classical formalism by the Landau-Lifshitz-Gilbert (LLG) equation since 1955. This principle is used in hard-drives, where a magnetic coil on the head scanning the disk is used to manipulate the magnetization direction of the media. However, this implies the addition of a mechanical part in the memory device to enable the magnetization manipulation. As introduced before, the spin transfer torque is due to the interaction between

the spin of the electrons and the magnetization of the layer, and is based on the conservation of angular momentum. In a first paragraph we introduce the equation of the magnetization dynamics under an applied field, and in a second one we describe the effect of the spin transfert torque, and discuss the assumptions governing its expression.

### I.3.1 Landau-Lifshitz-Gilbert equation

The equation of the dynamics of the magnetization has been introduced by Landau and Lifshitz in 1935 [57] and later on refined by Gilbert whom added an different form of the phenomenological damping term in 1955 [58]. For a magnetization $\boldsymbol{M}$ depending on the position in the thin film $\boldsymbol{r}$, under an effective magnetic field $\mu_0 \boldsymbol{H}_{eff}$, it is given by:/

$$\frac{d\mathbf{M}(\boldsymbol{r})}{dt} = -\gamma_0 \mathbf{M}(\boldsymbol{r}) \times \boldsymbol{H}_{eff}(\boldsymbol{r}) + \frac{\alpha}{M_S}\mathbf{M}(\boldsymbol{r}) \times \frac{d\mathbf{M}(\boldsymbol{r})}{dt} \tag{I.22}$$

the first term on the right-hand side of the equation is a conservative precessional term corresponding to the field torque (figure I.8 a) and the second is a phenomenological term representing the damping torque that forces the relaxation of the magnetization toward its stable position (figure I.8 b). This equation is also called the "LLG equation".

#### *Precessional term*

The term of precession around a magnetic field $\mu_0 \boldsymbol{H}$ is obtained by considering the conservation of the angular momentum over the sum of the moment in the material. The sum of the magnetic moments is linked to the angular momentum $\mathbf{L}$ of the material by the gyromagnetic ratio $\gamma$ and by definition, the magnetization of the material of volume $\mathcal{V}$ is $\mathbf{M} = \frac{1}{\mathcal{V}} \sum_i \boldsymbol{m}_i$.

$$\gamma \mathbf{L} = \sum_i \boldsymbol{m}_i = \mathcal{V}\mathbf{M} \tag{I.23}$$

And placing the material in $\mu_0 \boldsymbol{H}$, each magnetic moment is subjected to a torque such as $\mu_0 \mathbf{m}_i \times \mathbf{H}$, thus, the conservation of angular moment of the material, $\mathbf{L}$, verifies:

$$\frac{d\mathbf{L}}{dt} = \mu_0 \sum_i \mathbf{m}_i \times \mathbf{H} \tag{I.24}$$

Given the relation between magnetic moments, angular moment and magnetization, the equation becomes the first term of the LLG equation:

$$\frac{d\mathbf{M}}{dt} = -\gamma_0 \mathbf{M} \times \mathbf{H} \tag{I.25}$$

where $\gamma_0 = \gamma\mu_0$ is the Larmor precession. This factor determines the precession frequency of the magnetization given by $\gamma_0 H$.

### *Damping term*

The saturation of the magnetization for large applied fields is a proof that the magnetization can fully align along a given direction if the field is large enough, independently of the initial position of the magnetization. This observation cannot be explained by the field torque alone; the damping torque describes the relaxation term caused by energy dissipation, for example energy transfer to spin waves (magnon).

This term has to be both orthogonal to $\mathbf{M} \times \boldsymbol{H}_{eff}$ and to $\mathbf{M}$. The first condition leads the magnetization to align with the effective field direction and the second guarantees that the norm of the magnetization is preserved. Thus the torque exerted by the damping on the magnetization takes the following expression, first presented by Gilbert:

$$\boldsymbol{\Gamma}_{\alpha} = \frac{\alpha}{M_S}\mathbf{M} \times \frac{d\mathbf{M}}{dt} \tag{I.26}$$

where $\alpha$ is the damping factor and represents the "rate" of the energy dissipation.

### *Effect of the two torques*

In figure I.8 the behavior of the magnetization under an applied magnetic field is represented. In figure I.8 a) only the conservative torque is represented (purple) and figure I.8 b) represents the effect of the damping torque (orange).

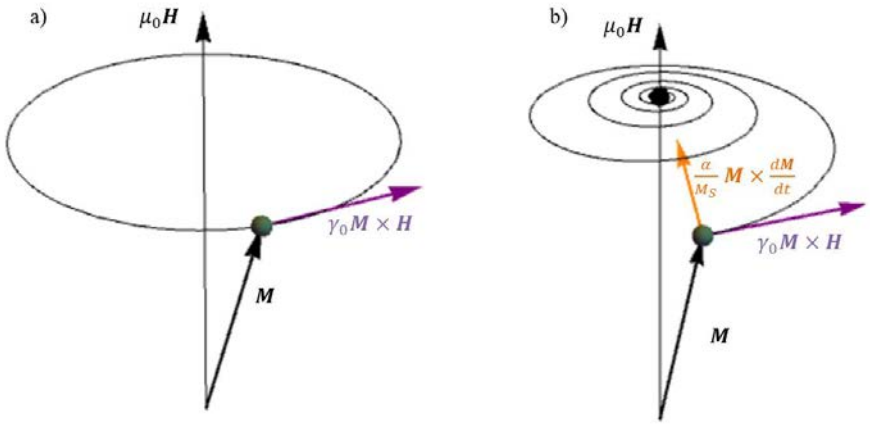


*Figure I.8: a) Principle of the dynamics of the magnetization $\boldsymbol{M}$ with only the precessional term of the LLG equation $\mu_0 \boldsymbol{M} \times \boldsymbol{H}$ in purple, b) modification of the trajectory when the damping term is added (orange).*

### I.3.2 Spin transfer torques

In the context of the MTJs, an additional torque can be introduced : if a spin-polarized current interacts with a magnetic material, due to the conservation of the angular momentum, it gives rise to a torque that can affect the magnetization dynamics, called the spin transfer torque. This was formally demonstrated by Slonczewski in 1989 and 2005 in magnetic tunnel junctions [38,59] and by both Berger and Slonczewski in 1996 [5,6] in spin-valves, in which the non-ferromagnetic material between the ferromagnetic electrodes is a conducting metal. Ralph and Stiles review summarizes the state of the art on spin transfer torque in spin-valves and magnetic tunnel junction up to 2008 [13].

In this part we will first describe succinctly the origin of spin transfer torque in spin-valves, before introducing the theory in MTJs.

#### *Origin and spin-valves*

Spin transfer torque effects may be observed for both spin-valves (ferromagnet/non-ferromagnetic metal/ferromagnet) and magnetic tunnel junctions (ferromagnet/insulator/ferromagnet). This phenomenon allows manipulating the magnetization of the ferromagnetic layers depending on the direction and amplitude of the applied current.

In spin-valves, the electrons are polarized by the first electrode and diffuse through a non-magnetic metal toward the other electrode. The spin torque is due to a spin filtering effect thought a ferromagnet and a spin-accumulation effect at the interface with the non-magnetic material. Both effects are described in the appendices in the form of a one dimension model. In this type of structures, the non-magnetic layer thickness must be smaller than the spin diffusion length so as to prevent "spin-flipping" effects. The two effects give information on the direction of the torque. From the spin filtering, one can observe that the torque has two components, one in the plane defined by the magnetization and the effective field, and one which is perpendicular to it. The spin accumulation represents the difference in chemical potential at the interface metal/ferromagnet. Its consequence is to create a spin-current and to inject a polarized current through the non-magnetic barrier. In 2002, Slonczewski [60] introduced a spin transfer torque given by:

$$\mathbf{\Gamma}_{ST} = g(\theta)\frac{\mu_B I}{e\mathcal{V}}\mathbf{m} \times (\mathbf{m} \times \mathbf{p}) \tag{I.27}$$

where I is the current, **m** and **p** the unit vector directions of the free layer and the reference layer, $\mathcal{V}$ the volume of the free layer, and $g(\theta)$ a function depending on the angle $\theta$ between **m** and **p** as well as a coefficient specific to the electrode material. When the polarizer (first electrode) magnetization direction is the same as the effective field in the second electrode, the direction of this spin transfer torque is the same as the damping, justifying its "damping-like" name. Depending on the sign of the applied current, the spin transfer torque can be parallel to the damping torque and therefore increasing the relaxation, or antiparallel to the damping torque, which can lead to a longer precession, a steady state precession [61–63] or even a magnetization switching [64, 65]. The equation proposed by Slonczewski was confirmed in the Boltzmann formalism [66, 67].

In first approximation, for spin-valves, the spin transfer torque can be mostly approximated by the in-plane component; however in certain cases a perpendicular component has to be added:

$$\mathbf{\Gamma}_{FL} = g_{\perp}(\theta)\frac{\mu_B I}{e\nu}\mathbf{m} \times \mathbf{p} \tag{I.28}$$

This torque is oriented perpendicular to the plane formed by the magnetizations of the free and reference layers, and called "field-like torque". The reflection of the electrons at the interface with the non-magnetic layer is almost negligible, which leads to a field-like torque value several orders of magnitude lower than the spin transfer torque [5, 13].

### Magnetic tunnel junctions

In 2005, Slonczewski [59] introduced the spin transfer torques for a magnetic tunnel junction. He based his model on the expression of the conductance for MTJs where the current density $J$ is expressed as:

$$J(V,\theta) = J_0(V)[1 + P_{rl}P_{fl}\cos\theta] \tag{I.29}$$

where $P_{rl}$ and $P_{fl}$ are the polarizations of the reference layer and the free layer, $J_0(V)$ an average current density, and the TMR of the corresponding device is given by:

$$TMR = 2\frac{P_{rl}P_{fl}}{1 - P_{rl}P_{fl}} \tag{I.30}$$

He uses the Bardeen transfer Hamiltonian method applied to a model junction where order is only assumed at the center of the tunnel barrier and uses it to extract the expression of the spin transfer torque at both interfaces ($\mathbf{\Gamma}_{fl}$ on the free layer's and $\mathbf{\Gamma}_{rl}$ on the reference layer's) as a function of the electric current channel. In order to obtain this expression, he assumes the decay of the transverse component of the polarization terms to zero in the barrier, and his work holds for tunnel barriers larger than 1nm.

He finds that the in-plane torques are symmetric on the two electrodes, and that the torque on the free layer $\mathbf{\Gamma}_{fl}$ and on the reference layer $\mathbf{\Gamma}_{rl}$ can be written as:

$$\begin{cases} \Gamma_{fl} &= \frac{\hbar\tau_{rl}}{2e}J_0(V)\mathbf{m}\times(\mathbf{m}\times\mathbf{p}) \\ \Gamma_{rl} &= \frac{\hbar\tau_{fl}}{2e}J_0(V)\mathbf{m}\times(\mathbf{m}\times\mathbf{p}) \end{cases} \tag{I.31}$$

where $\tau_{rl}$ and $\tau_{fl}$ are coefficients depending on the torque, and which can be respectively approximated by $P_{fl}$ and $P_{rl}$ when the current can be separated into interface dependent coefficients. In magnetic tunnel junctions, due to the large values of the device resistance, the spin torque is found to have a linear dependence with the voltage, instead of the current. Moreover, from eq. (I.29), the spin transfer torque coefficient depends on the sine of the angle between the magnetizations of the free and reference layers [68–71].

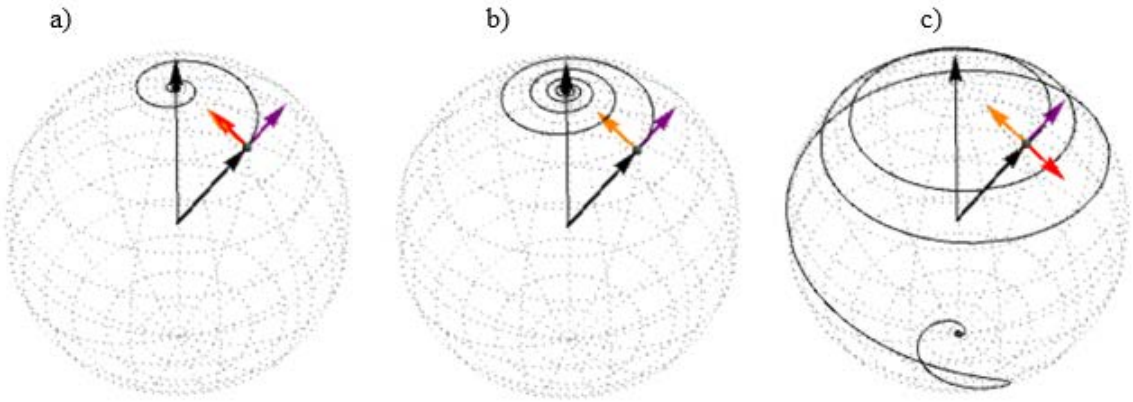


*Figure I.9: Trajectory of the magnetization (in black) in presence of effective field torque (purple), the damping torque (orange) and the spin transfer torques (red arrow) a) adding to the damping torque, b) no spin transfer torque and c) opposing the damping torque.*

Another effect discussed in this paper is the experimentally observed TMR decrease as a function of the bias voltage. It may be understood as voltage dependence of the interfacial transmission, special state density distribution, extrinsic purity effect, or inelastic tunneling. This effect proves the assymetric voltage dependence of the torques. Indeed, during the tunneling, the electrons from the reference layer close to the Fermi level are preponderant, They are "hot-electrons" and due to their tunneling, they form an energy shift that has to be taken into account in the polarization coefficent of the free layer [38, 72].

The torkance [73, 74], defined as $\frac{d\mathbf{\Gamma}_{fl}}{dV}$, is a mean to compare the conductance of the device when the magnetizations of the two layers are aligned parallel or antiparallel to each other, and especially the relation of this conductance to the spin transfer torque efficiency. The resistance of the antiparallel state decreases faster than the resistance of the parallel state. However, at large bias the tunnel current polarization remains constant and as a consequence so does the efficiency of the torque in both configurations. Under an increasing bias, the TMR ratio decreases faster than the efficiency of the spin transfer torque [75].

As in spin-valves, the spin transfer torque can either add to the damping or impede it, and can switch the magnetization from one stable state to the other. In spin-valves, the spin transfer torque coefficient depends on the angle between the magnetization direction of the magnetic layers, whereas in MTJs, this coefficient is shown to depend on the cosine of the angle between

the magnetizations.

The second difference with spin-valves is the larger presence of the field-like torque. Slonczewski predicted for MTJs the existence of a spin transfer torque perpendicular to the current direction. This field-like torque is linked to a phenomenological coupling between the electrode directions [59]. Its intensity can be $10 - 30\%$ of the spin transfer torque [76–78]. In a first order this coefficient has a quadratic dependence with the bias, leading to the creation of an offset field in one direction. The square dependence of its coefficient on bias voltage at low voltages was investigated and it appears that a linear term can be obtained as a consequence of the asymmetry in exchange splitting [79,80], the dependence with bias is shown to depend on the asymmetry of the interfaces of the tunnel barrier [81].

As a consequence of the quadratic dependence of the field-like torque, for one bias polarity it will favor the same transition as the Slonczewski spin transfer torque and for the other polarity its effect will be opposed. When the two torques are of the same order of magnitude, the two torques compete, and for one transition, the free layer magnetization jumps back and forth between the two possible configurations (parallel and antiparallel): this effect is called back-hopping. However, if this back switching is present for both configurations, the underlying physical principle is thought to be the anisotropy field reduction with bias voltage [82,83].

Using the tight binding ab initio calculation, Theodonis et al. [84] demonstrated the existence of this perpendicular torque. They concluded that the bias voltage should have a quadratic dependence on the bias voltage and that the field-like torque coefficient had a cosine dependence of with the angle between the magnetizations of the two layers. The presence of this torque was experimentally proved in a magnetic tunnel junction with an in-plane magnetization in 2006 by different groups [76,77,84–86] using the techniques of spin transfer ferromagnetic resonance [76] and thermally activated resonance [87]. It is then of the following form, with $b_V$ a phenomenological coefficient.

$$\Gamma_{flt} = b_V V^2 \mathbf{m} \times \mathbf{p} \tag{I.32}$$

### Landau-Lifshitz-Gilbert–Slonczewski equation for MTJs

The spin transfer torque and the field-like torque are added to the LLG equation in order to describe the dynamics of magnetization under an effective magnetic field $\mu_0 \boldsymbol{H}_{eff}$ and bias voltage $V$ in a magnetic tunnel junction:

$$\frac{d\mathbf{M}(\boldsymbol{r})}{dt} = \gamma_0 \mathbf{M}_{eff}(\boldsymbol{r}) \times \boldsymbol{H} + b_V V^2 \mathbf{M}(\boldsymbol{r}) \times \mathbf{p} + \frac{\alpha}{M_S} \mathbf{M}(\boldsymbol{r}) \times \frac{d\mathbf{M}(\boldsymbol{r})}{dt} + \frac{a_V V}{M_S} \mathbf{M}(\boldsymbol{r}) \times (\mathbf{M}(\boldsymbol{r}) \times \mathbf{p}(\boldsymbol{r})) \tag{I.33}$$

where $a_V$ and $b_V$ are the torque coefficients respectively of the Slonczewski torque and the field-like torque. The spin torque driven magnetization dynamics can be probed by looking at the ferromagnetic resonance (FMR) in magnetic tunnel junctions using thermally activated FMR or spin torque driven FMR.

### Optimization of the MTJ for STT-switching

For industrial use, there is a need to reduce the power used to write the information, as well as to have a writing voltage $V_{write}$ larger than the voltage used to read the information $V_{read}$, and lower than the voltages potentially damaging to the tunnel barrier $V_{break}$. Moreover, the error-rate obtained during writing has to be kept to a minimum, even with low writing voltage values.

$$V_{read} < V_{write} < V_{break} \tag{I.34}$$

The writing voltage is shown to be linked to the thermal stability of the free layer magnetic configurations. This thermal stability can be represented by an energy barrier $\Delta E$, whose parameters will be discussed in part II. When the magnetization of the electrode is in-plane, it is shown that the internal field generated by the layer, or dipolar field, impedes the magnetization direction reversal, adding an offset to the writing voltage. On the contrary, when the magnetization is out-of-plane of the thin film, the dipolar field is included in the energy barrier expression. Such devices are called perpendicular magnetic tunnel junctions (pMTJs) and in that case, the writing voltage expression is directly proportional to the energy barrier of the junction $\Delta\mathcal{E}$ that the magnetization has to overcome to switch direction:

$$V_{write} \propto \frac{\alpha}{a_V} \Delta\mathcal{E} \tag{I.35}$$

From the expression of the switching voltage, its scalability stems from either reducing the damping factor, increasing the spin transfer factor or tunning the energy barrier magnitude. For the

first solution, materials are investigated for their low damping MTJs such as the Heusler alloys [88, 89], the value of $a_V$ is linked to the quality of interface, and thus enhanced by elaboration solutions. Finally the tuning of the energy barrier will be discussed in part II, but it has to be realized while keeping a thermal stability of the setup large enough for memory applications [90].

In 2013, Worledge *et al.* [9] presents a comparison of in-plane and out-of-plane performances of a tunnel junction. They found a switching voltage ratio between the perpendicular to in-plane technologies of of eight to one for the same thermal stability. The switching is also faster as the total moment of the electrode is lower in the out-of-plane magnetization configuration. In a magnetic tunnel junction, the resistance versus field loop can be off-centered because of the stray field from the reference layer on the free layer. In order to avoid this effect, "synthetic antiferromagnetic" structures (SAF) have been used to partially cancel the stray field. SAF are made of two magnetic layers which present an antiferromagnetic coupling [91–94]. The role of this structure on the reversal of the free layer is discussed in parts III and IV.

Two different types of material with out-of-plane magnetizations are of interest for magnetic tunnel junctions, such as [Co/Pt] multilayers and CoFeB thin films. In [Co/Pt] multilayers, the interface anisotropy comes from a strong interfacial hybridization between the thin layers that enhances the cobalt out-of-plane moment [95, 96]. This material is used in SAF structures. For CoFeB thin films, it has been shown that out-of-plane anisotropy can be obtained thanks to an annealing process with a Ta seed and an MgO capping [97–100]. Numerous studies discuss the origin of this anisotropy. The hybridization of Fe 3d and O 2p orbitals were predicted to lead to PMA [101]. Moreover, the importance of the Ta has been confirmed to be main element of the PMA, as it migrates during the annealing and absorbs the B. However, the Ta/Fe/MgO stack does not have a magnetic signature due to the interactions Fe-Ta.

The good scalability of MRAM has been demonstrated with 30nm tunnel junctions with PMA and a good error rate [7]. To reach a macrospin-like behavior and optimize the spin transfer torque efficiency, it is necessary to increase the exchange constant in the materials used [102–104].

## Conclusion

This part presents the basic notions in the field of magnetism and spintronics in order to introduce the concepts necessary to follow in the next chapters. The importance of thin films growth for the development of spintronics in general and magnetic tunnel junctions (MTJs) for magnetic random access memory (MRAM) is highlighted. This evolution was enabled by the technological improvement of the ultra-high vacuum elaboration chambers and lithography techniques, as well as a better understanding of the material parameters constituting the junction. This also led to a better understanding of the spin transfer torque effects in such devices, opening a way to industrial applications of the spin transfer driven in magnetic tunnel junctions through the STT-MRAM.

To be viable for industrial technologies, the magnetic tunnel junctions have to display a low writing error rate [11], a fast switching process [4], a large spin transfer efficiency [12] and the possibility to scale down [7]. This research of efficiency induced the development of magnetic tunnel junctions with a perpendicular magnetic anisotropy and a large TMR ratio, further refined by the scaling down of the technologies in view to embed it with transistors.

Both the thermal stability, ensuring the conservation of the information on large time scales, and the writing error rate is an important characteristic of the junction as it denotes the reliability of the memory point. To improve them, there is a need to better understand the spin transfer torque driven switching process of the magnetization in perpendicular magnetic tunnel junctions, and also to determine the influence of the structure of the junction as well as its size and aspect ratio in the switching.

In the next part we propose a simple model to further our understanding of the stability of the magnetic configuration in pMTJs as a function of the applied magnetic field and applied bias. A power-based approach will be used to represent the torque applied on the magnetization.

# Chapter II

# Macrospin model to describe MTJs behavior

## Résumé en français

Cette partie présente le modèle macrospin que j'ai développé pour décrire les diagrammes d'état tension – champ magnétique d'une jonction tunnel magnétique à aimantation perpendiculaire. Le dispositif étudié a deux états stables : un alignement parallèle (P) ou antiparallèle (AP) de l'aimantation des deux couches magnétiques. Il est nécessaire de pouvoir prédire les conditions de stabilité de ces deux états en fonction du champ magnétique et de la tension appliqués.

Tout d'abord le calcul du paysage énergétique permet de déterminer la stabilité d'un état en fonction du champ magnétique et de la tension appliqués. En se positionnant sur les extrema d'énergie du système, les deux couples non conservatifs (l'amortissement et le couple de transfert de spin) peuvent être décrits comme une puissance échangée qui vient stabiliser ou déstabiliser l'état : une puissance dissipée négative stabilise un minimum d'énergie, et inversement, une puissance reçue positive stabilise un maximum.

Nous avons comparé ces résultats avec ceux obtenus par une résolution directe de l'équation Landau-Lifshitz-Gilbert-Slonczewski, le modèle de la puissance dissipée diminue les temps de calcul pour obtenir des diagrammes d'état de taille et de précision similaires. Il est important de noter que ces deux modèles ne prenent pas en compte l'effet de la température.

Ainsi les deux modèles ont été utilisés pour plusieurs géométries :

- Le cas de grande symétrie où le champ magnétique, l'axe d'anisotropie et la direction de la tension appliquée sont le long de l'axe hors du plan.
- Le cas où le champ magnétique appliqué est orienté selon un axe défini incliné par rapport à l'axe hors du plan.
- Le cas où l'axe d'anisotropie est incliné par rapport à l'axe hors du plan.
- Le cas où un second ordre d'anisotropie est ajouté, créant un état stable conique.

Dans le cas où la symétrie est haute, les diagrammes d'états obtenus en utilisant les deux modèles sont identiques. Dans le cas où l'axe d'anisotropie est incliné, les deux couples non conservatifs ne s'annulent plus exactement au niveau des extrema d'énergie, et les deux modèles divergent pour les petites valeurs de la barrière d'énergie. Lors de l'ajout d'un terme d'anisotropie d'ordre deux, les deux couples non conservatifs ne sont plus colinéaires, tout comme dans le cas de l'axe d'anisotropie incliné. De ce fait, de larges discordances sont observées entre les deux diagrammes d'états.

De plus, à partir d'une certaine valeur du terme d'anisotropie d'ordre deux, deux tensions spécifiques sont nécessaires pour décrire la dynamique de l'aimantation : une tension de précession et une tension de retournement de l'aimantation. Au-delà de la tension de précession, le dispositif devient un oscillateur dont la fréquence de précession dépend uniquement de la tension appliquée. Le courant de retournement est réduit de 40% au maximum, pour une même barrière d'énergie.

## Introduction

In part I, the different parameters governing the pMTJs magnetization behavior were described. The junction is considered to have two magnetic states described by the angle between the magnetization directions of the free and reference layers: parallel ($P$) or antiparallel ($AP$). It is of interest to be able to predict in which state the MTJ will be for given values of applied voltage and applied magnetic field. The stability of state in the pMTJ can be described by minimizing the energy density of the free layer. This energy density takes into account the different magnetic interactions exerted on the free layer (Zeeman interaction, magnetocrystalline anisotropy, dipolar field) to determine the magnetization direction.

These magnetic states are represented in voltage – field state diagrams. The stable configurations of the free layer magnetization for a given applied magnetic field and voltage are generally obtained by solving the Landau-Lifshitz-Gilbert-Slonczewski differential equation and computing the trajectory of the magnetization for this layer [105]. Another way to predict the stabilized configurations of the magnetization is to consider the sign of the power exchanged between the magnetization and the surroundings close to an energy density extremum. In this part, a model based on this method, called power dissipation model, is presented and is used to describe the stability of the states of the free layer of a magnetic tunnel junction. It also enables obtaining analytical expressions of the equations governing the switching voltages and switching magnetic fields between the states in the state diagrams.

In order to simplify the problem, we will consider the macrospin approximation in the thin films. In this approximation all the magnetic moments are considered behaving as one single moment, removing the spatial dependence of the magnetization. In order to model a system close to our experimental samples, we fix the reference layer magnetization in the out-of-plane direction. This direction is used as the direction of the spin current polarizer, which gives rise to the spin transfer torque.

In the following, we first introduce the magnetic interactions acting on the free layer, then present two macrospin descriptions of the free layer magnetization, one model based on power dissipation and a second one on a direct integration of the LLGS equation. They give comple-

mentary information on the magnetization trajectory and on the energetic vision of the stability of state in the pMTJs. We compare both approaches for different geometries. Both models are computed at zero Kelvin.

## II.1 Macrospin models

In order to introduce the two macrospin models, we first define the external and internal interactions acting on the magnetization direction, defining an effective field on which the magnetization direction will align according to the LLG equation.

### II.1.1 Magnetic interactions

In a ferromagnetic material, the magnetization can be subjected to an external magnetic field but also to an internal contribution that stems from the interaction, of electric and magnetic origin, between the moments. In order to describe its behavior, it is possible to construct an effective field $\boldsymbol{H}_{eff}$ that takes into account the magnetic interactions in the material and the external contributions. It is defined as:

$$\boldsymbol{H}_{eff} = -\frac{1}{\mu_0}\boldsymbol{\nabla}_{\boldsymbol{M}}\mathcal{E}_{tot} \tag{II.1}$$

where $\mathcal{E}_{tot}$ is the sum of the energy density in the system. In this part, we define four interactions responsible for the magnetic configuration in a ferromagnetic material.

#### *Zeeman energy*

A magnetic sample in an external field $\mu_0\mathbf{H}$, tends to align with it as the energy density representing the cost of the magnetization $\boldsymbol{M}$ deviating from the applied field direction is called the Zeeman energy density $\mathcal{E}_{zee}$:

$$\mathcal{E}_{zee} = -\mu_0\mathbf{M}\cdot\mathbf{H} \tag{II.2}$$

The Zeeman energy is the only external magnetic interaction taken into account in this model.

### *Dipolar energy and demagnetizing field*

The demagnetizing field, also called dipolar field, is a field inside the material in the opposite direction to the magnetization, hence his name. In ellipoids with a uniform magnetization, the demagnetizing field is written as:

$$\boldsymbol{H}_{dem} = -\overline{N_{dem}} \cdot \boldsymbol{M} \tag{II.3}$$

where $\overline{N_{dem}}$ is the demagnetization tensor whose expression depends on the shape of the magnetic volume in the considered system.The corresponding demagnetization energy density $\mathcal{E}_{dem}$, also called the shape anisotropy is given by:

$$\mathcal{E}_{dem} = \frac{1}{2}\mu_0 \mathbf{M} \overline{N_{dem}} \mathbf{M} \tag{II.4}$$

The representative matrix of $\overline{N_{dem}}$ is diagonal for an ellipsoid with $x$, $y$ and $z$ symmetry axes. Moreover, the demagnetization tensor matix trace satisfies:

$$N_{xx} + N_{yy} + N_{zz} = 1 \tag{II.5}$$

For a sphere, $N_{xx} = N_{yy} = N_{zz} = \frac{1}{3}$, and in a ellipsoid of revolution with the shortest direction along the $z$ axis: $N_{xx} = N_{yy} = \frac{1-N_{zz}}{2}$. In this manuscript, the focus is on thin films, which is an extrapolation of the previous ellipsoid; the demagnetization coefficients are reduced to $N_{zz} = 1$. The demagnetization energy density can be written in that case as:

$$\mathcal{E}_{dem} = \frac{1}{2}\mu_0 M_S^2 \cos^2\theta \tag{II.6}$$

where $M_S$ is the magnetization at saturation of the thin film and $\theta$ the angle between the magnetization and the $z$-axis. Previously, we have only considered the demagnetizing field of a magnetic object acting on itself. If we consider the dipolar field from one object to another we use the term stray field $\mu_0 \boldsymbol{H}_{str}$, however the physical origin is the same. Figure II.1 represent the values and direction of the demagnetizing field in a ferromagnetic thin film as a function of the magnetization direction.

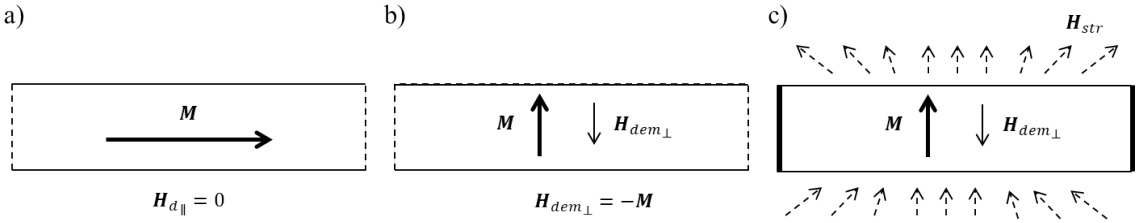


*Figure II.1: Schematics of the dipolar field $\mu_0 \boldsymbol{H}_{dem}$ value (a) in an infinite thin film with in-plane magnetization $\boldsymbol{M}$, (b) in an infinite thin film with an out-of-plane magnetization and (c) in a finite thin film with out-of-plane magnetization creating a stray field $\mu_0 H_{str}$.*

From a simple calculation, in an infinite thin film with an in-plane magnetization, the demagnetizing field $\boldsymbol{H}_{dem_\parallel}$ is nul, whereas for an out-of-plane magnetization it is $\boldsymbol{H}_{dem_\perp} = -\boldsymbol{M}$. In a finite size of ellipse, the presence of edges induce the creation of a stray field $\boldsymbol{H}_{str}$ that can interact with neighbouring magnetic structures.

### *Magneto-crystalline anisotropy*

In a crystal, the orbital moments depend on the symmetry axes and planes of the material. The magnetocrystalline anisotropy is the interaction describing the influence of the electronic orbitals on the spin direction through the spin coupling and by consequence on the magnetization direction. The magnetocrystalline anisotropy can take several forms, but here an uniaxial anisotropy is considered. In that case, magnetization tends to orient itself along one direction called the easy axis of anisotropy. The corresponding energy density $\mathcal{E}_{ani}$ is written as:

$$\mathcal{E}_{ani} = -K \left(\boldsymbol{u}_k \cdot \mathbf{m}\right)^2 - K_2 \left(\boldsymbol{u}_k \cdot \mathbf{m}\right)^4 \tag{II.7}$$

with $\mathbf{u}_k$ the anisotropy easy axis, $\mathbf{m}$ the normalized direction of the magnetization, $K$ and $K_2$ the first and second order anisotropy coefficient in $J/m^3$. The second order anisotropy coefficient $K_2$ is usually much smaller than the first order one $K$, and is often neglected in a first approximation. In part II.3, we discuss $K_2$ effects on the magnetization behavior in a macrospin approximation.

The contribution of the crystal structure, and of the atom orbitals, on the magnetocrystalline anisotropy are actually two folds: first a bulk contribution due to the crystalline organization of the material as stated before, and second a surface contribution either due to the strain at the interface of the material that stems from lattice mismatches or as in CoFeB/MgO structure due to

the electronic structure at the interface [97]. In thin films, this latter contribution can dominate and thus give rise to an out-of-plane easy axis, which lead to a perpendicular magnetic anisotropy (PMA). The surface magneto-crystalline anisotropy energy density to the first order is:

$$\mathcal{E}_{anis} = -\frac{K_s}{t} \left( \boldsymbol{u}_k \cdot \mathbf{m} \right)^2 \tag{II.8}$$

where $K_s(J/m^2)$ is the surface anisotropy and $t$ the thickness of the thin film. However the elaboration of a thin film with perpendicular magnetization is challenging: as previously reported the demagnetization energy tends to align the magnetization in-plane therefore the only way to obtain a perpendicularly magnetized materials is to grow a system with and out-of-plane magnetocrystalline anisotropy stronger than the demagnetizing field. In that case the demagnetization energy of a thin film creates an easy plane of anisotropy, which facilitate the switching of the magnetization.

### *Stoner-Wohlfarth model and hysteretic behaviors*

The Stoner-Wohlfarth model [106] enable to study the magnetization reversal in a macrospin. It assumes that all magnetization variations consist in a uniform change of the moments. Here, we consider the uniaxial magnetocrystalline anisotropy which would stem from an out-of-plane easy axis, the shape anisotropy due to thin film geometry and an external magnetic field along applied the $z$-axis. Due to the macrospin approximation, the exchange energy density is not taken into account in the model, as all moments are already considered aligned and there is no spacial dependence included in the model, thus the free layer volume $\mathcal{V}$ links the energy density $\mathcal{E}$ of the system to the energy value $E = \mathcal{E} \times \mathcal{V}$.

$\mathcal{E}_{tot}$ is the total energy density of the system, the sum of the Zeeman energy density, the magneto crystalline energy density and the demagnetization energy density:

$$\mathcal{E}_{tot} = \mathcal{E}_{zee} + \mathcal{E}_{ani} + \mathcal{E}_{dem} \tag{II.9}$$

Thus, as a function of the position angle $\theta$:

$$\mathcal{E}_{tot} = -\mu_0 M_S H \cos\theta - \left( K - \frac{1}{2}\mu_0 M_S^2 \right) \cos^2\theta \tag{II.10}$$

We define the switching field $\mu_0 H_{sw}$, as the field needed to go from one minimum of energy to the other minimum for $\theta = 0$. It can be found as the maximum value of the field for which $\frac{d\mathcal{E}_{tot}}{d\theta} = 0$.

At this value the minimum of energy becomes a maximum. $\mu_0 H_{sw}$ is given by:

$$H_{sw} = \frac{2K}{\mu_0 M_S} - M_S \tag{II.11}$$

where $\frac{2K}{\mu_0 M_S}$ corresponds to the anisotropy magnetic field obtained from the magnetocrystalline anisotropy energy density. The solutions for the equilibrium positions are:

- $\theta = 0$ and $\theta = \pi$ which are local minimum and maximum of energy for no applied field.
- $\cos\theta = -\frac{\mu_0 M_S H}{2\left(K - \frac{1}{2}\mu_0 M_S^2\right)}$ is a maximum of energy that exists only for $H \in [-H_{sw}, H_{sw}]$

Figure II.2 represents the typical reponse for a magnetization with a magnetization at staturation $M_S$ under a magnetic field $\mu_0 H$ applied along the easy axis anisotropy (figure II.2 a) or perpendicular to the easy axis of anisotropy (figure II.2b), such as denoted by the arrows. In figure II.2 a), in green are represented the values of magnetization when the the applied field starts in the same direction as the easy axis, then decrease toward the antiparallel direction, and the inverse sweeping direction is represented in red. When the applied magnetic field exceeds $-H_{sw}$ first, then $H_{sw}$, the magnetization changes sign. In figure II.2 b) the magnetization behavior is represented in black, and goes continuously from $M_S$ to $-M_S$.

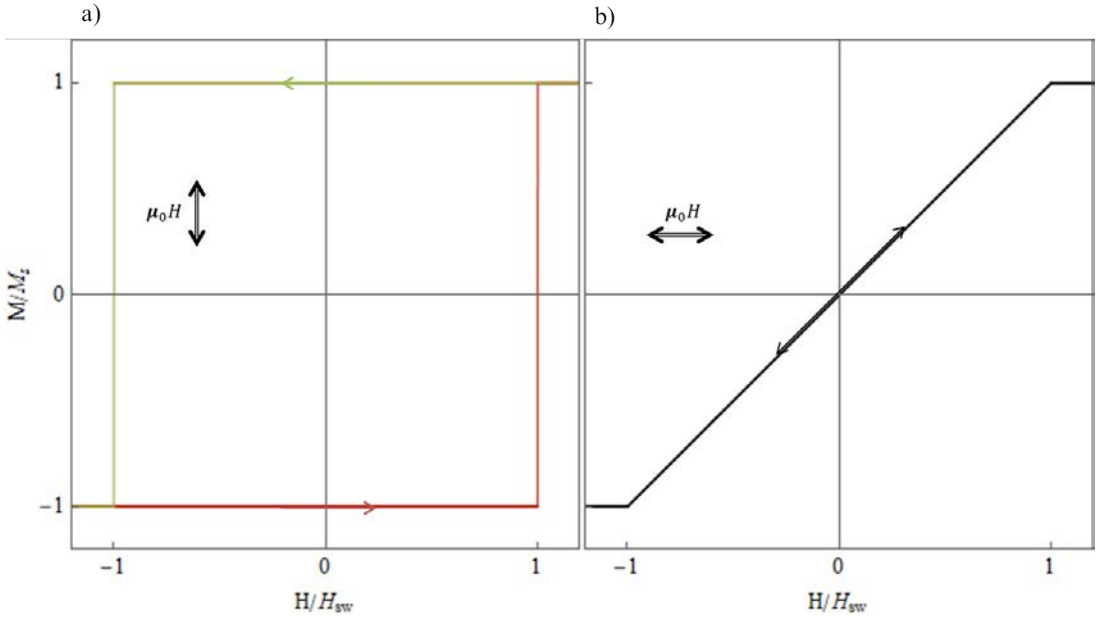


*Figure II.2: Hysteresis loops for a ferromagnet with an applied magnetic field in the a) easy axis of anisotropy direction and b) hard axis of anisotropy direction, the arrows indicate the sweeping directions of the magnetic field.*

This model gives a static representation of the magnetization behavior, evolving between two static equilibrium states.

### II.1.2 Notations and parameters

In this chapter, a thin film with an out-of-plane easy axis of anisotopy is considered. Figure II.3 represents the axis convention used. The parallel state $P$ is defined for $\theta$ close to $0$ and the parallel hemisphere for $\theta \in [0, \frac{\pi}{2}]$ and reciprocally for the antiparallel hemisphere, the antiparallel state ($AP$) is defined for $\theta$ close to $\pi$, and the antiparallel hemisphere for $\theta \in [\frac{\pi}{2}, \pi]$. If the energy extrema are canted away from the out-of-plane direction, for example in the geometries with a broken symmetry, we choose to keep the $P$ and $AP$ denominations.

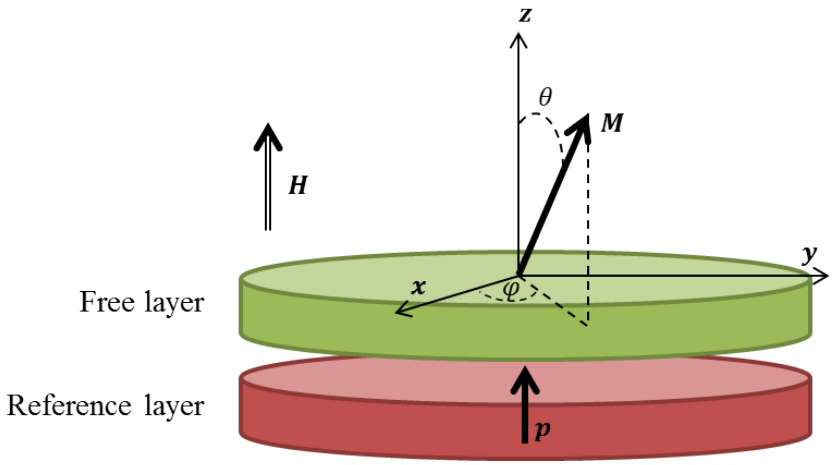


*Figure II.3: Axes and angles of the system with $z$ the out-of-plane direction, and $x$ and $y$ the in-plane directions, $\boldsymbol{M} = M_s\boldsymbol{m}$ the free layer magnetization direction, $\boldsymbol{p}$ the reference layer magnetization direction, $\boldsymbol{H}$ the applied magnetic field direction, $\theta$ the polar angle and $\varphi$ the azimuthal angle for the magnetization.*

In the following, due to the preservation of the norm of the magnetization, the total energy density $\mathcal{E}_{tot}$ is only given by $\theta$ and $\varphi$.

$$\mathcal{E}_{tot}(\theta,\varphi) = -\mu_0 M_S \mathbf{m}\cdot\mathbf{H} + \frac{\mu_0}{2} M_S^2 \mathbf{m}\cdot\overline{N_{dem}}\cdot\mathbf{m} - K(\boldsymbol{u}_k\cdot\mathbf{m})^2 - K_2(\boldsymbol{u}_k\cdot\mathbf{m})^4 - \mu_0 b_V V^2 M_S \mathbf{m}\cdot\mathbf{p} \tag{II.12}$$

The difference with eq. (II.10) is the addition of the field like torque, with $b_V$ the field-like torque coefficient, introduced in part I. Due to the macrospin approximation, the contribution of the stray field will be uniform, its value is obtained by averaging its contribution over the free

layer. It can be included in the applied magnetic field.

The trajectory of the magnetization of the free layer at zero Kelvin is computed using the Landau-Lifshitz-Gilbert-Slonczewski equation. In the macrospin approximation the magnetization depends on $\theta$ and $\varphi$ only, leading to a reduced expression of the LLGS equation (eq. II.13):

$$\frac{d\mathbf{m}}{dt} = -\gamma_0 \mathbf{m} \times \mathbf{H}_{eff} - \alpha \mathbf{m} \times \frac{d\mathbf{m}}{dt} + \gamma_0 a_V V \mathbf{m} \times (\mathbf{m} \times \mathbf{p}) \tag{II.13}$$

with **m** the normalized magnetization direction ,**p** the normalized direction of the spin polarizer, $\gamma_0$ the gyromagnetic factor (set to $2.228 \times 10^7 GHz \cdot (Am^{-1})^{-1}$ ), $\alpha$ the damping, $a_V$ the Slonczewski spin transfer torque coefficient and $V$ the applied voltage. As the macrospin approximation is used, this equation uses the reduced version of the torques to describe the magnetization trajectory. The first term on the right-hand side of the equation represents all the conservative torques and describes the Larmor precession around the effective field. Finally, the last two terms on the right-hand side of the equation represent respectively the damping torque and the Slonczewski spin-transfer torque. These two torques are non-conservative torques and therefore cannot be expressed from a potential energy.

The numerical values used for the different parameters in equation II.12 are gathered in table II.1 and they correspond to material parameters for a CoFeB/MgO/CoFeB MTJ [9, 105].

| | | |
|---|---|---|
| $M_S$ | $10.5 \times 10^5$ | $A \cdot m^{-1}$ |
| $K$ | $7.18 \times 10^5$ | $J \cdot m^{-3}$ |
| $\alpha$ | $0.01$ | (-) |
| $a_V$ | $6.37 \times 10^3$ | $A \cdot m^{-1} \cdot V^{-1}$ |
| $b_V$ | $2.39 \times 10^4$ | $A \cdot m^{-1} \cdot V^{-2}$ |
| $K_2$ | $-1.5 \times 10^4$ | $J \cdot m^{-3}$ |

*Table II.1: Free layer material parameters*

The macrospin model is developped at zero Kelvin, however one of the main characteristic parameters of MTJs is their thermal stability, i.e. if the energy density barrier between two stable states is large enough to prevent switching due to thermal excitation. In order to ensure this, we compare the energy barrier $\Delta E$ to $k_B T$ at room temperature ($T = 298°C$), thus $k_B T =$

$1.38 \times 10^{-23} \times 298 = 4.11 \times 10^{-21} J$. As introduced before, in the macrospin approximation, we consider $\Delta E = \Delta\mathcal{E} \times \mathcal{V}$. The free layer is $1nm$ thick over a surface of $100nm$ of width and length, thus $\mathcal{V} = 10^{-23} m^3$. With these parameters, the corresponding energy barrier is $\Delta E = \Delta\mathcal{E} \times \mathcal{V} \approx 64 k_B T$. This value meets the industry requirements for the data stability; and $\Delta E = 60 k_B T$ is expected to preserve the configuration for 10 years (cf part III).

### II.1.3 Power dissipation model

Magnetization excitation and reversal induced by the combined effects of field and spin-transfer torques are described in terms of the potential energy density and the power exchanged with the surroundings. Starting with the Stoner-Wohlfarth model [106] the extrema of the energy density landscape are computed. These extrema (minimum and maximum) of the total energy density, in regard to position angles $\theta$ and $\varphi$ are the possible equilibrium magnetization states. As the power of this system exchanged with the surrounding is due to the non-conservative torques, the study of its sign close to each extremum tells us if the corresponding magnetization positions are stabilized or destabilized. When the power is dissipated from the system the minimum of the energy density lanscape is stabilized and, on the contrary when power is transferred to the system the maximum of the energy density landscape, normally unstable, is stabilized.

The model based on this statement is called “power dissipation model”. It has been developed by Cucchiara *et al.* for out-of-plane spin valves [107]. Here we expand the application of this model to pMTJs and we focus on the advantages and limitations of this model, comparing it to the direct integration of LLGS.

In order to give some insight into this approach, let us first consider the expression of a mass that rotates due to an applied external force $\mathbf{F}(t)$. The power $P(t)$ is given by the force $\mathbf{F}(t)$ and the velocity $\mathbf{v}(t)$.

$$P(t) = \mathbf{F}(t) \cdot \mathbf{v}(t) \tag{II.14}$$

Considering only the rotational motion of the mass and noting $\boldsymbol{r}(t)$ the position vector and $\boldsymbol{\Omega}(t)$ the angular velocity vector, the velocity is now expressed as:

$$\mathbf{v}(t) = \frac{d\boldsymbol{r}}{dt} = \boldsymbol{r}(t) \times (-\boldsymbol{\Omega}(t)) \tag{II.15}$$

Thus (II.14) becomes:

$$P(t) = -\mathbf{F}(t) \cdot (\boldsymbol{r}(t) \times \boldsymbol{\Omega}(t)) \tag{II.16}$$

Which, by the properties of the cross product, gives:

$$P(t) = \boldsymbol{\Omega}(t) \cdot (\boldsymbol{r}(t) \times \mathbf{F}(t)) \tag{II.17}$$

As the torque $\boldsymbol{\Gamma}$ is defined as $\boldsymbol{\Gamma}(t) = \boldsymbol{r}(t) \times \mathbf{F}(t)$, using the mixed product properties, we obtain:

$$P(t) = \boldsymbol{\Omega}(t) \cdot \boldsymbol{\Gamma}(t) \tag{II.18}$$

We studied the motion of $\boldsymbol{m}$ with this approach. From eq. (II.15), the expression of the time derivative of the magnetization gives $\frac{d\boldsymbol{m}}{dt} = \boldsymbol{m}(t) \times \boldsymbol{\Omega}(t)$ and by identification in the LLGS equation, the angular velocity vector is given by $\boldsymbol{\Omega}(t) = -\gamma_0 \boldsymbol{H}_{eff}$ in the limits of small damping parameters and low voltages. Let us then calculate the dissipative powers of each non-conservative torque in LLGS.

The damping torque $\boldsymbol{\Gamma}_\alpha$ is written as follows using the LL expression of the damping:

$$\boldsymbol{\Gamma}_\alpha = -\mu_0 M_S \alpha \mathbf{m} \times (\mathbf{m} \times \boldsymbol{H}_{eff}) \tag{II.19}$$

The power dissipated by the damping torque $P_\alpha$ is then obtained:

$$P_\alpha = \boldsymbol{\Omega}(t) \cdot \boldsymbol{\Gamma}_\alpha = \gamma_0 \boldsymbol{H}_{eff} \cdot \mu_0 M_S \alpha \mathbf{m} \times (\mathbf{m} \times \boldsymbol{H}_{eff}) \tag{II.20}$$

With the properties of the mixed product, the final expression becomes:

$$P_\alpha = -\gamma_0 \mu_0 M_S \alpha (\mathbf{m} \times \boldsymbol{H}_{eff})^2 \tag{II.21}$$

The power coming from the damping torque is always negative (dissipative), it will always tend to bring the magnetization back to the minimum of energy. In the same way, we find the power $P_{STT}$ due to the spin transfer torque.

The spin transfer torque $\boldsymbol{\Gamma}_{STT}$ is:

$$\boldsymbol{\Gamma}_{STT} = \mu_0 M_S a_V V \mathbf{m} \times (\mathbf{m} \times \mathbf{p}) \tag{II.22}$$

and the power dissipated by the spin transfer torque, $P_{STT}$:

$$P_{STT} = \boldsymbol{\Omega}(t) \cdot \boldsymbol{\Gamma}_{STT} \tag{II.23}$$

finally:

$$P_{STT} = \gamma_0 \mu_0 M_S a_V V \boldsymbol{H}_{eff} \cdot (\mathbf{m} \times (\mathbf{m} \times \mathbf{p})) \tag{II.24}$$

The sign of the power coming from the spin transfer torque depends on the sign of the applied voltage. The total dissipative power, $P_{tot}$, is defined as the sum of these two dissipative powers. As the criterium to stabilize a maximum of energy is that the total power has to be positive, in these cases, the spin transfer torque dissipated power has to overcome the damping torque dissipated power.

Since the power exchanged with the surroundings is always zero at the extrema of energy (figure II.4 a and b)), the state diagrams are built by computing the curvature of the dissipated power at these points. Indeed, if the dissipative power value is an extremum, the curvature indicates its behavior close to the extremum position; in that case a concave curvature is equivalent to a negative dissipative power, whereas a convex curvature corresponds to a positive power, as shown in figure II.4 c).

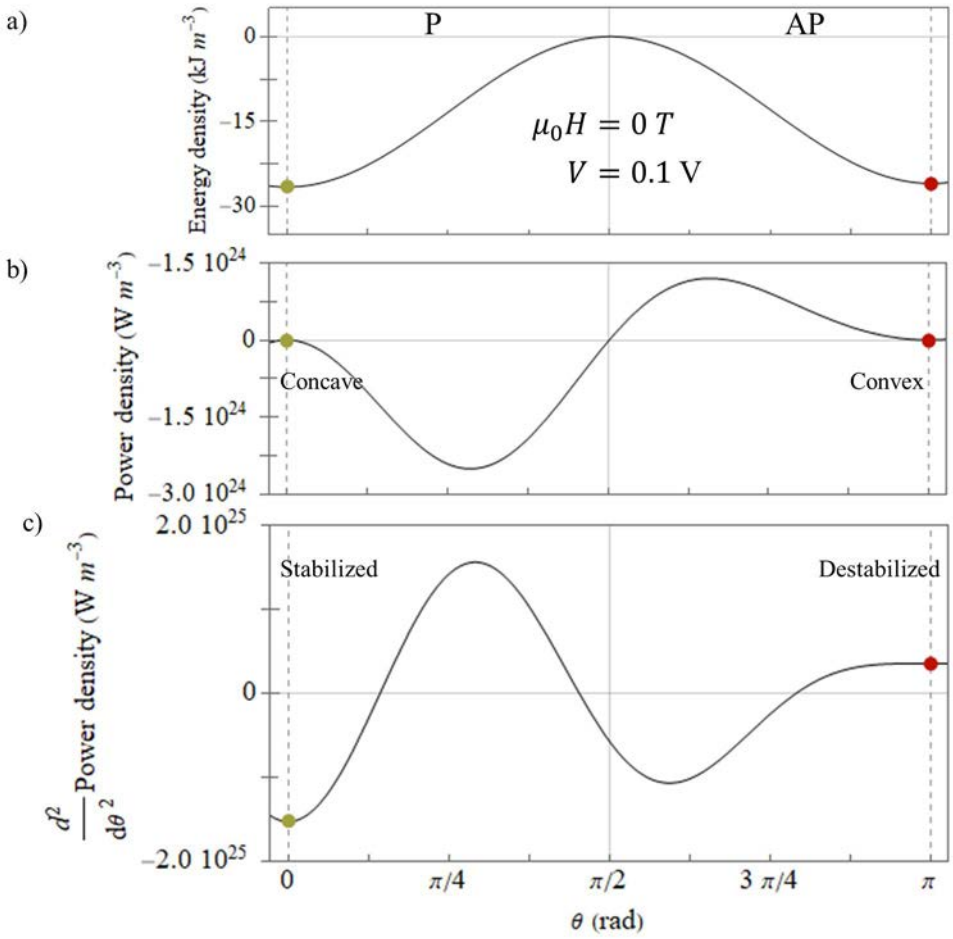


*Figure II.4: a) energy density at $\mu_0 H = 0T$ and $V = 0.1V$ with P (green) and AP (red) minima of energy density. b) corresponding power density, with a concave / convex function close to the minima, c) curvature of the power density with stabilized/destabilized energy extrema.*

This model is first used to calculate the voltage – field state diagram, mapping the stable magnetic configuration of a pMTJ. The calculation method used is presented in the following section.

### II.1.4 LLGS direct integration model

The direct integration of LLGS over a given time will give the evolution of the system, depending on the initial angle, the applied magnetic field and the applied voltage. Due to the norm conservation of the magnetization, it is convenient to express LLGS in the spherical coordinates. In spherical coordinates, $\boldsymbol{e}_r$ is given by the direction of the magnetization, $\boldsymbol{m} = \boldsymbol{e}_r$, and forms with $\boldsymbol{e}_\theta$ and $\boldsymbol{e}_\varphi$ a direct base.

A time derivation gives $\frac{d\mathbf{m}}{dt} = \dot{\theta}\boldsymbol{e}_\theta + sin(\theta)\dot{\varphi}\boldsymbol{e}_\varphi$ and the fact that LLGS equation preserves the magnetization, all the torques in the right-hand side of LLGS are perpendicular to the direction of the magnetization. Then, in spherical coordinates there is a set of two differential equations respectively along $\boldsymbol{e}_\theta$ and $\boldsymbol{e}_\varphi$, describing the dynamics of the magnetization with a Newtonian type description.

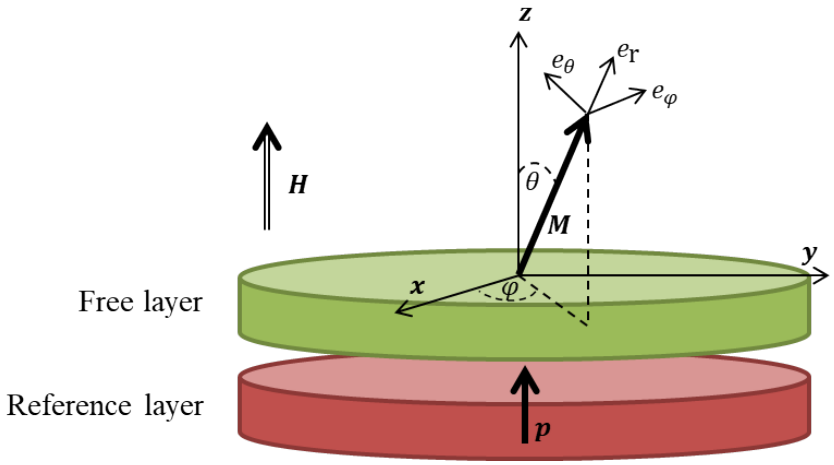


*Figure II.5: Axes and angles of the system with the spherical coordinate system referential: $e_r$ the unit vector in the magnetization direction, $e_\theta$ the polar angle unit vector and $e_\varphi$ the azimuthal angle unit vector.*

Another elegant way to obtain this set of two equations is to use the Lagrangian approach. Instead of describing the system evolution with the action of set of forces, the Lagrangian approach is based on an energy point of view. In order to do so, the Lagrangian physics is based on generalized coordinates that depend on the number of free parameters and constraints in the system. The Lagrangian operator $\mathcal{L}$ is then defined as the difference between the kinetic energy and the potential energy and the Lagrangian is a function of the global coordinates $(q_1(t), ..., q_i(t), ..., q_n(t))$ and their time derivatives $(\dot{q}_1(t), ..., \dot{q}_i(t), ..., \dot{q}_n(t))$. When the system is conservative, the time evolution between $t_0$ and $t$ of the global coordinates is obtained by minimizing the action, which is the integration over time of the Lagrangian. The time evolution of the global coordinates, solutions of the problem, are then the solutions of the Euler-Lagrange equations:

$$\frac{d}{dt}\frac{\partial \mathcal{L}}{\partial \dot{q}_i} - \frac{\partial \mathcal{L}}{\partial q_i} = 0 \tag{II.25}$$

The obtained set of equations is equivalent to the Newton equations describing the motion of the system. When the system can exchange work with its surroundings, the work of the non-conservatives forces is included in the action by the mean of Rayleigh dissipation function $\mathcal{F}$.

Thus the Rayleigh dissipation function represents the power exchanged by the non-conservative forces with the surroundings. The time evolution of the global coordinates solutions of the problem are then the solutions of the modified Euler-Lagrange equations:

$$\frac{d}{dt}\frac{\partial \mathcal{L}}{\partial \dot{q}_i} - \frac{\partial \mathcal{L}}{\partial q_i} = \frac{\partial \mathcal{F}}{\partial \dot{q}_i} \tag{II.26}$$

The concept of the Lagrange equations can be transposed to describe the magnetization dynamics. The canonical global coordinates are naturally $\varphi$ and $\theta$ in the macrospin approximation. The Lagrangian of the considered system can be written as [108]:

$$\mathcal{L} = -\frac{M_S}{\gamma_0}\dot{\varphi}\cos\theta - E_{tot}(\theta,\varphi) \tag{II.27}$$

where $E_{tot}(\theta,\varphi)$ plays the role of the potential energy and $-\frac{M_S}{\gamma_0}\dot{\varphi}\cos\theta$ plays the role of the kinetic energy. If the system is isolated (no damping), the Euler-Lagrange equations give directly the Larmor precession equations in spherical coordinates. To take into account the non-conservative torques, we introduce respectively the two Rayleigh dissipation functions [109], corresponding respectively to the damping torque (eq. (II.28)) and the Slonczewski spin transfer torque (eq. (II.29)):

$$\mathcal{F}_\alpha = \alpha\frac{\mu_0 M_S}{2\gamma_0}\left(\frac{d\mathbf{m}}{dt}\right)^2 \tag{II.28}$$

$$\mathcal{F}_{STT} = \mu_0 M_S a_V V \mathbf{p}\left(\mathbf{m}\times\frac{d\mathbf{m}}{dt}\right) \tag{II.29}$$

with $\mathbf{m} = \mathbf{m}(\theta(t),\varphi(t))$. Because the Rayleigh dissipation functions represent the power exchanged with the surroundings, we verify that they are equivalent to the power function (eq.(II.21) and eq.(II.24)) in the limit of the LL formulation. Finally, introducing them in generalized Euler-Lagrange equations, we can express LLGS in the generalized coordinates, leading to two coupled equations.

$$\begin{cases} \frac{d}{dt}\frac{\partial \mathcal{L}}{\partial \dot{\theta}} - \frac{\partial \mathcal{L}}{\partial \theta} = \frac{\partial \mathcal{F}_\alpha}{\partial \dot{\theta}} + \frac{\partial \mathcal{F}_{STT}}{\partial \dot{\theta}} \\ \frac{d}{dt}\frac{\partial \mathcal{L}}{\partial \dot{\varphi}} - \frac{\partial \mathcal{L}}{\partial \varphi} = \frac{\partial \mathcal{F}_\alpha}{\partial \dot{\varphi}} + \frac{\partial \mathcal{F}_{STT}}{\partial \dot{\varphi}} \end{cases} \tag{II.30}$$

The last equation to consider in the system is the conservation of the norm of $\mathbf{m}$ (i.e. $\|\mathbf{m}\| = 1$).

We numerically solve eq. (II.30) using a classical Runge-Kutta method with adaptive time steps for different applied magnetic fields and bias voltages. The state diagrams are obtained by mimicking a voltage sweep. The magnetic field value is fixed, and the initial applied voltage value

is set; at each voltage step the magnetization trajectory is computed for a given time and the final angle is the angle used as the intial angle of the next voltage step.

In the following, first we compare the two models for a fully out-of-plane geometry, then we will study different effects that can lead to symmetry breaking. In experimental systems, a broken symmetry could result from the presence of the polarizer, a misalignment with the applied field (tilted fied) or due to the surface roughness of the layer (tilted anisotropy). Finally, we will discuss the influence of a second order uniaxial anisotropy, which can stabilize a cone state for the magnetization without breaking the symmetry.

## II.2 Model comparison for different geometries

The first geometry considered is the highly symmetrical case where the easy axis of the magnetocrystalline anisotropy of the free layer, the polarizer and the applied magnetic field are set in the out-of-plane direction (along the z axis).

### II.2.1 Full out-of-plane geometry

The first geometry investigated represents a high symmetry configuration for the pMTJ: the applied magnetic field direction, the magnetocrystalline anisotropy easy axis and the polarizer direction are aligned perpendicular to the plane of the junction. The high symmetry of the system allows us to compute an analytical expression of the characteristic equations describing the state diagrams: the switching voltages, $V_{sw}$, and limit magnetic fields, $H_{lim}$. In this geometry, due to the symmetries, the total energy is invariant in the azimuthal angle $\varphi$ and the total energy density of the free layer magnetization, eq. (II.12) is reduced to:

$$\mathcal{E}_{tot} = -\mu_0 H M_S \cos\theta - K_{eff} \cos^2\theta - b_V V^2 M_S \cos\theta \tag{II.31}$$

We introduce the notation $K_{eff} = \left(K - \frac{\mu_0}{2} M_S^2\right)$, which represents the effective anisotropy of the system. For different applied fields, neglecting the effect of the field-like torque, we find three extrema for the energy density function as a function of the polar angle; two of them refer to a free layer aligned parallel ($P$ for $\theta = 0$) or antiparallel ($\theta = \pi$) to the reference layer and the last one is a maximum, function of the applied magnetic field that exists between the fields at which the

P and AP states extrema change from minima of energy density to maxima. The corresponding magnetic fields are noted $\mu_0 H_{sw_{P\to AP(AP\to P)}}$ respectively for the considered extrema.

$$\begin{cases} \theta = 0 & \Rightarrow & H_{sw_{P\to AP}} & = & -\frac{2K_{eff}}{\mu_0 M_S} \\ \theta = \pi & \Rightarrow & H_{sw_{AP\to P}} & = & \frac{2K_{eff}}{\mu_0 M_S} \end{cases} \tag{II.32}$$

Figure II.6 represents the energy density of the free layer as a function of the polar angle $\theta$. The parallel state (green dots) and the antiparallel state (red dots) for different applied magnetic fields and at zero voltage are presented on the graph. In the following, $P_{min}$ ($AP_{min}$) corresponds to the magnetization stabilized in the $P$ ($AP$) state as a minimum of energy density and respectively, $P_{max}$ ($AP_{max}$) is for the magnetization stabilized in the $P$ ($AP$) state as a maximum of energy density.

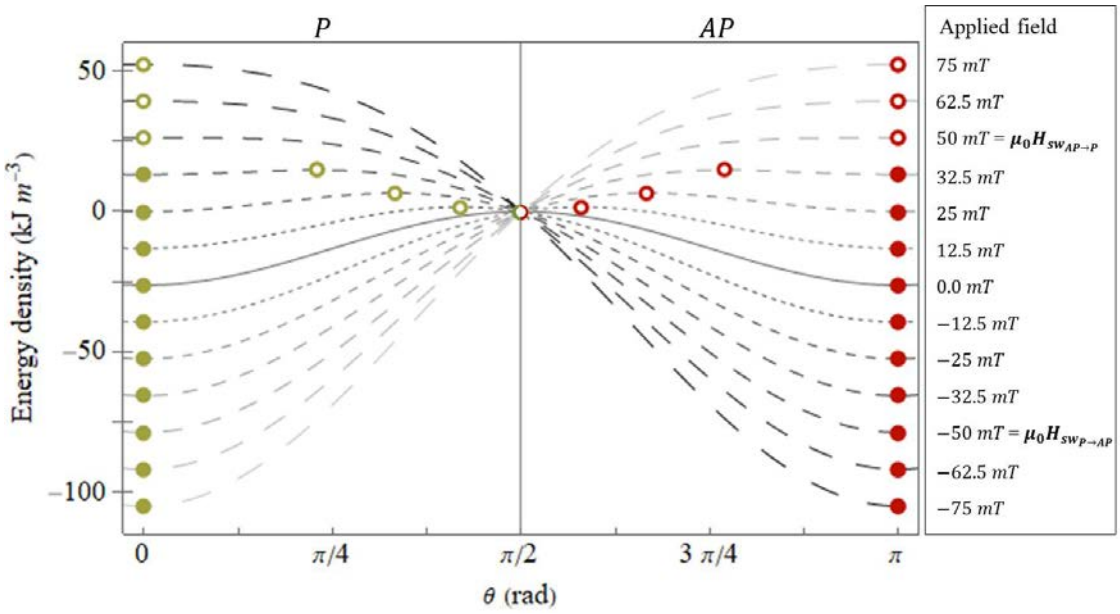


*Figure II.6: Energy density of a fully out-of-plane magnetic tunnel junction, as a function of the polar angle $\theta$ for applied magnetic fields from $75mT$ (light gray) to $-75mT$ (dark gray), by steps of $12.5mT$. The full green (red) dots represent the $P(AP)$ state as minimum of energy density, the empty dots represent the corresponding state as maximum of energy density.*

From this energy density landscape, we can infer at least three different magnetization configurations for the state diagram:

- For $H < H_{sw_{P\to AP}}$: $P_{max}$ (green circles) and $AP_{min}$ (red dots).
- For $H > H_{sw_{AP\to P}}$: $P_{min}$ (green dots) and $AP_{max}$ (red circles).

- For $H \in [H_{sw_{P\to AP}}, H_{sw_{AP\to P}}]$: $P_{min}$ (green dots), $AP_{min}$ (red dots) and an intermediary maximum (circles)

The area for $H \in [H_{sw_{P\to AP}}, H_{sw_{AP\to P}}]$ is noted $P/AP$. The switching fields computed are $\mu_0 H_{sw_{P\to AP(AP\to P)}} = \pm 0.05T$. In the $P/AP$, the difference in energy between the intermediary maximum and either minima is the energy density barrier of the system $\Delta\mathcal{E}_{P\to AP}$ and $\Delta\mathcal{E}_{AP\to P}$ depending on the transition. At $\mu_0 H = 0T$ and $V = 0V$, (plain line in figure II.6), and for a volume $\mathcal{V}$, the corresponding energy barrier is $\Delta E = \Delta\mathcal{E} \times \mathcal{V} \approx 64 k_B T$ as expected from part II.1.

Figure II.7 shows the state diagrams obtained after computing the two macrospin models: LLGS integration in figure II.7a) and power dissipation in figure II.7b). The perfect agreement between the two state diagrams validates the power dissipation approach for this geometry. $P$ and $AP$ are both stabilized as maxima or minima of energy density. The intermediary maxima of the energy density barrier are not stabilized in either model and as described in part II.1.2, the power dissipated in this state changes signs on each side of the maxima.

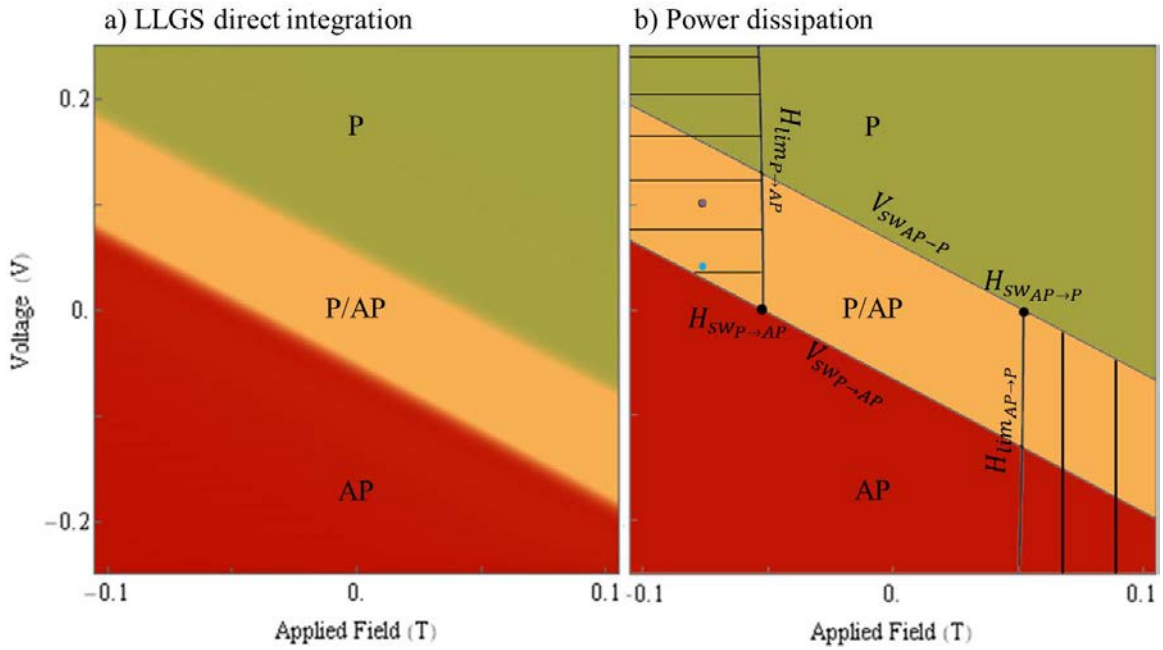


*Figure II.7: Voltage – field state diagrams for the "all out-of-plane" geometry, computed by the direct integration of the LLGS equation (a) and the power dissipation model (b), in green the region where the P state is stable, in red the AP state is stable, in orange both states are stable. Hatched regions correspond to the stabilization of a maximum of energy density, P state for horizontal hatches, AP for vertical hatches.*

The LLGS direct integration diagram (figure II.7 a) presents the expected three areas: $P$ in green, $AP$ in red, $P/AP$ in orange. This model does not give indication if it is a minimun or a maximum of energy density stabilized in this configuration, but the trajectory of the magnetization for each condition in magnetic field and voltage is rendered. The same three areas are represented in the state diagram for the power dissipation model (figure II.7 b). The stabilized minima of energy density are the plain areas, whereas the stabilized maxima of energy density are in the hatched regions, vertical for $AP$ and horizontal for $P$.

The delimitation field $H_{lim_{P\to AP(AP\to P)}}$ between the stabilized minimum and maximum of energy density is given by the magnetic field expression as a function of the voltage canceling the derivative of the total energy density function. For one state, it starts at the corresponding $H_{sw_{P\to AP(AP\to P)}}$ and the curvature of the delimitation is governed by the field-like torque term. Their expressions are given by eq. (II.33)). When there is no field-like spin transfer torque, the delimitation fields are constant for all voltages and $\mu_0 H_{lim_{P\to AP(AP\to P)}} = \mu_0 H_{sw_{P\to AP(AP\to P)}}$.

$$\begin{cases} H_{lim_{P\to AP}} = -b_V V^2 + H_{sw_{P\to AP}} = -b_V V^2 - \frac{2K_{eff}}{\mu_0 M_S}, & V \geq 0 \\ H_{lim_{AP\to P}} = -b_V V^2 + H_{sw_{AP\to P}} = -b_V V^2 + \frac{2K_{eff}}{\mu_0 M_S}, & V \leq 0 \end{cases} \tag{II.33}$$

The second set of equations needed to describe the diagrams are the switching voltages that are observed in both models: $V_{sw_{P\to AP(AP\to P)}}$. They correspond to the minimum voltage needed to overcome the energy density barrier and as a consequence this voltage is the one for which the total power exchanged in the system is zero for $\theta = 0$ and $\theta = \pi$; it is given by:

$$b_V V^2_{sw_{P\to AP(AP\to P)}} + \frac{a_V}{\alpha} V_{sw_{P\to AP(AP\to P)}} = -(H + H_{sw_{P\to AP(AP\to P)}}) \tag{II.34}$$

While the field-like torque coefficient is in general small compared to the ratio between the spin transfer torque coefficient and the damping, the $V_{sw}$ expressions are mostly linear, parallel and the state diagram is centered in zero voltage. In this approximation, three ways are infered to reduce the switching voltage in pMTJs. First by reducing the energy barrier ($2^{nd}$ term of equation (II.34)) however it would reduce the thermal stability; secondly by increasing the spin transfer parameters and thirdly by decreasing the damping parameter. For larger field-like torque coefficients, $V_{sw_{P\to AP(AP\to P)}}$ are not parallel between themselves not linear and the state diagram presents a voltage offset due to the parabolic contribution of the term.

Moreover in MTJs, the spin transfer torque coefficient does not depend on the angle between the free layer magnetization and the polarizer direction, and consequently there is no oscillatory state that can be reached in this fully perpendicular geometry. In part II.3, we investigate the means to create a steady precessional state without breaking the symmetry.

These two macrospin models give a better understanding of the junction state stability in relation to its energy density landscape and we are interested in the effect of thermal agitation on the stability of the state and especially when maxima of energy density are stabilized. The relative stability of the states is determined by the angle $\theta_{lim}$ at which the dissipative power changes sign, this was verified by computing the magnetization trajectory for different initial angles around $\theta_{lim}$. For voltage values larger than $V_{sw}$, the power function is always positive and only the maximum state can be stabilized (green and red hatched areas in figure II.7 b). In the bistable area, $\theta_{lim}$ tends to $\pi$ when the voltage gets closer to $V_{sw}$.

Figure II.8 displays the power density (a) and the energy density (b) as a function of $\theta$ for $V = 0.05V$ and $V = 0.1V$ when $\mu_0 H = -75mT$, denoted in figure II.7 b by a corresponding blue and purple dot in the horizontally hatched area. The power density changes sign for $\theta_{lim}$, and if the difference in energy density $\Delta\mathcal{E}$ between the stable maximum position and $\theta_{lim}$ is in the same order of magnitude as $k_B T$ per units of volume we can conclude that the state will be unstable when temperature effects are considered.

In this numerical application, for $V = 0.05V$, the stability of $P_{max}$ is given by $\Delta E \approx 24 k_B T$, which corresponds to a lifetime of $7s$ at $T = 300K$ for a given state, whereas it is of $\Delta E \approx 150 k_B T$ for $V = 0.1V$ which gives a lifetime larger than the age of the universe for the state. This large difference is due to exponential dependence on the thermal activation (cf. part III) and the quadratic dependence of energy barrier with both the applied voltage and the applied magnetic field, thus this result could explain part of the results observed in the experimental data and especially the shape of the state diagram (cf figure III.2).

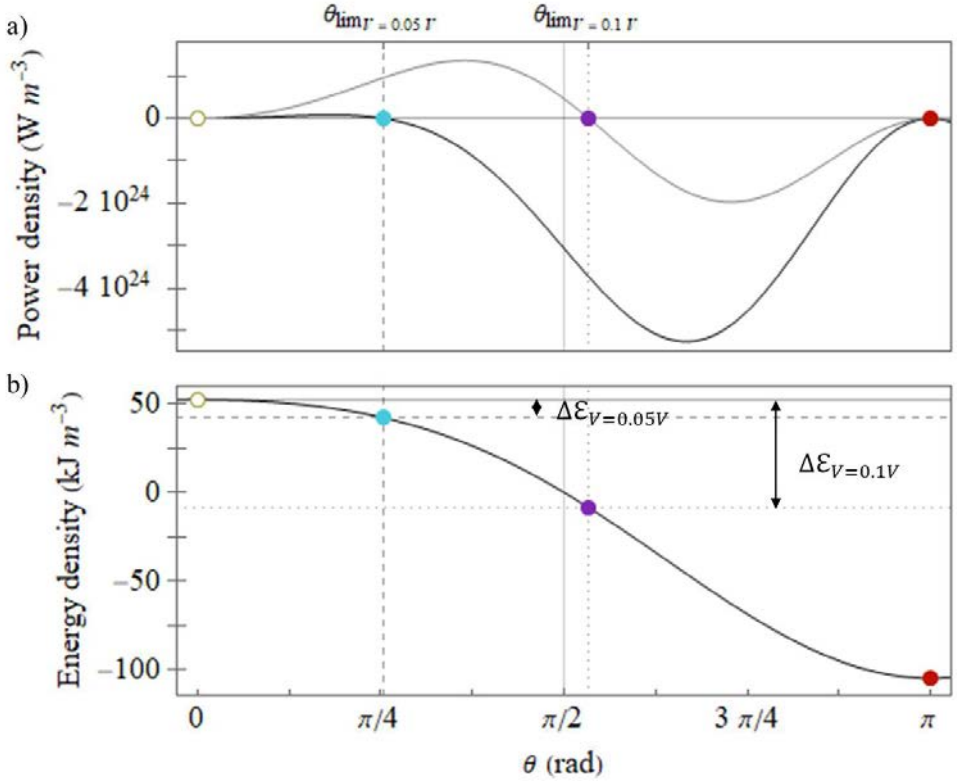


*Figure II.8: For $\mu_0 H = -75mT$, a) power density and b) energy density for $V = 0.05V$ in black and $V = 0.1V$ in gray. The P state (green circle) is maximum and the AP state (red dot) is minimum of energy density. The blue (purple) dot locates the angle $\theta_{lim}$ for which the power density changes sign for $V = 0.05V$ ($V = 0.1V$). $\Delta\mathcal{E}$ is the energy density barrier between $P_{max}$ and $AP_{min}$*

The LLGS direct integration model gives access to the stable states of the magnetization as a function of the applied magnetic field and applied voltage by computing the magnetization trajectory starting from an initial state on the initial parameter for these conditions. The power dissipation model gives the same information by calculating the dissipated power curvature for the extremum of energy. This model also brings information on the stability of the configuration and the limit position angle of the stabilized maxima.

In order to study the limits of the power dissipation model in a more complex geometry, we have tested several hypotheses where the uniaxial symmetry is broken, first by considering that the applied magnetic field is tilted by an angle of $5°$ from the $z$-axis along the $y$-axis, and secondly that the magnetocrystalline anisotropy easy axis is tilted by an angle of $1°$ from the $z$-axis along the $y$-axis.

### II.2.2 Tilted applied magnetic field

In this part, the applied magnetic field is tilted by an angle of $5°$ from the $z$-axis along the $y$-axis ($\varphi = \frac{\pi}{2}$). Figure II.9 shows the modification in the energy density landscape as a function of $\theta$ for $\varphi = \frac{\pi}{2}$.

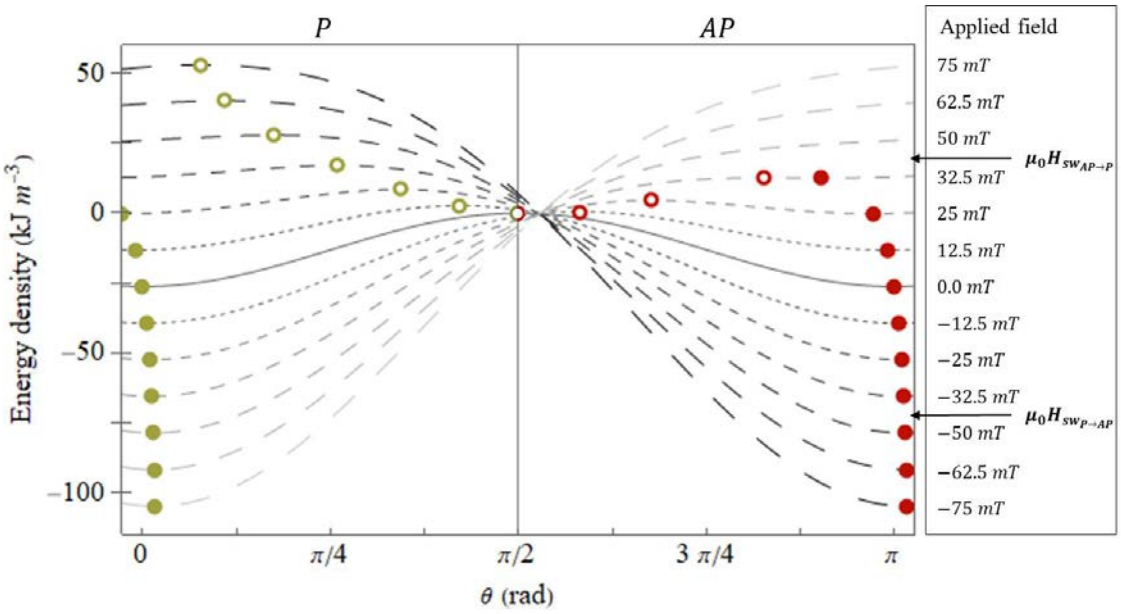


*Figure II.9: Energy density of a magnetic tunnel junction with a tilted applied field direction ($5°$ from the $z$-axis) as a function of the polar angle $\theta$ for applied magnetic fields from $75mT$ (light gray) to $-75mT$ (dark gray), by steps of $12.5mT$. The full green (red) dots represent the $P(AP)$ state as a minimum of energy density, the empty dots represent the corresponding state as a maximum of energy density.*

We observe that the energy density is asymmetric as a function of the polar angle and for larger fields, the stable positions are no longer aligned with the out-of-plane direction. When there is no applied magnetic field, the situation is the same as the previous case. When the applied field increases, the direction of magnetization leading to the energy extrema, whether there be minima and maxima, aligns with the applied magnetic field. The magnitude of switching magnetic fields $\mu_0 H_{sw_{P\to AP(AP\to P)}}$ decreases in this geometry compared to the all out-of-plane case, in accordance with the Stoner - Wohlfarth model, as shown in figure II.9.

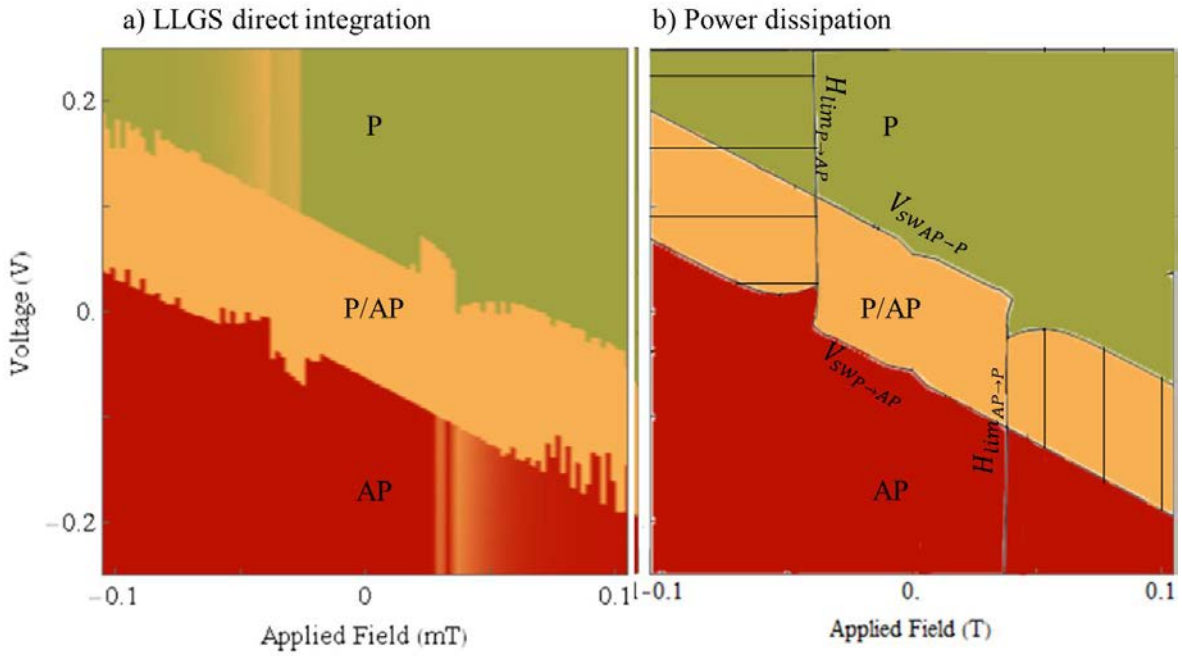


*Figure II.10: Voltage – field state diagrams for the "tilted field" geometry (5° from the $z$-axis), computed by the direct integration of the LLGS equation (a) and the power dissipation model (b), in green the region where the $P$ state is stable, in red the $AP$ state is stable, in orange both states are stable. Hatched regions correspond to the stabilization of a maximum of energy density, $P$ state for horizontal hatches, $AP$ for vertical hatches.*

In Figure II.10, we compare the two macrospin models for a pMTJ with a tilted applied magnetic field. They are still in perfect agreement, the $P$ area is in green, the $AP$ in red and the bistability area $P/AP$ in orange. The maxima stabilized are noted with hatches, horizontal for $P_{max}$ and vertical for $AP_{max}$. The difference with the state diagrams for the previous geometry is the presence of notches reducing the stability area of the maxima of energy density in between the $V_{sw}$ values and close to $H_{lim}$. For a symmetric system or a system with a geometry close to symmetric, the state diagrams obtained are similar using both models. Tilting the polarizer direction away from the out-of-plane direction gives a similar result for the state diagram. The corresponding computation was realized, but the corresponding figures are not shown.

Finally, one can note that when the non-conservative torques are not colinear, the energy extrema have no reason to be the stable states. The Slonczewski spin-transfer torque direction only depends on the polarizer direction (here out-of-plane) whereas the damping torque direction hinges on the effective field direction. For small applied fields, the effective field direction is out-of-plane and the non-conservative torques are aligned, but for larger applied fields, the angle

between both torques is not negligible. The power dissipated at the energy density maximum is zero however it changes sign on each side of the extremum, meaning that the stabilized state is at a different position from the extrema of energy density. This effect is not taken into account by the power dissipation model, but the good agreement between the disclosed state diagrams shows that the stable state in this case is near the energy density extrema.

### II.2.3 Tilted anisotropy: limits of the model

In this geometry, the magnetic anisotropy axis is tilted $1^\circ$ away from the $z$-axis. The aim of this geometry is to increase the limit angle up to which the torques can cancel each others compared to the previous geometry. The modified energy landscape is presented in figure II.11.

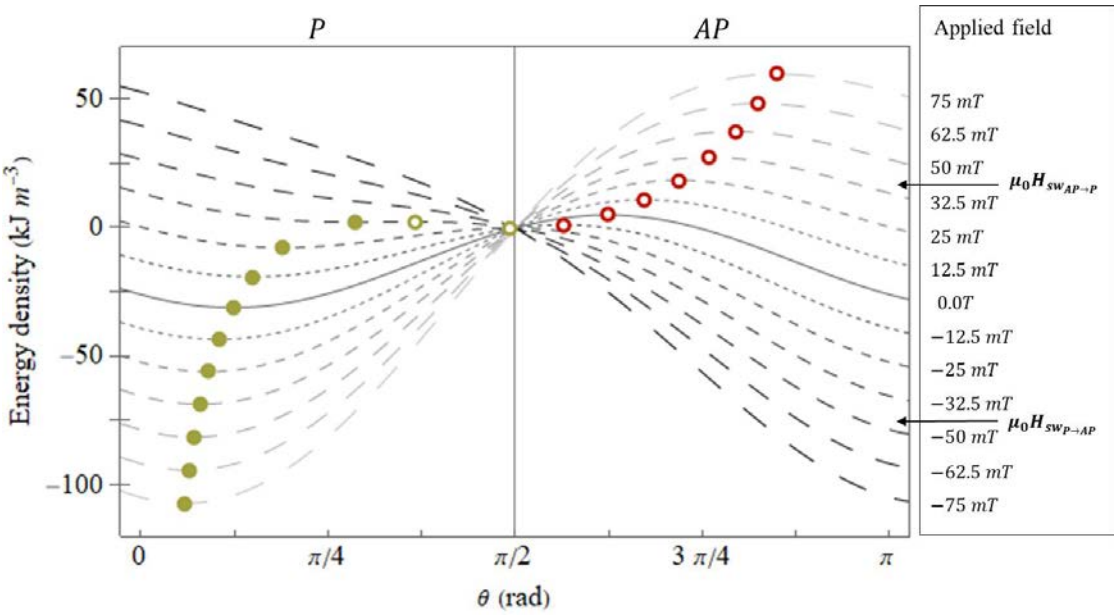


*Figure II.11: Energy density of a MTJ with anisotropy axis $1^\circ$ from the $z$-axis as a function of the polar angle $\theta$ for applied magnetic fields from 0.075T (light gray) to -0.075T (dark gray), by steps of 0.0125T. The full green dots represent the P state as a minimum of energy density, the empty red dots represent the AP state as a maximum of energy density.*

The full green dots represent the minimum of the $P$ state and the empty green and red dots represent the maximum of the $P$ and $AP$ states. As in the tilted field case, there is no intermediary extrema, but a continuous transition of energy extrema from minimum to maximum. The stable states are canted away from the out-of-plane direction for smaller applied magnetic field values, and tend to align with the out-of-plane axis for the larger ones. The large effect of the

tilting is due to the competition of quadratic terms in the energy expression.

The power dissipation is not an extremum for both maxima and minima of energy density as the non-conservative torques are not aligned even for small field values. The state diagrams for both macrospin models are presented in figure II.12 and for this geometry, the power dissipation model state diagram shows artefacts compared to the LLGS state diagram.

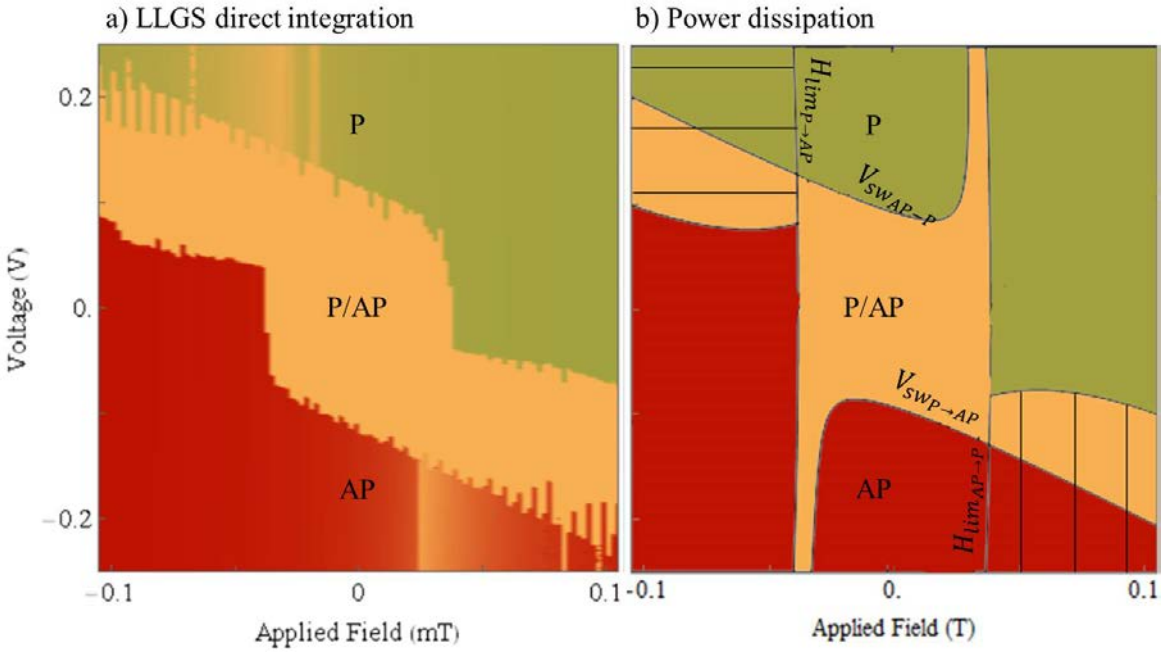


*Figure II.12: Voltage – field state diagrams for the "tilted anisotropy axis" geometry (1° from the z-axis), computed by the direct integration of the LLGS equation (a) and the power dissipation model (b), in green the region where the P state is stable, in red the AP state is stable, in orange both states are stable. Hatched regions correspond to the stabilization of a maximum of energy density, P state for horizontal hatches, AP for vertical hatches.*

The LLGS direct integration diagram (figure II.12a) and the power dissipation diagram (figure II.12b) display similar $\mu_0 H_{lim_{P\to AP(AP\to P)}}$ and $V_{sw_{P\to AP(AP\to P)}}$ values. Moreover, $V_{sw_{P\to AP(AP\to P)}}$ increased compared to the values obtained in the previous geometries. As in the tilted applied magnetic field geometry, the sizes of the areas where a minimum and a maximum of energy density are both stable are reduced.

The power dissipation state diagram displays additional vertical branches that are not present in the LLGS state diagram. These branches are close to the prolongation of the equation of

$\mu_0 H_{lim_{P\to AP(AP\to P)}}$ and inside the area of bistability between minima of energy density. In order to understand the origin of this artefact, we studied the $P$ to $AP$ reversal for $\mu_0 H = -35mT$ and $V = -0.2V$. Figure II.13 displays the energy landscape (figure II.13a) and the trajectory of the magnetization (figure II.13b) of this transition.

In figure II.13a, the initial magnetization point, in green, is the supposed stable minimum of energy in the P configuration obtained by the power dissipation method for $\mu_0 H = -35mT$ and $V = -0.2V$ (cf. point in figure II.12). The trajectory of the magnetization is computed using the direct integration model. The magnetization starts precessing around a position shifted from the $y$-axis, and escapes the parallel state potential well. It converges in the $AP$ hemisphere to a position (red dot) corresponding to the minimum of energy in the $AP$ state. In figure II.13 b) we mapped the trajectory of the magnetization on the energy density landscape in the $P$ hemisphere. The green dot is the position of the energy minimum of the P state, and the black dot is the attractor of the magnetization trajectory.

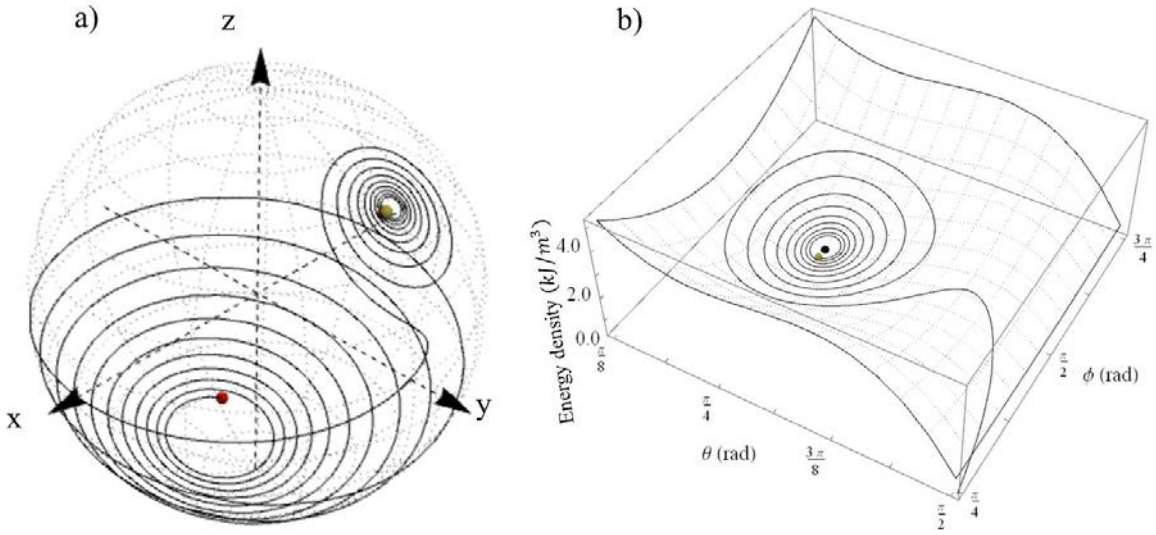


*Figure II.13: For $V = -0.2V$ and $\mu_0 H = -0.035T$, (a) trajectory of the magnetization from the local minimum of energy in the $P$ state (green dot) to the local minimum of energy in the $AP$ state (red dot), (b) mapping of the trajectory of the reversal on the energy density landscape, the green dot is the minimum of energy in the $P$ state, the black dot the compensation point of the non-conservative torques.*

In this configuration, the polarizer direction is not aligned with the effective field. The effect of the angle, compared to the tilted field case, is enhanced by the quadratic dependence of the magnetic anisotropy field. In the previous cases, the power dissipation model holds as the sym-

metry breaking remains minimal. This case presents some artefacts that could appear when the geometry is broken, however the $H_{lim}$ and $V_{sw}$ values found with the power dissipation model match the boundaries found using the LLGS direct integration, and it enables finding the energetic stability of the considered state.

## II.3 $2^{nd}$ order anisotropy

In spin valves, the angular dependence of the spin transfer torque gives rise to oscillator behaviors for certain conditions of applied magnetic field and current [107]. In the next part, we look at a geometry favorable for the creation of such states in fully perpendicular magnetic tunnel junction and how it affects the switching voltage as well as the time of switching. As presented in part II.1, the uniaxial magnetocrystalline anisotropy energy density can be expressed with several terms with increasing power order. We are interested in adding a second order term, as it can create a stable cone state in the free layer energy density that does not break the symmetry.

The effect of the second order term was reported in recent experiments, and its origin as been found resulting from the atomic structure at the interface as well as from strains due to lattice mismatch [110–112]. The interest of this geometry is twofold: first the initial angle between the magnetization in the cone state and the polarizer direction due to the cone state is supposed to reduce the switching voltage – the efficency of the torque is then increased for non-collinear vectors – and secondly the cone state forms an oscillator which precession frequency is only governed by the applied voltage. In this part, we want to compare the switching dynamics in the cone-state geometry to the one in the fully-perpendicular MTJ.

The uniaxial magnetocrystalline anisotropy energy density taking into account the second order anisotropy is written as:

$$E_{ani} = -K\left(\boldsymbol{u}_k \cdot \mathbf{m}\right)^2 - K_2\left(\boldsymbol{u}_k \cdot \mathbf{m}\right)^4 \tag{II.35}$$

We remind the following notation: $K_{eff} = K - \frac{\mu_0 M_S^2}{2}$ representing an effective anisotropy coefficient composed of the contribution of the first order anisotropy and the demagnetizing field. In the following, for the fully perpendicular geometry, $K_2 = 0$, we use the notations $K_{eff_{ref}}$ and $M_{s_{ref}}$ respectively for the effective anisotropy coefficient and the saturation magnetization and

for $K_2 \neq 0$, these two parameters are noted $K_{eff}$ and $M_s$. This part will focus on the relative contribution of the first order effective anisotropy and the second anisotropy. The conditions on $K$, $K_{eff}$ and $K_2$ to obtain a cone state are:

- $K_{eff} > 0$ to have a perpendicularly magnetized system,
- $K > 0$ & $K_2 < 0$ to have opposite contributions of the anisotropy terms,
- $|K_2| > \frac{K_{eff}}{2}$ for a large enough contribution of the second order of anisotropy.

In the following, the sign of $K_2$ is always opposed to the sign of $K$, as a $K_2$ of the same sign as K only increases the out-of-plane anisotropy. Figure II.14 represents the evolution of the energy density landscape as a function of $\theta$ for different values of $\frac{|K_2|}{K_{eff}}$.

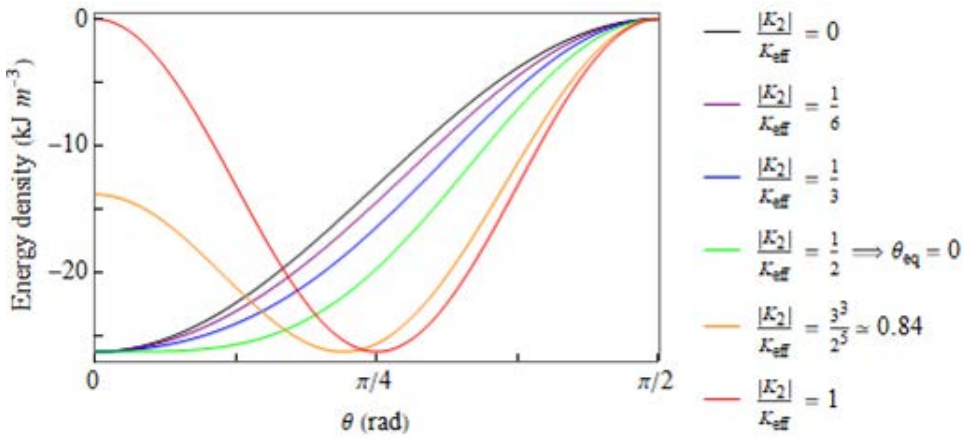


*Figure II.14: Energy density landscape as a function of the free layer magnetization position for a pMTJ with different values of second order anisotropy coefficient but a constant energy barrier.*

For $|K_2| < \frac{K_{eff}}{2}$, the energy density extrema are out-of-plane, and for $|K_2| > K_{eff}$, the cone states are preserved, however the geometry is closer to an in-plane MTJ, and for very large values of $K_2$, the system can be considered in-plane. In these systems, for no applied voltage, the equilibrium magnetization position corresponds to the cone state position and is given by:

$$\cos(\theta_{eq}) = \sqrt{\frac{K_{eff}}{2|K_2|}} \tag{II.36}$$

For $\frac{|K_2|}{K_{eff}} \in [0, \frac{1}{2}]$ the energy density landscape widens around the out-of-plane stable position, then for $\frac{|K_2|}{K_{eff}} \in ]\frac{1}{2}, 1]$ a cone state appears around the out-of-plane position up to $\frac{\pi}{4}$. For larger values of $\frac{|K_2|}{K_{eff}}$, the cone state becomes closer to the easy plane created by the demagnetizing field of the junction.

### II.3.1 Stability of the cone states in MTJs

We study the effect of the voltage and the applied field on the stability of the states in a magnetic tunnel junction with a second order anisotropy. The first and second order anisotropy coefficients used are $K = 7.18 \times 10^5 J \cdot m^{-3}$ and $K_2 = -1.5 \times 10^4 J.m^{-3}$ as stated in part II.1. This material choice gives rise to a cone state clearly visible in figure II.15. The energy density landscape shown in figure II.15 is in the shape of a "sombrero" for the applied fields between the switching magnetic fields $\mu_0 H_{sw_{P\to AP(AP\to P)}}$, and the energy density barrier $\Delta\mathcal{E}$ is the difference of energy density between the cone state minimum of energy density and the maximum of energy density, $\left(\theta = \frac{\pi}{2}\right)$ for $\mu_0 H = 0T$ and $V = 0V$.

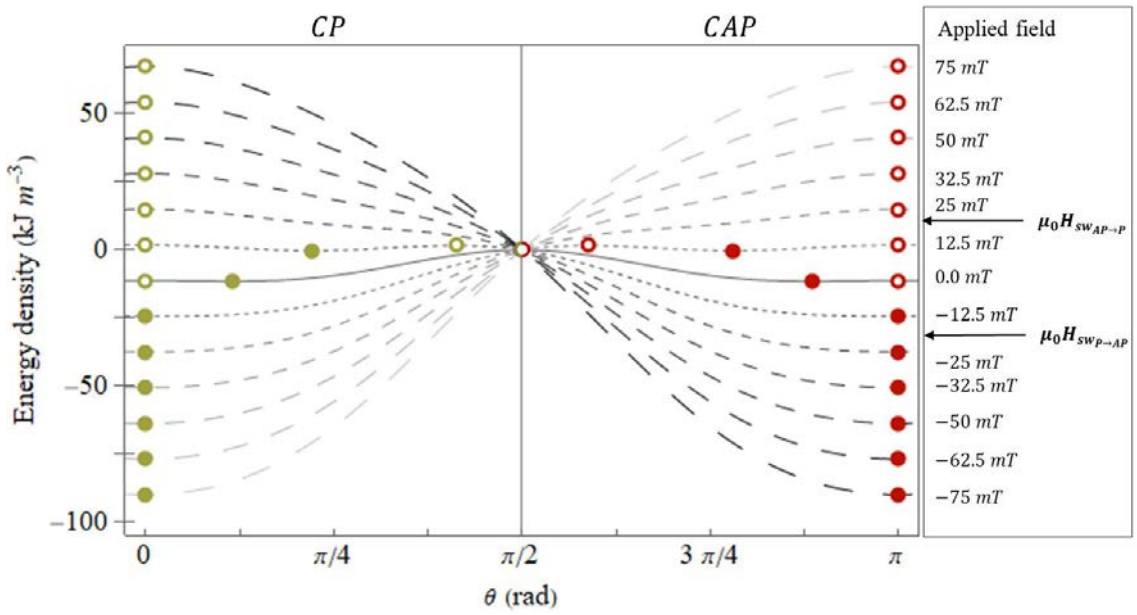


*Figure II.15: Energy density of a magnetic tunnel junction with a $2^{nd}$ order anisotropy as a function of polar angle $\theta$, for applied magnetic fields from 0.075T (light gray) to -0.075T (dark gray), by steps of 0.0125T. The full green (red) dots represent the P (AP) or CP (CP) state as a local minimum of energy density, the empty dots represent the P (AP) local maxima of energy density.*

The cone state minima of energy density are called $CP$ state if they are in the hemisphere of the $P$ state, and $CAP$ state respectively for the $AP$ state. In between the switching fields, the ground states of the system are the cone states, as seen before. Thus seven energy extrema are identified. As in the fully perpendicular geometry, we observe $P_{min}$ (green dots), $P_{max}$ (green circles), $AP_{min}$ (red dots) and $AP_{max}$ (red circles) as well as an intermediary maximum (red and green empty dots) never stabilized between the switching fields and the cone states, one for each

hemisphere, $CP$ (green dots away from $\theta = 0$) and $CAP$ (red dots away from $\theta = \pi$).

The state diagrams of the MTJ computed with the two codes are represented in figure II.16, and large disparities are observed. The state diagram from the LLGS direct integration (figure II.16a) is similar to the one for an "all-perpendicular" geometry, with a reduced switching voltage, as the energy barrier is decreased by the addition of the $K_2$ term .

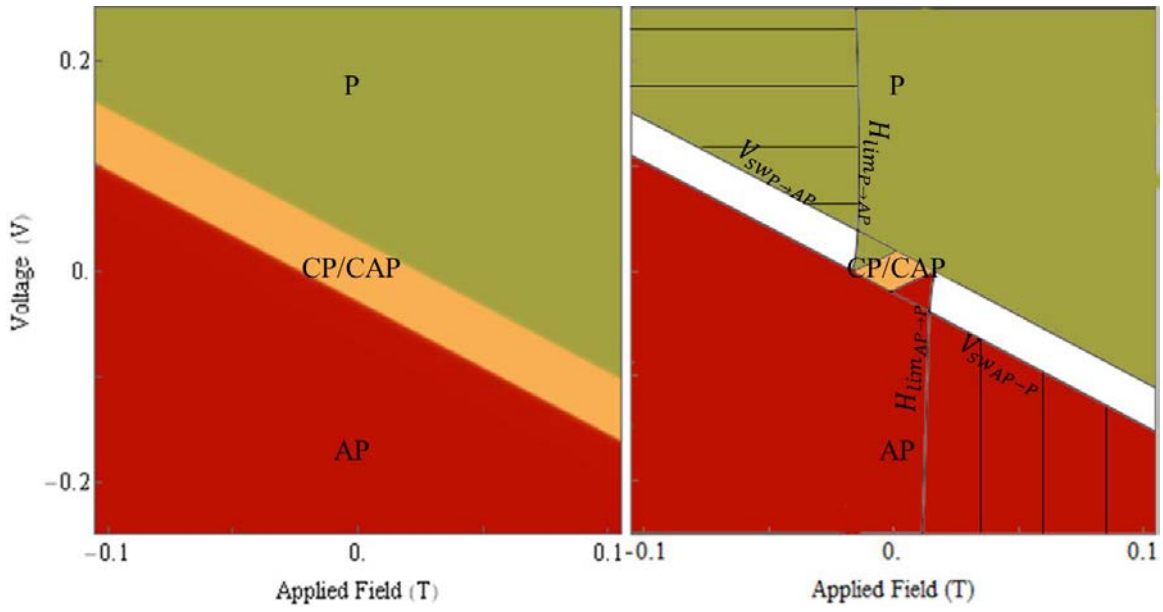


*Figure II.16: Voltage – magnetic field state diagrams with a $2^{nd}$ order anisotropy, computed by the power dissipation model (a) and the direct integration of the LLGS equation (b), in green the region where the $P$ or $CP$ state is stable, in red the $AP$ or $CAP$ state is stable, in orange both cone states are stable. Hatched regions correspond to the stabilization of a maximum of energy density, $P$ state with horizontal hatches, $AP$ with vertical hatches, in the white region none of the states are stabilized.*

The state diagram from the power dissipation (figure II.16b) is more complex than in the previous geometries, as we have now six states to consider ($P_{min}$, $P_{max}$, $CP$, $AP_{min}$, $AP_{max}$, and $CAP$). The cone states are only stabilized between the limit magnetic fields ($H_{lim_{P\to AP(AP\to P)}}$) and switching voltages ($V_{sw_{P\to AP(AP\to P)}}$). The $P$ and $AP$ states can only be stabilized for voltage values larger than the switching voltage. When the voltage value increases, $\theta_{eq}$ becomes indistinguishable from the out-of-plane stabilized state $0$ or $\pi$, and the precession is reduced to an axis precessing on itself. Furthermore, the state diagram presents an area (in white) where none of the energy extrema can be stabilized by the power dissipation. As in the tilted anisotropy case,

this is due to the misalignment of $\boldsymbol{H}_{eff}$ and $\boldsymbol{p}$, the dissipated power changes sign on each side of the energy extremum position. It will be shown in the following that in the cone state, the magnetization precesses, and the polar angle $\theta$ at which it stabilizes is directly linked to the applied voltage value, but does not correspond to the energy extremum position.

With this geometry, we managed to create a stable cone state, without any preferred direction for the azimuthal angle $\varphi$. In the absence of additional forces, the stable position is independent of this angle, but when a voltage is added, the spin transfer torque must act on the magnetization direction. The state consequently obtained is an oscillator. In the next part, both the dynamics of precession in the cone state and the difference in switching voltages between the state diagrams are studied.

### II.3.2 Energy density barriers and switching voltages

In this part, we look at the effect of the voltage for different ratios of magnetocrystalline anisotropy coefficients $\frac{|K_2|}{K_{eff}}$, while keeping a constant energy density barrier $\Delta\mathcal{E}$. The aim is to characterize the dependence of the magnetization dynamics as a function of the voltage in cone-state MTJs. The two effects of the voltage expected in this geometry are the precession and the switching of the magnetization. The two voltages $V_1$ and $V_2$ denoting regime transitions are expressed as functions of $\frac{|K_2|}{K_{eff}}$. In this part the field-like torque is neglected and we do not consider the effect of the applied magnetic field on the system, it is set to $\mu_0 H = 0T$. In this geometry, LLGS is expressed as:

$$\dot{\theta}\boldsymbol{e_\theta} + sin(\theta)\dot{\varphi}\boldsymbol{e_\varphi} = (\gamma_0 a_V V - \alpha\dot{\varphi})sin(\theta\boldsymbol{e_\theta} + (\gamma_0 H_{eff} + \alpha\dot{\theta})\boldsymbol{e_\varphi} \tag{II.37}$$

with $\boldsymbol{H}_{eff} = \frac{2}{\mu_0 M_S}\left(K_{eff} + 2K_2\cos^2\theta\right)\cos\theta\sin\theta\boldsymbol{e}_\varphi$. Projecting onto the $\boldsymbol{e}_\theta$ and $\boldsymbol{e}_\varphi$ axis, LLGS gives the following system:

$$\begin{cases} \dot{\theta} &= (\gamma_0 a_V V - \alpha\dot{\varphi})\sin(\theta) \\ \sin(\theta)\dot{\varphi} &= \frac{2\gamma_0}{\mu_0 M_S}\left(K_{eff} + 2K_2\cos^2\theta\right)\cos\theta\sin\theta + \alpha\dot{\theta} \end{cases} \tag{II.38}$$

We consider $\theta \in [0, \frac{\pi}{2}]$ and the solution is symmetric for the second hemisphere. This system has a trivial solution with $\theta = 0$ that gives $\dot{\theta} = 0$ and induces that there is no motion possible for the magnetization. If $\theta \neq 0$, the previous system can be simplified by $\sin\theta$, and the resulting equations cannot be solved without integration. However, if there is a precession, due to the

cylindric symmetry of the system, it verifies $\dot{\theta} = 0$ and the precession frequency is given by $\dot{\varphi}$. Consequently, the system can be rearranged as:

$$\begin{cases} \dot{\varphi} &= \frac{\gamma_0 a_V V}{\alpha} \\ \dot{\varphi} &= \frac{2\gamma_0}{\mu_0 M_S}\left(K_{eff} + 2K_2\cos^2\theta\right)\cos\theta \end{cases} \tag{II.39}$$

The first line of the system shows that the magnetization precession frequency is an increasing monotonous function, linear with the voltage. Moreover, combining the two equations of the system (II.40), we can get the evolution of the voltage with respect to the dynamic equilibrium polar angle $\theta_{dyn}$:

$$V(\theta_{dyn}) = \frac{\alpha}{a_V}\frac{2}{\mu_0 M_S}\left(K_{eff} + 2K_2\cos^2\theta\right)\cos\theta \tag{II.40}$$

The right-hand side of eq.(II.40) is bounded; the upper bound $V_2$ is obtained for $\cos\theta_{dyn_{max}} = \sqrt{\frac{K_{eff}}{6|k_2|}}$, giving:

$$V_2 = \frac{4}{3}\frac{\alpha}{a_V}\frac{K_{eff}}{\mu_0 M_S}\sqrt{\frac{K_{eff}}{6|K_2|}} \tag{II.41}$$

The lower bound $V_1$ corresponds to $\theta = 0$ for $\frac{|K_2|}{K_{eff}} < \frac{1}{2}$ and to $\cos(\theta_{dyn_{min}}) = \sqrt{\frac{K_{eff}}{2|K_2|}}$ for $\frac{|K_2|}{K_{eff}} > \frac{1}{2}$, giving:

$$V_1 = \begin{cases} \frac{\alpha}{a_V}\frac{2}{\mu_0 M_S}\left(K_{eff} + 2K_2\right) & \text{for} \quad \frac{|K_2|}{K_{eff}} < \frac{1}{2} \\ 0 & \text{for} \quad \frac{|K_2|}{K_{eff}} > \frac{1}{2} \end{cases} \tag{II.42}$$

In order to understand the meaning of $V_1$ and $V_2$, we represent them as a function of $\frac{|K_2|}{K_{eff}} > \frac{1}{2}$ in figure II.17 b). In this diagram, energy density barrier was kept constant to compare the efficiency of each voltage. The energy density barrier expression in this system depends on the presence of the cone state, and we obtain the following relation:

$$\begin{cases} \Delta\mathcal{E} &= K_{eff} + K_2 \quad \text{for} \quad |K_2| < \frac{K_{eff}}{2} \\ \Delta\mathcal{E} &= \frac{K_{eff}^2}{4|K_2|} \quad \text{for} \quad |K_2| > \frac{K_{eff}}{2} \end{cases} \tag{II.43}$$

Figure II.17 b) shows that $V_1$ and $V_2$ are equal for $\frac{|K_2|}{K_{eff}} = \frac{1}{6}$. This point, noted by a black dot, is called a bifurcation.

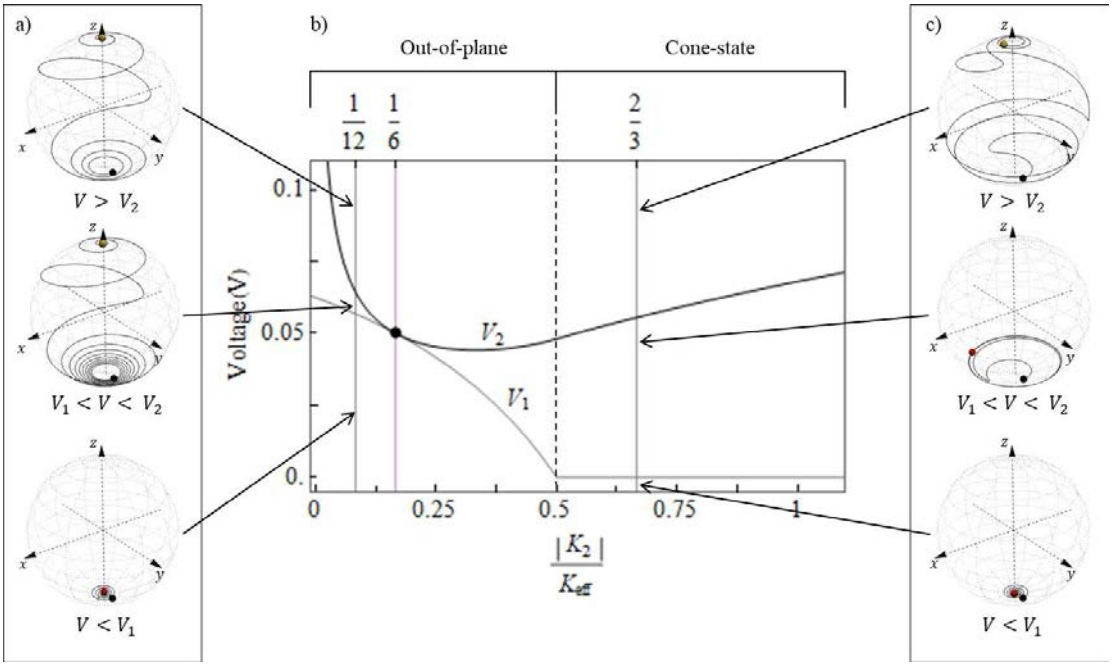


*Figure II.17: a) Magnetization trajectory at different voltages for $\frac{|K_2|}{K_{eff}} = \frac{1}{12}$ from the inital point in black to the final point in red (AP) or green (P), b) $V_2$ (thick line) and $V_1$ (thin line) as a function of $\frac{|K_2|}{|K_{eff}|}$ and at constant energy density barrier with the black dot denoting the bifurcation between the two voltages, c) magnetization trajectory at different voltages for $\frac{|K_2|}{K_{eff}} = \frac{2}{3}$ from the inital point in black to the final point in red (AP) or green (P)*

Figure II.17 a) and c) represents the magnetization trajectory at different voltages before and after the bifurcation, respectively $\frac{|K_2|}{K_{eff}} = \frac{1}{12}$ and $\frac{|K_2|}{K_{eff}} = \frac{2}{3}$. In both cases, when $V < V_1$, the magnetization ends in the static out-of-plane state. When $V > V_1$, the behavior of the magnetization depends on $\frac{|K_2|}{K_{eff}}$. Before the bifurcation, the magnetization switches whereas afterwards, it stays in a dynamic stable state at an angle $\theta_{dyn}$ and only switches when $V > V_2$. We define the switching voltage $V_{sw}$ as $V_1$ for $\frac{|K_2|}{K_{eff}} < \frac{1}{6}$ and $V_2$ for $\frac{|K_2|}{K_{eff}} > \frac{1}{6}$ and the precession voltage $V_p$ as $V_1$ for $\frac{|K_2|}{K_{eff}} > \frac{1}{6}$.

### II.3.3 Optimization of $V_{sw}$

In this part we compare the efficiency of the switching voltage for a pMTJ and a cone-state MTJ, with $\frac{|K_2|}{K_{eff}} > \frac{1}{6}$ at constant energy density barrier. The calculations to find $\frac{|K_2|}{K_{eff}}$ minimizing the switching voltage are done in Appendix II. It is realized by optimizing the following equation

for equal energy barriers:

$$\frac{V_{sw}}{V_{sw_{ref}}} = \frac{2}{3\sqrt{6}} \frac{M_{S_{ref}}}{M_S} \frac{K_{eff}}{K_{eff_{ref}}} \sqrt{\frac{|K_2|}{K_{eff}}} \tag{II.44}$$

In order to compare the same type of device, we are interested in the conditions on the magnetizations at saturation $M_{s_{ref}}$ and $M_s$ for which the introduction of a cone state reduces the switching voltage compared to the fully-perpendicular geometry. In the general case, $M_{s_{ref}}$ and $M_s$ have no reason to be equal, however it is shown in the appendix that to verify $\frac{V_{sw}}{V_{sw_{ref}}} \leq 1$ the conditions on $\frac{M_{S_{ref}}}{M_S}$ are:

$$\frac{M_{S_{ref}}}{M_S} \leq \begin{cases} \frac{3\sqrt{3}}{2} & \text{for} \quad \frac{1}{6} < \frac{|K_2|}{K_{eff}} < \frac{1}{2} \\ \frac{3\sqrt{3}}{4} & \text{for} \quad \frac{1}{2} < \frac{|K_2|}{K_{eff}} < \frac{27}{32} \end{cases} \tag{II.45}$$

both of which are larger than 1. Given theses conditions, we take $M_{S_{ref}} = M_S$ to simplify the following calculations. In that case, the gain of $\frac{V_{sw}}{V_{sw_{ref}}} \leq 1$ is valid for $\frac{|K_2|}{K_{eff}} \leq \frac{27}{32}$. The minimum ratio of switching voltages $\frac{V_2}{V_{sw_{ref}}} = 0.71$ is obtained for $\frac{|K_2|}{K_{eff}} = \frac{1}{3}$. The main result of this study is that, at constant energy barrier, the maximum of efficiency in switching voltage for a MTJ with a second order anisotropy is obtained when the cone state is not yet created, and $V_{2_{min}} = 0.71 V_{sw_{ref}}$. A junction elaborated with this ratio in anisotropy would see its switching voltage having decreased but few variations of the TMR ratio.

### II.3.4 Magnetization switching trajectories

With the LLGS Lagrangian integration code introduced before, we modeled several cases of switching trajectories in all-perpendicular MTJs and cone state MTJs for various ratios $\frac{|K_2|}{K_{eff}}$. For all ratios, the trajectories were computed for $\mu_0 H = 0T$ and a bias voltage close to the switching voltage determined in figure II.17. The voltage values are represented by black dots on figure II.18a. The saturation magnetization, the damping and the Slonczewski coefficient were kept identical to the previous simulation. The only material coefficient allowed to vary is the anisotropy coefficient.

We focused on five cases; $\frac{|K_2|}{K_{eff}} \in \{\frac{1}{6}, \frac{1}{3}, \frac{1}{2}, \frac{27}{32}, 1\}$. As described before, they correspond to the following geometries:

- $\frac{|K_2|}{K_{eff}} = \frac{1}{6}$: the switching voltage is equal to the precessional voltage as $V_1 = V_2$ (purple).

- $\frac{|K_2|}{K_{eff}} = \frac{1}{3}$: the switching voltage $V_2$ is minimum (blue).
- $\frac{|K_2|}{K_{eff}} = \frac{1}{2}$: the cone state is not yet defined, but the equivalence in energy density holds. The initial angle is the largest (green).
- $\frac{|K_2|}{K_{eff}} = \frac{27}{32}$: the switching voltage $V_2$ is equal to $V_{sw_{ref}}$ (orange).
- $\frac{|K_2|}{K_{eff}} = 1$: the equilibrium position is $\theta_{eq} = \frac{\pi}{4}$, it is the limit of the out-of-plane cone states (red).

The energy density landscapes of the investigated cases are plotted in figure II.14, so as to compare the initial angle of the magnetization and the curvature of the potential well for a constant energy density barrier.

Figure II.18 shows the switching voltage (a) and the switching time (b) in pMTJs with different values of the $2^{nd}$ order coefficient. Figure II.18 a) compares the evolution of the switching voltage $V_{sw}$ (thick line) and the precession voltage $V_p$ (thin line) in relation to $V_{sw_{ref}}$ (dashed line). Before the bifurcation point, $V_{sw}$ is identifyied to $V_1$ and $V_p$ to $V_2$, and in reverse after the bifurcation point. The dots in figure II.18 a) correspond to the voltages used to calculate the switching time plotted in figure II.18 b). The initial angle is 0.05 rad and the switching time ends when the magnetization changes hemisphere. The dashed line in this figure corresponds to the switching time for the MTJ with no $2^{nd}$ order anisotropy. Between $V_2$ and $V_1$ we obtain a precessional steady state.

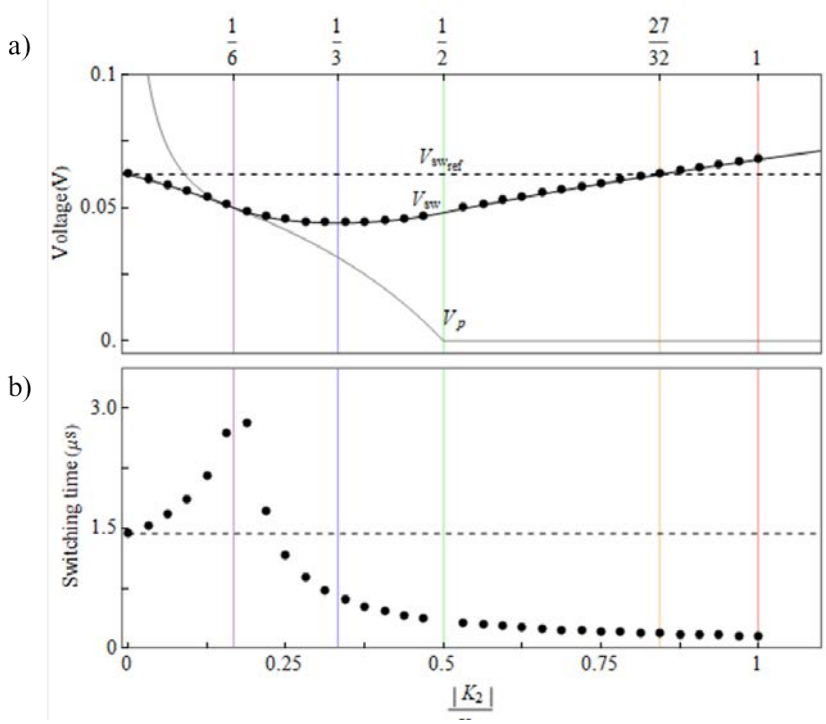


*Figure II.18: a) Switching voltage $V_{sw}$ (thick line) and precession voltage $V_p$ (thin line) for a pMTJ with $2^{nd}$ order anisotropy as a function of $\frac{|K_2|}{K_{eff}}$ at constant energy density barrier, compared to the switching voltage $V_{sw_{ref}}$ (dashed line) of a pMTJ with no $2^{nd}$ order anisotropy. Black dots represent the voltage value used in b) to compute the duration of the switching in the corresponding MTJ.*

Coming from $\frac{|K_2|}{K_{eff}} = 0$, the switching time increases when the switching voltage follows $V_p$, reaches an asymptote in $\frac{|K_2|}{K_{eff}} = \frac{1}{6}$ and starts decreasing after the bifurcation. As expected, at constant energy barrier, the switching time in the $V_{sw}$ branches decreases when the applied voltage increases. For the minimum in $V_{sw}$, the switching is about two times faster than for the all-perpendicular geometry.

## Conclusion

In this part, state diagrams for pMTJs were computed using two macrospin models, one based on the power dissipation model and the other a direct integration of the LLG equation. Different geometries were investigated. The state diagrams present three stable states, that correspond to the extrema of the energy density as a function of the polar angle, and noted $P$, $AP$ and a bistable state $P/AP$. For highly symmetric cases, or close to it (weakly tilted field), both models show a

perfect agreement with one another.

From the power dissipation model, it is shown that maxima of the energy density landscape are stabilized by the spin transfer torque. The limit of stability between the states is described by $V_{sw_{P(AP)}}$ and the limit of the stability condition on the maxima is described by $H_{lim_{P(AP)}}$. Both $V_{sw_{P(AP)}}$ and $H_{lim_{P(AP)}}$ were expressed analytically for a fully perpendicular geometry. When the symmetry is further broken (tilted anisotropy axis), due to the non-colinearity of the non-conservative torques, the state diagrams do not agree, especially for values close to $H_{sw}$, a large difference between the models can be observed. In these cases, the energy extremum positions do not correspond to extremum positions of the dissipated power, it follows that the power changes sign on each side of the energy density extremum positions in that case, one stabilizing them, the other destabilizing them.

The interest of this method is to help undestanding the experimental state diagram realized at room temperature. In these state diagrams discussed in part III, the area where the maximum states should be stabilized according to the macrospin models do not exist. Plotting their energy barrier shows that for these applied magnetic field and voltage, the heigth of the energy barrier depends quadratically on both parameters, and can be in the range of thermal activation of the switching. Moreover, we compute that when the symmetry is broken, the conditions of stability of this maximum state are reduced, a result which is obtained for both macrospin models.

Another geometry studied consists in introducing a second order anisotropy. The addition of this term creates stable cone states where the precession is driven by the voltage. We show that a precessional state appears even before the occurence of the cone states in the energy density landscape. In that case, we identified two voltages, one for the onset of the precession and one for the switching. At constant energy barrier but with a varying ratio of magnetocrystalline anisotropy, the switching voltage can be lowered by 40%, the switching time is vastly reduced. This occurs before the apparition of the cone state.

In the next part, we will discuss the difference between our experimental state diagrams and the macrospin computation and develop a probabilistic approach to characterize the energy barrier between the two magnetic configurations taking into account both the field and the voltage.

# Chapter III

# Switching probablity in pMTJs

## Résumé en français

Cette partie présente une étude expérimentale du retournement de l'aimantation dans des jonctions tunnels fabriquées par IBM. Ces jonctions tunnels sont composée de matériaux a aimantation perpendiculaire et leur surfaces elliptiques varient de $60 \times 80 nm^2$ à $65 \times 240 nm^2$. La couche de référence est une structure antiferromagnétique synthétique (SAF).

Les diagrammes d'état obtenus expérimentalement diffèrent de ceux obtenus par la modélisation macrospin de la partie précédente. On observe un décalage en champ et en tension du diagramme ainsi qu'une différence des coefficients directeurs de la tension de retournement en fonction du champ. Ce décalage en champ provient de l'effet moyen du champ magnétique rayonné par la couche de référence sur la couche libre

Nous proposons deux approches probabilistes du retournement de l'aimantation afin de déterminer la hauteur de la barrière d'énergie existant entre les deux configurations magnétiques stables. Les deux méthodes se basent sur l'expression thermiquement activée du retournement de l'aimantation.

La première approche consiste à utiliser le bruit télégraphique, observé à haute température pour estimer la valeur du temps de vie moyen d'un état. La seconde approche s'intéresse au retournement de l'aimantation par l'effet du couple de transfert de spin. L'effet de la tension

appliquée est traité comme une température effective. L'expression de la probabilité de retournement utilisée permet de prendre en compte le balayage en tension utilisé expérimentalement. Les hypothèses effectuées sur l'expression du couple de transfert de spin, sont l'indépendance du coefficient du couple de transfert de spin de Slonczewski en fonction de la transition, $AP \rightarrow P$ et $P \rightarrow AP$, et que le couple field-like est négligeable.

La première approche met en avant la nécessité de définir un champ pour lequel les barrières d'énergies sont égales. La deuxième approche montre une différence de ce champ avec le champ de décalage. Cet effet est présent pour toutes les tailles de jonctions considérées. La valeur des barrières d'énergie pour ce nouveau champ augmente avec la taille des jonctions.

Nous nous sommes ensuite intéressés à l'effet du champ rayonné par la couche de référence sur la couche libre en imposant à la couche de référence une configuration ferromagnétique. Le résultat est une réduction de la coercivité du diagramme d'état, une modification des coefficients directeurs des tensions de retournement et une augmentation du décalage en tension. Cet effet est observé pour toutes les tailles de jonctions et il est assorti d'une augmentation des valeurs de barrière d'énergie

# Introduction

In the previous chapter we presented model voltage – magnetic field state diagrams for a pMTJs in different geometries. The free layer magnetic orientations were described using a macrospin model at zero Kelvin. Comparing this state diagram to experimental state digram yields general differences, implying a much complex system. The macrospin model does not take into account the spacial dependence of the magnetization, the interaction of the other layers on the free layer, the size, aspect-ratio and edge influences on the magnetization, and the temperature effect on the magnetization.

In this part we study experimentally the influence of the junction sizes and of the stray field on the magnetization reversal, and we aim to extract key structural parameters that can be responsible for the assymetry in switching voltage and energy barriers observed.

The experimental state diagrams that will be studied are obtained by sweeping the voltage at a constant rate and fixed field, then extracting the switching voltage for each polarity. This section introduces probabilistic quasi-static models based on the magnetization switching temperature dependence that describe the voltage driven - or spin transfer torque driven - switching for each transition and aim to discuss the discrepencies with the macrospin models. First the energy barrier corresponding to the switching are defined using a Néel - Brown equation, then similarly to the work of Koch and Katine, we introduce the voltage as an effective temperature. The validity of these approaches is discussed.

## III.1 Samples description and comparison to model

### III.1.1 Sample description

The pMTJs studied are elliptical nanopillars provided by IBM. Their surface sizes range from $60 \times 80nm^2$ to $65 \times 240nm^2$, they have a tunnel magneto resistance of about $40\%$ for the larger junctions to $55\%$ for the smaller, and a resistance area parameter of about $14\Omega\mu m^2$, which correspond to a base resistance (parallel state) that varies between $900\Omega$ for the $60 \times 80nm^2$ to $350\Omega$ for the $65 \times 240nm^2$ samples. The nanopillar shapes come from the choice of the industry to reuse lithographic masks for in-plane samples in these new stacks, as well as the attempt to realize

a uniform demagnetization field.

The MTJ stack is described in figure III.1 with the thicknesses in nanometers. From top to bottom, the stack is: $CoFeB(0.8)//MgO(0.9)//CoFeB(1.3)/Ta(0.3)/Co(0.25)|Pt(0.8)$ $/[Co(0.25)|Pd(0.8)]_4/Co(0.3)//Ru(0.9)//[Co(0.25)|Pt(0.8)]_{14}$, with the number of repetition of the deposited layer in index. On top of the structure, the free layer is in dark green and below, the SAF structure formed by the reference layer and pinned layer in red. On top of the SAF, the polarizer is strongly coupled with the rest of the structure with the Ta layer. The SAF structure is obtained using the RKKY coupling through the Ruthenium layer, as presented part I [113–115].

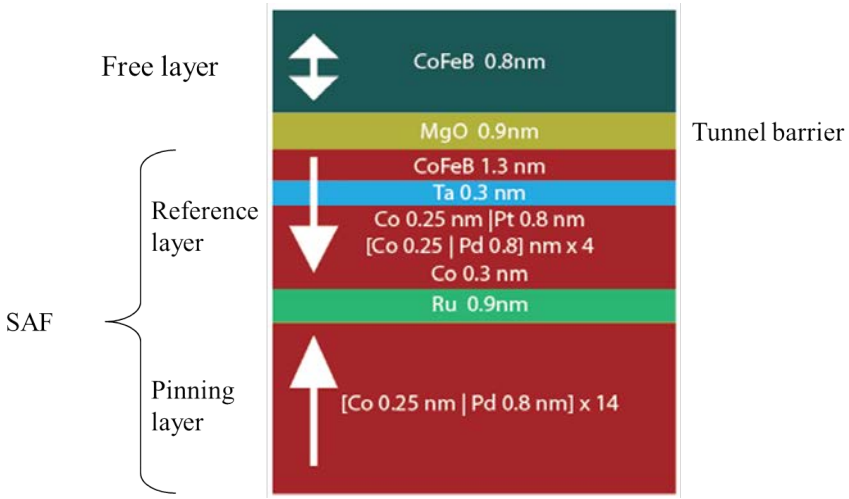


*Figure III.1: composition of the pMTJ. The top green CoFeB layer is the free layer, the red layers compose the SAF structure ending with the referencing layer.*

We first realized experimental state diagrams for different sizes of MTJs then used a probabilistic approach to study the switching mechanism in the junctions.

### III.1.2 State diagrams comparison to model

In this part we aim to characterize the switching voltage of pMTJs to infer information on the stability of the corresponding state and the magnetization reversal process. In order to do so, we construct the state diagram of a pMTJ at room temperature using voltge sweep with a fixed rate at fixed field. In figure III.2b) is represented such a state diagram for a $70 \times 100nm^2$ junction, where we can extract the switching voltages and the limit magnetic fields as described in part II. In the macrospin approximation, we showed that the switching voltage depends both on the energy

barrier and the ratio of the spin transfer torque coefficient over the damping coefficient. With the aim to quantify the later of these two parameters, in figure III.2 we compare the experimental state diagram (figure III.2b) to an all perpendicular modeled one (figure III.2a) obtained from the power dissipation model described in part II.

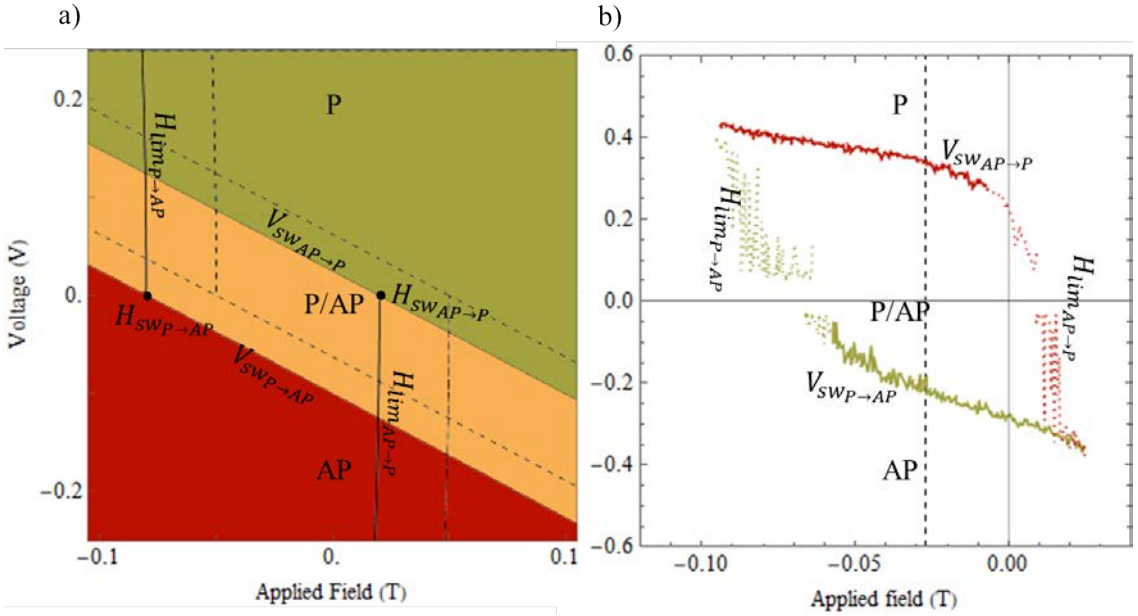


*Figure III.2: a) State diagram computed with the power dissipation model with the previous parameters without the offset field, in plain lines with an offset field $\mu_0 H_{off} = 0.05T$. b) Experimental state diagram for a $70 \times 100nm^2$ junction: in red the $AP \to P$ transition, in green the $P \to AP$ transition.*

The first notable difference between the two state diagrams is that the bistablity area of the experimental state diagram only correspond to the bistability area of the minima of energy in the calculated one. In the areas where both a minimum and a maximum of energy can be stablized, a result found using the LLGS direct integration and the power dissipation model, only the minimum of energy is stablized whereas in the areas where only a maxima of energy can be stabilized, we observe that this later is stabilized. This may also be similar to the reduction of the $Min/Max$ areas of bistability observed when the symmetry of the geometry is broken.

The second main difference is the presence of an offset field $\mu_0 H_{off}$, shifting the limit fields of the experimental state diagram of about $\mu_0 H_{off} = -27mT$ and noted by the vertical dashed axis in the figure III.2b). It is caused by the stray field from the reference layer on the free layer. In first approximation, we will consider it to be uniform and out-of-plane, which only requires the

addition of a new term in the expression of the switching voltage in eq.(II.34) as shown in (III.1). In figure III.2 a) the dashed line is the computed fully-perpendicular state diagram not taking into account this new offset term, whereas the full black delimitation is the state diagram corrected with this offset term. The result of this addition is the translation of the limit fields and switching voltages of this offset along the field axis. The slopes of the switching voltages are not modified, and the intercept at the origin is transposed of $\mu_0 H_{off}$. In the macrospin approximation, taking into account an averaged stray field due to the reference layer in $\mu_0 H_{off}$ and neglecting the field-like torque coefficient, according to part II.2, the switching voltages $V_{sw_{P\to AP(AP\to P)}}$ in the state diagram can now be expressed as eq. (III.1):

$$V_{sw_{P\to AP(AP\to P)}} = -\frac{\alpha}{a_V}(H + H_{sw_{P\to AP(AP\to P)}} + H_{off}) \tag{III.1}$$

As in part II, the switching fields are defined as $\mu_0 H_{sw_{P\to AP(AP\to P)}} = \mp\frac{2K_{eff}}{M_S}$ and the ratio between $\alpha$ the damping parameter of the free layer and $a_V$ the Slonczewski spin transfer torque coefficient determines the slope of the switching voltage with respect to the applied magnetic field $\mu_0 H$.

The third difference between state diagrams is the dependence of the switching voltage parameters with the transition. Using equation (III.1) to fit the state diagram in figure III.2b, we observe that the switching voltage slopes and the absolute voltage values at the offset field $V(\mu_0 H_{off})$ depend on the transition in the experimental data. In the $70 \times 100nm^2$ junction, the slopes of the switching voltages have been extracted: $\frac{\alpha}{\mu_0 a_{V_{P\to AP}}} = -2.68V.T^{-1}$ and $\frac{\alpha}{\mu_0 a_{V_{AP\to P}}} = 1.42V.T^{-1}$ , and the switching voltage value for the offset field are $V_{P\to AP}(\mu_0 H_{off}) = -0.24V$ and $V_{AP\to P}(\mu_0 H_{off}) = 0.33V$. In part II, based on litterature, the STT coefficient was taken independent of the angle between the free layer magnetization and the polarizer. Moreover, if we look at the limit field branch of the experimental state diagram, the dispersion of the corresponding switching voltages is larger for the $P \to AP$ transition than for the $AP \to P$ transition. This hints toward a difference in energy barriers as a function of the transition.

From the study of figure III.2 several discrepancies between the quasi-static measurment of a state diagram and the model were listed, showing the limitations of the approach proposed in part II to describe expererimental results. Among the assumptions made in part II that we will

revise in this part are the temperature effects on magnetization reversal - as the magnetization is a thermally activated process we will characterize the thermal stablity of MTJs through a probabilistic analysis -, the interaction of the free layer with the stray field, and the size of the junction and try to extract the corresponding energy barriers.

## III.2 Thermally activated switching

The Stoner Wohlfarth model describes the magnetization behavior at zero Kelvin. In a general case, when the variations of the energy of the system are large compared to the thermal energy, the thermal agitation can be neglected and the system follows the Stoner-Wohlfarth model. In the case when the energy variation is comparable to the thermal energy, the thermal agitation makes the magnetization fluctuate. In our system at room temperature, the magnetization behavior with field can be explained by the Stoner-Wolhfarth model away from the switching, but close to the switching the thermal agitation will be of comparable magnitude. In order to describe an intermediary case, it is possible to introduce a random field in the LLG equation. Néel [116] first described the thermal fluctuation by considering fluctuations of the effective field. Brown [117] used the Langevin equation of a stochastic process (eq. (III.2)) by introducing a random field $\mathbf{h}(t)$ in the LLG equation:

$$\frac{d\mathbf{m}}{dt} = -\gamma_0 \mathbf{m} \times \boldsymbol{H}_{eff} + \alpha \mathbf{m} \times \frac{d\mathbf{m}}{dt} + \gamma_0 \mathbf{m} \times \mathbf{h}(t) \tag{III.2}$$

The thermal fluctuation of the magnetization direction means that, at finite temperature, there is a non-zero probability that the system can reverse back and forth between the stable states described by the Stoner Wohlfarth model. In order to understand the behavior of the magnetization and quantify the stability of each state, we now look at a statistical approach of the reversal of the magnetization in the system. The statistics developed by Néel first, and later by Brown was for a nanoparticle with a uniaxial anisotropy and uniform magnetization. Using the assumption that the thermal agitation is much faster than the system response, it can be considered as a Brownian motion, and the random field can be described as a white spectrum. Brown used then the Fokker-Plank equation to obtain the expression of the switching probability. The switching probability obtained is exponential and depends on a time constant that follows the Boltzmann statistics as we will discuss in the next paragraph.

### III.2.1 Thermal activation theory

#### *Non-switching probability*

The magnetization switching process can be considered as a two-states system and we consider that the probability of switching only hinges on the state before the measurement. This correspond to a discrete Markovian random process. In this part, we aim to discuss the expression of the non-switching probability of a state noted $P_{NS}$ with the assumption that the observation time $t_m$ is many orders of magnitude larger than the equilibration time - time taken by the system to reach its equilibrium position -, and the latter is much larger than the attempt rate of the system $\tau_0$. From Néel works in 1949, we know that the mean lifetime of a state $\langle\tau\rangle$ follows an Arrhenius-Néel law [116].

$$\langle\tau\rangle = \tau_0 \exp\left(\frac{\Delta E_H}{k_B T}\right) \tag{III.3}$$

In this expression, $\frac{\Delta E_H}{k_B T}$ is the normalized energy barrier expression and is composed of the energy barrier as function of the applied magnetic field $\Delta E_H$, the Boltzmann constant $k_B$ and the temperature, $T$. The attempt rate $\tau_0$ is intrinsic to the system and hinges on the damping constant and the magnetic properties of the free layer[118, 119]. Its inverse, the attempt frequency $f_0$, should be in the same order of magnitude as the spin precession period and is usually taken between $10^9$ Hz and $10^{12}$ Hz [120, 121].

In this context, the probability of switching $P$ per units of time can be defined as [21]:

$$P = \frac{1}{\langle\tau\rangle} = \frac{1}{\tau_0} \exp\left(-\frac{\Delta E_H}{k_B T}\right) \tag{III.4}$$

At a given temperature, this probability only hinges on the energy barrier height, therefore if the P state and the AP state have the same energy, the switching probability is expected to be independent of the initial state, as the expected situation should happen in a zero applied field in a macrospin model. If we look at the system that has not switched during a time $t_m$ longer than the relaxation time of the system, $t_m$ represents the $ith$ attempt to switch ($t_m = i\tau_0$), and the corresponding probability of non-switching $P_{NS}(t)$ during the measurement time $t_m$ is given by [122]:

$$P_{NS}(t_m) = (1 - P\tau_0)^{\frac{t_m}{\tau_0}} = \left(1 - \exp\left(-\frac{\Delta E_H}{k_B T}\right)\right)^{\frac{t_m}{\tau_0}} \tag{III.5}$$

However there is another way to express the non-switching probability. If we consider directly the Kolmogorov equation that represents the probability of being in a certain state between

$t_m$ and $t_m + dt_m$ [123], the corresponding decay rate of the non-switched fraction of the system is given by:

$$\frac{dP_{NS_K}(t_m)}{dt} = -\frac{1}{\langle\tau\rangle} P_{NS_K}(t_m) \tag{III.6}$$

Which gives:

$$P_{NS_K}(t_m) = \exp\left(-\frac{t_m}{\langle\tau\rangle}\right) = \exp(-t_m P) = \exp(-\frac{t_m}{\tau_0}\exp\left(-\frac{\Delta E_H}{k_B T}\right)) \tag{III.7}$$

In order to compare the two expressions, we use the Taylor series of eq.(III.5) for $\tau_0$ close to 0, which is coherent as for the relatve values of $t_m$ and $\tau_0$, and we obtain:

$$\ln P_{NS}(t_m) = \frac{t_m}{\tau_0}\ln\left(1 - P\tau_0\right) \simeq -\frac{t_m}{\tau_0} P\tau_0 = -Pt_m = \ln P_{NS_K}(t_m) \tag{III.8}$$

Both equations are equivalent in the first order of the Taylor expansion, that corresponds to the framework of the model. From these expressions, with an attempt frequency fixed at $\frac{1}{\tau_0} = 1$ GHz and considering an energy barrier larger than $\Delta E = 25 k_B T$, the state is stable for $\langle\tau\rangle \simeq 75$ s and as this evolution is exponential, for $\Delta E = 40 k_B T$, the state lifetime goes up to $7.5$ years[124].

### *Energy barriers*

In a magnetic nanoparticle, for a given field, the energy barrier is given by the potential energy landscape. And the total energy barrier of a transition $\Delta E$ can be linked to the energy barrier for a given magnetic field, written as $\frac{\Delta E_H}{k_B T} = \frac{\Delta E}{k_B T}\left(1 - \frac{H}{H_{sw_0}}\right)^{\eta}$. $H_{sw_0}$ is the zero-temperature magnetic field switching around the offset field and $\eta$ is an index that only depends on the geometry. In his article Néel shows that a power law can describe the energy barrier as a function of the applied field.

When the energy landscape is symmetric between the stable states, such as in the fully perpendicular macrospin case, $\eta = 2$, however when the potential barrier is no more symmetric, for example when the field is tilted away from the out-of-plane direction in the macrospin case or for most of domain wall nucleation and propagation mecanisms, $\eta \in [\frac{3}{2}, 2]$ and is closer to $\eta = \frac{3}{2}$ [124]. This value, $\eta = 1.5$, is set for the rest of the manuscript. In the following, considering the effect of the stray field from the reference layer, we write the energy barrier as a function of the applied magnetic field centered on an offset magnetic field value [125]:

$$\frac{\Delta E_H}{k_B T} = \frac{\Delta E}{k_B T}\left(1 - \frac{H - H_{off}}{H_{sw_0}}\right)^{\frac{3}{2}} \tag{III.9}$$

Here we want to remember that this model is accurate away from the switching field values. Indeed close to them, the energy barrier is of the same order of magnitude as the thermal perturbation, thus the assumption made to use the Arrhenius law are no more fully verified [117].

### III.2.2 Experimental study

The measurement was realized in a probe station with an out-of-plane superconductive magnet. The study was realized at 420K, 425K and 440K, at which we observe thermally activated switching under a small bias in contrast to the switching voltages, $V = 0.005V$, for various applied magnetic fields. Backhopping was observed in the smallest of our samples at high temperature, starting from $420K$ and studied up to $440K$. The study was realized for several samples, but we chose to present only one that will present the measurment trends. We mesured the hysteresis loop of our sample at $420K$ to define the range of recording (figure III.3). We found it to be countained between $\mu_0 H = 25mT$ and $\mu_0 H = 39mT$ for $420K$ and as expected the size of the hysteresis loop decreases with the temperature.

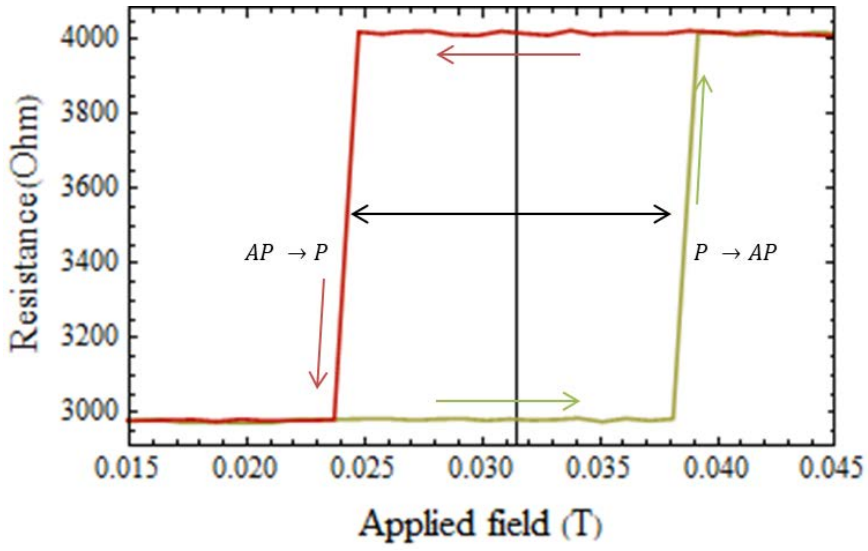


*Figure III.3: Resistance as a function of the applied field at 420K for increasing (green) and decreasing (red) magnetic field.*

In order to assess the probabilistic model presented previously, we studied the thermally activated switching in pMTJs and the dependence of the mean lifetime on the applied magnetic field value, keeping the voltage at $V = 5mV$, much lower than the switching voltages. The recording

duration was of 30 minutes per measurement and recorded with a Keithley 2400. The measurement time is sufficiently long compared to the switching time to assume a Markov process.

### *Data recording*

Based on the previous model, there are two ways of extracting the mean life time of the states for a given applied field: first by computing the mean length of the plateau in each state and second by studying the switching probability such as described in part III.2.1. In figure III.4 quarter-hour part of half-hour recordings at $425K$ and $440K$ are presented for an applied field of $\mu_0 H = 30mT$. In figure III.4 a) we see the thermally activated switching at $425K$ from the lower resistance state, assimilated to the P state to the higher resistance state, AP. This is called telegraph noise and figure III.4 b) presents the corresponding probability of non-switching as a function of the duration of the plateaus in the P state (green) and the AP state (red). The dots are the empirical cumulative function (ECDF) of the plateau length obtained from figure III.4 a). Similarly, figure III.4 c) shows the thermally activated switching at $440K$ for the same sample and figure III.4 d) presents the corresponding probability of non-switching as a function of the duration of the plateaus.

For the results at $440K$, the acquisition time of the Ohm-meter was of the same order as the event, and we observe intermediate points in the diagram corresponding to non-completed transition. We choose to consider all points on each side of an average resistance of $\bar{R} = 3400\Omega$ to be attributed to the corresponding fully switched plateaus. This measure is at the limit of validity of the model.

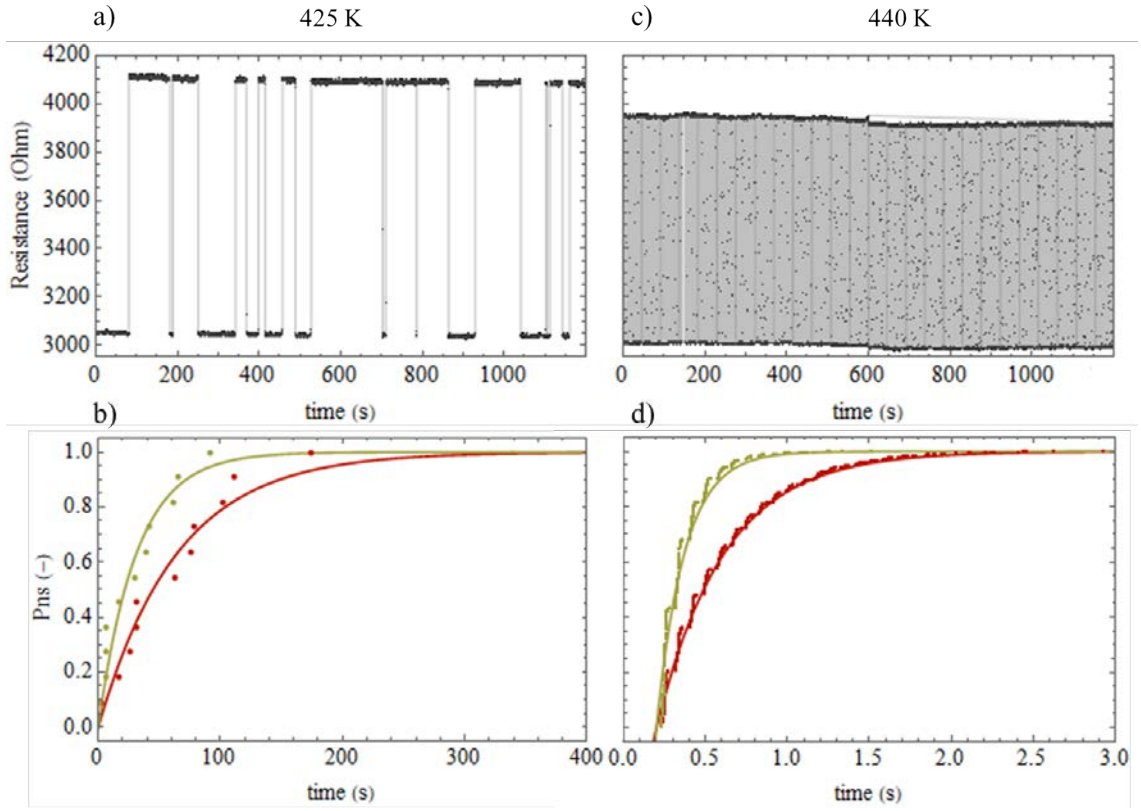


*Figure III.4: Temperature switching at $\mu_0 H = 30mT$ for a) $T = 425K$ and b) $T = 440K$, and fitting of the corresponding empirical cumulative function (dots) by $P_{NS}$, in red for the $AP \rightarrow P$ transition and in green for the $P \rightarrow AP$ transition for c) $T = 425K$ and d) $T = 440K$.*

## *Extraction of the mean life parameters*

For each field, temperature and transition, the mean lifetime value is extracted using two methods: first by using eq. (III.3) expression and second by averaging the plateau lengths. In figure III.5, we compare the mean life time $\langle \tau \rangle$ extracted from the probability function (in plain lines) and the mean duration of the plateau (dashed lines) for different applied magnetic fields at $420K$, $425K$ and $440K$, in green for the $AP \rightarrow P$ transition and in red for the $P \rightarrow AP$ transition. Both analyses give similar results for the mean lifetime, especially away from the switching fields. In the following, the fitting results obtained for the mean lifetime acquired by averaging of plateau lengths are between brackeets and the mean lifetime obtained from the switching probability expression fitting are plain.

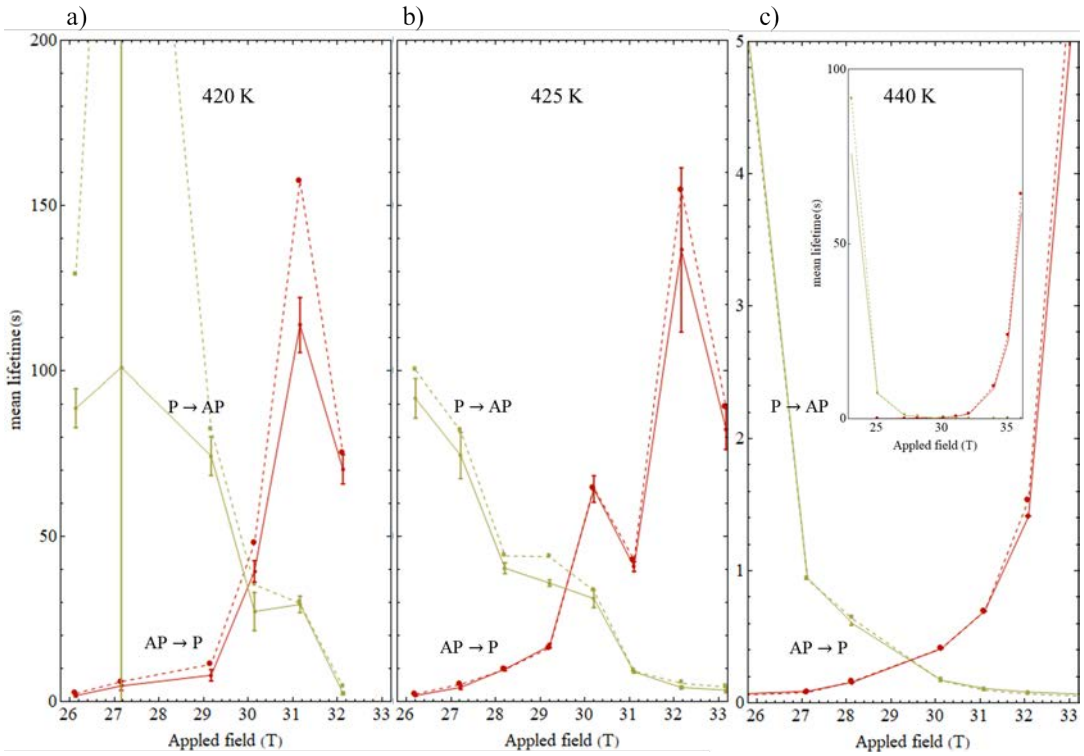


*Figure III.5: Comparison of the mean lifetime $\langle\tau\rangle$ extracted from the switching probability (plain lines) with the mean duration in the telegraph noise measuremenst (dashed line) as functions of the applied field a) at $420K$, b) at $425K$ and c) at $440K$. The P state is in green and the AP state is in red.*

From the comparison of the energy barrier as a function of the field for different temperature, we see that for measurement at $420K$ and $425K$ (figures III.5 a) and b)) are in the same range of magnitude, compared to measurements at $440K$, which is linked to the exponential trend of $\langle\tau\rangle$ as a function of temperature (eq.(III.3)). For 420K, as less events were recorded, therefore there are more discrepancies between the two acquisition methods for the mean lifetime $\langle\tau\rangle$.

The expression of the mean lifetime has four parameters, and among them we chose to set $\tau_0 = 10^{-9}s$ as the characteristic time of the magnetization precession, and we are interested in finding the free parameters $\mu_0 H_{off}$, $\frac{\Delta E}{k_B T}$, and $\mu_0 H_{sw_0}$. During the fitting, we observe that the free parameters present few difference depending on the extraction method used. If all three free parameters are left to converge freely, they all do toward different absolute values. We observe that $\mu_0 H_{off}$ values converge toward two different values as a function of the transition considered, which is in contradiction with the precedent part where we made the assumption to treat $\mu_0 H_{off}$ as a constant magnetic field. There are several ways to define the offset field values in this case.

It can either be defined as the average center of field hyteresis loops or consider that the energy landscape corresponding to each transition should be similar, to be the field for which the energy barrier is equal for both transition. We chose this latter method to estimate $\mu_0 H$. In table III.1 are sumarized the results from fitting at all the temperature and for both method of extraction for $\tau$ and keeping $\tau_0$ constant.

| $\tau_0 = 1.00$ ns | | $P \rightarrow AP$ fitting $\langle\tau\rangle$ (plateau mean) | $AP \rightarrow P$ fitting $\langle\tau\rangle$ (plateau mean) | $\langle\tau\rangle(\mu_0 H_{off})$ |
|---|---|---|---|---|
| T = 420K | $\Delta E$ ($k_B T$) | $24.2 \pm 0.2 (24.2 \pm 0.2)$ | $24.2 \pm 0.1 (24.0 \pm 0.3)$ | 32.4 s |
| $\mu_0 H_{off} = 30.25mT$ | $\mu_0 H_{sw_0}(mT)$ | $44 \pm 6 (80 \pm 20)$ | $-68 \pm 10 (-68 \pm 7)$ | |
| T = 425K | $\Delta E$ ($k_B T$) | $23.8 \pm 0.1 (23.7 \pm 0.1)$ | $23.8 \pm 0.1 (23.8 \pm 0.1)$ | 21.7s |
| $\mu_0 H_{off} = 29.75mT$ | $\mu_0 H_{sw_0}(mT)$ | $74 \pm 8 (75 \pm 6)$ | $-71 \pm 7 (-68 \pm 7)$ | |
| T = 440K | $\Delta E$ ($k_B T$) | $19.4 \pm 0.1 (19.0 \pm 0.5)$ | $19.4 \pm 0.1 (19.7 \pm 0.1)$ | 0.3s |
| $\mu_0 H_{off} = 29.5mT$ | $\mu_0 H_{sw_0}(mT)$ | $52 \pm 6 (35 \pm 30)$ | $-47 \pm 3 (-57 \pm 7)$ | |

*Table III.1: Energy barrier $\Delta E$ and zero Kelvin switching magnetic field $\mu_0 H_{sw_0}$ for the two transitions at $420K$, $425K$ and $440K$, with $\tau_0 = 1.00$ ns and different $\mu_0 H_{off}$, extracted from the mean lifetime obtained by the fitting of the switching probabiltiy.*

With this definition of $\mu_0 H_{off}$, the values found for the offset field decrease for an increasing temperature, in the same way that the height of the energy barrier decreases which result in a decrease of the meanlife time values for the same field. The values found of $\langle\tau\rangle$ at $\mu_0 H_{off}$ for the two lower temperatures are in accordance with the time scale of switching recorded, but not for $T = 440K$, wherethe meanlife time value obtained is much larger than the observed switching time. This prove to be the limits of this experiment. Due to mechanical limitations, we were not able to take an additional intermediary temperature that would have assessed the previous results.

The $\mu_0 H_{sw_0}$ values are not symmetric for any of the temperature, and whereas for the $AP \rightarrow P$ transition, $\mu_0 H_{sw_{0_{AP \rightarrow P}}}$ stays in the same order of magnitude, for the $P \rightarrow AP$ transition, the values are spread over a large range of values. This raises questions on the equivalence of the switching process depending on the transition considered and hints toward a difference in mechanisms for the switching depending on the transition. This cannot be explained by a macrospin model, as the switching process would be a coherent reversal of the free layer magnetization.

Indeed, the lateral size of the nanopilar is larger than the requisite for a macrospin domain, and in such a case, the switching reversal can be represented by a nucleation/propagation process. This process is decribed by several energy barriers, one for the nucleation and one for the propagation, however the nucleation process is the less energy favored and the main energy barrier. In a first approximation, we identify this energy barrier to the one in the switching probability described in part III.2.1 and we use this expression to introduce the STT driven switching probability.

## III.3 STT driven switching

The previous part shows the dependence of the energy barrier as a function of the applied field and temperature, however in the STT-MRAM, the switching is also driven by the spin transfer torque. For industrial applications, it is important to control both the height of the energy barrier and the switching voltage in order to optimize the energy consumption of the device. In the next part, we will study the switching probability as a function of the voltage.

### III.3.1 STT driven switching probability

#### *Statistical properties of the Langevin field in the thermodynamic equilibrium*

In part III.2, we expressed the LLG equation at finite temperature by introducing a random Langevin field $\mathbf{h}(t)$ (eq. (III.2)). For a system at the thermodynamical equilibrium, we can find the expression of the fluctuating field by using the equilibrium position of the magnetization: the magnetization is fixed in this direction, and the fluctuations only contribute to the components of the magnetization in the plane perpendicular to this direction; we assume fluctuations in these two directions, denoted $x$ and $y$. From the assumptions made, the random Langevin field is expressed as:

$$\mathbf{h}(t) = \begin{bmatrix} h_x(t) \\ h_y(t) \end{bmatrix} \tag{III.10}$$

with the following correlation function $\phi_h$:

$$\underline{\underline{\phi_h}}(t) = \begin{bmatrix} \phi_x(t) & 0 \\ 0 & \phi_y(t) \end{bmatrix} \delta(t) \tag{III.11}$$

with $\delta(t)$ a Dirac function. Following the theorem of equipartition of energy, we have:

$$\phi_x = \phi_y = \frac{2\alpha}{\gamma_0 \mathcal{V}} k_B T \tag{III.12}$$

with $\mathcal{V}$ the magnetic volume, and we can write:

$$\underline{\underline{\phi_h}}(t) = \phi_h(t)\underline{\underline{\mathcal{I}}} = \frac{2\alpha}{\gamma_0 \mathcal{V}} k_B T \delta(t) \underline{\underline{\mathcal{I}}} \tag{III.13}$$

with $\underline{\underline{\mathcal{I}}}$ the identity matrix. While, by definition $\phi_h(0) = \langle |\mathbf{h}|^2 \rangle$, thus:

$$\sqrt{\langle |\mathbf{h}(t)|^2 \rangle} = \sqrt{\frac{2\alpha}{\gamma_0 \mathcal{V}} k_B T} \tag{III.14}$$

By introducing $\mathbf{k}(t)$ a random Gaussian field in $x$ and $y$ direction, verifying $\langle \mathbf{k}(t) \rangle = 0$ and $\langle \mathbf{k}^2(t) \rangle = 1$, we can finally write the expression of our fluctuating field as follows:

$$\mathbf{h}(t) = \sqrt{\frac{2\alpha}{\gamma_0 \mathcal{V}} k_B T}\, \mathbf{k}(t) \tag{III.15}$$

with this conditions, the energy of the system achieves an equilibrium Boltzmann distribution in the limit of long times for the temperature T [126]. The main assumption here is that the system is at the thermodynamic equilibrium.

### *Modification of the Langevin field in the presence of STT*

The effect of spin transfer torque on the magnetization dynamics are added to the Landau-Lifshitz-Gilbert-Langevin equation by introducing the Slonczewski torque. This new term describes a transfer of angular moments to the system, which is no longer at the thermodynamic equilibrium. So as to describe the STT driven switching we will present in this part a model adapting the expression of the Langevin field in presence of the spin transfer torque, then we will discuss the necessary assumptions, and finally we will derive the expression of the switching probability, first for out-of-plane spin valves, and then for pMTJs.

#### Case of GMR

Revisions of the mean lifetime $\langle \tau \rangle$ expression to include the spin transfer torque switching in an in-plane spin valve were developed in the early 2000. One of the solutions is to present the effect of the applied current (magnitude and direction) as an activation energy, and including it as an effective temperature to describe the switching behavior [127].

Li and Zhang [128] investigated the modification of the Néel-Brown equation when the system is no longer a closed system at the thermodynamic equilibrium with the aim to describe a thermally activated switching - as explained in the precedent section - under the application of a

magnetic field and a current. They linked the effective temperature expression to the spin transfer torque coefficient. The fluctuating thermal field was assumed to be independent of the spin transfer torque as the latter is deterministic. They introduced the concept of effective temperature as stationary solution of the probability solution. With the same idea, R.H Koch, J.Katine and J Sun [129] characterized the STT driven switching probability in an in-plane spin valve with an applied current in the magnetic anisotropy axis direction.

Here, the model is developed for monodomain nanomagnets with a magneto-crystalline anisotropy in the out-of-plane direction. The polarization of the spin current is in the direction of the unit vector $\boldsymbol{p}$. In a magnetic monodomain with a uniform magnetization composing the free layer of a spin valves with an applied current under a finite temperature, the reduced Landau-Lifshitz-Gilbert-Langevin-Slonczewski equation becomes:

$$\frac{d\mathbf{m}}{dt} = -\gamma_0 \mathbf{m} \times \boldsymbol{H}_{eff} + \alpha \mathbf{m} \times \frac{d\mathbf{m}}{dt} + \gamma_0 a_I I \mathbf{m} \times (\mathbf{m} \times \mathbf{p}) + \gamma_0 \mathbf{m} \times \mathbf{h}(t) \tag{III.16}$$

For a spin valve, the current density is the relevant parameter and the Slonczewski spin transfer torque coefficient is $a_I = \frac{P\hbar}{2em^2}$, where $P$ is the spin polarization factor. This parameter hinges on the relative orientation of the magnetic direction of the free layer and the polarizing layer [60]. Similarly to part II.1, we can define the switching current in the macrospin approximation with no thermal fluctuation [130], as a function of the applied magnetic field $H$.

$$I_{sw0}(H) = -\frac{\alpha}{a_I} H_{eff} \tag{III.17}$$

For $\mathbf{p}$ collinear to $\boldsymbol{H}_{eff}$ and considering that $\frac{dm}{dt} \simeq \gamma_0 \mathbf{m} \times \boldsymbol{H}_{eff}$ i.e. for a low damping coefficient and small currents, the LLGS equation is equivalent to:

$$\frac{d\mathbf{m}}{dt} = -\gamma_0 \mathbf{m} \times \boldsymbol{H}_{eff} + \gamma_0 \alpha \left(1 + \frac{a_I I}{\alpha H_{eff}}\right) \mathbf{m} \times (\mathbf{m} \times \boldsymbol{H}_{eff}) + \gamma_0 \mathbf{m} \times \mathbf{h}(t) \tag{III.18}$$

Then $\tilde{\alpha}$ is introduced as an effective damping parameter, with $\tilde{\alpha} = \alpha \left(1 + \frac{a_I I}{\alpha H_{eff}}\right)$. Then the authors define $\tilde{T}$ a fictitious temperature that verifies $\tilde{\alpha}\tilde{T} = \alpha T$. This expression agrees with Li and Zhang effective temperature expression. If we consider that the applied current is small enough to be close to the thermodynamic equilibrium [131], the Langevin random field of eq.(III.15) expressed for $\tilde{\alpha}$ and $\tilde{T}$ becomes:

$$\mathbf{h}(t) = \sqrt{2\frac{\tilde{\alpha}}{\gamma_0 V} k_B \tilde{T}}\, \mathbf{k}(t) \tag{III.19}$$

It corresponds to studying a magnetic layer with a damping parameter $\tilde{\alpha}$ at a temperature $\tilde{T}$. We can write the thermally activated mean lifetime expression $\langle\tau\rangle$, as we developed in part III.2, for the $\tilde{T}$ temperature:

$$\langle\tau\rangle = \tau_0 \exp\left(\frac{\Delta E_H}{k_B \tilde{T}}\right) \tag{III.20}$$

with $\tilde{T}$:

$$\tilde{T} = \frac{1}{1 + \frac{a_I I_{sw}}{\alpha H_{eff}}} T \tag{III.21}$$

The switching current $I_{sw}(T)$ is expressed as a function of $\tilde{T}$ eq.(III.21) and by replacing $\tilde{T}$ by its value found in eq.(III.20), it gives:

$$I_{sw}(T) = -\frac{\alpha}{a_I} H_{eff}\left[1 - \frac{k_B T}{\Delta E_H}\log\frac{\langle\tau\rangle}{\tau_0}\right] = I_{sw0}(H)\left[1 - \frac{k_B T}{\Delta E_H}\log\frac{\langle\tau\rangle}{\tau_0}\right] \tag{III.22}$$

From this expression, we see that the switching at a finite temperature is a rescaling of the switching current at zero Kelvin. It follows that the expanded expression of $\tilde{T}$ introduced in the mean lifetime $\langle\tau\rangle$ gives [125, 132]:

$$\langle\tau\rangle = \tau_0 \exp\left[\frac{\Delta E_H}{k_B T}\left(1 - \frac{I}{I_{sw0}(H)}\right)\right] \tag{III.23}$$

This expression is valid when $|I| \ll |I_{sw0}|$ as described in the article of Koch [129], and by consequence for $|I| \ll |I_{sw}|$ at room temperature. The corresponding thermal activation are modified with the introduction of the spin transfer torque, however the introduction of an effective temperature enable to define again these equation in the presence of the spin transfer torque, regardless of $I_{sw}(T)$ value. [128]

### The case of MTJs

The previous model had been developed for spin valves, we now want to adapt it to describe MTJs. As described in part I, in spin valves structures, $a_I$ is dependent on the angle between the magnetization direction and the polarizer, thus on the transition considered [60]. In MTJs, the Slonczewski spin transfer torque coefficient $a_V$ is independent of the angle between the magnetization direction and the polarizer, and moreover the additional field-like term can be added[59]. In 2006, Theodonis *et al.* presented [84] an ab initio model for the STT in MTJs where they discuss the expression of the parallel (Slonczewski term) and perpendicular (field-like) to the interface torques, and find a linear (Slonczewski term) and quadratic (field-like torque) dependences with bias of the torque. Experimental verification of the voltage dependence of the STT coefficient has

been realized using several methods [76, 87].

In a symmetric barrier system, we consider respectively a linear and a quadratic dependences of the Slonczewski and field-like spin transfer torques, both independent of the angle between the magnetization and the polarizer. The precedent model is then transposed, with $a_I I$ becoming $a_V V$, which does not change the magnetization dynamic in itself. The field-like torque is included in the effective field expression that becomes $\boldsymbol{H}_{eff} + b_V V^2 \boldsymbol{p}$. We can write:

$$\frac{d\mathbf{m}}{dt} = -\gamma_0 \mathbf{m} \times (\boldsymbol{H}_{eff} + b_V V^2 \boldsymbol{p}) + \alpha \mathbf{m} \times \frac{d\mathbf{m}}{dt} + \gamma_0 a_V V \mathbf{m} \times (\mathbf{m} \times \mathbf{p}) + \gamma_0 \mathbf{m} \times \mathbf{h}(t) \quad \text{(III.24)}$$

Assuming that $\boldsymbol{H}_{eff}$ and $\boldsymbol{p}$ are both out-of-plane, the effective temperature $\tilde{T}$ as a function of the switching voltage $V_{sw}$ is now:

$$\tilde{T} = \frac{1}{1 + \frac{a_V V_{sw}}{\alpha(H_{eff} + b_V V_{sw}^2)}} T \quad \text{(III.25)}$$

The addition of the field-like torque modifies the total expression of the corresponding switching voltage $V_{sw}$. By realizing a Taylor expansion around zero to the second order for the voltage values, the effective temperature expression found is analogous to the one for the spin valves, thus the term carrying $b_V V^2$ can be neglected in the switching voltage expression. In order to assess this simplification for our system, we compared the order of magnitude of $H_{eff}$ and $b_V V_{sw}^2$ for typical material parameters in a tunnel junction: For a $100 \times 100 nm^2$ wide nanopilar, with a $1nm$ thick free layer, an energy barrier of $60 k_B T$ at the offset field and a magnetization at saturation of $10^5 Am^{-1}$, on the one hand $H_{eff} = \frac{2K_{eff}}{\mu_0 M_s} = \frac{2 \times 60 k_B T}{\mu_0 M_s} = 3.75 \times 10^4 Am^{-1}$ and on the other hand, the maximum applied voltage are in the order of $V_{max} = 0.5V$, and for $b_V = 2.39 \times 10^4 Am^{-1}V^{-2}$, thus $b_V V^2 = 6.0 \times 10^3 Am^{-1}$. For this set of parameters, we observe that the effect of the field-like torque coefficent is small in the switching voltage value. In a first time this term will be discarded from the energy barrier expression, and its effect will be dicussed with the experimental data. Finally, with the reasoning presented previously, the mean lifetime in pMTJs is expresssed as:

$$\langle \tau \rangle = \tau_0 \exp\left( \frac{\Delta E}{k_B T} \left( 1 - \frac{H - H_{off}}{H_{sw_0}} \right)^{\frac{3}{2}} \left( 1 - \frac{V}{V_{sw_0}(H)} \right) \right) \quad \text{(III.26)}$$

with the condition that the applied voltage $V$ must be smaller than $V_{sw_0}$. This latter is found experimentaly to be larger than the voltage responsible for the breaking of the junction.
Moreover, from the macrospin approximation, we can infer a linear dependence of $V_{sw_0}$ with the applied field, and $H_{sw_0}$ independent of the voltage when the field-like torque is neglected.

### Switching probability

In order to estimate the switching probability under an applied voltage in our samples, we use eq. (III.26). As shown in eq. (III.26), the mean lifetime is a function of the magnetic field and the voltage, which gives that $P_{NS}$ depends on both parameters. For a voltage variation at fixed field, the magnetization evolves on a fixed energy landscape and on the contrary, if the applied voltage is fixed and the magnetic field varies the magnetization evolves on a changing energy landscape, with only the non-conservative torques kept constant. This later method assumes the knowledge of the evolution of the energy landscape as a function of the applied voltage and makes the data intepretation difficult to conduct, thus this manuscript focuses on the voltage variations at fixed field.

The experiments were realized for voltage sweep, and the non-switching probability was adapted by considering the probability of non having switched before $V$:

$$\ln P_{NS}(V,H) = -\frac{1}{\tau_0 r}\int_0^V \exp\left(-\frac{\Delta E}{k_B T}\left(1-\frac{H}{H_{sw_0}}\right)^{\frac{3}{2}}\left(1-\frac{\nu}{V_{sw_0}(H)}\right)\right)d\nu \quad \text{(III.27)}$$

with $r$ the sweeping rate. In our experiment the sweeping rate was fixed by the DAQx board used to be $r = 10V.s^{-1}$. In figure III.6, we represent the STT driven non-switching probability for different rates with zero applied field $\mu_0 = 0T$ and a given zero Kelvin switching voltage $V_{sw_0} = -0.8V$.

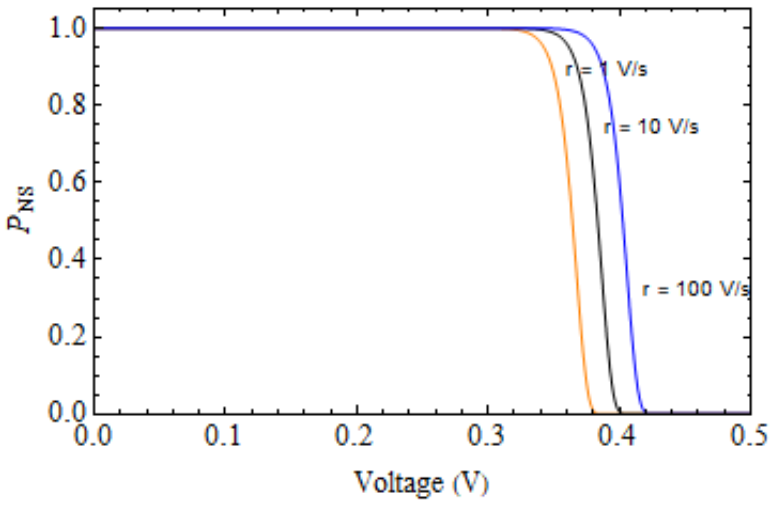


*Figure III.6: Modeled non-switching probability for different rates for $H = 0T$ and $V_{sw_0} = 0.5V$, in orange for $r = 1V/s$, in black for $r = 10V/s$ and in blue for $r = 100V/s$*

We observe that for a fixed energy barrier, a larger sweeping rate will increase the onset voltage of the switching. It is coherent with the fact that a slower sweeping means that the magnetization stays longer at the given voltage corresponding to more switching attempts.

### III.3.2 Experimental study

In the interest to extract the energy barrier $\Delta E$ for each transition, we studied the switching voltage distribution at different applied fields in several junctions. For each transition, $1000$ events were recorded. The samples were connected to the DAQ board acquisition system through a probe.

#### *Data recording*

The state diagram of a pMTJ obtained by voltage sweeping at room temperature is presented in figure III.7, with the transition border represented in color. The $AP \rightarrow P$ transition is in red and the $P \rightarrow AP$ transition is in green. This nanopillar has a surface of about $70 \times 100nm^2$, a a TMR of about 55% and the parallel state resistance is of $650\Omega$ at low applied voltages. From this state diagram, an offset field of $\mu_0 H_{off} = -27mT$ can be defined, taken as the center of the magnetic field hysteresis loop for $0.05V$ applied voltage. Moreover the voltage transition also presents an offset, where the $AP \rightarrow P$ transition requires a larger applied voltage than the $P \rightarrow AP$ transition voltage. Finally, there is a large dispersion of switching voltages close to the switching field, more prominent for the $P \rightarrow AP$ switching than for the $AP \rightarrow P$ switching. These different observations will be discussed in the following.

We define four branches in the borders of the state diagram: first two corresponding to the switching voltages (green and red plain lines in figure III.7) and then two corresponding to the limit fields (green and red dashed lines in figure III.7). As the state diagram is recorded using a voltage sweep, the maximum of dispersion occurs close to the switching field branches. The slopes of the switching voltage branches correspond in the macrospin model to the ratio between the Slonczewski spin transfer coefficient and the damping parameter. We can notice that the state diagram presents a different slope depending of the transition considered, which is in disagreement with the macrospin model, and will be discussed further.

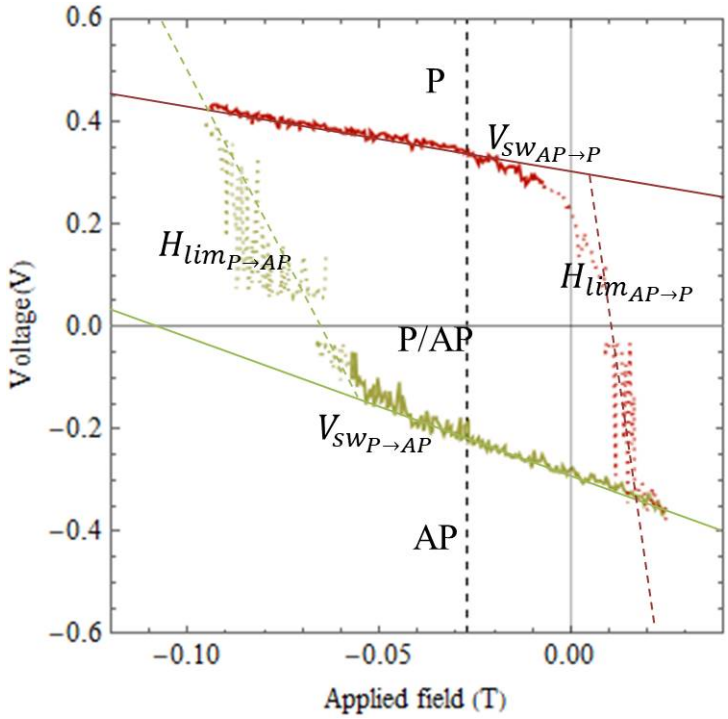


*Figure III.7: Voltage – field state diagram for* $70 \times 100nm^2$*, in red the* $AP \to P$ *transtion and in green the* $P \to AP$ *transtion. The dots correspond to experimental data, the lines are guide for the eyes for the switching voltages (plain lines) and switching fields (dashed lines) of the transitions. The vertical dashed line correspond to the offset field at* $\mu_0 H_{off} = -27mT$*.*

In order to investigate further the expression of the energy barrier for a voltage sweep, we studied the switching voltage distribution at a fixed field and fitted the probability of non-switching to the empirical cumulative distribution function (ECDF), as shown in figure III.8. At fixed field, here $\mu_0 H = -32mT$, we swept $1000$ times the voltage from one polarity to the other and return, in order to obtain the dispersion of the switching voltage for both transitions. In figure III.8a), is displayed the resistance of the tunnel junction as a function of the voltage for several sweeps, from which we extract the switching voltages. In figure III.8b) we look at the corresponding dispersion of the switching voltages for both transitions. The width of the bins in the histogram is fixed at $0.005V$, corresponding to the voltage acquisition steps. We observe a larger distribution for the $P \to AP$ than $AP \to P$ transition. In figure III.8c), we use the empirical cumulative distribution function corresponding to each histogram and fit them with eq.(III.27), with $r = 10V.s^{-1}$ and $\tau_0^{-1} = 1GHz$.

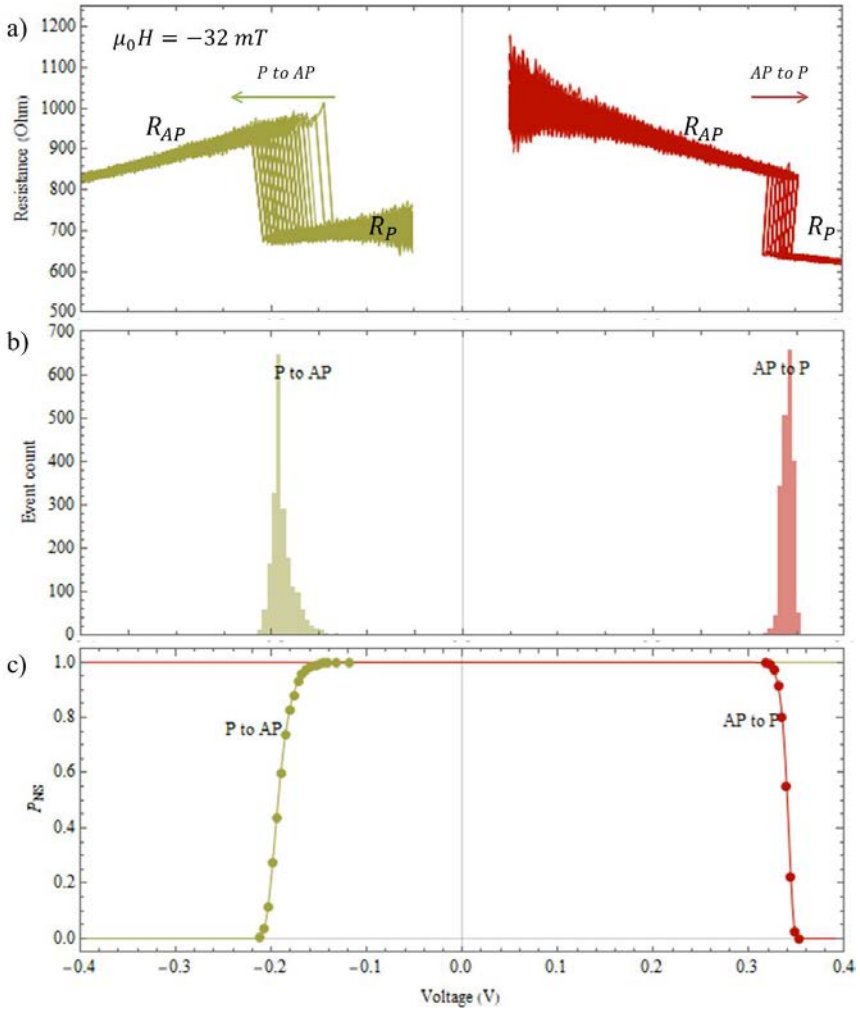


*Figure III.8: a) Voltage sweeps (arrows indicate the direction of sweeping), b) switching distribution for 1000 measurements with a bin width of 0.005V, c) fitting of the empirical cumulative function of the previous distribution for an applied field $\mu_0 H = -32mT$ in a $70 \times 100nm^2$ junction, in red (green) the $AP \rightarrow P$ ($P \rightarrow AP$) transition.*

The results of the fitting are noted in table III.2. For this field close to the offset field, we see a notable assymetry in both the energy barriers and the switching voltages at zero Kelvin, this hints toward the need to find an other definition of the offset field.

| | $P \rightarrow AP$ | $AP \rightarrow P$ |
|---|---|---|
| $\Delta E\ (k_B T)$ | $35.2 \pm 0.4$ | $85 \pm 4$ |
| $V_{sw_0}(V)$ | $-0.32 \pm 0.003$ | $0.406 \pm 0.004$ |

*Table III.2: Extracted energy barrier $\Delta E$ and switching voltage at zero Kelvin $V_{sw_0}$ for the two transitions, for $\mu_0 H = -32mT$ in a $70 \times 100nm^2$ junction.*

By reproducing the procedure for different fixed magnetic fields, we obtain an estimate of the energy barrier of the transition by fitting $\frac{\Delta E_H}{k_B T}(H)$ equation (III.28):

$$\frac{\Delta E_H}{k_B T}(H) = \frac{\Delta E}{k_B T}\left(1 - \frac{H - H_{off}}{H_{sw_0}}\right)^{\frac{3}{2}} \tag{III.28}$$

The results of the measurement on a $70 \times 100nm^2$ are presented in Figure III.9, the $AP \rightarrow P$ transtion is in red, the $P \rightarrow AP$ in green. Figure III.9a) represents the energy barriers values, obtained through the previous method and their fitting as a function of the applied field. Figure III.9b) displays the room temperature state diagram (small dots) with the extracted values of the switching voltages at zero Kelvin (large dots) and the corresponding fittings added to it. The fitting parameters are sumarized in table III.3. From figure III.9a), the shape of the experimental energy barrier dependence agrees well with the exponent chosen in the energy barrier expression, as expected from the geometry of the system, and similarly, $V_{sw_0}$ is linear validating the shape of the probability of non switching used.

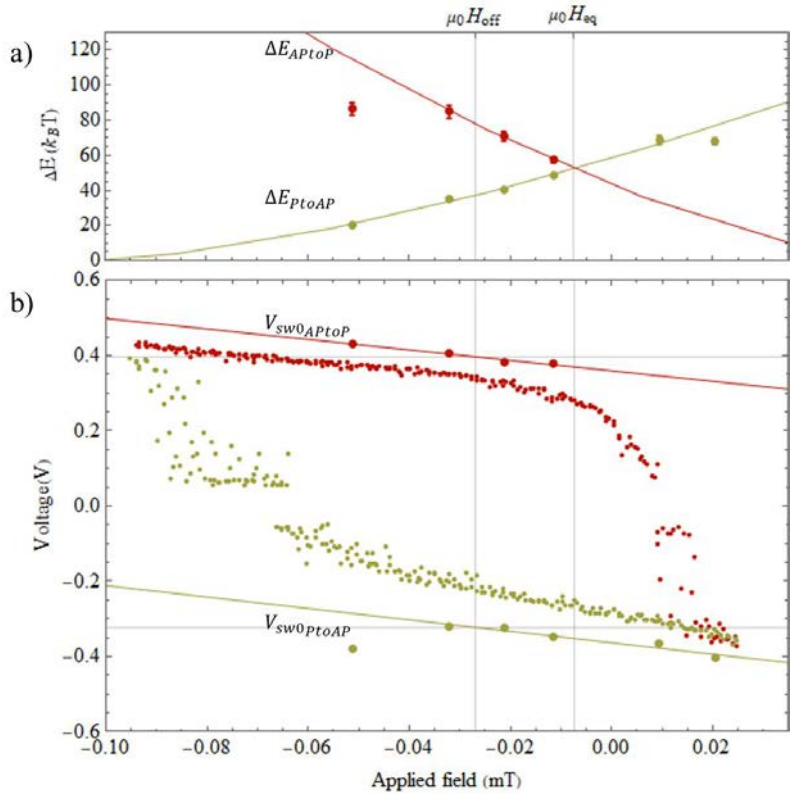


*Figure III.9: STT driven switching for a $70 \times 100nm^2$ junction considering the two transitions ($AP \rightarrow P$ in red and $P \rightarrow AP$ in green) with a) the energy barriers as a function of the applied field with the corresponding fittings and b) switching voltages at zero Kelvin (large dots), their fitting (lines) and room temperature switching voltages (small dots).*

The fitted results for the energy barrier extractions are summarized in the following table:

| $\mu_0 H_{off} = -27mT$ | $P \rightarrow AP$ | $AP \rightarrow P$ |
|---|---|---|
| $\Delta E\ (k_B T)$ | $37 \pm 1$ | $78 \pm 6$ |
| $\mu_0 H_{sw_0}(mT)$ | $-76 \pm 3$ | $83 \pm 5$ |

*Table III.3: Extracted energy barrier $\Delta E$, switching field $\mu_0 H_{sw_0}$ at zero Kelvin for the two transitions for a $70 \times 100nm^2$ tunnel junction considering $\mu_0 H_{off} = -27mT$ .*

The main result from figure III.9a) is the large asymmetry between the two energy barriers extracted with respect to $\mu_0 H_{off}$. The ratio $\frac{E_{AP\rightarrow P}}{E_{P\rightarrow AP}} \approx 2.1$, moreover, as in the thermally activated switching study, the values of $\mu_0 H_{sw_0}$ also depend on the transition considered. The trend of $\Delta E$ experimental values are well matched by the fitting expression except for the larger field values where outliers are observed both transitions. This is due to the width of the dispersion in the same order of magnitude as the voltage step used. For the $AP \rightarrow P$ transition at positive fields, the switching voltage distribution spreads over the two polarities, and due to the expression of the non-switching probability, the corresponding energy barriers and switching voltages extrapolated at 0K could not be extracted.

A point of interest in the previous study is the existence of a magnetic field $\mu_0 H_{eq}$ for which the energy barriers are equals. From figure III.9b) we observe that $\mu_0 H_{eq}$ is excentred toward the limit field of the $AP \rightarrow P$ transition. For this junction, $\mu_0 H_{eq} = -7.4mT$ and $\Delta E = 52 k_B T$, which is in the order of the industrial requirements. The results of the fitting are given table III.4. When using $\mu_0 H_{eq}$ instead of $\mu_0 H_{off}$, the assymetry between the $\mu_0 H_{sw_0}$ values is increased.

| $\mu_0 H_{eq} = -7.4mT$ | $P \rightarrow AP$ | $AP \rightarrow P$ |
|---|---|---|
| $\Delta E\ (k_B T)$ | $52 \pm 2$ | $52 \pm 2$ |
| $\mu_0 H_{sw_0}(mT)$ | $-95 \pm 3$ | $65 \pm 5$ |

*Table III.4: Extracted energy barrier $\Delta E$, switching field $\mu_0 H_{sw_0}$ at zero Kelvin for the two transitions for a $70 \times 100nm^2$ tunnel junction considering $\mu_0 H_{eq} = -7.4mT$ .*

Other parameters reflecting the assymetry of the transition are the slopes and switching voltages for $\mu_0 H_{eq}$ and $\mu_0 H_{off}$ observed at room temperature and extracted at zero Kelvin, represented in figure III.9b) and with fitting results summarized in table III.5. For $V_{sw_{0K}}$, the fittings do not include the values close to the switching fields branches of the diagram, as the energy barrier in the vicinity of the switching is too close to the thermal activation value and in that case we reach the limits of the probability model used.

| | $P \rightarrow AP$ | | $AP \rightarrow P$ | |
|---|---|---|---|---|
| | from $P_{NS}$ fitting | $298K$ | from $P_{NS}$ fitting | $298K$ |
| Slope $(V/T)$ | $-1.5 \pm 0.2$ | $-2.68 \pm 0.05$ | $-1.4 \pm 0.2$ | $-1.42 \pm 0.03$ |
| $V_{sw}(\mu_0 H_{off})$ (V) | $-0.322 \pm 0.005$ | $-0.213 \pm 0.001$ | $0.397 \pm 0.007$ | $0.336 \pm 0.002$ |
| $V_{sw}(\mu_0 H_{eq})$ (V) | $-0.352 \pm 0.005$ | $-0.265 \pm 0.001$ | $0.370 \pm 0.007$ | $0.308 \pm 0.002$ |

*Table III.5: slope of the switching voltage at zero Kelvin (room temperature) $V_{sw_0}(V_{sw})$ and switching voltage for the offset field at from the fitting of $P_{NS}$ (room temperature) for the two transitions for a $70 \times 100nm^2$ tunnel junction considering $\mu_0 H_{off} = -27mT$ and $\mu_0 H_{eq} = -7.4mT$.*

At room temperature and at zero Kelvin (from the fitting of $P_{NS}$), both $V_{sw}$ present a negative linear trend with applied magnetic field, but the slopes value depend on the transitions, unlike expected from the model assumptions. At room temperature, there is a ratio of about two between the switching voltages, whereas they are of a smilar order at zero Kelvin. Moreover, neither the $\mu_0 H_{eq}$ nor $\mu_0 H_{off}$ is a center of symmetry for the switching voltage values, but the difference is reduced for $\mu_0 H_{eq}$ at both temperature.

Another remark is the accuracy of the parameter extracted: the $V_{sw_0}$ values extracted are much lower than the experimental ones: it has been verified at $10K$ that the breaking voltage (about $0.7V$) was reached before the switching voltages for these junctions. This may come from the choice for $\tau_0 r$, and does not undermine our results for the energy barriers that have to be taken as qualitatives

All the different observations corroborate the hypothesis of a difference of switching mechanism depending on the transition considered. The main result of this part is the large asymmetry in the energy barrier, depending on the considered transition; the second result is that the field for which the energy barriers are equal is closer to the $AP \rightarrow P$ switching voltage than the $P \rightarrow AP$ one, and $V_{sw_0}$ has a linear dependence with the applied field. The difference of slope in $V_{sw}$ can be the results of a difference in efficiency of the Slonczewski spin transfer torque coefficient.

In order to assess the validity of our model for the samples considered, we discuss here the main assumptions on the spin transfer torque expression and on the macrospin approximation made in the previous section. We assumed, as in Slonczewski 2005 paper [59], that the coefficient

of the Slonczewski spin transfer torque does not depend on the transition, as for an "ideal middle" tunnel junction. However Theodonis *et al.* showed, with tight-binding calculations, that the Slonczewski spin transfer torque presents an assymetric quadratic behavior at larger voltage, and depending on the exchange splitting between the two spin channels, and can even change sign without inversing of the bias polarity. Using spin-transfer-driven ferromagnetic resonance technique, Kubota *et al.* showed experimentally similar trends for the spin transfer torque in in-plane MTJs [77, 84]. The difference in efficiency of the torque as a function of the bias sign can explain the offset in voltage observed in the state diagram , however the introduction of this effect in the effective temperature model would make the data analysis difficult. The effect of this assumption will be discussed in more details in part IV and in the following. And we keep the assumption that the Slonczewski STT depends linearly on the bias, as the STT expression obtained by Slonczewski correspond to a Taylor expansion to the first order around zero voltage of Theodonis STT expression.

The second assumption made on the spin transfer torque expression is that the field-like torque is negligible compared to the stray field and the switching field at zero Kelvin, thus do not take part in the magnetization reversal, as discussed at the end of part III.2.1. However, it has been shown that the sign competition between the Slonczewski spin transfer torque and the field-like torque can lead to the back-hopping of the magnetization for one of the two transitions while it can facilitate the switching for the other. In our samples, this back-hopping can be seen for the switching voltage for the $AP \rightarrow P$ transition close to $\mu_0 H_{sw_{P\rightarrow AP}}$. It indicates that this effect should not be neglected in our case, and can actually participates in the offset bias of the state diagram, however, in order to include the field like torque, the expression of the switching probability becomes difficult to obtain, as all the probabilities for one transition have to be fitted in parallel. Therefore this effect is too difficult to introduce in our model.

The other main assumption made in our model is the macrospin approximation of the considered MTJ behavior, which postulate that the magnetization shows a coherent reversal during the switching. Due to the material parameters, the free layer area needed to obtain a coherent macrospin behavior is lower than $20 \times 20nm^2$, which is much smaller than the size considered in our samples, where the switching occurs via nucleation-propagation. Switching via a nucleation-propagation process may requier several energy barriers, for example one to create the domains

of inverse magnetization direction, and an other to spread the domain accross the nanopillar surface but if the propagation is favored, the system may present only one energy barrier. The corresponding energy lanscape is thus much complex than the macrospin one, however if one of the mechanisms is preponderant, the total energy barrier of the system will mostly dependent on it. In our case, the nucleation takes this role, and the model seems to hold.

Finally, still considering the macrospin model, the applied magnetic fields are supposed uniform accross the nanopillar surface. However for the width considered, it is possible to estimate the inhomogeneities in the stray field coming from the SAF reference layer. A calculation of that field (done in part IV) shows a compensation at the center of the pillar, and an accumulation of the magnetization values close to the edges of the junction. This can influence the nucleation origin for the reversal, depending on the transition considered. If the nucleation volumes are different it would influence the nucleation energy barrier. In that way, a more accurate model would take into account a different offset field for each transition and by consequence explain the difference between $\mu_0 H_{off}$ and $\mu_0 H_{eq}$.

Considering the assumption made, it is possible to relate the assymetry seen in the state diagram either to the spin transfer torque effects negleted in effective temperature model or to the limitation of the macrospin approximation to describe the switching mechanism in the junction. In the following we study the evolution of the switching assymetry as a function of the junction size and aspect ratio. The fitting will be given by chosing $\mu_0 H_{eq}$ as a reference point for the fitting.

### *Energy barrier dependence on the pMTJ size*

We reproduced the same study on junctions with surface dimensions of $60 \times 80nm^2$, $65 \times 200nm^2$ and $65 \times 240nm^2$. The resistance area is a constant of $RA = 14.7\Omega\mu m^2$ and the TMR is about $55\%$ for the smallest junction and $40\%$ for the two larger junctions. In figure III.10, the state diagram of the $70 \times 100nm^2$ junction (black dots) is compared to a junction with a $65 \times 200nm^2$ surface ( figure III.10) with in red switching voltages for the $AP \rightarrow P$ transition and green for the $P \rightarrow AP$ transition. In appendix III are presented the state diagrams for all the junctions.

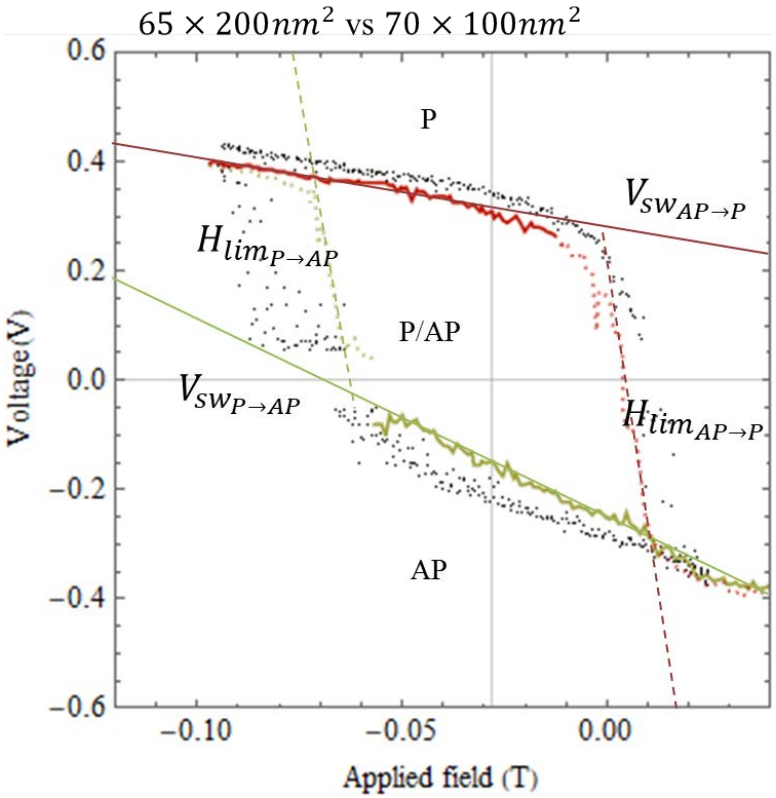


*Figure III.10: comparison between the* $70 \times 100nm^2$ *junction state diagram (black dots) and a)* $65 \times 200nm^2$ *junction state diagram (*$\mu_0 H_{off} = 28mT$*) with in red the* $AP \to P$ *transition and in green the* $P \to AP$ *transition.*

From the comparison of all the states diagrams, we observe that the stochastic dispersion of switching voltages close to the limit magnetic field branches (closing of the state diagram) vary strongly from one junction to the other, especially close to the limit field of the $P \to AP$ transition, but no correlation with the size has been found. Furthermore, the offset fields in the different MTJs, calculated as previously from the center of the field hysteresis loop at low voltage, range from $-27.0mT$to $-30.0mT$ and do not present relation with the size either. We obtained the $\mu_0 H_{eq}$ values from the energy barrier fitting, with no correlation to the $\mu_0 H_{off}$ value. Considering the stray field in the expression to be $\mu_0 H_{eq}$, we obtain $\Delta E$ and $\mu_0 H_{sw_0}$. The results are sumarized in table III.6, where the first line is the energy barrier $\Delta E$ in $k_B T$ and the second is $\mu_0 H_{sw_0}$ in $mT$.

| $60 \times 80nm^2$ $\mu_0 H_{eq} = -13.2mT$ | | $70 \times 100nm^2$ $\mu_0 H_{eq} = -7.4mT$ | | $65 \times 200nm^2$ $\mu_0 H_{eq} = -15.9mT$ | | $65 \times 240nm^2$ $\mu_0 H_{eq} = -10.1mT$ | |
|---|---|---|---|---|---|---|---|
| $P \to AP$ | $AP \to P$ | $P \to AP$ | $AP \to P$ | $P \to AP$ | $AP \to P$ | $P \to AP$ | $AP \to P$ |
| $41 \pm 1$ | $41 \pm 2$ | $52 \pm 2$ | $52 \pm 2$ | $52 \pm 2$ | $52 \pm 2$ | $55 \pm 1$ | $55 \pm 2$ |
| $-151 \pm 6$ | $59 \pm 4$ | $-95 \pm 3$ | $65 \pm 5$ | $-78 \pm 9$ | $64 \pm 5$ | $-95 \pm 2$ | $66 \pm 11$ |

*Table III.6: Extracted energy barrier $\Delta E(k_B T)$ (first line) and switching field $\mu_0 H_{sw_0}(mT)$ (second line) at zero Kelvin from the fitting of the $P_{NS}$ for the two transitions for four tunnel junctions considering $\mu_0 H_{eq}$ for the stray field .*

From this table, no clear trend of $\mu_0 H_{eq}$ can be extracted, nonetheless, they are all shifted toward the $AP \to P$ transition limit field. We observe a clear increasing dependence of the energy barrier on the pillar surface. In all junction $\mu_0 H_{sw_0}$ for each transition is in the same order of magnitude, with a larger dispersion for the $P \to AP$ transition (between -80mT and -150mT) than for the $AP \to P$ transition (about 65mT). The smallest junction shows a larger assymmetry in the values of $\mu_0 H_{sw_0}$. In order to compare the junctions, in figure III.11 is plotted the energy density barrier of the system - the energy barrier at $\mu_0 H_{eq}$ divided by the volume of the free layer- as a function of the magnetic volume of the free layer for all four junctions.

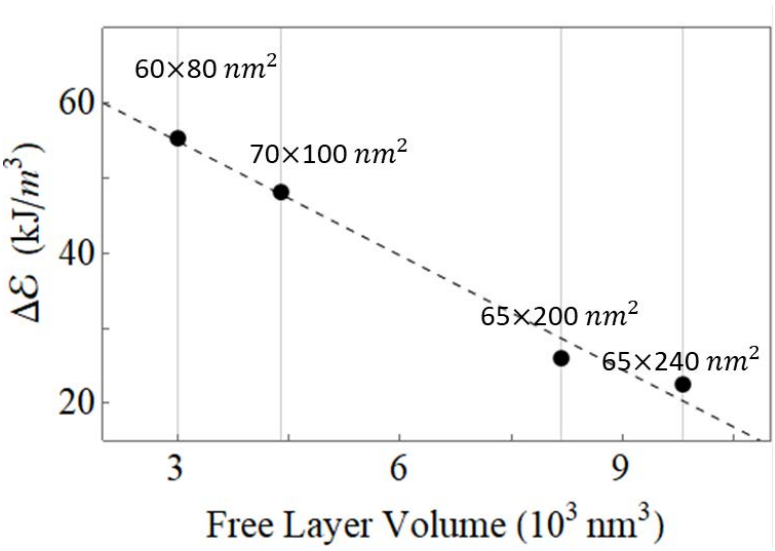


*Figure III.11: Energy density barrier at $\mu_0 H_{eq}$ as a function of the free layer magnetic volume for the four junctions.*

In figure III.11 we observe a linear decreasing trend of the energy density barrier as a function of the free layer volume. In a macrospin system, the energy density of the system remains constant regarless of the size, which indicate a clear nucleation-propagation switching process. The linear trends is believed to indicate a constant energy density barrier at the onset of the switch-

ing, regardless of the size and aspect-ratio of the junction.

With the $\mu_0 H_{eq}$ values, we can now compare the slopes and switching voltage at room temperature and the results from the fitting of $P_{NS}$ for this magnetic field value, and link them to a difference in coefficient of the Slonczewski spin transfer torque as a function of the transition. The fittings are given in table III.7.

| | | $298K$ | | from $P_{NS}$ fitting | |
|---|---|---|---|---|---|
| | | $P \rightarrow AP$ | $AP \rightarrow P$ | $P \rightarrow AP$ | $AP \rightarrow P$ |
| $60 \times 80$ $nm^2$ | Slope $(V/T)$ | $-2.93 \pm 0.08$ | $-0.71 \pm 0.03$ | $-1.3 \pm 0.1$ | $-2.6 \pm 0.2$ |
| | $V_{sw}(\mu_0 H_{eq})$ (V) | $-0.21$ | $0.31$ | $-0.34$ | $0.37$ |
| $70 \times 100$ $nm^2$ | Slope $(V/T)$ | $-2.68 \pm 0.05$ | $-1.42 \pm 0.03$ | $-1.5 \pm 0.2$ | $-1.4 \pm 0.2$ |
| | $V_{sw}(\mu_0 H_{eq})$ (V) | $-0.20$ | $0.30$ | $-0.35$ | $0.37$ |
| $65 \times 200$ $nm^2$ | Slope $(V/T)$ | $-3.39 \pm 0.06$ | $-1.39 \pm 0.04$ | $-1.3 \pm 0.1$ | $-2.6 \pm 0.2$ |
| | $V_{sw}(\mu_0 H_{eq})$ (V) | $-0.20$ | $0.29$ | $-0.42$ | $0.49$ |
| $65 \times 240$ $nm^2$ | Slope $(V/T)$ | $-2.74 \pm 0.03$ | $-1.47 \pm 0.03$ | $-0.5 \pm 0.2$ | $-0.9 \pm 0.3$ |
| | $V_{sw}(\mu_0 H_{eq})$ (V) | $-0.23$ | $0.28$ | $-0.29$ | $0.34$ |

*Table III.7: $V_{sw_0}$ and $V_{sw}$ slopes and values for $\mu_0 H_{eq}$ for all the junctions sizes and transitions.*

From these results, there is a clear distinction of $V_{sw}$ behavior as a function of the transition, for both temperature considered. First, at room temperature, the slopes of $V_{sw}$ for the $P \rightarrow AP$ transition vary for the different junction areas, without a clear correlation with the surface increase. For the $AP \rightarrow P$ transition, the slope values are two to three time smaller than for the other transition. For this transition the slopes are all in the same order of magnitude except for the junction with the smallest surface. Despite the slope variation observed, at room temperature, the switching voltage values at $\mu_0 H_{eq}$ are all of the same magnitude in each transition, independently of the surface size. $V_{sw}(\mu_0 H_{eq})$ values for the $AP \rightarrow P$ transition are larger than the $P \rightarrow AP$ transition.

The results of the fitting of the $P_{NS}$ function for the $P \rightarrow AP$ transition show that $V_{sw}$ slopes are all in the same range with each other, except for the largest one; they are about two times smaller than their room temperature counterpart. This trend is inverted for $V_{sw}(\mu_0 H_{eq})$ values that are almost twice as large as their room temperature counterparts. For the $AP \rightarrow P$ transition, the slopes of $V_{sw}$ present a lot of variation as a function of the surface area of the nanopillar. They are overall larger than for the $P \rightarrow AP$ transtition, and except from the $70 \times 100 nm^2$

junction, present no correlation with their room temperature equivalent.

As the slope of $V_{sw}$ is proportionel to the inverse of the Slonczewski spin transfer torque coefficient, the slope values at room temperature depending on the transition denote a change in this coefficient as a function of the transition, as discussed in the previous part. Furthermore, the value of the swiching voltage, and overall the voltage offset of the state diagrams maybe due to the field-like torque effect. The back hopping effect is present for all the junctions except the $60 \times 80nm^2$ one, which may indicate a size dependence of this effect, or a larger effect of the stray field.

In all the state diagram considered, there is an assymetry of the switching voltage slopes, and the equal value of the energy barrier is obtained for a field value different than the offset field defined for the state diagram, implying a difference in mechanism during the switching process and an action of the spin transfer torque different than expected. The energy barrier of the junction is found depending on the junction size, and the smaller junction presents outlier results compared to the other samples.

The inhomogenities of the stray field, due to the SAF configuration and the shape of the nanopillar, can influence the nucleation point of the magnetic domain at different location for the two transitions. In order to assess the influence of the stray field inhomogeneities on the switching process, we studied the same junctions where the SAF configuration was "broken", i.e. the two layers of the SAF take a parallel alignment.

### *Energy barrier dependence on the stray field*

There is few way to study the effect of the stray field from the reference layer on the free layer without changing the stack. Nonetheless, using the spin transfer torque at applied field close to the switching field of the reference layer, it was possible to break the antiferromagnetic coupling between the layers. In this magnetic configuration, that we call "no SAF" , the same study as before will be realized and will be compared to the one for the same junction in the SAF configuration. The only differences with the SAF configuration is the stray field mean values and its inhomogeneities. The state diagram of the $70 \times 100nm^2$ junction in this new configuration is shown in figure III.12.

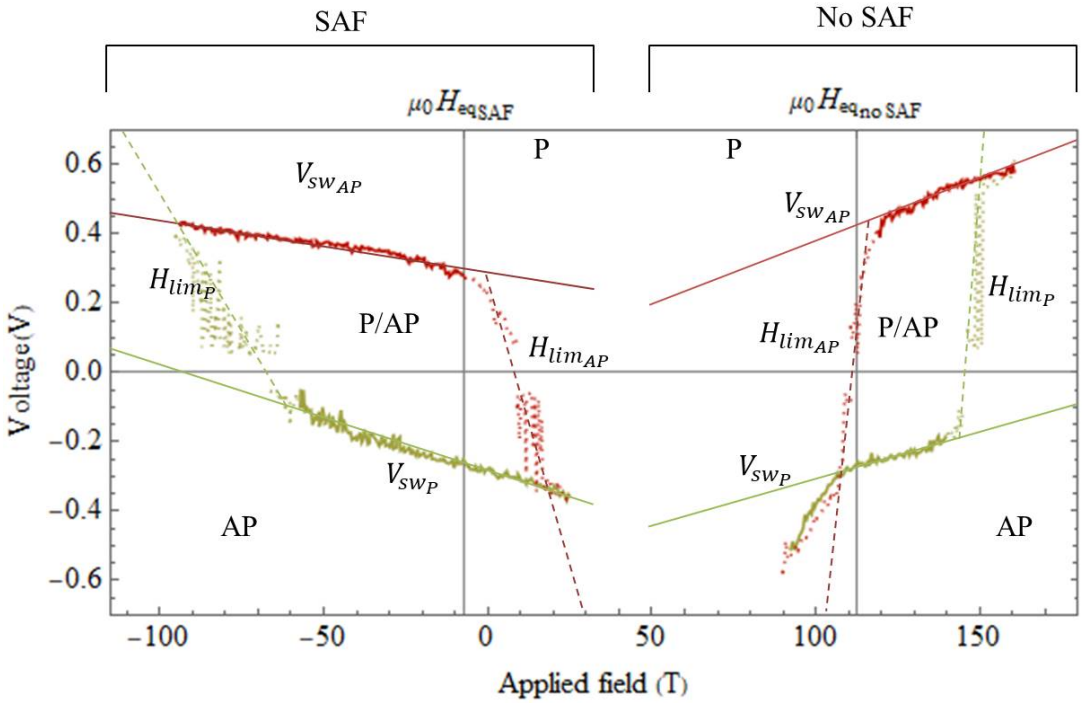


*Figure III.12: comparison the* $70 \times 100nm^2$ *junction state diagrams with a SAF (left hand side) and with "no SAF"(right-hand side). Red is for the* $AP \rightarrow P$ *transition and green for the* $P \rightarrow AP$ *transition,* $\mu_0 H_{eq}$ *is the field for which the energy barrier are equal for both transition*

On the left-hand side of the figure is the state diagram with the junction in its inital configuration, on the right-hand side is the state diagram for the same junction in the “no SAF” configuration. The vertical gray axes represent the magnetic field $\mu_0 H_{eq}$ for which the energy barrier is the same in both diagrams. For both diagram, this field is closer to the limit field of the $AP \rightarrow P$ transition, than the $P \rightarrow AP$ transition.

In the "no SAF" configuration, as expected, the switching voltage polarity for each transition remains the same whereas the limit fields for the two transition are inverted: the $P \rightarrow AP$ transition occurs for large positive fields instead of negative applied fields and the $AP \rightarrow P$ transition is found for lower positive fields. Our interpretation is that when the SAF is “broken”, both the upper layer of the reference layer and the free layer switch directions, thus inverting the switching field positions but not the switching voltage ones.

Further discrepancies with the SAF state diagram are observed; first in the “no SAF” state diagram, we observe that the magnetic field width of the bistable area is reduced from about 80mT wide to about 40mT, whereas the voltage width and the voltage offset are increased; second, the

limit field slopes are small for each transition, with little dispersion due to the temperature. The smallest junction is an exception to this observation, where the shape of the state diagram is closer to the one in the SAF configuration " (figures in Appendix III).

In this part, we discuss the "no SAF" configuration for all the junction considering the same parameters as before: energy barriers and switching voltages at room temperature and at zero Kelvin. We fitted the following data considering the stray field to be $\mu_0 H_{eq}$ and as in the previous part, this parameter is found depending on the junction considered. The fitting of the energy barriers expression are summarized in table III.8 where the first line is the energy barrier $\Delta E$ in $k_B T$ and the second is $\mu_0 H_{sw_0}$ in $mT$.

| $60 \times 80nm^2$ $\mu_0 H_{eq} = 138.5mT$ | | $70 \times 100nm^2$ $\mu_0 H_{eq} = 112.5mT$ | | $65 \times 200nm^2$ $\mu_0 H_{eq} = 102.7mT$ | | $65 \times 240nm^2$ $\mu_0 H_{eq} = 105.7mT$ | |
|---|---|---|---|---|---|---|---|
| $P \to AP$ | $AP \to P$ | $P \to AP$ | $AP \to P$ | $P \to AP$ | $AP \to P$ | $P \to AP$ | $AP \to P$ |
| $49 \pm 1$ | $49 \pm 1$ | $65 \pm 3$ | $65 \pm 2$ | $74 \pm 6$ | $74 \pm 3$ | $67 \pm 3$ | $67 \pm 2$ |
| $69 \pm 1$ | $-36 \pm 1$ | $78 \pm 4$ | $-78 \pm 10$ | $74 \pm 7$ | $-58 \pm 6$ | $74 \pm 2$ | $-37 \pm 3$ |

*Table III.8: Extracted energy barrier $\Delta E(k_B T)$ (first line) and switching field $\mu_0 H_{sw_0}(mT)$ (second line) at zero temperature from the fitting of $P_{NS}$, considering the stray field to be $\mu_0 H_{eq}$ for the two transitions in four junctions of increasing size with the reference layer in the "no SAF" configuration.*

From table III.8, we observe that for the three larger junctions, $\mu_0 H_{eq}$ is closer to the limit field of the $AP \to P$ transition, and for the $60 \times 80nm^2$ junction, it is closer to the other transition. For all the junctions, the energy barrier extracted are larger than for the same junction when the reference layer is a SAF. The energy barrier is the smallest for the smallest junction ($\Delta E \approx 49 k_B T$), whereas it is of the same magnitude for all the other junctions ($\Delta E \approx 65 k_B T$), except for the $65 \times 200nm^2$ junction, where it is higher. However in that case, the fitting for the $P \to AP$ transition carries more incertainties. In figure III.13 is represented the energy density barrier at $\mu_0 H_{eq}$ for all the junctions as a function of free layer volume.

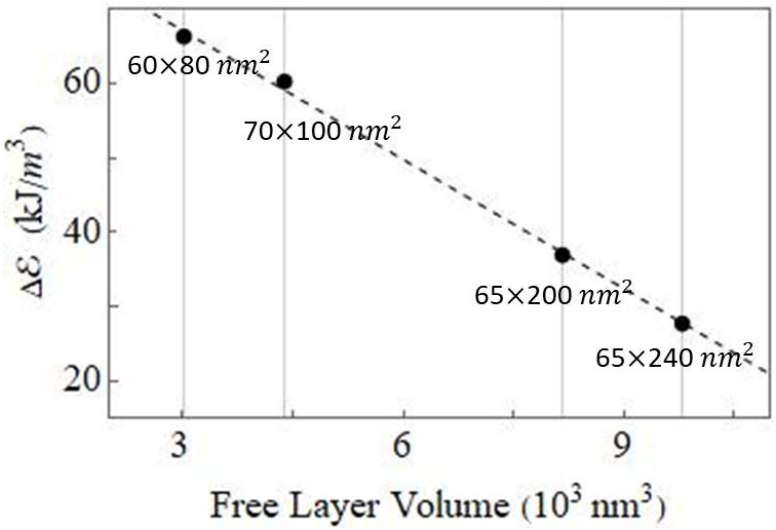


*Figure III.13: Energy density barrier at $\mu_0 H_{eq}$ as a function of the free layer magnetic volume for the four junctions in the "noSAF" configuration.*

As in the previous section, the energy density barrier as a function of the free layer volume present a decreasing linear trend. In this configuration, all the energy barriers are found larger than their counterpart in the junctions with SAF, which lead consider a clear influence of the stray field on the switching process in pMTJs.

Concerning the values of the $\mu_0 H_{sw_0}$, there is no clear trend found as a function of the size. The $P \rightarrow AP$ value of $\mu_0 H_{sw_0}$ is in the same order of magnitude for all the junction, whereas the $AP \rightarrow P$ one varies. In order to highlight the influence of the SAF on the switching voltages, in table III.9 are summarized the values of slopes and switching voltage for both transition at room temperature and at zero Kelvin.

| | | $298K$ | | from $P_{NS}$ fitting | |
|---|---|---|---|---|---|
| | | $P \rightarrow AP$ | $AP \rightarrow P$ | $P \rightarrow AP$ | $AP \rightarrow P$ |
| $60 \times 80$ $nm^2$ | Slope $(V/T)$ | $5.3 \pm 0.1$ | $5.4 \pm 0.2$ | $2.3 \pm 0.3$ | $2.9 \pm 0.4$ |
| | $V_{sw}(\mu_0 H_{eq})$ (V) | $-0.30$ | $0.40$ | $-0.47$ | $0.56$ |
| $70 \times 100$ $nm^2$ | Slope $(V/T)$ | $2.5 \pm 0.1$ | $4.3 \pm 0.1$ | $0.5 \pm 0.8$ | $4.1 \pm 0.4$ |
| | $V_{sw}(\mu_0 H_{eq})$ (V) | $-0.27$ | $0.4$ | $-0.37$ | $0.51$ |
| $65 \times 200$ $nm^2$ | Slope $(V/T)$ | $4.3 \pm 0.1$ | $3.5 \pm 0.05$ | $2.0 \pm 0.2$ | $2.8 \pm 0.1$ |
| | $V_{sw}(\mu_0 H_{eq})$ (V) | $-0.30$ | $0.39$ | $-0.35$ | $0.47$ |
| $65 \times 240$ $nm^2$ | Slope $(V/T)$ | $4.1 \pm 0.1$ | $3.3 \pm 0.01$ | $1.5 \pm 0.6$ | $2.2 \pm 0.3$ |
| | $V_{sw}(\mu_0 H_{eq})$ (V) | $-0.27$ | $0.40$ | $-0.51$ | $0.22$ |

*Table III.9: $V_{sw_0}$ and $V_{sw}$ slopes and values for $\mu_0 H_{eq}$ for the two transitions in four junctions of increasing size with the stray field in the "no SAF" configuration.*

At room temperature, the slopes of $V_{sw}$ for both transition are from twice to four time the ones for the same junction with the reference layer in the SAF configuration. That would implies a change of spin transfer torque efficiency in the junction depending on the stray field value. Back hopping is still observed at larger positive bias close to the $AP \rightarrow P$ limit field. Despite the difference in $\mu_0 H_{eq}$ and $\Delta E$, the switching voltages at $\mu_0 H_{eq}$ are all in the same range for each transition for all junctions, about $-0.27V$ for the $P \rightarrow AP$ transition and $0.40V$ for the $AP \rightarrow P$ transition.

At zero Kelvin, we obtained, overall smaller slopes for both transition, in the same range than the one with a SAF reference layer. No particular trend as a function of the temperature can be extracted, whether for the slopes values of the switching voltages at $\mu_0 H_{eq}$. The smaller junction follows the same trends as the others, and the larger junction is the only one where the switching voltage at zero Kelvin for the $P \rightarrow AP$ transition is larger in absolute value than the one for the $AP \rightarrow P$ transition.

From this study, we extracted a clear influence of the stray field value on the energy barrier and the Slonczewski spin transfer torque coefficients for both transitions. It is also expected to find a difference in switchig process for the two transitions. As the system can not be represented by a macrospin approximation, the spacial dependence in the representation of the fields have to be considered, and especially the inhomogeneities of the stray field. The breaking of the SAF is thought to increase these inhomogeneities, leading to larger energy barriers in this configuration.

These observations have also to be put in relation to the two neglected effects discussed : the STT coefficient dependence with the bias being not be linear as presented by Theodonis and the presence of the field-like torque, reduced or enhanced. Both effect could explain part of the assymetry in width and height of the state diagrams, but not the drastic modifiations between the two SAF confugurations.

## Conclusion

State diagrams for MTJ nanopillars are measured and compared to the macrospin model develloped in part II. In the experimental data, the first discrepency with the macrospin model is

the presence of a field offset, the second is the difference in switching voltage slopes, and third the distribution of the switching voltages due to the thermal activation of the switching. These effects are linked to the finite size of the junction and the influence of the stack on the free layer behavior. There is also a disapearance of the bistability area where both a maximum and minimum of energy were stabilized in the fully perpendicular macrospin computation and were not in the broken-symmetry ones.

In this part we studied the dependence of the switching for both transition in MTJs nanopillars as a function first of the temperature, then of the applied voltage. The relevant parameters in this study are the energy barrier and the limit fields at zero Kelvin extracted from the fitting of the $P_{NS}$, as well as the extracted switching bias voltage at zero Kelvin and room temperature in the second case.

The introduction of the temperature dependence enables to define first the expression of the non-switching probability, and the need to define two magnetic fields, namely $\mu_0 H_{eq}$ where energy barriers are equal for both transition and $\mu_0 H_{off}$ as the center of the field hysteresis loop. The large difference between these two fields hints toward a difference in reversal mechanism and maybe the need to introduce the field-like torque in the fitting model.

In the spin-transfer-torque driven switching study, we first introduce the effect of the Slonczewski spin transfer torque as an effective temperature. The effect of the field-like torque are neglected in the expression, as its value is assumed to be small compared to the other fields taken into account. We use the non-switching probability expression thus found to investigate the evolution of the energy barrier as a function of the size of the junction and of the effect of the stray field coming from the reference layer. In both case the field for which the energy barrier are equal for both transition is offseted compared to the computed center of the diagram.

A size dependence of the energy barrier is observed, but no clear dependence of the switching voltage slopes are seen. The switching voltages at the field for which the energy barriers are equal are found in the same range, independently of the size of the junction but depending on the transition. When the reference layer SAF is "broken" such has having a parallel alignment, a clear distortion of the state diagram is seen. The offset field changes polarity and increases, the width

in field is reduced and the switching voltage for the $AP \rightarrow P$ is shifted toward large positive values. Consequently, the energy barriers for all the junction increase, and their evolution with the size of the junction is observed as in the SAF configuration.

From our study, three phenomena can explain the difference between the transition. First the spin transfer torque coefficient may not be independent of the bias as proposed by Slonczewski, but present for example a parabolic dependence as stated by Theodonis *et al.* [84], conducing for one polarity to enhance its effect and for the other to reduce it. Second, the field like torque may not be negligible, as the presence of back hopping for the $AP \rightarrow P$ transition close the the limit field for the $P \rightarrow AP$ transition seems to indicate. This effect is seen for the larger junctions independently of the reference layer configuration. Third, due to the size of the junction, the switching mechanism may be a nucleation - propagation regime, where the initial location of the nucleation depends on the local stray field value. This phenomenon is a more complex mode of reversal than the coherent switching. Finally, the distance between the macrospin model and the considered samples indicates that the stray field can present inhomogeneities that would influence differently the center of the junction or the edges. Even if it is supposed to cancel the stray field at the center of the junction, the configuration makes it so that it has an added effect on the edges of the junction. This inhomogeneity would change the nucleation point of the spin transfer torque driven switching, depending on the transition, and thus modify the energy barrier.

In order to decorelate the influence of the spin transfer torque and of the stray field inhomogeneities as well as to identify the different mechanisms in the switching processes, we used micro-magnetic simulation software, FASTMAG to represent both the energy barrier and the switching voltage behavior for different fields in a magnetic tunnel junction with out-of-plane magnetization.

# Chapter IV

# Micromagnetic simulations of pMTJs

## Résumé en français

Dans cette partie nous utilisons un code micromagnétique appelé FASTMAG pour décrire le comportement de l'aimantation dans une jonction tunnel. Ce programme est développé par le groupe "Computational electromagnetics and micromagnetics" à UC San Diego et dirigé par Vitaliy Lomakin. La particularité de ce programme est d'utiliser les éléments finis pour résoudre l'équation de la dynamique de l'aimantation. Il est optimisé pour le calcul parallèle sur cartes graphiques.

Pour une jonction tunnel de surface $60 \times 80nm^2$, nous avons utilisé des paramètres magnétiques basés sur la composition de nos échantillons. Les matériaux sont choisis égaux pour la couche libre et la couche supérieure de la couche de référence et de même pour les deux couches de la structure antiferromagnétique synthétique (SAF). La couche supérieure de la couche de référence est fortement couplée ferromagnétiquement avec la couche supérieure du SAF, tandis que les couches du SAF sont couplées antiferromagnétiquement. Les valeurs de polarisations du courant de spin des deux côtés de l'interface sont choisies égales. Deux géométries sont étudiées, une où tous les axes magnétiques sont orientés hors du plan, l'autre où l'axe d'anisotropie de la couche libre présente un léger angle.

Nous avons simulé le comportement de l'aimantation dans la structure en fonction d'un champ magnétique appliqué pour trouver les champs coercitifs de la couche libre, puis utilisé ce résultat pour modéliser un diagramme d'état courant – champ magnétique. Le couple field-like est négligé. Nous étudions aussi la dépendance des barrières d'énergies en fonction du champ

magnétique par la méthode "Nudged Elastic Band".

La première conclusion de cette partie est la confirmation de l'inhomogénéité du champ magnétique rayonné par le SAF sur la couche libre. Il s'annule au centre de la jonction mais n'est pas compensé proche du bord. Cette répartition influence clairement la position de la nucléation du retournement de l'aimantation quand la symétrie du système est brisée. Il s'effectue au centre pour la transition $P \rightarrow AP$ et sur le bord de la jonction pour la transition $AP \rightarrow P$. L'influence du champ rayonné est confirmé par l'étude du retournement en champ de la couche libre seule.

Briser la symétrie réduit la largeur des champs coercitifs du système, mais ne change pas la hauteur de barrière d'énergie. Le diagramme d'état champ – tension est aussi modifié, ce qui lie l'efficacité du couple de transfert de spin au volume nucléé initialement.

Quand la couche de référence est mise en configuration ferromagnétique, nous observons une réduction des champs coercitifs et des diagrammes d'états dans la même direction qu'observée expérimentalement. Les points de nucléations sont sur les bords dans les deux transitions. Pour finir la barrière d'énergie est réduite, ce qui est contraire aux résultats expérimentaux mais peut être lié à l'absence du couple field-like dans ce modèle.

# Introduction

From the results of the previous chapter, there is a need to differenciate the effect of the spin transfer torque and of the stray field on the switching process of the magnetization depending on the transition. One the one hand, the spin transfer torque is assumed to be responsible of the switching voltage slope differences and the back hopping at large bias and magnetic field, on the other hand the stray field was shown to be responsible of the shape of the width of the state diagram as well as an offset in field and in voltage. In this part, we use a micromagnetic model to describe the evolution of the magnetic configuration inside a magnetic tunnel junction under an applied magnetic field and an applied current and isolate the contribution of the two parameters.

The software used is FASTMAG. It is a a micromagnetic simulator developed by the “Computational electromagnetics and micromagnetics” group at UC San Diego led by Vitaliy Lomakin. The particularity of this software is that it uses the finite element to solve the LLG equation. This enable a larger flexibility for the shape and the meshing of the structure considered compared to finite difference solutions, especially at the boudaries.

The structure chosen is a $60 \times 80nm^2$ nanopillar, composed of one free layer and a three layers structure forming the SAF. The switching of the free layer magnetization have been studied for both magnetic field and STT driven processes, and to compare the nucleation points of the reversal depending on the transition. The energy barrier of the field driven transitions were obtained using the "Nudged Elastic Band" (NEB) method. This allows us to compare current-field state diagram at the field for which the energy barriers are equal for both transitions.

The effect of symmetry breaking compared to a fully perpendicular junction are compared. The pMTJs elaborated may present defects on the edges, roughness at the interface, or measured under a tilted field. For these reasons we introduced a tilt in the free layer magnetocrystalline anisotropy axis of $0.6$ degree, enough to modify position of the nucleation point in the free layer for both transition. Finally the effect of the reference layer configuration is studied, and its role on the nucleation position, and the height of the energy barrier are discussed.

# IV.1 Description of FASTMAG

As presented, FASTMAG is a finite element micromagnetic software, and the calculations are optimized for GPU use, enabling a good efficiency for various problems and structures. In FASTMAG, the dynamics of magnetization is coded as:

$$\frac{d\mathbf{m}}{dt} = -\frac{\gamma}{1+\alpha^2}\mathbf{m}(\boldsymbol{r}) \times \boldsymbol{H}_{eff}(\boldsymbol{r}) - \frac{\alpha\gamma}{1+\alpha^2}\mathbf{m}(\boldsymbol{r}) \times (\mathbf{m}(\boldsymbol{r}) \times \boldsymbol{H}_{eff}(\boldsymbol{r})) \tag{IV.1}$$

with an effective field that classically contains the applied field, the magnetocrystalline anisotropy field, the exchange field and the magneto-static field.

## IV.1.1 STT driven switching and energy barriers simuulations

### *Spin transfer torque computations*

The spin transfer torque is defined between two interfaces separated by a nonmagnetic layer and depends on the polarization attributed respectively to each surface. It is defined as in the work of Zhu & Zhu [133] for spin valves, but adapted to magnetic tunnel junctions by removing the angle dependence of the torque. The effect of the field like torque where not introduced in the study. The expressions of the spin transfer torques on the interfaces on each side of the tunnel barrier, noted 1 and 2, are given the general expressions given as follow:

$$\begin{cases} \frac{d\boldsymbol{m}_1}{dt} &= -\gamma \boldsymbol{m}_1 \times \boldsymbol{H}_{eff_1} + \alpha \boldsymbol{m}_1 \times \frac{d\boldsymbol{m}_1}{dt} - \frac{\gamma p_0 p_1}{\delta_1}\frac{\hbar}{2}\frac{J}{e}\boldsymbol{m}_1 \times \boldsymbol{m}_1 \times \boldsymbol{m}_2 \\ \frac{d\boldsymbol{m}_2}{dt} &= -\gamma \boldsymbol{m}_2 \times \boldsymbol{H}_{eff_2} + \alpha \boldsymbol{m}_2 \times \frac{d\boldsymbol{m}_2}{dt} - \frac{\gamma p_0 p_2}{\delta_2}\frac{\hbar}{2}\frac{J}{e}\boldsymbol{m}_2 \times \boldsymbol{m}_2 \times \boldsymbol{m}_1 \end{cases} \tag{IV.2}$$

with $p_0$ the spin polarization factor of the current, $p_1(p_2)$ and $\delta_1$ ($\delta_2$) the polarization factor and effective thicknesses of the electrode 1 (2), $J$ the current density and $\theta_{12}$ the angle between $m_1$ and $m_2$ . The last terms of the right-hand side of the equation is the Slonczewsli spin transfer torque. For the field and STT driven switching simulation, the output files are the image files of magnetic configurations and a file containing the average magnetization in the three directions and the applied field as functions of time.

### *Energy barriers computation*

Energy barrier calculation is based on the Nudged Elastic Band method (NEB) developed by Dittrich *et al.* in 2002 [134] and implemented in FASTMAG so as to represent the energy path of the switching. The energy path is represented by a set of images corresponding to the magnetic

configuration at different points of the transition. To find the energy profile of the transition, each of the "steps" of the energy path is minimized. In the case of the presented results, only the initial mid-point and final configuration were given as a first guess. The minimum of energy is found by the minimization of:

$$\mathbf{d} = \mathbf{M} \times \mathbf{M} \times (\boldsymbol{H}_{eff} - (\boldsymbol{H}_{eff} \cdot \mathbf{t})\,\mathbf{t}) + \mathbf{F} = 0 \tag{IV.3}$$

where **M** is a vector of three times the size of the number of image (here three) times the number of vertices in the mesh, **t** the tangent vector corresponding to the difference of magnetization states in the images of the energy path and **F** a perturbation vector, implemented in order to prevent the resolution in local minima of energy. The minimization is obtained by considering a high damping version of LLG, and thus tends to converge fast on the minima of energy. The NEB method does not take into account the spin transfer torque and thus should give results closer to the thermally activated switching.

The process used to obtain the energy barriers was to consider the two extreme configurations, the P and AP states, and an intermediary one, with a domain wall in the center. The three configurations were let to relax until stability. This intermediary state is a saddling point for the magnetization between both configurations. The energy barriers plotted in this part correspond to the subtraction of the energy of the stable initial states to intermediary state energy. The formula for the energy as a function of the applied magnetic field is the same as in the experimental part and is given by:

$$\frac{E_H}{k_B T}(H) = \frac{E}{k_B T}\left(1 - \frac{H - H_{eq}}{H_{sw_0}}\right)^{\frac{3}{2}} \tag{IV.4}$$

We fitted the energy obtained from the NEB method in the same way as in the experimental part: first by finding the offset field for which the energy barriers of the transitions are equals, then using eq. IV.4

### IV.1.2 Stack used

These simulation are realised in a structure based on the sample described in part III and with an area of $60 \times 80nm^2$ with $x$ the long axis of the ellipse and $y$ the short axis. The stack is composed of four different layers: the free layer and reference layer, and the SAF is composed of two others layers, as shown in figure IV.1. The reference layer and the upper layer of the

SAF present a strong ferromagnetic exchange coupling, while the two layers of the SAF have an antiferromagnetic coupling. These layers are meshed by tetrahedral cells whose size is user-defined. The structure is cylindrical and, to insure the continuity of the calculation between each layer, the mesh of the bottom surface is mirrored to all the other ellipsical surfaces. The meshing at the top surface of the second layer is replicated at the bottom of the first layer, and a polarization value is attributed to each surface.

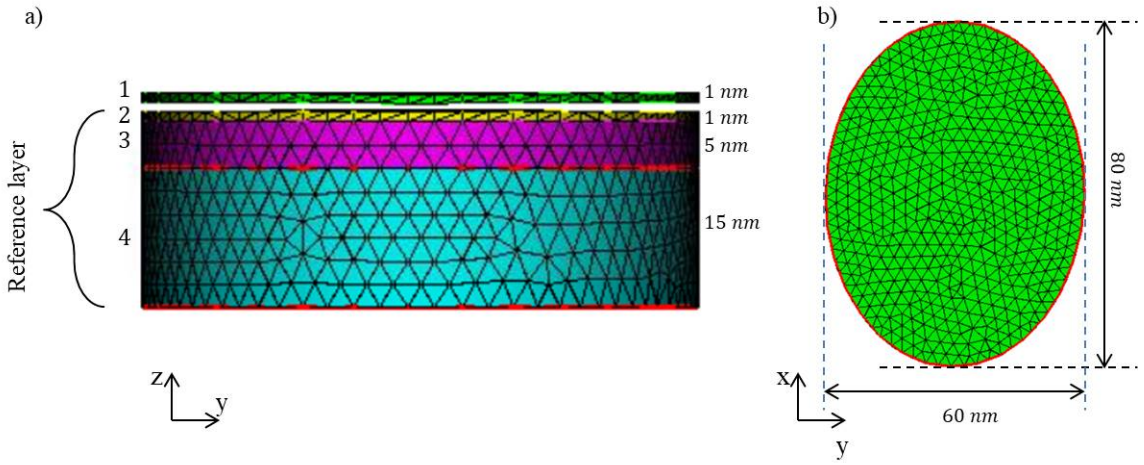


*Figure IV.1: Layer thicknesses and meshes of a) the face view and b) the top view of the modeled* $60 \times 80nm^2$ *magnetic tunnel junction.*

The minimum thickness resolution is 1 nm, thus our stack is adapted to it. We also considered the [Co|Pd] and [Co|Pt] multilayers to be one single block. In figure IV.1, the free layer (1), the barrier layer (gap) and the reference layer (2) are set to be 1nm thick each, the upper SAF layer (layer 3) to be 5nm thick and the lower SAF layer (layer 4) to be 15nm thick. The mesh is replicated from surface to surface so as to keep its continuity and model interface effects, even between the layers 1 and 2. The materials parameters used are summarized in table IV.1. The white gap shown on figure IV.1 is the spacer, left blank as meshing of nonmagnetic layers is not necessary in FASTMAG.

| Layers | $K(J.m^{-3})$ | $M_S(A.m^{-1})$ | $A_x(J.m^{-1})$ | $\alpha$ (–) |
|---|---|---|---|---|
| 1 & 2 | $7.2 \cdot 10^5$ | $10.5 \cdot 10^5$ | $1.3 \cdot 10^{-11}$ | 0.01 |
| 3 & 4 | $3 \cdot 10^5$ | $3.5 \cdot 10^5$ | $1.3 \cdot 10^{-11}$ | 0.01 |

*Table IV.1: Values of the materials parameters for the 4 layers modeled.*

The magnetocrystalline anisotropy, given by the constant K, is considered a bulk out-of-plane easy axis. $M_S$ is the magnetization at saturation of the layers. The surface exchange coupling

between the upper SAF layer and the reference layer is set to $1.242 \cdot 10^{-3} J.m^{-2}$ , and the one between the two layers of the SAF is set to $-1.242 \cdot 10^{-5} J.m^{-2}$.

For the STT driven switching, the software calculate at each time the applied current density as the applied voltage is the value set. The polarizations of the current at the electrodes interfaces, $p_1$ and $p_2$, and the current polarizations in the material, $p_0$ in equation (IV.2) are arbitrarily set to $p_0 = p_1 = p_2 = 0.66$. Two strong assumptions are made, first, as using Julliere's model with these values of polarization the TMR ratio in the simulation differs from the experimental one, and second, symmetric electrodes are not ensured in the experimental samples[76]. In a more general case, due to the substrate of the electrode and the roughness of the interface with the MgO, the parameters describing the free layer and the reference layer, especially the magnetization at saturation, the magnetic anisotropy coefficients and the polarization at the interface, could be different with each others.

The junction modeled is a perfect symmetrical approach of our samples. Due to defects, surface roughness, as a result of the etching of the structure, or by appling a magnetic field tilted, the symmetry of the sample can be broken. This can be represented by adding a tilt to the magnetocystalline anisotropy axis of the free layer, the reference layer anisotropy axis is kept fully out-of-plane. We choose a tilt is of $0.6$ degree to estimate the effect of the breaking of symmetry and compare this case to a fully perpendicular device.

For the two configurations of the reference layer (SAF and "no SAF") and the two free layer magnetocrystalline anisotropy axis direction, we simulated field hysteresis loop, voltage – magnetic field state diagram and energy barrier as a function of the transition. In all of these cases we are interested in the switching mechanism and the nucleation point position.

## IV.2 Micromagnetic simulation of pMTJ switching

### IV.2.1 pMTJ in the SAF configuration

#### *Field switching*

A way to characterize our simulated structure is to extract the hysteresis loop of the magnetization as a function of the applied magnetic field. The parameters of interest are the switching fields and the switching duration for each transition, as well as a the offset field of the hysteresis loop. For the pMTJs with a reference layer in the SAF configuration, figure IV.2 a) present the normalized average out-of-plane magnetization of the free layer in green for the $P \rightarrow AP$ transition and in red for the $AP \rightarrow P$ transition for both the fully perpendicular structure and the tilted free layer anisotropy axis structure. The switching fields of the hysteresis loop were obtained by increasing the applied field by steps of $10$ns, waiting for the magnetization to stabilize until the switching occurs. The switching field values correspond to theses latter.

For the fully perpendicular case, the switching fields are much larger than for the case with tilted anisotropy, going from $\mu_0 H_{SW_{P\rightarrow AP}} = -230mT$ and $\mu_0 H_{SW_{AP\rightarrow P}} = 200mT$ for the first to $\mu_0 H_{SW_{P\rightarrow AP}} = -120mT$ and $\mu_0 H_{SW_{AP\rightarrow P}} = 100mT$ for the latter. The offset field for the fully perpendicular case is of $\mu_0 H_{off} = -15mT$ and is noted by the gray vertical axis in the figure. For the tilted anisotropy case, it is of $\mu_0 H_{off} = -10mT$,

From figure IV.2, we observed a decrease of $50\%$ of the hysteresis loop by introducing a $0.6$ degree tilt of the anistropy axis. By ploting the switching of magnetizations as a function of times (figures IV.2 b),c),d and e)), we observe also an effect on the switching duration and the nucleation points due to the breaking of the symmetry.

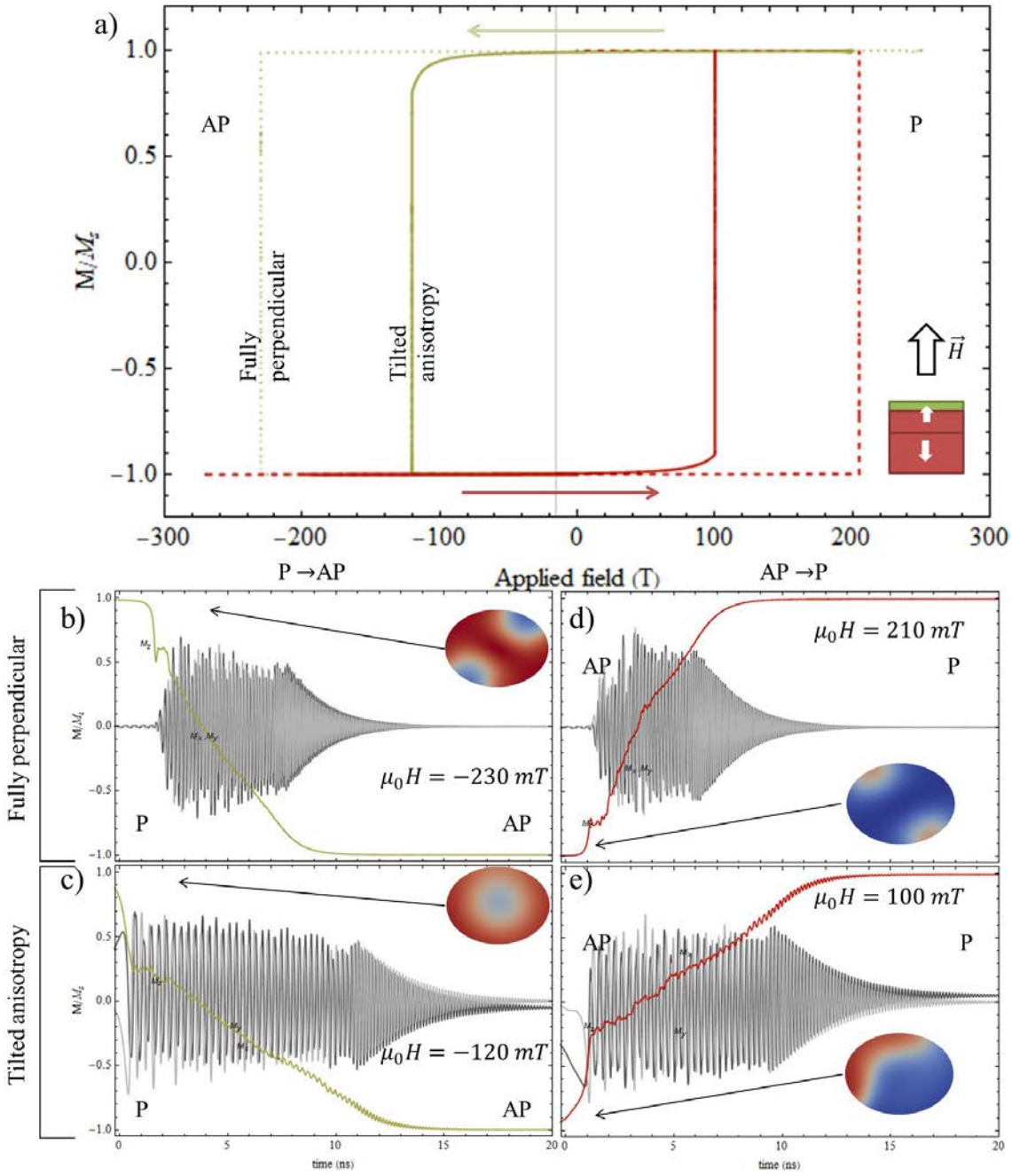


*Figure IV.2: a) Normalized magnetization as a function of the applied magnetic field for the full stack in the SAF configuration for both the fully perpendicular case and the tilted anisotropy case. The positive field direction is given by the black arrow. The magnetization components along the $z-axis$ (in green for the $P \rightarrow AP$ transition and in red for the $AP \rightarrow P$ transition), the $x$-axis (light gray) and the $y$-axis (dark gray) as a function of time for b) the $P \rightarrow AP$ transition in the fully perpendicular case at $\mu_0 H = -230mT$, c) the $P \rightarrow AP$ transition in the tilted anisotropy case at $\mu_0 H = -120mT$, c) the $AP \rightarrow P$ transition in the fully perpendicular case at $\mu_0 H = -210mT$, c) the $AP \rightarrow P$ transition in the tilted anisotropy case at $\mu_0 H = -100mT$, in inset are the representation of the magnetization configuration at the onset of the switching, with P in red and AP in blue.*

In figures IV.2 b) c) d) and e) are represented the $P \rightarrow AP$ and $AP \rightarrow P$ transitions for the normalized average magnetization components as a function of time for the fully perpendicular case (figures IV.2 b) and d)) and the tilted anisotropy case (figures IV.2 c) and e)). In gray are the in-plane components, light gray for $M_x$ and dark gray for $M_y$, in green (red) is the $M_z$ component of the magnetization for the $P \rightarrow AP$ ($AP \rightarrow P$) transition. The insets represent the magnetic configuration of the free layer at the onset of the transition. In this geometry, the P state is represented in red and the AP state in blue.

For the fully perpendicular case, it can be seen that both averaged in-plane components are equal to zero before and after the switching, implying a symmetric distribution of the two components over the surface. We observe that both switching processes display the same time trends: first the onset time after applying the switching field is about $1ns$ and second the switching in itself takes about $10ns$ to be completed. There are two nucleation points per transition corresponding to the creation of vortices in the tunnel junction. The demagnetizing field of the free layer is the weakest at the edge of the junction along the long axis, where vortices appear in the two directions due to the symmetry of the system. Then they start rotating along the edge of the ellipsoid and the nucleation points correspond to $45$degree of the long axis of the free layer. The two nucleation points are symmetric in each transition, but the process is also symmetric between the transitions.

For the tilted anistopy case, the symmetry of the situation is broken. The $M_y$ component is zero before and after the switching, but the $M_x$ present an offset, opposite as a function of the direction of the magnetization, that is directly related to the tilt in anisotropy. The magnetization has already started to rotate when the switching field is reach, and thus the onset times are much shorter than for the fully perpendicular case and hence the rounded curves at the onsets of the switchingd. Eventhough, the switching times in themselves are larger than for the fully perpendicular geometry; the magnetizations need about $20ns$ to settle in their new configurations. In that case the nucleation points position depend on the transition and is no longer symmetric: for the $P \rightarrow AP$ switching the nucleation point appears at the center of the junction whereas for the $AP \rightarrow P$ transition, it appears at the edge of the junction.

### Stray field in the SAF configuration

In order to understand the difference in position of nucleation points depending on the geometry and the transition for the tilted anisotropy case, the stray field from the SAF reference layer acting on the free layer at the center of the fully perpendicular anisotropy hysteresis loop ($\mu_0 H_{off} = -15mT$) is plotted in figure IV.3. In blue are the arrow along the $z$-axis, in red along the $x$-axis and in green along the $y$-axis. The cones give the direction of the field at the mesh node.

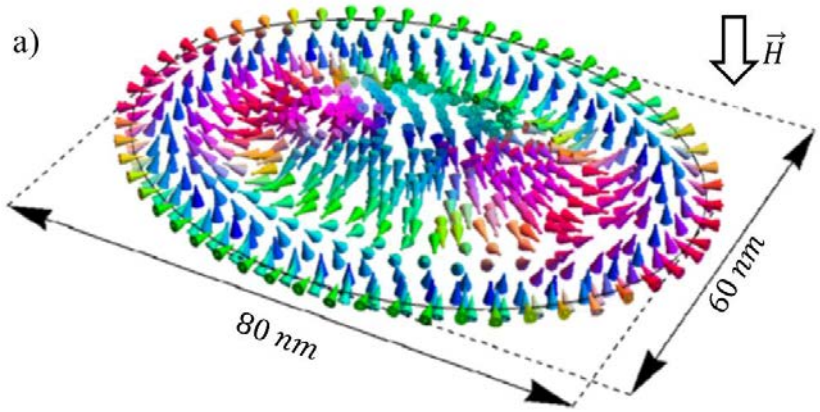


*Figure IV.3: a) Stray field from the reference layer in the SAF configuration to the free layer at the center of the hysteresis loop ($\mu_0 H_{off} = -15mT$). The arrows indicate the field direction, in blue for the $z$-axis , in green for the $x$-axis and in red for the $y$-axis, the black arrow indicates the direction of the applied field.*

The stray field in figure IV.3 presents two regions of opposite directions: at the center of the junction, the stray field points in the direction of the applied field, whereas close to the edges it is in the opposite direction, and at the edge of the junction the stray field is in-plane. For the fully perpendicular case, as the geometry is perfectly symmetric, the nucleation of domain of opposite magnetization occurs where the dipolar field of the free layer on itself is the smallest. On the contrary, breaking the symmetry of the system can induce a more proeminent part of the stray field configuration on the magnetization, thus favor the center or the edge of the junction to nucleate. A way to complement this hypothesis is to assess the switching process in the free layer alone in a fully perpendicular geometry and with a broken symmetry geometry.

### Free layer switching

In this part, the free layer has been isolated from the rest of the structure. Its behavior as a function of applied field for the transitions $P \rightarrow AP$ and $AP \rightarrow P$, keeping the same field

convention as before is studied to differentiate the effect of the dipolar field and of the stray field on the nucleation point, especially when the symmetry is broken.

The behavior of its normalized average out-of-plane magnetization as a function of the applied field is presented in figure IV.4 a) for both the fully perpendicular configuration (dashed line) and the tilted anisotropy configuration (plain line). Both hysteresis loops are centered in $\mu_0 H_{off} = 0mT$ as expected from the absence of the reference layer. In the same way than in the full stack, the tilted anisotropy field hysteresis loop width is reduced by $50\%$, from $|\mu_0 H_{SW}|= 280mT$ for the fully perpendicular case and $|\mu_0 H_{SW}|= 140mT$ for tilted anisotropy case.

In figures IV.4 b) c) d) and e) are represented the $P \rightarrow AP$ and $AP \rightarrow P$ transitions for the normalized average magnetization components as a function of time for the fully perpendicular case (figures IV.2 b) and d)) and the tilted anisotropy case (figures IV.2 c) and e)). In this geometry, green correspond to the positive to negative transition and red to the negative to positive transition. In the insets, red correspond to the positive configuration and blue to the negative configuration.

In the fully perpendicular case (figures IV.2 b) and d)), the behavior of the magnetization is entirely similar to the full stack one. Both switching present onset time of about $2ns$, and a total switching duration of $10ns$. The nucleation points correspond exactly to the one in the full stack switching. This preview corroborate the assumption made of a predominant role of the dipolar field of the free layer on the nucleation points in the fully perpendicular case. The positions of the nucleation points in the free layer were confirmed by a finite difference simulation of the free layer using mumax3, for the same parameters as in the finite element simulations.

In the tilted anisotropy case (figures IV.2 c) and e)), the magnetization behaves similarly for both transition, at the difference of its behavior in the full stack. At the application of the switching field the magnetization has not started to rotate, but the onset of the switching is immediate; the switching occurs in about $12ns$ for the positive to negative transition, and in about $10ns$ for the other transition. The addition of the tilted anisotropy also broke the symmetry of switching processes in the free layer. Nevertheless, the nucleation points are singles and located at the edge of the junction for both transitions.

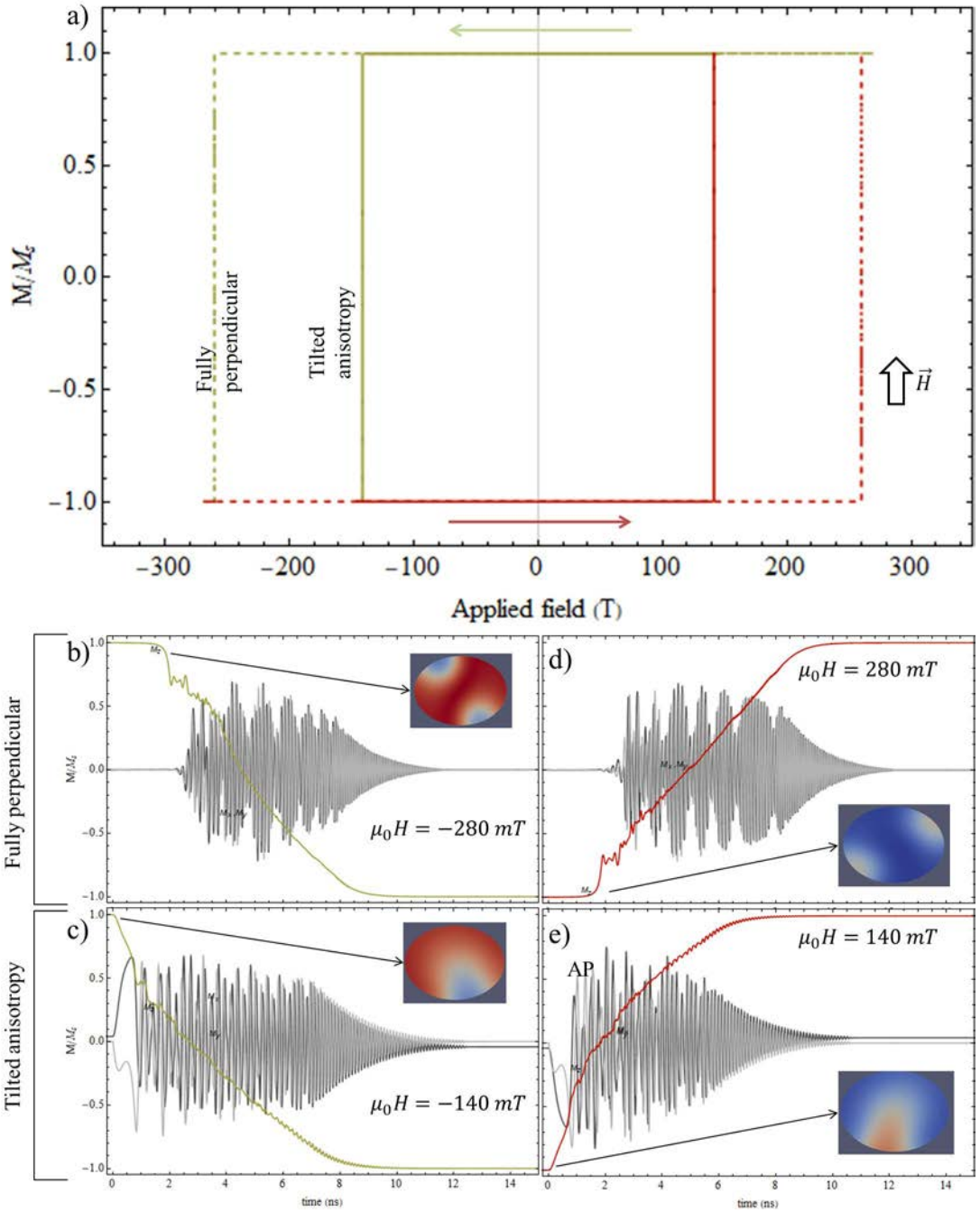


*Figure IV.4: a) Normalized magnetization as a function of the applied magnetic field for the free layer for both the fully perpendicular case and the tilted anisotropy case. The magnetization components along the $z-axis$ (in green for the positive to negative ("P to N") applied field transition and in red for the inverse ("N to P") transition), the $x$-axis (light gray) and the $y$-axis (dark gray) as a function of time for b) the "P to N" transition in the fully perpendicular case at $\mu_0 H = -280mT$, c) the "P to N" transition in the tilted anisotropy case at $\mu_0 H = -140mT$, c) the "N to P" transition in the fully perpendicular case at $\mu_0 H = 280mT$, c) the "N to P" transition in the tilted anisotropy case at $\mu_0 H = 140mT$, in inset are the representation of the magnetization configuration at the onset of the switching, with positive magnetization direction in red and negative in blue.*

From theses observations, it is possible to relate the position of the nucleation points in the full stack to the influence of the stray field. In that case, the breaking of symmetry might be important to explain certain features in the experimental state diagrams.

### *Energy barriers and state diagram*

After having characterized the field driven switching process in the simulated pMTJs, we are interested in reproducing the spin transfer torque driven switching process, as well as estimating the energy barrier height of the transitions to estimate the effect of the stray field on these two parameters dissociated from the spin transfer torque part in the switching. Figure IV.5 present the energy barriers and the voltage - field state diagram for both the fully perpendicular geometry (circles) and the tilted anisotropy geometry (dots), with the corresponding fittings (respectively dotted and plain lines).

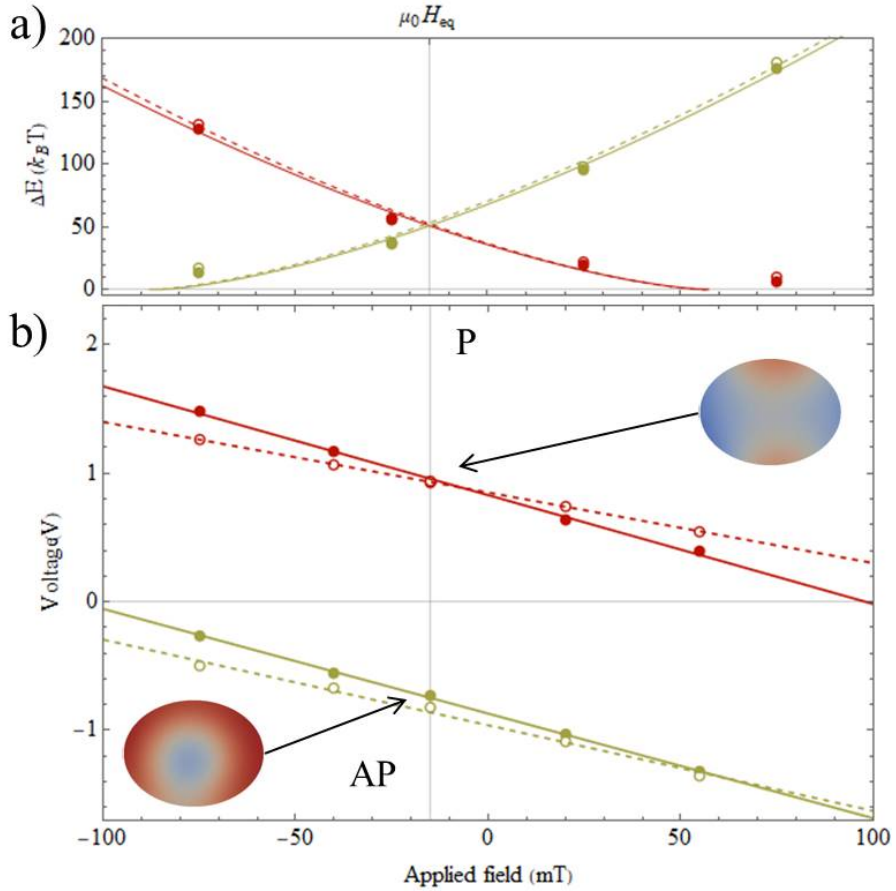


*Figure IV.5: For the full stack in the SAF configuration for both the fully perpendicular (circle) and the tilted anisotropy case (full dot) a) Energy barrier and b) Current - field state diagram, with the fitting of the switching voltages represented for the fully perpendicular case (dotted line) and the tilted anisotropy case (plain line).*

Figure IV.5 a) shows the energy barriers obtained with the nudged elastic band method for both transitions, in green for the $P \rightarrow AP$ transition and in red for the $AP \rightarrow P$ transition. For both geometries, the fittings match well with the power low of the energy, keeping $\eta = 1.5$. The results of the fitting are noted in table IV.2. We find the magnetic field at which the energy barriers are equal to be $\mu_0 H_{eq} = 15mT$, which is equal to the offset field found for the fully perpendicular hysteresis loop. The energy barriers obtained are of the same magnitude for both geometries despite the change in coercive field (figure IV.2).

The switching fields found with this method are smaller than the coercive fields obtained through the hysteresis loops, for both geometries. This may be due to the exponent choice of eq. (IV.4), as discussed in part III. In a first approximation, for nucleation propagation processes this exponent $\eta$ is taken between $\eta = 1.5$ and $\eta = 2$ that corresponds to the macrospin. With a larger exponent, the switching fields obtained are large, but due to the difficulty to determine $\eta$ value and in the continuity of the part III, it is kept at $\eta = 1.5$ in the following.

| $\mu_0 H_{eq} = 15mT$ | Fully perpendicular | | Tilted anisotropy | |
|---|---|---|---|---|
| | P to AP | AP to P | P to AP | AP to P |
| $\Delta E$ ($k_B T$) | $51 \pm 6$ | $51 \pm 5$ | $53 \pm 5$ | $53 \pm 6$ |
| $\mu_0 H_{sw_0}(mT)$ | $-71 \pm 11$ | $-73 \pm 11$ | $-73 \pm 9$ | $72 \pm 8$ |

*Table IV.2: Extracted energy barrier $\Delta E$ and switching field $\mu_0 H_{sw_0}$, considering the stray field to be $\mu_0 H_{eq}$ for the two transitions in to modeled structures*

Figure IV.5 b) presents the voltage - field state diagrams obtained for both geometries. The simulation of the voltage sweep is done as such: the voltage is increased from zero to 2V in the suitable polarity until the switching happens. The results of the fittings are given in table IV.3. The simulated data, for both the slopes values and the switching voltages for the equivalent field are found larger than the experimental values obtained from the fitting of $P_{NS}$. This maybe due to either the parameters chosen for the polarization of the electrodes or the absence of temperature in the model.

The slope values differ between geometries, and they are different for the transition in the fully perpendicular geometres, but present a smaller difference between transitions for the tilted anisotropy case. In this latter case, it corresponds to the assumption made on the spin transfer torque to not depend on the transition. The difference in slope coefficient may come from the

efficiency of the Slonczewski spin transfer torque modulated with the initial volume of magnetization switched during the nucleation, and its propension to propagate. The slope values in the fully perpendicular geometry are smaller than their equivalent in the tilted anisotropy one, implying an increased efficiency of the torque in the latter case. This effect is believed tocause the lower duration of the reversal observed in the field loops. We link the effiency of the torque to the dimensions of the nucleated volumes of inverse magnetization, and this is belived to come from the inhomogeneities of the stray field and of the demagnetizing field in the junction.

The switching voltages at $\mu_0 H_{eq}$ depend on the transition considered, and the state diagram presents an offset in the same direction of the experimental data. The switching voltage are equal for the $AP \rightarrow P$ transition in both geometries but differs for the $P \rightarrow AP$. In that way the stray field configuration influences the switching voltages without considering the effects of the field-like torque.

| | Fully perpendicular | | Tilted anisotropy | |
|---|---|---|---|---|
| | P to AP | AP to P | P to AP | AP to P |
| Slope $(V/T)$ | $-6.7 \pm 0.4$ | $-5.5 \pm 0.1$ | $-8.2 \pm 0.1$ | $-8.5 \pm 0.3$ |
| $V_{sw}(\mu_0 H_{eq})$ (V) | $-0.86$ | $0.93$ | $-0.75$ | $0.96$ |

*Table IV.3: $V_{sw}$ slopes and values for $\mu_0 H_{eq}$ for the two transitions in the two simulated structures.*

Finally, we observe in the state diagram, that for spin transfer torque driven switching, unlike field driven switching, independently of the geometry and the applied field value, the nucleation process depends on the transition considered: for the $AP \rightarrow P$ transition the nucleation starts at the center of the junction whereas for the $P \rightarrow AP$ it occurs on two points at the edge of the junction. This shows the importance of the stray field configuration during the spin transfer torque driven switching, and can explain the difference in slopes for the two transitions in the two geometries.

In this part, the switching processes for the magnetization of the free layer was proved to be influenced of the breaking of symmetry in the junction and of the presence of the SAF structure. The difference in nucleation points for the two transitions were found for both field and spin transfer torque driven switchings.

### IV.2.2 Effect of the stray field

In order to assess the role of the stray field on both the energy barrier and the switching , we modelize the same pMTJs with the reference layer in the "no SAF" configuration.

#### *Stray field in the "no SAF" configuration*

Figure IV.6 a) presents the stray field from the reference layer in the "no SAF" configuration acting on the free layer. In blue are the arrow along the $z$-axis, in red along the $x$-axis and in green along the $y$-axis. The cones give the direction of the field at the mesh node. The stray field points toward the negative fields, and unlike the previous case, there is no region where the magnetic field direction is inverted. Thus it is less likely to have a strong difference in nucleation point position and nucleation volumes.

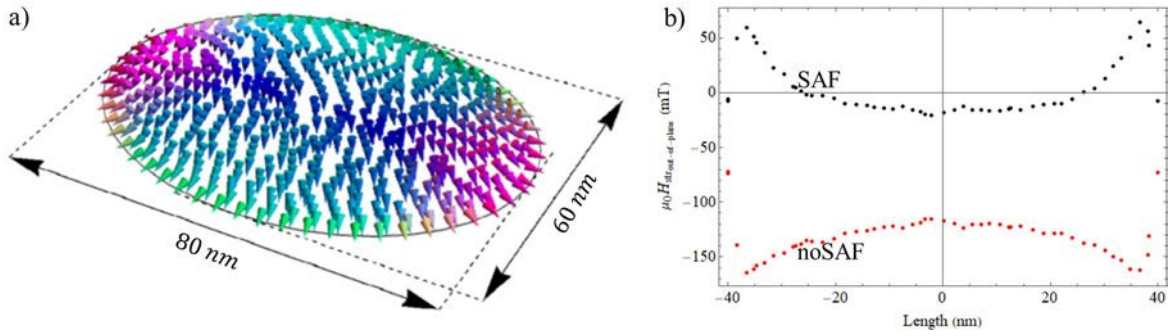


*Figure IV.6: a) Stray field from the reference layer in the SAF configuration to the free layer at the center of the hysteresis loop, the arrows indicate the field direction, in blue for the $z$-axis , in green for the $x$-axis and in magenta for the $y$-axis. b) Comparison of the out-of-plane component of the stray field along the large axis of the nanopillar in black for the SAF configuration and red for the "no SAF" configuration.*

Figure IV.6 b) compares the magnitude of the out-of-plane component of the stray field in the SAF configuration in black and in the "no SAF" configuration in red as a function of the position on the long axis of the junction. The SAF configuration presents an overall larger difference between the maximum of stray field and the value at the center of the juction compared to the "no SAF" configuration stray field. This latter have a larger mean values, which is expected to be reflected in the field hysteresis loop offset value.

#### *Field switching*

For the pMTJs with a reference layer in the "no SAF" configuration, figure IV.7 a) presents the normalized average out-of-plane magnetization of the free layer in green for the $P \rightarrow AP$

transition and in red for the $AP \rightarrow P$ transition for both the fully perpendicular structure and the tilted free layer anisotropy axis structure.Compared to the SAF configuration, the hysteresis loops in the "no SAF" configuration have a smaller width. As in the SAF configuration, for the fully perpendicular case, the switching voltages are larger than for the geometry with tilted anisotropy, going from $\mu_0 H_{SW_{PtoAP}} = 30mT$ and $\mu_0 H_{SW_{APtoP}} = 250mT$ for the first to $\mu_0 H_{SW_{PtoAP}} = 40mT$ and $\mu_0 H_{SW_{APtoP}} = 220mT$ for the latter. The offset field for the fully perpendicular case is of $\mu_0 H_{off} = 140mT$, and is noted by the gray vertical axis in the figure. The offset of the tilted anisotropy geometry is $\mu_0 H_{off} = 135mT$. As in the SAF configuration these offsets differ slightly, which is likely due to the breaking of symmetry.

In the SAF configuration, there was a decrease of $50\%$ the hysteresis loop widths from one geometry to the other (figure IV.2a)) whereas in the "no SAF" configuration ( IV.7 a)) the hysteresis loops display a reduction of $20\%$ of the width from the fully perpendicular geometry to the titled geometry. By ploting the switching of magnetizations as a function of times (figures IV.7 b),c),d and e)), we observe also a less pronunced effect on the switching process due to the breaking of the symmetry, as the switching time are in the same order.

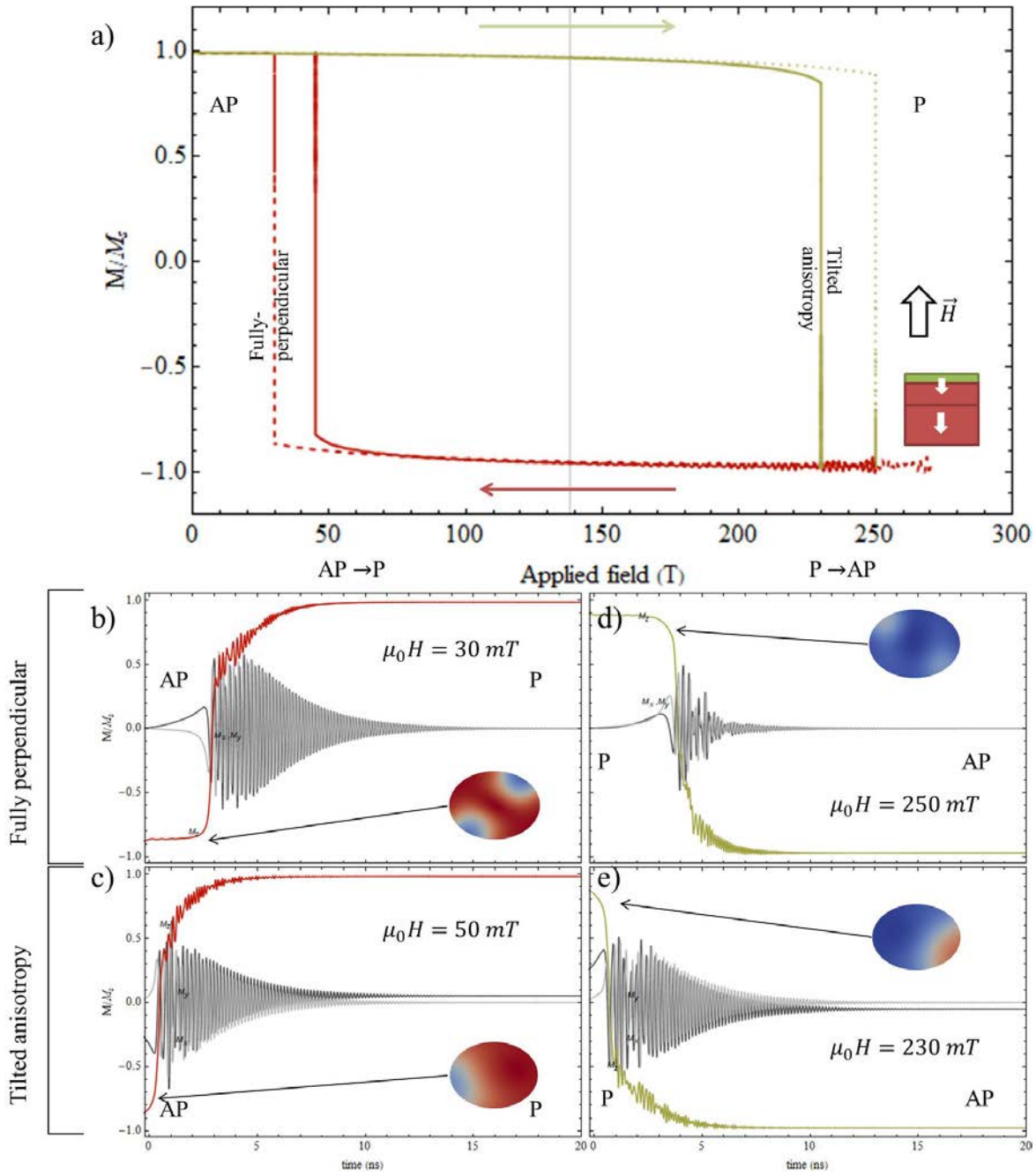


*Figure IV.7: a) Normalized magnetization as a function of the applied magnetic field for the full stack in the "no SAF" configuration for both the fully perpendicular case and the tilted anisotropy case. The magnetization components along the $z-axis$ (in green for the $P \rightarrow AP$ transition and in red for the $AP \rightarrow P$ transition), the $x$-axis (light gray) and the $y$-axis (dark gray) as a function of time for b) the $AP \rightarrow P$ transition in the fully perpendicular case at $\mu_0 H = 30mT$, c) the $AP \rightarrow P$ transition in the tilted anisotropy case at $\mu_0 H = 50mT$, c) the $P \rightarrow AP$ transition in the fully perpendicular case at $\mu_0 H = 250mT$, c) the $P \rightarrow AP$ transition in the tilted anisotropy case at $\mu_0 H = 230mT$, in inset are the representation of the magnetization configuration at the onset of the switching, with AP in red and P in blue.*

In figures IV.7 b) c) d) and e) are represented the $P \rightarrow AP$ and $AP \rightarrow P$ transitions for the normalized average magnetization components as a function of time for the fully perpendicular

case (figures IV.7 b) and d)) and the tilted anisotropy case (figures IV.7 c) and e)). In gray are the in-plane componenents, light gray for $M_x$ and dark gray for $M_y$, in green (red) is the $M_z$ component of the magnetization for the $P \rightarrow AP$ ($AP \rightarrow P$) transition. The insets represent the magnetic configuration of the free layer at the onset of the transition. In this geometry, the AP state is represented in the red and the P state in blue.

For the fully perpendicular case, it can be seen that both averaged in-plane components are equal to zero before and after the switching, implying a symmetric distributions of the two components over the surface. In this case the switching processes differs. They share an onset time of about $3ns$ but the switching for the $P \rightarrow AP$ transition is three time faster than the $AP \rightarrow P$ transition. This may be due to the shape of the stray field, favoring one transition over the other. The nucleation points appear to be the same than in the fully perpendicular geometry for the SAF configuration and the free layer switching. The nucleation points are symmetrics and they appear on opposite locations at $45$ degree of the long axis of the free layer.

For the tilted anistopy case, the offset in $M_x$ is found again, but the nucleation point is located at the edge of the junction for both transition, and there is no onset time and both switching duration is about $10ns$. As in the previous case studied, the main effect of the symmetry breaking is to change the nucleation points, where they were two vortices entering the junctions along the large axis in the fully perpendicular case, in this case the nucleation occurs only in one point, at the edge of the junction close to the large axis, which is consistant with the breaking of symmetry and the smaller influence of the SAF observed in the field hysteresis loops.

### *Energy barriers and state diagram*

As in the SAF configuration, simulations of the energy barriers and of the state diagram of the junction in the "no SAF" configuration were realised and are presented respectively in figure IV.8 a) and figure IV.8 b). In both figures, the two geometries are represented, the values extracted for the fully perpendicular case is represented with circles and the fitted functions with dahsed lines, and respectively with dots and plain lines for the tilted anisotropy extracted data and fitting functions. These figures give indication of the relation between the Slonczewski spin transfer torque efficiency and the energy barrier of the system.

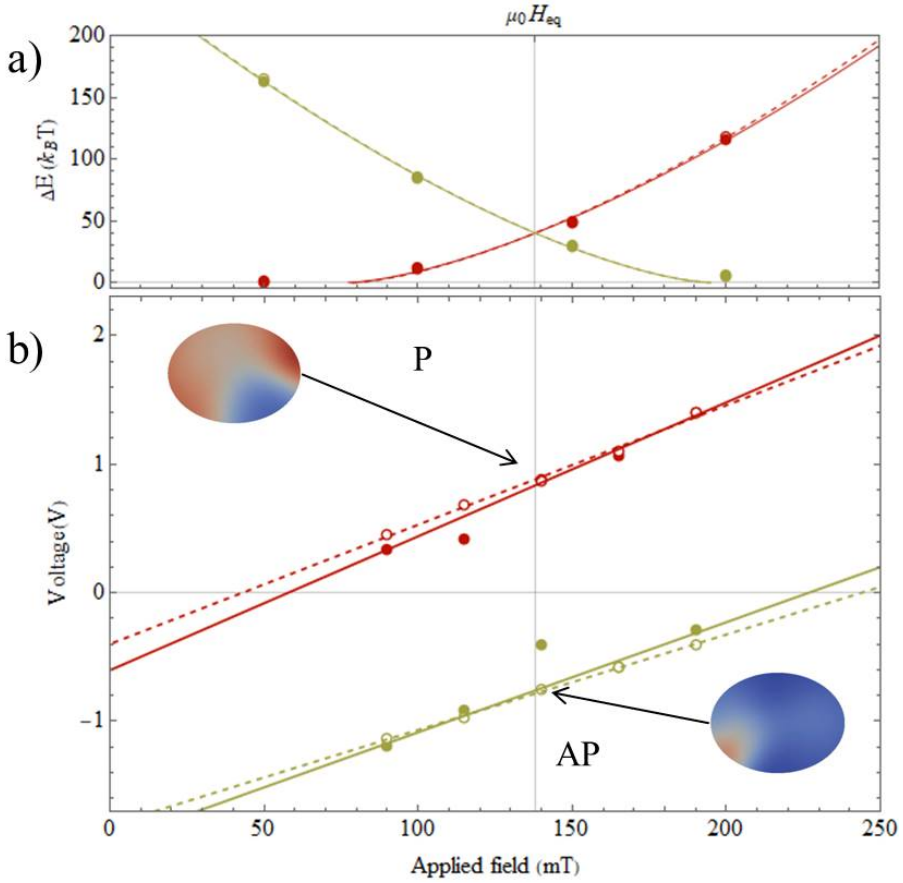


*Figure IV.8: For the full stack in the "no SAF" configuration for both the fully perpendicular (circle) and the tilted anisotropy case (full dot) a) Energy barrier and b) Current - field state diagram, with the fitting of the switching voltages represented for the fully perpendicular case (dotted line) and the tilted anisotropy case (plain line).*

Figure IV.8 a) shows the energy barriers obtained with the nudged elastic band method for both transitions, in green for the $P \rightarrow AP$ transition and in red for the $AP \rightarrow P$ transition. The values obtained by fitting with eq. (IV.4) are summarized in IV.4. The energy barrier values obtained from the simulations are almost mingled, and this is reflected in the value of the field for which the energy barriers are equal ($\mu_0 H_{eq} = 138mT$) and the height of theses energy barriers ($\Delta E = 40 k_B T$). This is coherent with the fact that the magnetization in both geometries behave in a more similar way for the "no SAF" configuration than in the SAF configuration. We can also note that the value of $\mu_0 H_{eq}$ correspond to the offset value of the fully perpendicular field hysteresis loop.

The influence of the stray field on the structure may also be the cause of the reduced energy barrier of the switching found in this case. As the stray field does not present a crown of opposite

field polarity, enhencing the capacity of the nucleated domain to propagate.

In the SAF configuration, the switching fields found with the fitting are smaller than the coercive fields obtained through the hysteresis loops, for both geometries, which is coherent with the choice of exponent. We observe an asymmetry of a few milliTesla between the switching voltages, increased compared to the previous case. In order to asses the relevance of this asymmetry, additional modelisations varying the strength of the stray field should be realized.

| $\mu_0 H_{eq} = 138mT$ | Fully perpendicular | | Tilted anisotropy | |
|---|---|---|---|---|
| | P to AP | AP to P | P to AP | AP to P |
| $\Delta E\ (k_B T)$ | $40 \pm 4$ | $40 \pm 2$ | $40 \pm 3$ | $40 \pm 3$ |
| $\mu_0 H_{sw_0}(mT)$ | $57 \pm 7$ | $-60 \pm 4$ | $57 \pm 6$ | $-61 \pm 6$ |

*Table IV.4: Extracted energy barrier $\Delta E$ and switching field $\mu_0 H_{sw_0}$ at zero temperature, considering the stray field to be $\mu_0 H_{eq}$ for the two transitions in to modeled structures*

Figure IV.8 b) presents the voltage - field state diagrams computed for both geometries and realized with the same process as described in the previous part. The results of the fittings are given in tabe IV.5. The same note on the magnitude of the results can be done for this configuration. We observe an decreased difference of slopes between the geometries but also an increased asymmetry of the slopes in between transition. These effects may be due to a difference in propension to propagate of the nucleated domain.

Comparing the switching voltages at $\mu_0 H_{eq}$ between transitions, there is an bias offset of the state diagram which is equal for both geometries, and is in the same direction as in the experimental data. This offset is however reduced compared to the SAF configuration. The equality of the offset is in accordance with the reduced effect of the stray field for the "no SAF" configuration.

| | Fully perpendicular | | Tilted anisotropy | |
|---|---|---|---|---|
| | P to AP | AP to P | P to AP | AP to P |
| Slope $(V/T)$ | $7.6 \pm 0.2$ | $9.4 \pm 0.4$ | $8.6 \pm 0.2$ | $10.4 \pm 0.6$ |
| $V_{sw}(\mu_0 H_{eq})$ (V) | $-0.76$ | $0.89$ | $-0.74$ | $0.87$ |

*Table IV.5: $V_{sw}$ slopes and values for $\mu_0 H_{eq}$ for the two transitions in the two simulated structures.*

The insets of figure IV.8 present the nucleation point positions for both geometries and transitions. As in the SAF configuration, the nucleation points for both geometries are similar to the

nucleation points for the geometry with a breaking of symmetry. For both transitions the nucleation occurs at the edge of the junction.

Comparing the two reference layer configurations, we observe a clear evidence of the stray field importance in the magnetization switching processes, an importance which is magnified when the structure considered present a breaking of symmetry. The stray field shape influence both the energy barriers of the transition and the efficiency of the spin transfer torque coefficient.

## IV.3 Comparison to experimental results

The state diagram obtained experimentally presented several features that we attributed either to the effect of the STT or to the inhomogeneities of the stray field. Regardeless of the junction size or reference layer configuration, the state diagram all presented an offset in field and in voltage, as well as different switching voltage slopes as a function of the transition. We also observed in the larger junctions, back-hopping for the $AP \rightarrow P$ attributed to the competition of the two spin transfer torques. An increase of junction size was translated to a modification of the switching voltages slopes, but no modifications of the offset field. Changing the configuration of the reference layer from SAF to "no SAF" lead to a drastic modification of the field width of the diagram, as well as an increase of the offset voltage and switching voltage slopes.

The study of the energy barriers corresponding to each transition showed the need to define an additional field at which the energy barrier for the two transitions are equal. This field was different than the offset field, effect which was attributed to the inhomogeneities of the stray field, and encouraged our interprestation of switching processes depending on the transition considered. The energy barrier at this field increased with the junction size. When the reference layer was in a "no SAF" configuration, the energy barrier increased for all junction sizes.

The simulations of voltage - field state diagrams were realized in this part for one junction size ($60 \times 80 nm^2$) using the assumptions of the model develloped in part III. This model described the STT-driven switching in pMTJs considering two strong hypothesis on the STT shape: first, the Slonczewski spin transfer torque was considered having a linear dependence with the bias and be independent of the transition considered, second the field-like torque effect was supposed

negligible in the state diagram. We discussed in part III the implications of these assumptions, and in this part we assessed their implications in the STT-driven switching processes.

First, the stray-field acting on the free layer is drastically modified by the reference configuration, both in mean value and in the position of its inhomogeneities. The field hysteresis loops are shown to depend on the presence of the reference layer, but also on its configuration. Their width decreases when the reference layer goes from SAF to "no SAF" and the offset field increases, in accordance with the experimental data. An addition of a tilt to the free layer magnetocrystalline anisotropy axis shows that the width of the field hysterisis loops are reduced when the symmetry of the system is broken. The second effect of the symmetry breaking is a modification of the nucleation points position in the junction surface, which may be needed to explain difference in efficiencies of the spin transfer torque. The offset field for the hysteresis loop with broken symmetry is slightly different (here $5$mT) from the one of the fully perpendicular geometry.

Second, in the state diagrams, the switching voltages slopes differ from one transition to the other and from one geometry to the other. As the damping and the spin transfer torque coefficient are equal for all the simulations, it implies that the torque efficiency may be linked to the inverse magnetization volume nucleated in the different cases. The difference in slopes in the experimental data was first attributed to a possible difference of spin transfer torque coefficient, as stated by Theodonis. It may not be the only parameter to be taken into account. The state diagram also present a small offset, in the same direction as the experimental data, but much smaller. However this offset is not magnifyied when the reference layer is in the "no SAF" configuration, which will be discussed later. We also shown in the simulation that the nucleation position during STT driven switching process depend on the stray-field inhomogeneities for both the fully perpendicular case and the tilted anisotropy case.

Third, we used the NEB method to extract the energy barriers of the transitions. We observe an evolution with field fitting the expression used in part III, but the exact exponent may differs and have to be addapted to obtain the same switching field as in the hysteresis loops. The breaking of symmetry does not change the fitting function, and the energy barrier obtained are similar for the two geometries. The field for which the energy barrier of the two transition is equal is the same as the offset field in the fully perpendicular hysteresis loop and thus differs slightly from

the one with the broken symmetry.

Finally, the energy barrier was reduced when the reference layer changed configuration at the difference with the experimental results. This is most likely due to the absence of the field-like torque term in the $P_{NS}$ expression.

Overall, the simulation reproduced quite accurately features of the experimental state diagram and energy barriers field dependence. The importance of symmetry breaking to describe switching process behavior was introduced in this part. Using strong assumption in the expression of the spin transfer torque, the effects of the inhomogeneities of the stray field were put in evidence, and are able to describe part of the experiemental state diagram, such as the switching voltage slope dependence on the nucleation volume, and the difference between $\mu_0 H_{off}$ and $\mu_0 H_{eq}$.

The discrepancies remaining, namely the larger offset voltage, the larger difference between the offset field and the field where the energy barriers are equal and the energy barrier evolution with the reference layer configuration could be explained by introducing the field like torque in the model. Additional simulations introducing this components of the spin transfer torque expression may help quantifying its effect on the state diagram.

## Conclusion

In this part we studied micromagnetic simulation of the magnetization behavior in pMTJs for two configurations of the reference layers: an antiferromagnetic and a ferromagnetic alignement of the layers. We especially focused on the magnetic field and bias dependence of the switching processes as a function of the transition considered. The energy barriers of the transition for different fields were acquiered using the nudged elastic band method. The finite element micromagnetic software FASTMAG was used to simulate the different configurations. The main result of this study is the clear influence of the stray field from this reference layer on the free layer in the switching process of the magnetization.

The shape of the stray field has been modeled in the two configurations, the main difference is the presence of a crown with an inverse field polarity close to the edge of the junction when the reference layer in the SAF configuration, whereas it is uniformly out of plane for the "no SAF" configuration with a spreading toward the in-plane direction at the edge of the junction. The energy barriers for both transitions when they are equal is reduced when the reference layer is in the "no SAF" configuration compared to the SAF configuration. This may be due to an easing of the propagation in the free layer for the "no SAF" configuration as the stray field is continuously in the same direction than the dipolar field.

When the structure simulated presented a perfect symmetry, the nucleation point positions in the junction depend only on the dipolar field of the free layer. The nucleated domain spread from two opposite points from the edge of the junction situated at 45 degree of the long axis of the surface. Introducing a breaking of symmetry by tilting the magnetocrystalline anisopy axis of the free layer make the influence of the stray field on the nucleation point to be preponderant. For the SAF configuration, the nucleation starts at the center of the junction for the $P \rightarrow AP$ transition and at the edge for the $AP \rightarrow P$ transition and for the "no SAF" configuration, the nucleation starts for both transitions in a single point at the edge of the junction.

This breaking of the symmetry also reduces the width of the field hysteresis loops, in the way than the macrospin computation of part II. Moreover the reduction of the hysteresis loop is larger when the reference layer is in the SAF configuration than in the "no SAF" configuration. Similar results were obtained by appling an small in-plane field during the simulation in a fully perpendicular geometry. In the experimental samples, breaking of symmetry may occurs in defaults due to etching, the surface roughness, or the application of an tilted field.

Finally, we simulated voltage - field state diagram for the different structures using the same strong assumption on the spin transfer torque as in the model used to analyse the experimental data; namely, we put the field-like torque to zero and considered the Slonczewski spin transfer torque coefficient to be independent of the transition considered, we also set equal electrode polarization values. The state diagram obtained did not present a clear offset field, different than the field for which the energy barriers are equal. However, for this field value, the state diagram displays a bias offset, magnifyied when the symmetry is broken. The slopes of the switching voltage

values also depend on the transition, even for the fully perpendicular geometry, at the difference with the macrospin model. The breaking of symmetry increase the slope values, which can be related to a decrease of the Slonczewski spin transfer torque efficiency in that case. Comparing to the experimental data, the relative strength of the spin transfer torque contributions to the asymmetry of the state diagram should be obtained by realizing additional simulation of the STT driven switching introducing the field-like torque and the asymmetry of the Slonczewski spin transfer torque.

# Conclusion – Français

Ce manuscrit s'intéresse à des mémoires magnétiques non-volatiles où l'écriture et la lecture de l'information se font grâce à l'application d'une tension, les STT-MRAM. Les points mémoires des MRAM sont des jonctions tunnels magnétiques composées de deux couches ferromagnétiques (une couche libre et une couche de référence) séparées par une couche isolante. La résistance de ces dispositifs dépend de l'orientation relative de l'aimantation de ces deux couches ; un phénomène appelé "magnétorésistance tunnel" (T.M.R.). Cette résistance est minimum quand les aimantations sont alignées parallèlement et maximum quand elles sont alignées antiparallèlement. Les jonctions tunnels sont élaborées de sorte que ces deux configurations soient les seules stables. La lecture de l'information est réalisée par une mesure de la résistance alors que l'écriture repose sur la possibilité de manipuler l'aimantation avec un courant polarisé grâce au couple de transfert de spin (S.T.T.).

Pour que les STT-MRAM soient une technologie compétitive, les jonctions tunnels magnétiques doivent pouvoir être de taille réduite, tout en demandant une faible puissance d'écriture, un bon rapport de T.M.R., un temps d'écriture rapide et une bonne stabilité thermique. La faible puissance d'écriture et la bonne stabilité thermique sont obtenues en utilisant des matériaux à aimantation perpendiculaire pour les jonctions tunnels magnétiques. De plus, pour éviter l'effet du champ magnétique rayonné sur la couche libre par la couche de référence, cette dernière est constituée de matériaux multicouches formant un antiferromagnétique synthétique (S.A.F.). Plus précisément, un S.A.F. est constitué de deux couches avec un couplage antiferromagnétique conduisant à une aimantation rayonnée nette nulle. Le développement de ces dispositifs est rendu possible par l'amélioration des techniques de dépôt sous vide, telles que les P.V.D. (Physical Vapor Deposition) et les M.B.E. (Molecular Beam Epitaxy).

Ce manuscrit présente une étude de la dynamique du retournement de l'aimantation de la couche libre en fonction du champ magnétique appliqué et de la tension appliquée dans les jonctions tunnels aimantées perpendiculairement (pMTJ).

La dynamique de l'aimantation en présence d'une tension est décrite par l'équation de Landau-Lifshitz-Gilbert-Slonczewski. Celle-ci est composée d'un couple conservatif lié à la densité d'énergie de la couche libre, un couple non-conservatif dû à l'amortissement et deux couples dûs à la tension : le couple de transfert de spin de Slonczewski peut s'ajouter ou s'opposer à l'amortissement et un couple "field-like" agit comme un champ magnétique.

Comprendre les mécanismes de retournement de l'aimantation et l'influence de la taille de la jonction et du champ rayonné généré par la couche de référence sur ces processus est intéressant industriellement pour optimiser l'élaboration des jonctions tunnels magnétiques. Au cours de ce manuscrit nous démontrons que la dynamique de l'aimantation de la couche libre lors du passage de la jonction tunnel d'un alignement parallèle à un alignement antiparallèle est différente de celle d'antiparallèle à parallèle.

Dans la première partie, nous présentons quelques concepts de base dans le domaine du nanomagnétisme et de l'électronique de spin, nécessaires à la compréhension du manuscrit. Nous donnons également une description générale des STT-MRAM et un aperçu de l'amélioration technique d'élaboration des jonctions tunnels magnétiques au cours des dernières décennies. Les expressions des couples de transfert de spin sont introduites et discutées, en particulier nous nous intéressons à l'indépendance du coefficient de transfert de spin sur la transition considérée, et les limitations de cette hypothèse, ainsi qu'à l'effet du couple "field-like" sur le retournement de l'aimantation.

Dans la deuxième partie du manuscrit nous présentons une approche macrospin du comportement des jonctions tunnels magnétiques ; c'est-à-dire quand l'ensemble des moments d'une particule magnétique considérée se comportent comme un seul moment. Nous avons développé un modèle dans cette approximation basé sur le principe de la puissance dissipée, pour décrire le comportement tension – champ magnétique de jonctions tunnels à aimantation perpendiculaire types. Ce comportement est représenté à travers un diagramme d'état de la tension en fonction

du champ magnétique.

Le modèle de la puissance dissipée est basé, pour un champ magnétique et une tension déterminés, sur le calcul des extrema d'énergie du système (maxima et minima), donc des configurations magnétiques stables (parallèle et antiparallèle) puis par la détermination de la puissance dissipée ou reçue due aux torques non-conservatifs (amortissement et couple de transfert de spin). L'avantage de ce modèle est qu'il n'est pas nécessaire de calculer la trajectoire complète de l'aimantation pour déduire si sa position est stable. Afin d'évaluer ce modèle, nous comparons les diagrammes d'état obtenus à ceux provenant de l'intégration directe de l'équation de Landau-Lifshitz-Gilbert-Slonczewski. Les deux modèles macrospin prennent en compte les deux termes du couple de transfert de spin.

L'étude d'une jonction où l'axe de l'anisotropie magnéto-cristalline, le champ magnétique et la direction de la polarisation de la tension sont tous alignés selon la direction hors du plan permet de déterminer les expressions des champs et des tensions de retournement, utiles pour décrire les diagrammes d'état. Cependant, un système de symétrie parfaite est limité pour décrire les résultats expérimentaux. Des géométries différentes sont dont testées : d'abord le champ magnétique, puis l'axe de l'anisotropie ont été légèrement éloignées de l'axe hors du plan. Cela a permis de faire apparaitre des états inclinés présentant des similitudes avec les diagrammes d'état expérimentaux. Dans ces cas nous atteignons aussi les limitations du modèle, car les torques non-conservatifs ne changent pas de signe au niveau des extrema d'énergie. Pour le champ d'axe incliné les diagrammes d'état obtenus par les deux modèles sont similaires, au contraire du cas où l'anisotropie est inclinée qui présente des différences.

Dans cette représentation macrospin, nous avons également pris en compte un terme d'ordre supérieur dans l'anisotropie magnéto-cristalline car, pour un choix approprié des paramètres magnétiques, un état conique stable peut être défini. Cet état permet d'obtenir une précession en régime stable dont la fréquence dépend de la valeur de tension appliquée. La présence de l'anisotropie d'ordre supérieur diminue la tension de retournement pour une barrière d'énergie donnée. La mise en précession de l'aimantation et le retournement de l'aimantation dans cette géométrie peuvent être décrites par deux expressions de la tension en fonction du ratio des coefficients d'anisotropie. Nous montrons que, avant même la formation de l'état conique dans le

paysage énergétique, une précession de l'aimantation est possible et que la tension de retournement peut être minimisée de $40\%$ pour un ratio de $\frac{1}{3}$ des coefficients d'anisotropie.

Dans la troisième partie du manuscrit, nous présentons une étude expérimentale sur des jonctions tunnels magnétiques fabriquées par IBM pour différentes tailles de nanopiliers. Le retournement de l'aimantation est un processus thermiquement activé, et pour étudier l'effet du couple de transfert de spin, nous avons traité l'introduction de la tension comme une température effective. Afin de réaliser cette étude, nous introduisons en premier lieu l'expression de la probabilité de non-retournement pour étudier le bruit télégraphique à haute température, où la fluctuation thermique permet de mesurer la probabilité de retournement de l'aimantation. À partir de la probabilité de retournement, nous avons pu extraire une expression de la barrière d'énergie, qui détermine la stabilité thermique de la jonction, en fonction du champ magnétique appliqué. Nous observons la décroissance attendue du temps de vie moyen d'un état. Cette étape montre aussi la nécessité de définir un champ pour lequel les barrières d'énergies sont égales.

Pour étudier l'effet du couple de transfert de spin, des diagrammes d'état tension – champ magnétique expérimentaux sont réalisés en fixant le champ et en balayant la tension. Par rapport aux modèles macrospins, les diagrammes d'état sont décalés par rapport à l'axe "champ zéro" et le coefficient directeur de la tension de retournement en fonction du champ magnétique est différente pour la transition de $AP \rightarrow P$ et celle de $P \rightarrow AP$, il y a aussi un décalage en tension au centre du diagramme. Pour étudier plus en détail le processus d'inversion de l'aimantation, nous avons adapté l'expression de la probabilité précédente pour représenter l'effet d'un balayage en tension. Des hypothèses fortes sur l'expression du couple de transfert de spin sont faites. En particulier, il est considéré indépendant de la transition considérée et le couple "field-like" est négligé. Cette dernière hypothèse est particulièrement forte car du "back-hopping" est observé pour la transition $AP \rightarrow P$, signe d'un couple "field-like" suffisamment fort pour entrer en compétition avec le couple de transfert de spin de Slonczewski.

Nous observons pour toutes les tailles de jonction une différence entre le champ de décalage du diagramme, qui est l'effet moyen du champ rayonné par la couche de référence, et le champ pour lesquelles les barrières d'énergie des deux transitions sont égales. De plus la valeur de la

barrière d'énergie augmente en fonction de la taille de la jonction.

Pour finir, nous avons étudié le rôle des inhomogénéités du champ rayonné par la couche de référence sur le processus de retournement de l'aimantation de la couche libre. Le couplage antiferromagnétique de la couche de référence est brisé et celle-ci prend une configuration ferromagnétique. Dans cette configuration, les diagrammes d'état tension – champ magnétique sont modifiés : les champs de retournement diminuent, la tension de retournement pour l'une des transitions est augmentée et les coefficients directeurs des tensions de retournement diffèrent. Le même constat d'une différence entre le champ de décalage et le champ où les barrières d'énergie sont égales est fait. Les barrières d'énergie obtenues sont plus élevées que quand la couche de référence est couplée antiferromagnétiquement, et elles augmentent avec le diamètre de la jonction. Dans les tailles de jonctions considérées, le retournement de l'aimantation se fait par un processus de nucléation propagation, et le champ rayonné peut jouer un rôle important dans la position du centre de nucléation. De ces observations nous déduisons un rôle non négligeable des inhomogénéités du champ rayonné sur le processus de retournement.

Dans le quatrième chapitre, nous utilisons le code micromagnétique FASTMAG afin d'isoler les contributions du champ rayonné et du couple "field-like" sur les processus de retournement de l'aimantation. Ce code utilisant les éléments finis est développé dans le groupe de Vitaliy Lomakin à UC- San Diego et a pu être utilisé pour ce projet grâce à la forte collaboration entre le groupe de Nancy et celui de UCSD. La structure d'une jonction tunnel magnétique est simulée en utilisant des paramètres matériaux proches des paramètres expérimentaux. Deux géométries sont étudiées, une entièrement symétrique hors du plan et une seconde où l'axe d'anisotropie magnéto-cristalline de la couche libre est légèrement incliné. Nous avons étudié le retournement en champ et en tension de l'aimantation de la couche libre ainsi que la barrière d'énergie des transitions grâce à la méthode "Nudged Elastic Band" implémentée dans FASTMAG. Pour les retournements d'aimantation utilisant le couple de transfert de spin, les hypothèses effectuées sont les mêmes que celles du modèle de la probabilité de non-retournement du troisième chapitre.

Les résultats obtenus montrent l'importance des inhomogénéités du champ rayonné sur la position des centre de nucléation, en particulier pour les simulations en fonction du champ quand la symétrie de la jonction est brisée ou pour les simulations en tension. Briser la symétrie de la

jonction entraine une diminution des valeurs des champs de retournement de la structure, mais aucune modification de la hauteur de barrière d'énergie. La nucléation se fait pour l'une transition au centre de la jonction et pour l'autre sur le bord. De plus, en dépit de l'hypothèse d'un coefficient du couple de transfert de spin égal pour les deux transitions, on observe une différence de coefficients directeurs pour les tensions de retournement des deux transitions. Ceci implique que l'efficacité du couple de transfert de spin lors du retournement de l'aimantation dépend aussi du volume initial nucléé. Enfin, la modification de la couche de référence dans une configuration ferromagnétique entraine une réduction des champs coercitifs de la couche libre, mais aussi une diminution de la barrière d'énergie. Ce dernier effet, qui est contraire à celui observé dans les résultats expérimentaux, peut être dû à la non-inclusion du couple "field-like" dans les simulations. Dans cette configuration, les points de nucléation redeviennent similaires pour les deux transitions (sur les bords).

Notre travail souligne clairement l'effet important du champ rayonné non uniforme créé par la couche de référence sur la couche libre. Celui-ci induit une différence de processus de retournement de l'aimantation en tension et en champ magnétique en fonction de la transition. Les mesures de probabilité du retournement de l'aimantation ont clairement mis en évidence que les barrières d'énergie doivent être considérées comme dépendantes de la transition. Pour abaisser davantage la tension de retournement sans affecter la stabilité thermique, nous essayons d'ajouter une tension R.F. à la tension de retournement D.C. pour améliorer la puissance d'écriture de l'information dans une jonction tunnel.

Ce travail représente une partie de mes travaux de thèse. Pour des raisons de cohérence du manuscrit, des mesures de résonance ferromagnétique (F.M.R.) sur des couches couplées antiferromagnétiquement et des mesures de FMR activée par couple de transfert de spin sur des jonctions tunnels magnétique cylindriques n'ont pas été incluses. J'ai aussi eu la chance de participer à la mise en place d'une nouvelle station sous pointe à champ perpendiculaire, ainsi qu'à l'instrumentation d'un analyseur de réseau et un analyseur de spectre.

# Conclusion – English

This manuscript focuses on random access memories, called STT-MRAM, where the recording and the reading of the information is done using a bias voltage. The data is stored in "magnetic tunnel junctions", devices composed of two ferromagnetic layers (one free layer and one reference layer) separated by an insulating layer. The resistance of such devices depends on the magnetizations relative orientation between the two layers, a phenomenon named "tunnel magnetoresistance" (TMR). The resistance of the device is minimized when the magnetizations are parallel and maximized when they are antiparallel. The junctions are elaborated to present stable states only in these two configurations. The information stored is read through a resistance measurement and the data recording is based on the possibility to manipulate the magnetization direction with a polarized current with the spin transfer torque (STT).

For the STT-MRAM to be a competitive technology, the magnetic tunnel junctions have to be able to be scaled down, present a large enough TMR ratio, a fast writing time; they also need a low writing power consumption and a good thermal stability. These last two requirements are met using perpendicularly magnetized materials for the magnetic layers. Moreover, to prevent the effect of the stray field of the reference layer on the free layer, the reference layer is composed of several layers with an antiferromagnetic coupling, forming a "synthetic antiferromagnet" (SAF). The average stray field from this structure is cancelled. The elaboration and development of the magnetic tunnel junction is made possible by the development of ultra-vacuum deposition techniques such as Physical Vapor Deposition (PVD) and Molecular Beam Epitaxy (MBE).

This manuscript presents a study of the dynamics of the free layer magnetization switching as a function of the applied field and applied voltage in perpendicularly magnetized tunnel junctions (pMTJs).

The dynamics of a pMTJ free layer magnetization subjected to a bias voltage is described by the Landau-Lifshitz-Gilbert-Slonczewski equation (LLGS). This equation is composed of a conservative torque due to the energy density of the free layer, a non-conservative torque describing the damping of its magnetization, and two torques due to the applied voltage: the Slonczewski spin transfer torque, which can enhance or oppose the effect of the damping, and a field-like torque.

Understanding the magnetization switching mechanisms as well as the influence of the junction size and the stray field of the reference layer on these mechanisms is of interest for the STT-MRAM industry in order to optimize the devices. In this manuscript, we show that the switching of the free layer magnetization is different as a function of the transition.

In the first part, we present some basic concepts of nanomagnetism and spintronics. We also describe the evolution of pMTJs elaboration during the last two decades. The spin transfer torque expressions are introduced and discussed, with a focus on the independence of the Slonczewski spin transfer torque with the transition and its implications. We also discuss the effects of the field-like torque on the magnetization switching.

In the second part of the manuscript, we present a macrospin approximation of the pMTJs behavior. The macrospin approach considers that the totality of the magnetic moments in a considered volume behaves coherently. We have developed a model in this approximation based on the dissipated power in order to describe the behavior of pMTJs subjected to an applied field and an applied voltage, leading to the elaboration of voltage – field state diagrams.

The dissipated power model is based on the computation of the energy extrema positions (minima and maxima), indicating the stable magnetic configurations possible in the junction, then determining the sign of the dissipated or received power from the non-conservative torques (Damping and STT) at this position. In this model, the magnetization trajectory does not have to be computed to obtain the stability of a state. In order to assess our results, we compared the state diagram obtained from this method to those obtained by a direct integration of the LLGS equation. Both models take into account the two spin transfer torques.

The study of an all-perpendicular tunnel junction, where the magnetocrystalline anisotropy axis, the applied magnetic field and the direction of the voltage polarization are all aligned out-of-plane enables the extraction of the expressions of the switching voltages and limit fields that describe the state diagrams. However, a system of perfect symmetry is too limited to model experimental results. Geometries with different kinds of symmetry breaking are tested: the applied magnetic field, then the anisotropy axis is tilted away from the out-of-plane direction. In the first case, the state diagrams obtained with the two methods are similar whereas for the second the state diagrams present large discrepancies. These cases explore the limits of the model as the non-conservative torques do not compensate each other on the energy extrema positions.

In this macrospin representation, we also introduced the second order term of magnetocrystalline anisotropy that, for an appropriate choice of parameters, creates a stable cone state in the energy landscape of the free layer. A steady state precession is obtained in this case, with a frequency depending on the applied voltage magnitude. The introduction of this higher order of anisotropy decreases the switching voltage magnitude for a given energy barrier. The precession onset and the switching of the magnetization can be described by two voltage expressions depending on the ratio of the anisotropy coefficient. We show that, before the apparition of the cone state, the magnetization can precess and that the switching voltage can be reduced of 40%.

In the third part of the manuscript, we present an experimental study on magnetic tunnel junctions elaborated by IBM. The study was conducted on several nanopillar sizes. The magnetization switching is a thermally activated process, and the study of the spin transfer torques effect on it was based on the introduction of the bias voltage as an effective temperature. We first developed the expression of the non-switching probability in order to study the telegraphic noise at large temperature, where the thermal fluctuations enable the measurement of this probability. From this experiment, we can extract an energy barrier that determines the thermal stability of the device as a function of the applied field. We observed the expected decrease of the mean lifetime as a function of the increasing temperature. This also highlights the need to define a magnetic field at which the energy barriers are equal.

In order to study the spin transfer torque, experimental tension – field state diagrams are realized by fixing the field and sweeping the voltage. In contrast to the macrospin models, the state

diagrams present an offset field and switching voltage slope coefficients dependent on the transition. There is also an offset voltage. The probability of non-switching was adapted to include the sweeping voltage, by considering the voltage an effective temperature. Strong assumptions are made on the expression of the spin transfer torques; in the Slonczewski term, the coefficient is considered independent of the transition, and the field-like torque is neglected. This latter assumption has to be tempered by the presence of back-hopping for one transition; sign that the spin transfer torques are in the same order of magnitude and compete with each other to favor one configuration.

We observe for all the studied junctions a difference between the offset field and the field at which the energy are equal, without correlation with the size increase. The offset field is the averaged effect of the stray field on the free layer. We also observe that the energy barrier increases as a function of the junction size.

Finally, we study the stray field inhomogeneity role on the free layer switching. The antiferromagnetic coupling from the reference layer is broken and the layer takes a ferromagnetic configuration. In this new configuration, the state diagrams are modified: their field width is reduced, the switching voltage slopes differ from the previous ones, and the offset voltage increases. The same observation as before on the offset field and the field for which the energy barrier are equal is done. The energy barriers have increased compared to the previous situation.

Considering the size of our samples, the magnetization switching occurs by a nucleation-propagation process and the stray field may play a strong part in the position of the nucleation point. These observations lead us to assume a large role of the stray field in the STT-driven switching processes.

In the fourth chapter, we use the micromagnetic code FASTMAG in order to differentiate the contributions of the stray field and the field-like torque on the switching processes. This finite difference code is developed by Vitaliy Lomakin's group in UCSD. A magnetic tunnel junction was simulated using material parameters close to our samples'. Two geometries are studied, one fully perpendicular, the second with a tilt in the anisotropy of the free layer. We modeled field –driven and STT-driven switchings using LLGS, using the same assumptions as in our model for

the spin transfer torques expressions. The energy barriers of the transitions were simulated using the "Nudged Elastic Band" method.

The results of the simulations show the importance of the inhomogeneity of the stray field on the nucleation center position, especially for the broken symmetry simulation and for the STT-driven ones. The symmetry breaking leads to a reduction of 50% of the width of the field hysteresis loops, but does not change the energy barrier of the structure. For the reference layer in the antiferromagnetic configuration, the nucleation occurs at the center of the junction for one transition and at the edge for the other. Moreover, despite the assumption of the independence of the spin transfer torque coefficient on the transition, the switching voltage slope differs from one transition to the other. This implies a difference in spin transfer torque efficiency linked to the initial volume of magnetization nucleated at the onset of the switching. Finally, when the reference layer is in a ferromagnetic configuration, the hysteresis loop width decreases and the nucleation points are at the edge of the junction for the two transitions. The energy barrier decreases as well, which is opposite to the effect observed experimentally. This may be the result of the non-inclusion of the field-like torque in the simulation.

Our work clearly highlighted the importance of the inhomogeneity of the stray field on the free layer. It induces a difference in field and STT-driven magnetization switching processes as a function of the transition, which is observed in the difference in switching voltage and thermal stability of the transition. The field-like torque may also play a part in the STT-driven switching. In order to characterize the effects of the spin transfer torque we are studying with thermal FMR and STT FMR cylindrical tunnel junctions.

# Appendix I

## Free electron approximation to the conduction electron

This model did not account for the difference in efficiency of the tunneling of the majority spin-electrons compared to the minority spin-electrons. In consequence, Stearn [37] proposed to take into account only the itinerant electrons density of states to compute the electrode polarization. The transmission probability depends on the effective mass of the electrons, which in turn hinges on the electronic band of the electron. In his model, the conductivity comes essentially from the most dispersive bands (s-like electrons) whereas the localized electrons (d-like) have a larger effective mass and decay faster in the barrier. At the Fermi level, the electronic bands depend on the spin-electrons considered. The majority spin-electrons have only dispersive bands, whereas the minority spin electrons have both dispersive and localized bands. In this case, the spin polarization of the ferromagnet depends on the wave vector ($k^\sigma, \sigma = \pm \uparrow, \downarrow$) at the Fermi level of the dispersive bands. And the polarization of the ferromagnetic electrode becomes:

$$P = \frac{k^\uparrow - k^\downarrow}{k^\uparrow + k^\downarrow} \tag{V.5}$$

## Conductance calculation in TMR according to Slonczewski:

In the chosen approximation, the longitudinal Hamiltonian of one electron is:

$$\mathcal{H}_x = -\frac{1}{2}\left(\frac{d}{dx}\right)^2 + U(x) - \boldsymbol{h}(x)\cdot\boldsymbol{\sigma} \tag{V.1}$$

with the first term of the R.H.S of the equation due to the kinetic energy, the second term is the potential of the system, and the last term the internal exchange energy, with $\boldsymbol{\sigma}$ the conventional Pauli spin operator, and $-\boldsymbol{h}(x)$ the molecular field. In the model, the potential is zero outside of the barrier and has a constant value $U_0$ in the barrier. Both ferromagnets have a molecular field of same norm $h_0$ but different direction with an angle $\theta$ between. By definition no field exists in the barrier. Inside the ferromagnets, the energy of one electron is:

$$\mathcal{E}_x = \frac{1}{2}k_\sigma^2 - \sigma h_0, \quad \sigma = \pm\uparrow,\downarrow \tag{V.2}$$

with $k_\sigma$ the electron momentum.

Inside the barrier the energy of one electron becomes:

$$\mathcal{E}_x = \frac{1}{2}\kappa^2 + U_0, \quad \sigma = \pm\uparrow,\downarrow \tag{V.3}$$

with $i\kappa$ an imaginary electron momentum, which correspond to the decay constant of the wave function in the barrier. It expression depends on the potential barrier height,

$$\kappa = \sqrt{(2m/\hbar)(U_0 - E_F)} \tag{V.4}$$

His approach is to take a large but finite value of the barrier thickness, d, and evaluate the areal charge current density and the spin current density using stationary wave functions for times close to zero. This condition ensures the constancy of the molecular fields. In the first ferromagnet, ($z \leq 0$):

$$\psi_{\uparrow\downarrow} = k_\uparrow^{-1/2} e^{ik_\uparrow x} + R_\uparrow e^{-ik_\uparrow x} \tag{V.5}$$

and

$$\psi_{\downarrow\uparrow} = R_\downarrow e^{-ik_\downarrow x} \tag{V.6}$$

In the barrier ($0 \leq x \leq d$):

$$\psi_{\sigma 2} = A_\sigma e^{-\kappa x} + B_\sigma e^{\kappa x}, \quad \sigma = \pm\uparrow,\downarrow \tag{V.7}$$

And in the second ferromagnet, ($d \leq x$) we only write the transmitted wave. Its referential is along the direction of its molecular field.

$$\psi'_{\sigma 3} = C_\sigma e^{ik_\sigma (x-d)}, \quad \sigma = \pm\uparrow,\downarrow \tag{V.8}$$

The eight unknown values, $R_\sigma$ $A_\sigma$, $B_\sigma$ and $C_\sigma$ are determined matching the spin waves and their derivative at the interface with the barrier. Note that there is a change of quantization axis

at $x = d$, and $\psi_{\sigma 2}$ has to be rewritten accordingly.

From this calculation, the spin transmissivity through the barrier is expressed, and the expression of the total charge and the spin current are not depending on the barrier thickness.

To compute the tunneling conductance, Slonczewski consider that for a small external field, and in the limit of small barrier factor, only the electrons with E_x in as small distribution around the fermi energy $E_F$ carry most of the current, thus we replace $\kappa_\sigma(E_x)$ and $k_\sigma(E_x)$ by $\kappa_\sigma(E_F)$ and $k_\sigma(E_F)$. And the conductance of the system is:

$$G = \frac{e^2}{8\pi^2\hbar}\frac{\kappa T_p}{d} \tag{V.9}$$

with $T_p$ the conventional particle transmissivity.

## Spin current density

Spin current density tensor is given by the outer product of the average electron velocity and the spin density:

$$\boldsymbol{I_S} = \frac{\hbar^2}{2m} Im(\psi^* \boldsymbol{\sigma} \otimes \boldsymbol{\nabla}\psi) \tag{V.10}$$

For a plane wave function:

$$\psi = \frac{e^{ikx}}{\sqrt{V}}(a|\uparrow\rangle + b|\downarrow\rangle \tag{V.11}$$

with $\mathcal{V}$ the normalized volume. We consider a spin-polarized current along the x axis, and the corresponding expressions of the spin density current are expressed as:

$$I_{s_{zx}} = \frac{\hbar^2 k}{2m\mathcal{V}} 2Re(ab^* \tag{V.12}$$

$$I_{s_{zy}} = \frac{\hbar^2 k}{2m\mathcal{V}} 2Im(ab^* \tag{V.13}$$

$$I_{s_{zz}} = \frac{\hbar^2 k}{2m\mathcal{V}} 2(|a|^2 - |b|^2) \tag{V.14}$$

To verify the conservation of the angular momentum, the spin transfer torque is considered as the net flux of non-equilibrium spin current through the surface of a given volume, which corresponds to a time rate of angular momentum variation.

## Spin filtering

To consider the spin filtering, we model the behavior of a single election with its wave vector along the $x$ axis and its spin direction is in the pale $z-x$. It forms an angle $\theta$ with the $z$ direction. The electron passes through a thin ferromagnetic layer with a magnetization along the $z$ axis. As in the TMR model, we assume that no spin flip is allowed in the layer. The spin filtering affects differently the amplitude of the transmission ($t_\sigma$, $\sigma = \pm 1$) and the reflection ($r_\sigma$, $\sigma = \pm 1$) of the scattering spin wave function of up and down electrons.

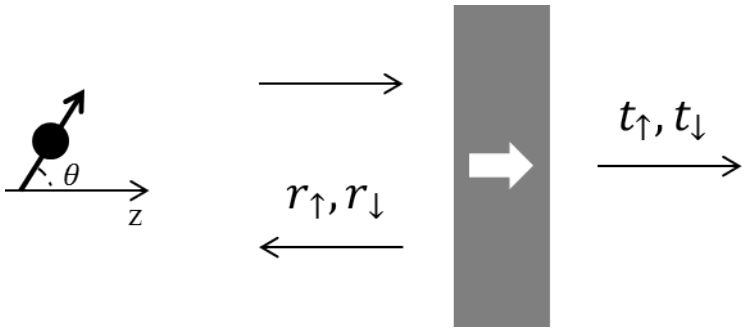


*Figure V.1: schematic of the transmission / reflexion of the electron spin waves in a ferromagnetic thin film.*

To consider the spin filtering, we model the behavior of a single election with its wave vector along the x axis and its spin direction is in the pale $z-x$. It forms an angle $\theta$ with the $z$ direction. The electron passes through a thin ferromagnetic layer with a magnetization along the $z$ axis . The spin filtering affects differently the amplitude of the transmission and the reflection of up and down electrons. As in the TMR model, we assume that no spin flip is allowed in the layer and we write the incident part of the wave function:

$$\psi_{in} = \frac{e^{ikx}}{\sqrt{V}}(cos(\theta/2)|\uparrow\rangle + sin(\theta/2)|\downarrow\rangle) \tag{V.15}$$

And the transmitted and reflected parts of the scattering wave function:

$$\psi_{tr} = \frac{e^{ikx}}{\sqrt{V}}(t_\uparrow cos(\theta/2)|\uparrow\rangle + t_\downarrow sin(\theta/2)|\downarrow\rangle) \tag{V.16}$$

$$\psi_{re} = \frac{e^{ikx}}{\sqrt{V}}(r_{\uparrow}cos(\theta/2)|\uparrow\rangle + r_{\downarrow}sin(\theta/2)|\downarrow\rangle) \tag{V.17}$$

And the spin currents are:

$$\boldsymbol{I_{s_{in}}} = \frac{\hbar^2 k}{2mV}[sin(\theta)\mathbf{x} + cos(\theta)\mathbf{z}] \tag{V.18}$$

$$\boldsymbol{I_{s_{tr}}} = \frac{\hbar^2 k}{2mV}[sin(\theta)Re(t_{\uparrow}t_{\downarrow}^*)\mathbf{x} + sin(\theta)Im(t_{\uparrow}t_{\downarrow}^*)\mathbf{y} + (|t_{\uparrow}|^2 cos(\theta/2)^2 - |t_{\downarrow}|^2 sin(\theta/2)^2)\mathbf{z}] \tag{V.19}$$

$$\boldsymbol{I_{s_{re}}} = -\frac{\hbar^2 k}{2mV}[sin(\theta)Re(r_{\uparrow}r_{\downarrow}^*)\mathbf{x} + sin(\theta)Im(r_{\uparrow}r_{\downarrow}^*)\mathbf{y} + (|r_{\uparrow}|^2 cos(\theta/2)^2 - |r_{\downarrow}|^2 sin(\theta/2)^2)\mathbf{z}] \tag{V.20}$$

By expressing the components of the spin density current in our model $\boldsymbol{I_{s_{in}}}$,$\boldsymbol{I_{s_{tr}}}$, and $\boldsymbol{I_{s_{re}}}$, it appears that the spin current density is not conserved. The spin transfer torque on a surface A :

$$\boldsymbol{\Gamma_{ST}} = A\mathbf{x} \cdot (\boldsymbol{I_{s_{in}}} - \boldsymbol{I_{s_{tr}}} + \boldsymbol{I_{s_{re}}} \tag{V.21}$$

$$\boldsymbol{\Gamma_{ST}} = \frac{A\hbar^2 k}{2mV} sin(\theta)\left(\left(1 - Re(t_{\uparrow}t_{\downarrow}^* + r_{\uparrow}r_{\downarrow}^*)\right)\mathbf{x} + Im(t_{\uparrow}t_{\downarrow}^* + r_{\uparrow}r_{\downarrow}^*\mathbf{y})\right) \tag{V.22}$$

## Spin accumulation

To consider the spin accumulation, we take again the behavior of a single election with its wave vector along the $x$ axis and its spin direction is in the pale $z - x$. It forms an angle $\theta$ with the $z$ direction.

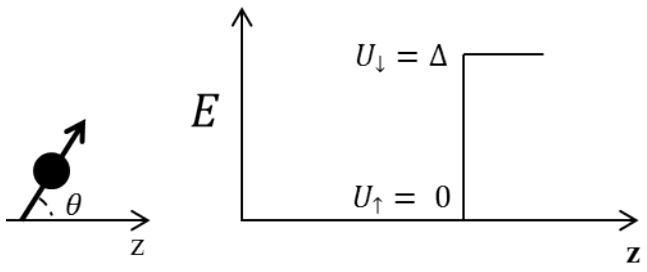


*Figure V.2: schematic of the energy barrier at the interface ferromagnet/insulator.*

The electron passes through a thin ferromagnetic layer with a magnetization along the z axis . the incident wave function has the same shape as previously:

$$\psi_{in} = \frac{e^{ikx}}{\sqrt{V}}(cos(\theta/2)|\uparrow\rangle + sin(\theta/2)|\downarrow\rangle) \tag{V.23}$$

Considering an electron energy $E = \frac{\hbar^2 k^2}{2m}$ and that the scattering at the interface shift the down electron to a potential $\Delta$, whereas the up electron have a zero potential. We have $E > \Delta$.

By matching wave function and their derivative at the interface:

$$\psi_{tr} = \frac{e^{ik_\uparrow x}}{\sqrt{V}}(cos(\theta/2)|\uparrow\rangle + \frac{e^{ik_\downarrow x}}{\sqrt{V}}sin(\theta/2)|\downarrow\rangle) \tag{V.24}$$

$$\psi_{re} = \frac{e^{-ikx}}{\sqrt{V}}\frac{k-k_\downarrow}{k+k_\downarrow}sin(\theta/2)|\downarrow\rangle) \tag{V.25}$$

with $k = k_\uparrow$ and $k_\downarrow = \frac{(2m(E-\Delta))^{1/2}}{\hbar} < k$

And the spin currents are:

$$\boldsymbol{I_{s_{in}}} = \frac{\hbar^2 k}{2mV}[sin(\theta)\mathbf{x} + cos(\theta)\mathbf{z}] \tag{V.26}$$

$$\begin{aligned} I_{s_{tr}} = &\frac{\hbar^2 k}{2mV}sin(\theta)\frac{2kk_\downarrow}{k+k_\downarrow}\,(cos[(k_\uparrow + k_\downarrow)x]\mathbf{x} + sin[(k_\uparrow + k_\downarrow)x]\mathbf{y}) \\ &+ \frac{\hbar^2 k_\downarrow}{2mV}\left(cos(\theta/2)^2 - \left(\frac{2k}{k+k_\downarrow}\right)^2 sin(\theta/2)^2\right)\mathbf{z} \end{aligned} \tag{V.27}$$

Due to the precession of the spin around the z position, the electron waves are approximately collinear with the magnetization direction in the ferromagnet. This means that the entire incident transverse spin current is absorbed at the interface. The spin transfer torque equation becomes:

$$\boldsymbol{\Gamma_{ST}} = Ax \cdot (\boldsymbol{I_{s_{in}}} - \boldsymbol{I_{s_{tr}}} + \boldsymbol{I_{s_{re}}}) \approx Ax \cdot \boldsymbol{I_{s_{in_\perp}}} \tag{V.28}$$

Comparing to the previous model, the dephasing at the interface leads to $\langle Re(t_\uparrow t_\downarrow^*)\rangle = \langle Im(t_\uparrow t_\downarrow^*)\rangle = \langle Im(r_\uparrow r_\downarrow^*)\rangle = 0$ and in a certain approximation $\langle Re(r_\uparrow r_\downarrow^*)\rangle \approx 0$.

$$\boldsymbol{\Gamma_{ST}} \approx \frac{A\hbar^2 k}{2mV}sin(\theta)\mathbf{x} \tag{V.29}$$

# Appendix II

## *Switching voltage in pMTJs*

For all geometries, the LLGS equation with the magnetization reduced to the unity sphere can be expressed as equation (VI.1), using its expression as function of the voltage. We chose to neglect the field-liKe torque in this model.

$$\frac{d\mathbf{m}}{dt} = -\gamma_0 \mathbf{m} \times \boldsymbol{H}_{eff} + \alpha \mathbf{m} \times \frac{d\mathbf{m}}{dt} + \gamma_0 a_V V \mathbf{m} \times (\mathbf{m} \times \mathbf{p}) \tag{VI.1}$$

This differential equation can be written in the spherical coordinates as:

$$\frac{d\mathbf{m}}{dt} = \gamma_0 H_{eff} \boldsymbol{e_\varphi} + \alpha \boldsymbol{e_r} \times \frac{d\mathbf{m}}{dt} + \gamma_0 a_V V sin(\theta) \boldsymbol{e_\theta} \tag{VI.2}$$

where $\boldsymbol{H}_{eff} = H_{eff}\boldsymbol{e}_\theta$, $H_{eff}$ espression depends on the geometry, $\mathbf{p}$ is out-of-plane and $\frac{d\mathbf{m}}{dt} = \dot{\theta}\boldsymbol{e}_\theta + sin(\theta)\dot{\varphi}\boldsymbol{e}_\varphi$ We obtain:

$$\dot{\theta}\boldsymbol{e}_\theta + sin(\theta)\dot{\varphi}\boldsymbol{e}_\varphi = (\gamma_0 a_V V - \alpha\dot{\varphi}) sin(\theta \boldsymbol{e}_\theta + (\gamma_0 H_{eff} + \alpha\dot{\theta})\boldsymbol{e}_\varphi$$

That gives the following system for all pMTJs :

$$\begin{cases} \dot{\theta} &= (\gamma_0 a_V V - \alpha\dot{\varphi}) \sin(\theta) \\ \sin(\theta)\dot{\varphi} &= \gamma_0 H_{eff} + \alpha\dot{\theta} \end{cases} \tag{VI.3}$$

## *First order anisotropy*

$$E_{tot} = -\left(K_{1_{ref}} - \frac{\mu_0 M_{S_{ref}}^2}{2}\right)\cos^2(\theta) = -K_{eff_{ref}}\cos^2(\theta) \tag{VI.4}$$

The equilibrium states $\theta_{eq}$ of the energy density function are found by solving $\frac{\partial E_{tot}}{\partial \theta} = 0$, for:

$$\frac{\partial E_{tot}}{\partial \theta} = -2K_{eff_{ref}}\cos(\theta)\sin(\theta) \tag{VI.5}$$

Thus $\theta_{eq} = 0[\frac{\pi}{2}]$ We then look at the synamical stability in the $\boldsymbol{H}_{eff}$ expression:

$$\boldsymbol{H}_{eff} = -\frac{1}{\mu_0 M_{S_{ref}}}\mathbf{grad}_{r,\theta,\varphi} E_{tot}$$

Thus

$$H_{eff} = \frac{2K_{eff_{ref}}}{\mu_0 M_{S_{ref}}} \sin(\theta)\cos(\theta)$$

and the system eq. (VI.3) becomes:

$$\begin{cases} \dot{\theta} & = & (\gamma_0 a_V V - \alpha\dot{\varphi})\sin(\theta) \\ \sin(\theta)\dot{\varphi} & = & -\frac{2K_{eff_{ref}}\gamma_0}{\mu_0 M_{S_{ref}}}\sin(\theta)\cos(\theta) + \alpha\dot{\theta} \end{cases} \tag{VI.6}$$

By replacing $\sin(\theta)\dot{\varphi}$ from the second line into the first, we have:

$$\dot{\theta} = \gamma_0 a_V V \sin(\theta) - \alpha\left(\frac{2K_{eff_{ref}}\gamma_0}{\mu_0 M_{S_{ref}}}\sin(\theta)\cos(\theta) + \alpha\dot{\theta}\right)$$

Which can be factorized to:

$$(1+\alpha^2)\dot{\theta} = \gamma_0 \sin(\theta)\left(a_V V - \alpha\frac{2K_{eff_{ref}}}{\mu_0 M_{S_{ref}}}\cos(\theta)\right)$$

For $\theta = 0$, either $\sin(\theta) = 0$ or $a_V V - \alpha\frac{2K_{eff_{ref}}}{\mu_0 M_{S_{ref}}} = 0$. The second expression allows us to express the switching voltage:

$$V_{sw_{ref}} = \frac{\alpha}{a}\frac{2}{\mu_0 M_{S_{ref}}} K_{eff_{ref}} \tag{VI.7}$$

### *Second order anisotropy*

When the second term of anisotropy is added in the total energy density function:

$$E_{tot} = -\left(K_1 - \frac{\mu_0 M_S^2}{2}\right)\cos^2(\theta) - K_2\cos^4(\theta) = -K_{eff}\cos^2(\theta) - K_2\cos^4(\theta) \tag{VI.8}$$

The equilibrium state are found by solving $\frac{\partial E_{tot}}{\partial\theta} = 0$ for:

$$\frac{\partial E_{tot}}{\partial\theta} = 2(K_{eff} + 2K_2\cos^2(\theta))\cos(\theta)\sin(\theta) \tag{VI.9}$$

From the previous equation, we obtain equilibrium states for the solving the following expressions:

$$K_{eff} + 2K_2\cos^2(\theta) = 0 \;\; or \;\; \cos(\theta_{eq}) = 0 \;\; or \;\; \sin(\theta_{eq}) = 0$$

On the one hand we find again $\theta_{eq} = 0[\frac{\pi}{2}]$ and on the other hand, an additional equilibrium state exists if $|K_2| > \frac{K_{eff}}{2}$, $\cos(\theta_{eq}) = \sqrt{\frac{K_{eff}}{2|K_2|}}$

In order to find the switching voltage expression, we solve:

$$\boldsymbol{H}_{eff} = -\frac{1}{\mu_0 M_{S_{ref}}}\mathbf{grad}_{r,\theta,\varphi} E_{tot}$$

The system eq. (VI.3) becomes in that case:

$$\begin{cases} \dot{\theta} &= (\gamma_0 a_V V - \alpha\dot{\varphi})\sin(\theta) \\ \sin(\theta)\dot{\varphi} &= -\frac{2\gamma_0}{\mu_0 M_{S_{ref}}}(K_{eff} + 2K_2\cos^2(\theta))\sin(\theta)\cos(\theta) + \alpha\dot{\theta} \end{cases} \tag{VI.10}$$

For $\theta = 0$, the system is trivial, and we discard this solution to focus on the condition needed to obtain a steady state precession. Due to the cylindrical symmetry around the out-of-plane direction, the precessional state can only be along the z axis, implying $\dot{\theta} = 0$. For $\theta \neq 0$:

$$\begin{cases} \dot{\varphi} &= \frac{\gamma_0 a_V V}{\alpha} \\ \dot{\varphi} &= -\frac{2\gamma_0}{\mu_0 M_{S_{ref}}}(K_{eff} + 2K_2\cos^2(\theta))\cos(\theta) \end{cases} \tag{VI.11}$$

This system is bounded. The frequency of precession increases linearly with the voltage, as well as the angle of the magnetization. The switching occurs when the magnetization reaches the extrema of the second line of the system.Considering the that the extrema of this term are solution of $(-6K_2\cos^2(\theta) + K_{eff})\sin(\theta) = 0$, the limit angles are $\theta_{lim} = 0[\pi]$ or $\cos(\theta_{eq}) = \sqrt{\frac{K_{eff}}{6|K_2|}}$. It means that $\theta_{lim} = 0[\pi]$ is both a static stable state and a dynamic stable state. The system can be rewritten to express the voltage expression as a function of the angle:

$$\frac{\gamma_0 a_V V}{\alpha} = \frac{2\gamma_0}{\mu_0 M_S}(K_{eff} + 2K_2\cos^2(\theta))\cos(\theta)$$

Thus, the switching voltage is given by:

$$V_{sw} = \frac{\alpha}{a}\frac{4}{3\mu_0 M_S}K_{eff}\sqrt{\frac{K_{eff}}{-6K_2}}$$

In the case of $|K_2| < \frac{K_{eff}}{2}$, the only stable state is $\theta_{eq} = 0[\frac{\pi}{2}]$. By mimickiing the reference geometry case, we obtain:

$$(1+\alpha^2)\dot{\theta} = \gamma_0\sin(\theta)(a_V V - \alpha\frac{2}{\mu_0 M_S}(K_{eff} + 2K_2\cos^2(\theta))\cos(\theta))$$

In the stable state, $\dot{\theta} = 0$ , and $a_V V - \alpha\frac{2}{\mu_0 M_S}(K_{eff} + 2K_2\cos^2(\theta)) = 0$, thus :

$$V_{sw} = \frac{\alpha}{a}\frac{2}{\mu_0 M_S}(K_{eff} + 2K_2)$$

### *Conditions for $\frac{V_{sw}}{V_{sw_{ref}}} < 1$:*

In order to compare the relative efficiency of the switching voltage with and without second order anisotropy coefficient, we want to extract the condititions on $\frac{|K_2|}{K_{eff}}$ for which $\frac{V_{sw}}{V_{sw_{ref}}} < 1$ is verified, at constant energy barrier and for the same $M_S$ value. The general equation is:

$$\frac{V_{sw}}{V_{sw_{ref}}} = \frac{2}{3\sqrt{6}}\frac{M_{S_{ref}}}{M_S}\frac{K_{eff}}{K_{eff_{ref}}}\sqrt{\frac{|K_2|}{K_{eff}}} < 1 \tag{VI.12}$$

We study two cases, as a function of the switching voltage expression.

- For $\frac{|K_2|}{K_{eff_{cone}}} > \frac{1}{2}$, the ratio $\frac{V_{sw}}{V_{sw_{ref}}}$ becomes:

$$\frac{V_{sw}}{V_{sw_{ref}}} = \frac{8}{3\sqrt{6}} \frac{M_{S_{ref}}}{M_S} \sqrt{\frac{|K_2|}{K_{eff}}}$$

Which means that:

$$\frac{8}{3\sqrt{6}} \frac{M_{S_{ref}}}{M_S} \sqrt{\frac{|K_2|}{K_{eff}}} < 1$$

With no conditions on the saturation magnetization, we have:

$$\frac{M_{S_{ref}}}{M_S} < \frac{3\sqrt{6}}{8} \sqrt{\frac{K_{eff}}{|K_2|}}$$

And with $\frac{|K_2|}{K_{eff_{cone}}} > \frac{1}{2}$ the condition becomes $\frac{M_{S_{ref}}}{M_S} < \frac{3\sqrt{3}}{4}$ that is verified by $M_{S_{ref}} = M_S$, thus:

$$\frac{V_{sw}}{V_{sw_{ref}}} < 1 \leftrightarrow \frac{8}{3\sqrt{6}} \sqrt{\frac{|K_2|}{K_{eff}}} < 1$$

which is verified for :

$$\frac{1}{2} < \frac{|K_2|}{K_{eff}} < \frac{27}{32}$$

- For $\frac{1}{6} < \frac{|K_2|}{K_{eff_{cone}}} < \frac{1}{2}$, the ratio $\frac{V_{sw}}{V_{sw_{ref}}}$ becomes:

$$\frac{V_{sw}}{V_{sw_{ref}}} = \frac{2}{3\sqrt{6}} \frac{M_{S_{ref}}}{M_S} \frac{K_{eff}}{K_{eff} + K_2} \sqrt{\frac{|K_2|}{K_{eff}}}$$

Which means that:

$$\frac{M_{S_{ref}}}{M_S} < \frac{3\sqrt{6}}{2} \sqrt{\frac{K_{eff}}{|K_2|}} (1 - \frac{|K_2|}{K_{eff}})$$

This function is decreasing, and for $\frac{1}{6} < \frac{|K_2|}{K_{eff_{cone}}} < \frac{1}{2}$, the condition becomes $\frac{M_{S_{ref}}}{M_S} < \frac{3\sqrt{3}}{2}$, which is verified by $M_{S_{ref}} = M_S$. Thus, $\frac{V_{sw}}{V_{sw_{ref}}} < 1$ is verified for :

$$\frac{1}{2} < \frac{|K_6|}{K_{eff}} < \frac{1}{2}$$

# Appendix III

State diagram comparison for four MTJs of decreasing sizes with the reference layer in the SAF configuration (figure VII.3) and in the "No SAF" configuration (figure VII.4)

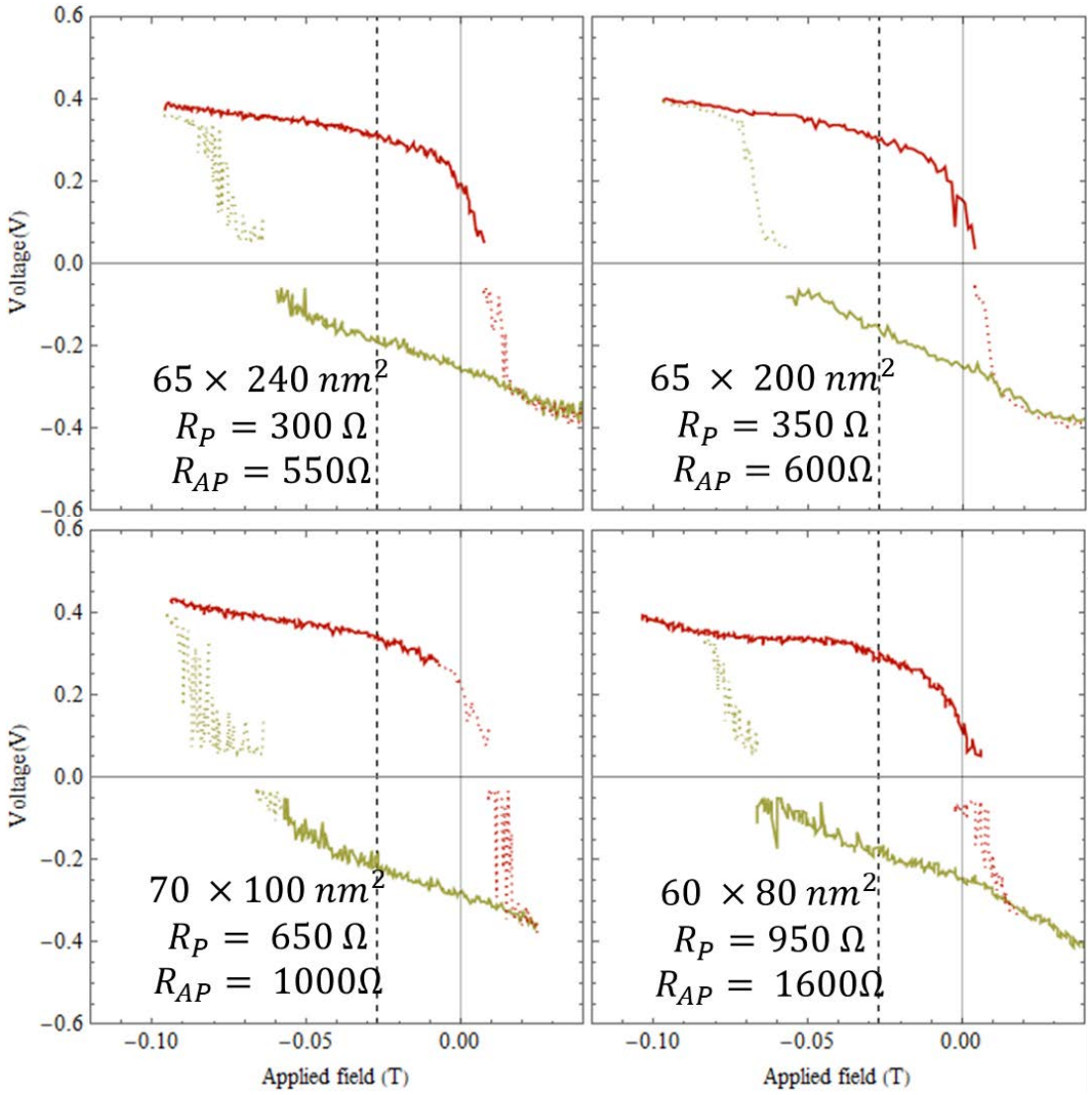


*Figure VII.3: Voltage - field state diagrams a room temperature for MTJs with the reference layer in the SAF configuration. The surface areas are of a)* $65 \times 240 nm^2$*, b)* $65 \times 200 nm^2$*, c)* $70 \times 100 nm^2$*, and d)* $60 \times 80 nm^2$

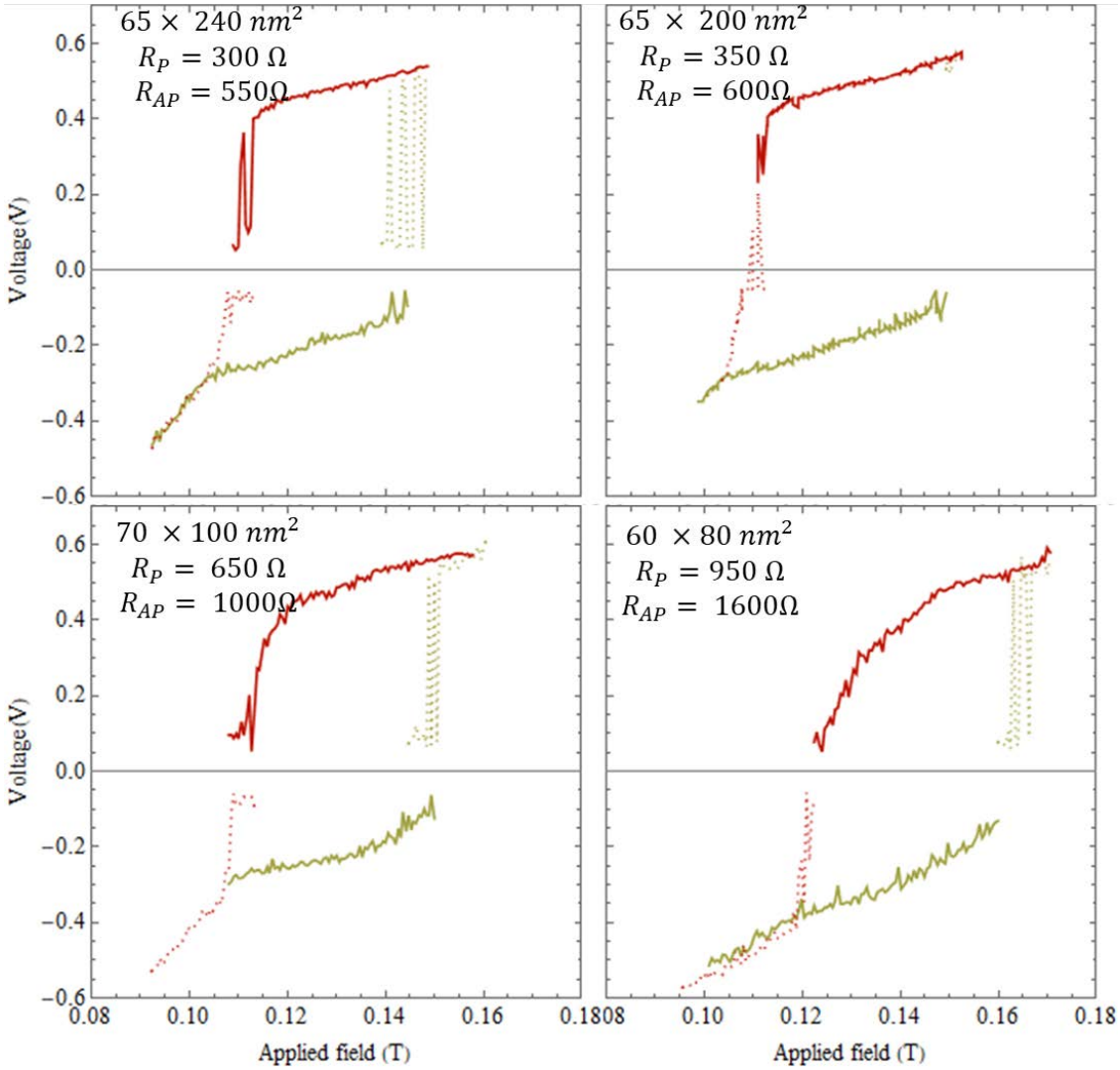


*Figure VII.4: Voltage - field state diagrams a room temperature for MTJs with the reference layer in the "no SAF" confugration. The surface areas are of a)* $65 \times 240nm^2$*, b)* $65 \times 200nm^2$*, c)* $70 \times 100nm^2$*, and d)* $60 \times 80nm^2$

# Bibliography


[1] M. Julliere. Tunneling between ferromagnetic films. *Phys. Lett. A*, 54(3):225–226, 1975.

[2] T. Miyazaki and N. Tezuka. Giant magnetic tunneling effect in fe/al2o3/fe junction. *J. Magn. Magn. Mater.*, 139(3):L231–L234, 1995.

[3] A. Brataas, A.D. Kent, and H. Ohno. Current-induced torques in magnetic material. *Nat. Mater.*, 11:372–381, 2012.

[4] D.C. Worledge, G. Hu, D.W. Abraham, J.Z. Sun, P.L. Trouilloud, J. Nowak, S. Brown, M.C. Gaidis, E.J. O'Sullivan, and R.P. Robertazzi. Spin torque switching of perpendicular ta|cofeb|mgo-based magnetic tunnel junctions. *Appl. Phys. Lett.*, 98:022501, 2011.

[5] J.C. Slonczewski. Current-driven excitation of magnetic multilayers. *J. Magn. Magn. Mater.*, 159(1-2):L1–L7, 1996.

[6] L. Berger. Emission of spin waves by a magnetic multilayer traversed by a current. *Phys. Rev. B*, 54(13), 1996.

[7] M. Gajek, J.J. Nowak, J.Z. Sun, P.L. Trouilloud, E.J. O'Sullivan, D.W. Abraham, M.C. Gaidis, G. Hu, S. Brown, Y. Zhu, R.P. Robertazzi, W.J. Gallagher, and D.C. Worledge. Spin torque switching of 20nm magnetic tunnel junctions with perpendicular anisotropy. *Appl. Phys. Lett.*, 100:132408, 2012.

[8] S. Ikeda, J. Hayakawa, Y. Ashizawa, Y.M. Lee, K. Miura, H. Hasegawa, M. Tsunoda, F. Matsukura, and H. Ohno. Tunnel magnetoresistance of 604% at 300k by suppression of ta diffusion in cofeb/mgo/cofeb pseudo-spin-valves annealed at high temperature. *Appl. Phys. Lett.*, 93:082508, 2008.

[9] D.C. Worledge, G. Hu, D.W. Abraham, P.L. Trouilloud, and S. Brown. Development of perpendicularly magnetized ta|cofeb|mgo-based tunnel junctions at ibm. *J. Appl. Phys.*, 115:172601, 2013.

[10] S. Ikeda, K. Miura, H. Yamamoto, K. Mizunuma, H.D. Gan, M. Endo, S. Kanai, J. Hayakawa, F. Matsukura, and H. Ohno. A perpendicular-anisotropy cofeb–mgo magnetic tunnel junction. *Nat. Mater.*, 9(2804):721–724, 2010.

[11] J.J. Nowak, R.P. Robertazzi, J.Z. Sun, G. Hu, D.W. Abraham, P.L. Trouilloud, S. Brown, M.C. Gaidis, E.J. O'Sullivan, W.J. Gallagher, and D.C. Worledge. Demonstration of ultralow bit error rates for spin-torque magnetic random-access memory with perpendicular magnetic anisotropy. *IEEE Magn. Lett.*, 2(3000204), 2011.

[12] J.Z. Sun, S.L. Brown, W. Chen, E.A. Delenia, M.C. Gaidis, J. Harms, G. Hu, X. Jiang, R. Kilaru, W. Kula, G. Lauer, L.Q. Liu, S. Murthy, J. Nowak, E.J. O'Sullivan, R.P. Robertazzi S. S. P. Parkin, P.M. Rice, G. Sandhu, T. Topuria, and D.C. Worledge. Spin-torque switching efficiency in cofeb-mgo based tunnel junctions. *Phys. Rev. B*, 88(104426), 2013.

[13] D.C. Ralph and M.D Stiles. Spin transfer torques. *J. Magn. Magn. Mater.*, 320:1190–1216, 2008.

[14] S.S.P. Parkin, M. Hayashi, and L.Thomas. Magnetic domain-wall racetrack memory. *Science*, 320(5873):190–194, 2008.

[15] B. Behin-Aein, D. Datta, S. Salahuddin, and S. Datta. Proposal for an all-spin logic device with built-in memory. *Nat. Nano.*, 5:266–270, 2010.

[16] T.J. Silva and W.H. Rippard. Developments in nano-oscillators based upon spin transfer point-contact devices. *J. Magn. Magn. Mater.*, 320:1260–1271, 2008.

[17] K. Kudo, T. Nagasawa, R. Sato, and K. Mizushima. Measurement of nonlinear frequency shift coefficient in spin-torque oscillators based on mgo tunnel junctions. *Appl. Phys. Lett.*, 95:022507, 2009.

[18] X. Cheng, J.A. Katine, G.E. Rowlands, and I.N. Krivorotov. Nonlinear ferromagnetic resonance induced by spin torque in nanoscale magnetic tunnel junctions. *Appl. Phys. Lett.*, 103(082402), 2013.

[19] L. Berger. Low-field magnetoresistance and domain drag in ferromagnets. *J. Appl. Phys.*, 49(3):2516–2161, 1978.

[20] M. Yamanouchi, D. Chiba, F. Matsukura, and H. Ohno. Current-induced domain-wall switching in a ferromagnetic semiconductor structure. *Nature*, 428:539–542, 2004.

[21] M. Kläui et al. Controlled and reproducible domain wall displacement by current pulses injected into ferromagnetic ring structures. *Phys. Rev. Lett.*, 94:106601, 2005.

[22] N. Vernier, D.A. Allwood, D. Atkinson, M.D. Cooke, and R.P. Cowburn. Domain wall propagation in magnetic nanowires by spin-polarized current injection. *Europhys. Lett.*, 65(4):526–532, 2004.

[23] A. Thiaville, Y. Nakatani, and J. Miltatand Y. Suzuki. Micromagnetic understanding of current-driven domain wall motion in patterned nanowires. *Europhys. Lett.*, 69:990–996, 2005.

[24] G.S.D. Beach, M. Tsoi, and J.L. Erkine. Current-induced domain wall motion. *J. Magn. Magn. Mater.*, 320(7):1272–1281, 2008.

[25] J.-C. Lee et al. Universality classes of magnetic domain wall motion. *Phys. Rev. Lett.*, 107:067201, 2011.

[26] I.M. Miron, G. Gaudin, S. Auffret, B. Rodmacq, A. Schuhl, S. Pizzini, J. Vogel, and P. Gambardella. Current-driven spin torque induced by the rashba effect in a ferromagnetic metal layer. *Nat. Mater.*, 9(3):230–234, 2010.

[27] A. Hoffmann. Spin hall effects in metals. *IEEE Trans. Magn.*, 49(10):5172–5193, 2013.

[28] J.C. Rojas Sanchez, L. Vila, G. Desfonds, S. Gambarelli, J.P. Attane, J.M. De Teresa, C. Magen, and A. Fert. Spin-to-charge conversion using rashba coupling at the interface between non-magnetic materials. *Nat. Comm.*, 4(3944), 2013.

[29] K.-S. Lee, S.-W. Lee, B.-C. Min, and K.-J. Lee. Threshold current for switching of a perpendicular magnetic layer induced by spin hall effect. *Appl. Phys. Lett.*, 102:112410, 2013.

[30] Y.-C. Lau, D. Betto, K. Rode, J.M.D. Coey, and P. Stamenov. Spin-orbit torque switching without external field with a ferromagnetic exchange-biased coupling layer. *Nat. Tech.*, 11:758–762, 2016.

[31] A. van den Brink, G. Vermijs, A. Solignac, J. Koo, J.T. Kohlhepp, H.J.M. Swagten, and B. Koopmans. Field-free magnetization reversal by spin-hall effect and exchange bias. *Nat. Comm.*, 7(10854), 2016.

[32] C. Kittel. *Introduction to Solid State Physics (Seventh ed.).* Wiley, 1996.

[33] A.P. Sutton. *Electronic Structure of Materials.* Clarendon Press, 1993.

[34] http://www.everspin.com/.

[35] R. Meservey and P.M. Tedrow. Spin-polarized electron tunneling. *Physics Reports*, 238(4):173–243, 1994.

[36] E.Y. Tsymbal, O.N. Mryasov, and P.R. LeClair. Spin-dependent tunneling in magnetic tunnel junctions. *Evgeny Tsymbal Publications*, 19, 2003.

[37] M.B. Stearns. Simple explanation of tunneling spin-polarization of fe, co, ni and its alloys. *J. Magn. Magn. Mater.*, 5(2):167–171, 1977.

[38] J.C. Slonczewski. Conductance and exchange coupling of two ferromagnets separated by a tunneling barrier. *Phys. Rev. B*, 39(10):6995–7002, 1989.

[39] J. Scola, H. Polovy, C. Fermon, M. Pannetier-Lecœur, G. Feng, K. Fahy, and J.M.D. Coey. Noise in mgo barrier magnetic tunnel junctions with cofeb electrodes: Influence of annealing temperature. *Appl. Phys. Lett.*, 90(252501), 2007.

[40] K. Oguz, P. Jivrajka, M. Venkatesan, G. Feng, and J.M.D. Coey. Magnetic dead layers in sputtered films. *J. Appl. Phys.*, 103(07B526), 2008.

[41] Y.M. Lee, J. Hayakawa, S. Ikeda, F. Matsukura, and H. Ohno. Effect of electrode composition on the tunnel magnetoresistance of pseudo-spin-valve magnetic tunnel junction with a mgo tunnel barrier. *Appl. Phys. Lett.*, 90(212507), 2007.

[42] Z.Diao, D. Apalkov, M. Pakala, Y. Ding, A. Panchula, and Y. Huai. Spin transfer switching and spin polarization in magnetic tunnel junctions with mgo and alox barriers. *Appl. Phys. Lett.*, 87:232502–232503, 2005.

[43] Y. Huai, F. Albert, P. Nguyen, M. Pakala, and T. Valet. Observation of spin-transfer switching in deep submicron-sized and lowresistance magnetic tunnel junctions. *Appl. Phys. Lett.*, 84(3118), 2004.

[44] K. Yagami, A.A. Tulapurkar, A. Fukushima, and Y. Suzuki. Low-current spin-transfer switching and its thermal durability in a low-saturation magnetization nanomagnets. *Appl. Phys. Lett.*, 85(5634), 2004.

[45] W.H. Butler, X.G. Zhang, T.C. Schulthess, and J.M. MacLaren. Spin-dependent tunneling conductance of fe|mgo|fe sandwiches. *Phys. Rev. B*, 63:054416, 2001.

[46] J. Mathon and A. Umerski. Theory of tunneling magnetoresistance of an epitaxial fe/mgo/fe(001) junction. *Phys. Rev. B*, 63(220403), 2001.

[47] S. Yuasa, T. Nagahama, A. Fukushima, Y. Suzuki, and K. Ando. Giant room temperature magnetoresistance in single-crystal fe/mgo/fe magnetic tunnel junctions. *Nat. Mat.*, 3:868–871, 2004.

[48] S.S.P. Parkin et al. Giant tunnelling magnetoresistance at room temperature with mgo (100) tunnel barriers. *Nat. Mat.*, 3:862–867, 2004.

[49] R. Shimabukuro, K. Nakamura, T. Akiyama, and T. Ito. Electric field effects on magnetocrystalline anisotropy in ferromagnetic fe monolayers. *Phys. E*, 42(4):1014–1017, 2010.

[50] H.X. Yang, M. Chshiev, B. Dieny, J.H. Lee, A. Manchon, and K.H. Shin. First-principles investigation of the very large perpendicular magnetic anisotropy at fe|mgo and co|mgo interfaces. *Phys. Rev. B*, 84(054401), 2011.

[51] S. Cardoso, R. Ferreira, P.P. Freitas, M. MacKenzie, J. Chapman, J.O. Ventura, J.B. Sousa, and U. Kreissig. Ferromagnetic coupling field reduction in cofeb tunnel junctions deposited by ion beam. *IEEE Trans. Magn.*, 40(4), 2004.

[52] S.Yuasa, T. Nagahama, A. Fukushima, Y. Suzuki, and K. Ando. Giant room-temperature magnetoresistance in single-crystal fe/mgo/fe magnetic tunnel junctions. *Nat. Mat.*, 3:868–871, 2004.

[53] K. Tsunekawa, D.D. Djayaprawira, S. Yuasa, M. Nagai, H. Maehara, S. Yamagata, E. Okada, N. Watanabe, Y. Suzuki, and K. Ando. Huge magnetoresistance and low junction resistance in magnetic tunnel junctions with crystalline mgo barrier. *IEEE Trans. Magn.*, 42(2), 2006.

[54] L.-X. Ye, C.-M. Lee, J.–W. Syu, Y.–R. Wang, K.-W. Lin, Y.-H. Chang, and T.-H. Wu. Effect of annealing and barrier thickness on mgobasedco/pt and co/pd multilayered perpendicular magnetic tunnel junctions. *IEEE Trans. Magn.*, 44(11), 2008.

[55] T. Niizeki, H. Kubota, Y. Ando, and T. Miyazaki. Nanofabrication of magnetic tunnel junctions by using electron beam lithography. *J. Magn. Magn. Mat.*, 3:272–276, 1947-1948.

[56] C. Mocuta, A. Barbier, A.V. Ramos, M.-J. Guittet, J.-B. Moussy, S. Stanescu, R. Mattana, C. Deranlot, and F. Petroff. Effect of optical lithography patterning on the crystalline structure of tunnel junctions. *Appl. Phys. Lett.*, 91(241917), 2007.

[57] E.M. Lifshitz 48. L.D. Landau. Theory of the dispersion of magnetic permeability in ferromagnetic bodies. *Phys. Z. Sowietunion*, 8:153–169, 1935.

[58] T.L. Gilbert. A lagrangian formulation of the gyromagnetic equation of the magnetic field. *Physical Review*, 100:1243, 1955.

[59] J.C. Slonczewski. Currents, torques, and polarization factors in magnetic tunnel junctions. *Phys. Rev. B*, 71:024411, 2005.

[60] J.C. Slonczewski. Currents and torques in metallic magnetic multilayers. *J. Magn. Magn. Mater.*, 247:324–338, 2002.

[61] Z. Li and S. Zhang. Magnetization dynamics with spin transfer torque. *Phys. Rev. B*, 68:024404, 2003.

[62] S.I. Kiselev, J.C. Sankey, I.N. Krivorotov, N.C. Emley, R.J. Schoelkopf, R.A. Buhrman, and D.C. Ralph. Microwave oscillations of a nanomagnet driven by a spin-polarized current. *Nature*, 425:380–383, 2003.

[63] W.H. Rippard, M.R. Pufall, S. Kaka, S.E. Russek, and T.J. Silva. Direct-current induced dynamics in co90fe10/ni80fe20 point contacts. *Phys. Rev. Lett.*, 92:027201, 2004.

[64] D. Kent, B. Özyilmaz, and E. del Barco. Spin-transfer-induced precessional magnetization reversal. *Appl. Phys. Lett.*, 84(3897), 2004.

[65] H. Liu, D. Bedau, J.Z. Sun, S. Mangin, E.E. Fullerton, J.A. Katine, and A.D. Kent. Dynamics of spin torque switching in all-perpendicular spin valve nanopillars. *J. Magn. Magn. Mater.*, 358-359:233–258, 2014.

[66] A. Zangwill and M.D. Stiles. Noncollinear spin transfer in co/cu/co multilayers. *J. Appl. Phys.*, 91(6812), 2002.

[67] J. Xiao, A. Zangwill, and M.D. Stiles. Boltzmann test of slonczewski's theory of spin-transfer torque. *Phys. Rev. B*, 70(172405), 2004.

[68] Y. Huai, F. Albert, P. Nguyen, M. Pakala, and T. Valet. Observation of spin transfer switching in deep submicron-sized and low-resistance magnetic tunnel junctions. *Appl. Phys. Lett.*, 84:3118–3120, 2004.

[69] Z. Diao et al. Spin transfer switching and spin polarization in magnetic tunnel junctions with mgo and alox barriers. *Appl. Phys. Lett.*, 87:232502–232503, 2005.

[70] K. Hitoshi et al. Evaluation of spin-transfer switching in cofeb/mgo/cofeb magnetic tunnel junctions. *Jpn. J. Appl. Phys.*, 44:L1237–L1240, 2005.

[71] H. Jun et al. Current-driven magnetization switching in cofeb/mgo/cofeb magnetic tunnel junctions. *Jpn. J. Appl. Phys.*, 44:L1267–L1270, 2005.

[72] S. Zhang, P.M. Levy, A.C. Marley, and S.S.P. Parkin. Quenching of magnetoresistence by hot electrons in magnetic tunnel junctions. *Phys. Rev. Lett*, 79(19), 1997.

[73] K. Carva and I. Turek. Landauer theory of ballistic torkances in non-collinear spin valves. *Phys. Rev. B*, 80:104432, 2009.

[74] J.C. Slonczewski and J.Z. Sun. Theory of voltage dirven current and torque in magnetic tunnel junctions. *J. Magn. Magn. Mater.*, 310:169–175, 2007.

[75] G.D. Fuchs, J.A. Katine, S.I. Kiselev, D. Mauri, K.S. Wooley, D.C. Ralph, and R.A. Buhrman. Spin torque, tunnel-current spin polarization, and magnetoresistance in mgo magnetic tunnel junctions. *Phys. Rev. Lett.*, 96:186603, 2006.

[76] J.C. Sankey, Y.-T. Cui, J.Z. Sun, J.C. Slonczewski, R.A. Buhrman, and D.C. Ralph. Measurement of the spin-transfer-torque vector in magnetic tunnel junctions. *Nat. Phys.*, 4:67–71, 2008.

[77] H. Kubota, A. Fukushima, K. Yakushiji, T. Nagahama, S. Yuasa, K. Ando, H. Maehara, Y.Nagamine, K. Tsunekawa, D.D. Djayaprawira, N. Watanabe, and Y.Suzuki. Quantitative measurement of voltage dependence of spin-transfer torque in mgo-based magnetic tunnel junctions. *Nat. Phys.*, 4:37–41, 2008.

[78] A.M. Deac, A. Fukushima, H. Kubota, H. Maehara, Y. Suzuki, S. Yuasa, Y. Nagamine, K. Tsunekawa, D.D. Djayaprawira, and N. Watanabe. Bias-driven high-power microwave emission from mgo-based tunnel magnetoresistance devices. *Nat. Phys.*, 4:803–809, 2008.

[79] S.-C. Oh, S.–Y. Park, A. Manchon, M. Chshiev, J.–H. Han, H.-W. Lee, J.–E. Lee, K.–T. Nam, Y.Jo, Y.-C. Kong, B. Dieny, and K.–J. Lee. Bias-voltage dependence of perpendicular spin-transfer torque in asymmetric mgo-based magnetic tunnel junctions. *Nat. Phys.*, 5:898–902, 2009.

[80] Y.-H. Tang, N. Kioussis, A. Kalitsov, W.H. Butler, and R. Car. Field-like spin torque in magnetic tunnel junctions. *Journal of Physics: Conference Series 200*, 06203, 2010.

[81] C. Wang, Y.-T. Cui, J.A. Katine, R.A. Buhrman, and D.C. Ralph. Time-resolved measurement of spin-transfer-driven ferromagnetic resonance and spin torque in magnetic tunnel junctions. *Nat. Phys.*, 7:496–501, 2011.

[82] T. Min, J.Z. Sun, R. Beach, D. Tang, and P.Wang. Back-hopping after spin torque transfer induced magnetization switching in magnetic tunneling junction cells. *J. Appl. Phys.*, 105:07D126, 2009.

[83] J.Z. Sun, M.C. Gaidis, G. Hu, E.J. O'Sullivan, S.L. Brown, J.J. Nowak, P.L. Trouilloud, and D.C. Worledge. High-bias backhopping in nanosecond time-domain spin-torque switches of mgo-based magnetic tunnel junctions. *J. Appl. Phys.*, 105:07D109, 2009.

[84] I. Theodonis, N. Kioussis, A. Kalitsov, M. Chshiev, and W.H. Butler. Anomalous bias dependence of spin torque in magnetic tunnel junctions. *Phys. Rev. Lett.*, 97:237205, 2006.

[85] J. Xiao, G.W. Bauer, and A. Brataas. Spin-transfer torque in magnetic tunnel junctions: Scattering theory. *Phys. Rev. B*, 77:224419, 2008.

[86] C. Wang, Y.-T. Cui, J.Z. Sun, J.A. Katine, R.A. Buhrman, and D.C. Ralph. Bias and angular dependence of spin-transfer torque in magnetic tunnel junctions. *Phys. Rev. B*, 79:224416, 2009.

[87] S. Petit, N. de Mestier, C. Baraduc, C. Thirion, Y. Liu, M. Li, P. Wang, and B. Dieny. In?uence of spin-transfer torque on thermally activated ferromagnetic resonance excitations in magnetic tunnel junctions. *Phys. Rev. B*, 78:184420, 2008.

[88] Z. Wen, H. Sukegawa, S. Kasai, M. Hayashi, S. Mitani, and K.Inomata. Magnetic tunnel junctions with perpendicular anisotropy using a co2feal full-heusler alloy. *Appl. Phys. Expr.*, 5(6), 2012.

[89] T. Scheike, H. Sukegawa, T. Furubayashi, Z. Wen, K. Inomata, and T. Ohkubo. Lattice-matched magnetic tunnel junctions using a heusler alloy co2feal and a cation-disorder spinel mg-al-o barrier. *Appl. Phys. Lett.*, 105(242407), 2014.

[90] R. Skomski, J. Zhou, R.D. Kirby, and D.J. Sellmyer. Micromagnetic energy barriers. *J. Appl. Phys.*, 99:08B906, 2006.

[91] G. Hu, T. Topuria, P.M. Rice, J. Jordan-Sweet, and D.C. Worledge. Optimization of tunneling magnetoresistance in perpendicular magnetic tunnel junctions with co|pd reference layers. *IEEE Magn. Lett.*, 4(3000104), 2013.

[92] E.P. Sajitha, J. Walowski, D. Watanabe, S. Mizukami, F. Wu, H. Naganuma, M. Oogane, Y. Ando, and T. Miyazaki. Magnetization dynamics in cofeb buffered perpendicularly magnetized co/pd multilayer. *IEEE Trans. Magn.*, 46(6), 2010.

[93] J.-H. Park, S. Ikeda, H. Yamamoto, H. Gan, K. Mizunuma, K. Miura, H. Hasegawa, J. Hayakawa, K. Ito, F. Matsukura, and H. Ohno. Perpendicular magnetic tunnel junctions with cofe/pd multilayer electrodes and an mgo barrier. *IEEE Trans. Magn.*, 45(10), 2009.

[94] J.W. Knepper and F.Y. Yang. Oscillatory interlayer coupling in co/pt multilayers with perpendicular anisotropy. *Phys. Rev. B*, 71(224403), 2005.

[95] R. Wu, C. Li, and A.J. Freeman. Structural electronic and magnetic properties of co/pd (111) and co/pt (111). *J. Magn. Magn. Mater.*, 99(13):71–80, 1991.

[96] D. Weller, Y. Wu, J. Stohr, M.G. Samant, B.D. Hermsmeier, and C. Chappert. Orbital magnetic moment of co in multilayers with perpendicular magnetic anisotropy. *Phys. Rev. B*, 49:12888–12896, 1994.

[97] M. Endo, S. Kanai, S.Ikeda, F. Matsukura, and H. Ohno. Electric field effects on thickness dependent magnetic anisotropy of sputtered mgo/co40fe40b20/ta structures. *Appl.Phys.Lett.*, 96:212503, 2010.

[98] D.C. Worledge. U.s. patent application us 20110303995 a1. 2010.

[99] N. Miyakawa, D.C Worledge, and K. Kita. Impact of ta diffusion on the perpendicular magnetic anisotropy of ta/cofeb/mgo. *IEEE Magn. Lett.*, 4, 2013.

[100] S. Peng, M. Wang, H. Yang, L. Zeng, J. Nan, J. Zhou, Y. Zhang, A. Hallal, M. Chshiev, K.L. Wang, Q. Zhang, and W. Zhao. Origin of interfacial perpendicular magnetic anisotropy in mgo/cofe/ metallic capping layer structure. *Nat. Sci. Rep.*, 5:18173, 2015.

[101] R. Shimabukuro, K. Nakamura, T. Akiyama, and T. Ito. Electric field effects on magneto crystalline anisotropy in ferromagnetic fe monolayers. *Physica E*, 42(4):1014–1017, 2010.

[102] J.Z. Sun, R.P. Robertazzi, J. Nowak, P.L. Trouilloud, G. Hu, D.W. Abraham, M.C. Gaidis, S.L. Brown, E.J. O'Sullivan, W.J. Gallagher, and D.C. Worledge. Effect of subvolume excitation and spin-torque efficiency on magnetic switching. *Phys. Rev. B*, 84(064413), 2011.

[103] J.Z. Suna, P.L. Trouilloud, M.J. Gajek, J. Nowak, R.P. Robertazzi, G. Hu, D.W. Abraham, M.C. Gaidis, S.L. Brown, E.J. O'Sullivan, W.J. Gallagher, and D.C. Worledge. Size dependence of spin-torque induced magnetic switching in cofeb-based perpendicular magnetization tunnel junctions. *J. Appl. Phys.*, 111(07C711), 2012.

[104] C.-Y. You and M.-H. Jung. Dependence of the switching current density on the junction sizes in spin transfer torque. *J. Appl. Phys.*, 113(073904), 2013.

[105] K. Bernert, V. Sluka, C. Fowley, J. Lindner, J. Fassbender, and A.M. Deac. Phase diagrams of mgo magnetic tunnel junctions including the perpendicular spin-transfer torque in different geometries. *Phys. Rev. B*, 89(134415), 2014.

[106] E.C. Stoner and E.P. Wohlfarth. A mechanism of magnetic hysteresis in heterogeneous alloys. *Philosophical Transactions of the Royal Society A: Physical, Mathematical and Engineering Sciences*, 240(826), 1948.

[107] J. Cucchiara, E.E. Fullerton, A.D. Kent, J.Z. Sun, Y. Henry, and S. Mangin. Current-induced magnetization reversal in terms of power dissipation. *Phys. Rev. B*, 84:100405(R), 2011.

[108] J.-E. Wegrowe and M.-C. Ciornei. Magnetization dynamics, gyromagnetic relation, and inertial effects. *Amer. Jour. Phys*, 80(607), 2012.

[109] C. Heiliger and M.D. Stiles. Ab initio studies of the spin-transfer torque in magnetic tunnel junctions. *Phys. Rev. Lett.*, 100(186805), 2008.

[110] J.M. Shaw, H.T. Nembach, M.Weiler, T.J. Silva, M. Schoen, J.Z. Sun, and D.C. Worledge. Perpendicular magnetic anisotropy and easy cone state in ta/co fe b /mgo. *IEEE Magn. Lett.*, 6(3500404), 2015.

[111] J.Z. Sun. Consequences of an interface-concentrated perpendicular magnetic anisotropy in ultrathin cofeb films used in magnetic tunnel junctions. *Phys. Rev. B*, 91(174429), 2015.

[112] A.Timopheev, R.Sousa, M.Chshiev, T. Nguyen, and B. Dieny. Second order anisotropy contribution in perpendicular magnetic tunnel junctions. *Scientific Reports*, 6(26877), 2016.

[113] M.A. Ruderman and C. Kittel. Indirect exchange coupling of nuclear magnetic moments by conduction electrons. *Phys. Rev.*, 96(99), 1954.

[114] Y. Yafet. Ruderman-kittel-kasuya-yosida range function of a one-dimensional free-electron gas. *Phys. Rev. B*, 36(3948), 1987.

[115] S.S.P. Parkin and D. Mauri. Spin engineering: Direct determination of the ruderman-kittel-kasuya-yosida far-field range function in ruthenium. *Phys. Rev. B*, 44(7131(R)), 1991.

[116] L. Néel. *Ann. Geophys.*, 5(99), 1949.

[117] W.F. Brown. Thermal fluctuations of a single-domain particle. *Phys. Rev.*, 130(5), 1963.

[118] W. F. Brown. Thermal fluctuation of fine ferromagnetic particles. *IEEE Trans. Magn.*, 15(1197), 1979.

[119] Hong-Ju Suh, Changehoon Heo, Chun-Yeol You, Woojin Kim, Taek-Dong Lee, and Kyung-Jin Lee. Attempt frequency of magnetization in nanomagnets with thin-film geometry. *Phys. Rev. B*, 78(064430), 2008.

[120] P. Gaunt. *J. Appl. Phys.*, 59(4129), 1986.

[121] R. Dittrich, T. Schrefl, A. Thiaville, J. Miltat, V. Tsiantos, and J. Fidler. *J. Magn. Magn. Mat.*, 272-276(747), 2004.

[122] J.W. Lau, J.K. Bording, M. Beleggia, and Y. Zhu. Energy barrier to magnetic vortex nucleation. *Appl. Phys. Lett.*, 88(012508), 2006.

[123] S. Kogan. *Electronic Noise and Fluctuations in Solids.* Cambridge University Press, 2008.

[124] R. Skomski, J. Zhou, R.D. Kirby, and D.J. Sellmyer. Micromagnetic energy barriers. *J. Appl. Phys.*, 99(08B906), 2006.

[125] G.D. Fuchs, I.N. Krivorotov, P.M. Braganca, N.C. Emley, A.G.F. Garcia, D.C. Ralph, , and R.A. Buhrman. Adjustable spin torque in magnetic tunnel junctions with two fixed layers. *Appl. Phys. Lett.*, 86(152509), 2005.

[126] G. Grinstein and R. H. Koch. Coarse graining in micromagnetics. *Phys. Rev. Lett*, 90(207201), 2003.

[127] S. Urazhdin, N.O. Birge, W.P. Pratt Jr., and J. Bass. Current-driven magnetic excitations in permalloy-based multilayer nanopillars. *Phys. Rev. Lett.*, 94(14), 2003.

[128] Z. Li and S. Zhang. Magnetization dynamics with a spin-transfer torque. *Phys. Rev. B*, 68(024404), 2003.

[129] R.H. Koch, J.A. Katine, and J. Z. Sun. Time-resolved reversal of spin-transfer switching in a nanomagnet. *Phys. Rev. Lett.*, 92(088302), 2004.

[130] J.Z. Sun. Spin-current interaction with a monodomain magnetic body: A model study. *Phys. Rev. B*, 62(570), 2000.

[131] S. Petit-Watelot. Influence du couple de transfert de spin sur les fluctuations magnétiques thermiquement activées dans les jonctions tunnel magnétiques. *TEl*, 2007.

[132] N. Krivorotov, N.C. Emley, A.G.F. Garcia, J.C. Sankey, S.I. Kiselev, D.C. Ralph, and R.A. Buhrman. Temperature dependence of spin-transfer-induced switching of nanomagnets. *Phys. Rev. Lett.*, 93(166603), 2004.

[133] X. Zhu and J.-G. Zhu. Angular dependence of the microwave excitation by direct current. *J. Appl. Phys.*, 95(7318), 2004.

[134] R. Dittrich, T. Schrefl, D. Suess, W. Scholz, H. Forster, and J. Fidler. A path method for finding energy barriers and minimum energy paths in complex micromagnetic systems. *J. Magn. Magn. Mat.*, 250(L12–L19), 2002.

## Résumé

Les mémoires non-volatiles magnétiques à effet de couple de transfert de spin - STT-MRAM sont un nouveau type de mémoire pouvant remplacer les mémoires DRAM ou SRAM. Chaque point de mémoire STT-MRAM est une jonction tunnel magnétique sous forme d'un pilier de taille nanométrique, composée de deux couches magnétiques séparées par une barrière d'oxide. L'empilement multicouche doit être élaboré sous ultravide par épitaxie par faisceau moléculaire (M.B.E.) ou par pulvérisation cathodique (P.V.D.). Ces méthodes d'élaboration sont développées par la société Vinci Technologies (finançant ce travail de thèse par une bourse CIFRE).

L'amplitude de la magnétorésistance tunnel, utilisée pour lire les informations stockées dans la mémoire, dépend de l'orientation relative des aimantations des deux couches magnétiques. Par ailleurs, l'écriture de l'information dans le dispositif est obtenue grâce à l'effet de couple de transfert de spin, qui permet la manipulation de l'aimantation en utilisant un courant polarisé. Enfin, la stabilité thermique du dispositif est donnée par la barrière en énergie séparant les deux orientations d'aimantation (vers le haut et vers le bas dans le cas d'un dispositif perpendiculaire). Pour que les STT-MRAM soient une technologie compétitive, la tension critique nécessaire au retournement de l'aimantation (tension d'écriture) ainsi que le temps de retournement doivent être réduits, tandis que la stabilité thermique doit rester suffisamment élevée pour assurer la conservation de l'information. Au cours de ma thèse, en collaboration avec Vinci Technologies, les équipements nécessaires à la croissance des couches minces composant les jonctions tunnels (M.B.E. et P.V.D.) ont été optimisées. Grâce à cela, nous avons pu obtenir des couches minces avec une anisotropie perpendiculaire (hors du plan) bien caractérisée. J'ai ensuite concentré mon étude sur les dispositifs STT-MRAM industriels (IBM et STT) présentant une aimantation perpendiculaire pour comprendre le mécanisme de retournement de l'aimantation induite par le courant. J'ai alors pu identifier les paramètres pertinents influençant la valeur de la tension de retournement et proposer des solutions pour l'abaisser tout en préservant la stabilité thermique.

Grâce à une étude concernant la probabilité de retournement d'aimantation, comparée à une modélisation macrospin et micromagnétique, j'ai mis en évidence un mécanisme de retournement variable en fonction de la configuration magnétique initiale. En effet, le champ rayonné par une couche magnétique sur une autre et la forme de la jonction tunnel ont un impact important sur la manipulation de l'aimantation.



## Abstract

Spin Transfer Torque - Magnetic Random Access Memories – STT-MRAM – are developed as a new type of memory which could replace DRAM or SRAM. In the case of STT- MRAM, each memory point is a nanopillar magnetic tunnel junction composed of two magnetic layers separated by an oxide barrier. The multilayer stack can be grown under ultra-high vacuum using Molecular Beam Epitaxy (MBE) or Physical Vapor Deposition (PVD). Those systems are developed by the company Vinci Technologies (sponsoring this PhD work). The tunnel magnetoresistance signal which depends on the relative orientation of the two magnetizations is used to read the information stored in the device. The writing of the information in the device is realized thanks to the spin transfer torque effect, which allows magnetization manipulation using a spin current. The thermal stability of the device is given by the energy barrier separating the two magnetization orientations (up and down in the case of a perpendicular device). For STT-MRAM to be a competitive technology, the critical voltage needed for magnetization switching (writing voltage) as well as the switching time have to be reduced while the thermal stability remains high enough to ensure the retention of information. During my thesis, in collaboration with Vinci-Technologies several tools to grow thin films have been optimized. With such equipment, we were able to grow thin films with well characterized perpendicular (out-of-plane) anisotropy.

I have then focused my study on industrial STT-MRAM devices (from two companies: IBM and STT) with an out-of-plane magnetization direction so as to understand the mechanism of current induced magnetization switching. By doing so, I could identify the relevant parameters influencing the switching voltage value and propose solutions to lower it while preserving thermal stability.

Through a probabilistic study of magnetization reversal, coupled with macrospin and micromagnetic modeling studies, I have evidenced different switching mechanisms depending on the initial magnetic configuration. Indeed both the stray field from one magnetic layer to the other and the shape of the nanopillar have a large impact on magnetization manipulation.